Dynamics of the Pitch-able VAWT
A Study of the Dynamics of the Vertical Axis Wind Turbine with Individual Pitch Control

LeBlanc, B.P.

DOI
10.4233/uuid:6abb764c-a884-4da9-9f89-7140ee8b097b

Publication date
2024

Document Version
Final published version

Citation (APA)
LeBlanc, B. P. (2024). *Dynamics of the Pitch-able VAWT: A Study of the Dynamics of the Vertical Axis Wind Turbine with Individual Pitch Control*. [Dissertation (TU Delft), Delft University of Technology]. https://doi.org/10.4233/uuid:6abb764c-a884-4da9-9f89-7140ee8b097b

Dynamics of the Pitch-able VAWT

A Study of the Dynamics of the Vertical Axis Wind Turbine with Individual Pitch Control

Dynamics of the Pitch-able VAWT

A Study of the Dynamics of the Vertical Axis Wind Turbine with Individual Pitch Control

Dissertation

for the purpose of obtaining the degree of doctor
at Delft University of Technology
by the authority of the Rector Magnificus, prof. dr. ir. T.H.J.J. van der Hagen,
chair of the Board of Doctorates
to be defended publicly on
Thursday 11, January 2024, at 12:30 o'clock

by

Bruce LeBlanc

Master of Science in Mechanical Engineering
University of Massachusetts Lowell, Lowell, Massachusetts, USA
born in East Templeton, Massachusetts, United States of America

This dissertation has been approved by the promotors.

Composition of the doctoral committee:

Rector Magnificus,	chairperson
prof. dr. G.J.W. van Bussel	Delft University of Technology, promotor
prof. dr. ir. C.S. Ferreira	Delft University of Technology, promotor

Independent members:

Prof. dr. F. Scarano	Delft University of Technology
Prof. dr. D.T. Griffith	U. of Texas Dallas, USA
Assoc. Prof. dr. A. Croce	Politecnico di Milano, Italy
Prof. dr. M. Muskulus	NTNU, Norway
Prof. dr. ir. H.A. Madsen	DTU, Denmark

Reserve members:

Prof. dr. S.J. Watson	Delft University of Technology

Keywords: Vertical Axis Wind Turbine, Pitch Control, PIV, Wake Steering, Structural Dynamics
Printed by: Ipskamp Printing

Front & Back: Bruce LeBlanc

Contents

Summary

Society is finally entering a new age of renewable energy development. For the first time it is truly conceivable to power a vast majority of global energy use with a combination of wind, solar, and other forms of low carbon, renewable power. The rise of electrification and so called ”Power to X”, where renewable energy is used to create other more condensed and potentially storable sustainable fuels, will require a significant increase in the capacity of electrical grid networks worldwide in the coming decades. One of the largest growing sectors in renewable energy is offshore wind power. With farms in operation for over two decades, offshore wind has been predominately deployed in relatively shallow water in the North Sea of Europe. While expanding to global markets is possible with fixed bottom machines, the resource is relatively limited based on the strict seabed requirements. Moving to floating offshore wind platforms, demonstrated in pilot projects like Hywind Scotland, has the potential to vastly expand the potential wind resource and open markets in the Americas and Asia which would otherwise be unreachable.

While there is considerable market pressure to capitalize on the vast knowledge of onshore and fixed bottom offshore wind turbine design and operation for floating applications, there is a large change in design constraints from these previous machines. Every so often it is necessary to step back, reexamine the problem statements being designed for with a fresh perspective, and adapt a first principles approach in order to see if the conventional wisdom is still wise. This thesis presents a body of research on the Vertical Axis Wind Turbine, which just may pose a better first principles approach to extremely large floating offshore wind turbines.

The layout of a vertical axis wind turbine allows for some unique opportunities for flow control on the individual airfoil, the turbine, and the wind farm scale. It may be possible to manipulate the circulation around a rotation of the VAWT in order to maximize power produced on the turbine, farm, and multi-farm scales. This is accomplished through manipulating the circulation of the blades over a rotation of the VAWT, to produce more power locally, and to better entrain energy into the wake of the turbine helping in the farm performance. It is also feasible to manipulate the direction of the receding wake in order to minimize wake loss effects within a wind farm.

Within this research, the aerodynamic loading and structural response of vertical axis wind turbines are studied. This is accomplished through the design, build, test, and analysis of a two bladed H-type VAWT with active pitch control known as the ”PitchVAWT”. The aerodynamic behavior of the VAWT is initially described through the adaptation of engineering level models to predict the loading and performance of a VAWT with pitch control. Based on these expected loads, a mechanical design of the turbine is performed, followed by the design of a control system for operation of the PitchVAWT. After the manufacturing of the turbine, each component is tested thoroughly to verify the mechanical properties. A digital twin of the turbine is then modeled using a one-way coupled multi-body dynamics model. The response of the digital twin was then validated to the fully assembled wind turbine in the Open Jet Facility at TU Delft through experimental modal analysis.

A series of experiments are carried out with a variety of fixed and active pitch conditions for the VAWT. Blade loading data is then compared from collected Particle Image Velocimetry on the operating turbine with measurements made from structural sensors mounted to the turbine struts and with predictions from the various aerodynamic models. Results show excellent agreement between the independent experimental measurements, fluid based and structure based. The ability for the models to capture the dynamics varies with the modeling technique. In general, both the lifting line free wake vortex based methods and the actuator cylinder flow models are able to predict the global behavior well. However, the ability to model higher order phenomena such as blade-vortex interaction, tower shadow, or stalling is generally limited by the inability to properly capture dynamic stall in the low Reynolds number regime in which the turbine was operating. Higher fidelity models will be necessary to properly capture these dynamics.

It was shown through experiments in the Open Jet Facility that by applying a sinusoidal pitch with a phase offset relative to the oncoming wind, the integrated thrust direction can be controlled. As shown in past work, this thrust vector has a direct impact on the evolution of the turbine wake. The global loading behavior of the turbine in active pitch scenarios for this experiment was well captured by the three dimensional free-wake vortex models. This experiment, extrapolated by wake evolution of the vortex models, is presented as a proof of concept for use of blade pitch to control the direction of the evolving wake behind the turbine. This may be performed for vertical axis wind turbines without the traditional cosine losses due to yawing out of the wind which is experienced in horizontal axis machines.

This research was sponsored by a Dutch consortium with partners ECN, GustoMSC, WMC, Marin, and TUDelft under the project Semi-Submersible Support Structure for Vertcal Axis Wind Turbines known as S4VAWT sponsored by TKI - Wind Op Zee.

Samenvatting

De samenleving betreedt eindelijk een nieuw tijdperk wat betreft de ontwikkeling van duurzame energie. Voor het eerst is het echt voorstelbaar om het grootste deel van de energie die wereldwijd gebruikt wordt op te wekken met behulp van wind, zon en andere vormen van koolstofarme, duurzame energie. De groei van elektrificatie en de zogenaamde "Power to X" - waarbij duurzame energie wordt gebruikt om andere, meer gecondenseerde duurzame brandstoffen te creëren die potentiëel opgeslagen kunnen worden - zal de komende decennia een aanzienlijke toename van de capaciteit van elektriciteitsnetwerken over de hele wereld vereisen. Een van de grootste groeisectoren op het gebied van duurzame energie is offshore windenergie. Met parken die al meer dan twee decennia in bedrijf zijn, wordt offshore windenergie voornamelijk ingezet in relatief ondiep water in de Noordzee. Hoewel uitbreiding naar wereldmarkten mogelijk is met 'vaste' windmolens, is het een bron van relatief beperkte omvang vanwege de strenge eisen die aan de zeebodem worden gesteld. De overstap naar drijvende offshore windplatforms, zoals aangetoond in proefprojecten zoals Hywind Scotland, biedt de mogelijkheid om de potentiële windbronnen enorm uit te breiden en markten in Noord- en Zuid-Amerika en Azië te openen die anders onbereikbaar zouden zijn.

Hoewel er een aanzienlijke marktdruk is om te profiteren van de enorme hoeveelheid kennis over het ontwerp en de werking van onshore en offshore windturbines met vaste fundering voor drijvende toepassingen, is er een grote verandering in ontwerpbeperkingen ten opzichte van deze eerdere machines. Soms is het nodig om een stap terug te doen, de probleemstellingen waarvoor wordt ontworpen opnieuw te onderzoeken vanuit een nieuw perspectief, en een first principles benadering toe te passen om te zien of de conventionele wijsheid nog steeds wijs is. Dit proefschrift presenteert een hoeveelheid onderzoek naar de Vertical Axis Wind Turbine (VAWT), die misschien wel een betere kijk biedt op de grondbeginselen ten aanzien van buitengewoon grote drijvende offshore windturbines.

Het ontwerp van een windturbine met verticale as biedt unieke mogelijkheden voor flow control op de individuele aërodynamische vleugel, de turbine en de schaal van het windpark. Het kan mogelijk zijn om de circulatie rond een rotatie van de VAWT te manipuleren om het geproduceerde vermogen op de schaal van turbines, windparken en multi-parken te maximaliseren. Dit wordt bereikt door de circulatie van de bladen, te manipuleren gedurende een rotatie van de VAWT, om plaatselijk meer vermogen te produceren en om energie beter mee te voeren in het kielzog van de turbine, wat helpt bij de prestaties van het windpark. Het is ook mogelijk om de richting van het terugtrekkende zog te manipuleren om het wake loss effect binnen een windpark te minimaliseren.

In het kader van dit onderzoek zijn de aerodynamische belasting en structurele respons van windturbines met verticale as bestudeerd. Dit is bereikt door het ont-

werp, de bouw, het testen en de analyse van een tweebladige H-type VAWT met actieve pitch control, bekend als de ”PitchVAWT”. Het aerodynamische gedrag van de VAWT is allereerst beschreven aan de hand van de aanpassing van modellen op technisch niveau om de belasting en prestaties van een VAWT met pitch control te voorspellen. Op basis van deze verwachte belastingen is een mechanisch ontwerp van de turbine gemaakt, gevolgd door het ontwerp van een besturingssysteem voor de werking van de PitchVAWT. Na de fabricage van de turbine is elk onderdeel grondig getest om de mechanische eigenschappen te verifiëren. Vervolgens is een digitale replica van de turbine gemodelleerd met behulp van een one-way coupled multi-body dynamics-model. De respons van de digitale replica werd vervolgens gevalideerd op de volledig geassembleerde windturbine in de Open Jet Facility van de TU Delft door middel van experimentele modale analyse.

Een reeks experimenten is uitgevoerd met verschillende vaste en actieve pitch conditions voor de VAWT. Bladbelastingsgegevens zijn vervolgens vergeleken aan de hand van verzamelde Particle Image Velocimetry op de in werking zijnde turbine met metingen van structurele sensoren die op de turbinesteunen zijn gemonteerd en met voorspellingen van de verschillende aerodynamische modellen. De resultaten laten een uitstekende overeenkomst zien tussen de onafhankelijke experimentele metingen, gebaseerd op vloeistof en structuur. Het vermogen van de modellen om de dynamiek vast te leggen varieert al naar gelang de modelleringstechniek. Over het algemeen zijn zowel de op lifting line free wake vortex gebaseerde methoden als de actuator cylinder flow modellen in staat om het globale gedrag goed te voorspellen. Het vermogen om fenomenen van hogere orde, zoals blad-vortex-interactie, torenschaduw of afslaan, te modelleren, wordt over het algemeen echter beperkt door het onvermogen om dynamische afslag correct vast te leggen in het lage Reynolds-getalregime waarin de turbine werkzaam was. Modellen met een hogere getrouwheid zullen nodig zijn om deze dynamiek goed vast te leggen.

Door experimenten in de Open Jet Facility werd aangetoond dat door toepassing van een sinusvormige pitch met een faseverschuiving ten opzichte van de tegemoetkomende wind, de geïntegreerde stuwkrachtrichting kan worden geregeld. Zoals aangetoond in eerder werk, heeft deze stuwkrachtvector een directe invloed op de evolutie van het turbinezog. Aangezien het globale belastingsgedrag van de turbine in actieve pitch-scenario’s goed werd vastgelegd door de driedimensionale free-wake vortexmodellen. Dit experiment, geëxtrapoleerd door zogevolutie van de vortexmodellen, is gepresenteerd als een proof of concept voor het gebruik van bladpitch om de richting van het zich ontwikkelende zog achter de turbine te regelen. Dit kan worden uitgevoerd voor windturbines met verticale as zonder de traditionele cosinusverliezen als gevolg van gieren uit de wind die worden ervaren bij turbines met horizontale as.

Dit onderzoek werd gesponsord door een Nederlands consortium met partners ECN, GustoMSC, WMC, Marin en TUDelft in het kader van het project Semi-Submersible Support Structure for Vertcal Axis Wind Turbines, bekend als S4VAWT, gesponsord door TKI - Wind Op Zee.

Nomenclature

Acronyms

AC	Actuator Cylinder
CAD	Computer-Aided Design
CMM	Coordinate Measurement Machine
cRIO	National Instruments Compact Real Time Input/Output Controller
DAQ	Data Acquisition
DIO	Digital Input / Output
DOF	Degree of Freedom
EMA	Experimental Modal Analysis
FEA	Finite-Element Analysis
FEM	Finite-Element Model
FOV	Field of View
FPGA	Field Programmable Gate Array
FRF	Frequency Response Function
HAWT	Horizontal Axis Wind Turbine
IEPE	Integrated Electronics Piezo-Electric
MAC	Modal Assurance Criterion
MBD	Multibody Dynamics
MPE	Modal Parameter Estimation
OJF	Open Jet Facility
PC	Personal Computer
PIV	Particle Image Velocimetry
PSD	Power Spectral Density
QMH	Queued Message Handler

RBE	Mass-less rigid body elements
RT	LabView Real-Time Environment
SCADA	Supervisory Control and Data Acquisition
SIMO	Single Input Multiple Output
UI	User Interface
VAWT	Vertical Axis Wind Turbine
VI	LabView Virtual Instrument

Greek Symbols

α	Angle of attack
β	Compressibility factor, $\sqrt{1-M^2}$
ϵ	Strain
λ	Tip speed ratio
μ	Dynamic viscosity
ν	Poisson’s ratio
Ω	Vorticity
ω	Rotational frequency
ρ	Density
σ	Rotor solidity $Nc/2R$
σ_n	Normal stress
θ	Azimuthal position

Roman Symbols

$\hat{n}$	Surface normal vector
A	Area
a	axial inflow factor
A_1, A_2, b_1, b_2	Beddoes-Leishman indicial-lift constants
B	Number of blades
c	Chord
C_D	Coefficient of drag

C_L	Coefficient of lift
C_n	Force coefficient normal to airfoil chord
C_P	Coefficient of power
C_Q	Coefficient of rotor torque
C_T	Coefficient of thrust
C_{fn}	Blade normal force coefficient
C_{N_α}	Normal force curve slope for dynamic stall model
C_{tan}	Blade tangential force coefficient
F	Force on body
F_n	Blade normal force
F_t	Blade tangential force
I	Identity matrix
k	reduced frequency $k = \frac{\omega c}{2V}$
$LC1, LC2, LC3, LC4$	PitchVAWT load cells
M	Mach number
N	Number of spatial dimensions
Q	Aerodynamic torque
Q_n	Normal volume force per unit blade length
Q_t	Tangential volume force per unit blade length
R	Radius
R_e	Reynolds number
S	Relative distance traveled by a semi-chord of airfoil in time in dynamic stall model
S_b	Surface of body
T	Viscous stress tensor
t	Time
T_p, T_f, T_v, T_{vl}	Beddoes-Leishman time constants
T_x	Thrust in x-direction

T_y	Thrust in y-direction
u	local flow velocity, Noca
U_∞	Free stream velocity
U_{loc}	Local velocity
V	Relative velocity of flow to airfoil used in dynamic stall model

I

Introduction

1

Introduction

For most of history, man has had to fight nature to survive;
in this century he is beginning to realize that in order to survive,
he must protect it.

Jacques-Yves Cousteau

This research takes place at an exciting time for the renewable energy sector, wind energy specifically. The wind energy industry has proven that it can compete on a global scale delivering cost effective, carbon-free, energy with no water consumption during normal operation. This is has been a monumental task requiring decades of scientific research, and engineering breakthroughs in many fields. From aerodynamics and airfoil design, to material science, aeroelastics and control methodology. It is a truly large success story, as clearly exhibited in figure 1.1. However, many hurdles still remain. Recycling of older turbines, namely the blades, remains a concern, as well as grid stability and pricing as variable supply renewable energy sources constitute a much larger percentage of the overall energy supply. The world energy supply is still overwhelmingly dominated by fossil fuel sources, 84.3 % as of 2019[1] and clearly shown in figure 1.2. Wind and renewable sources in general are a small fraction of current energy use. With every kilogram of green house gases emitted into the environment, the effects of global climate change increase. To say that society has a large task ahead of it is a vast understatement. However, it is important to recognize the growth of renewables and perhaps most importantly, the recognition by the general public that a clean, sustainable world is not only possible, but mandatory for the continued advancement of our society.

This thesis focuses on the Vertical Axis Wind Turbine, or VAWT. A type of turbine with a long history which for various reasons was mostly left behind in the expansion of wind energy as a utility scale energy source. However, times have changed in the wind energy world. The design and cost drivers have evolved, along

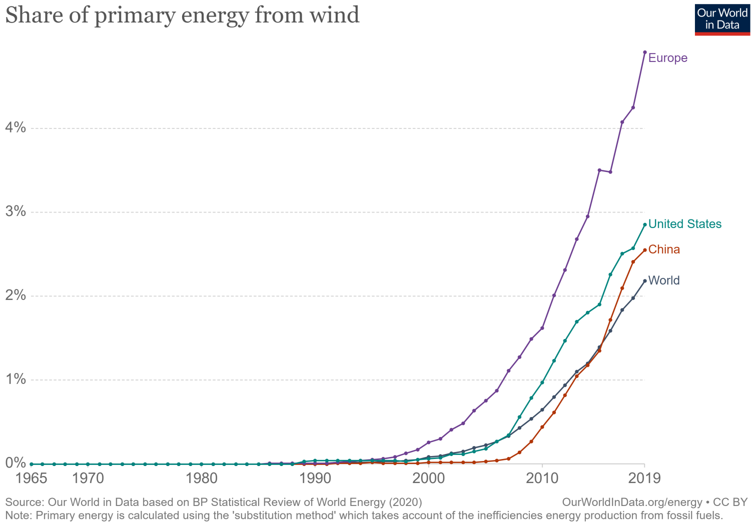

Share of primary energy from wind

Source: Our World in Data based on BP Statistical Review of World Energy (2020) OurWorldInData.org/energy • CC BY
Note: Primary energy is calculated using the 'substitution method' which takes account of the inefficiencies energy production from fossil fuels.

Figure 1.1: Share of wind energy in the global energy supply.[1]

with advancements in analysis techniques and materials science. With these improvements in mind, researchers and engineers have been looking at the VAWT with renewed interest. Predominantly, this research looks into the complex loading of the VAWT with an eye of understanding its strengths and weaknesses, with the aim of contributing useful knowledge in the evaluation of a potential future in the energy mix.

1.1. Historical Perspective

Primitive windmills with vertical axis configurations are known to date back to the ninth century A.D. and potentially as early as the seventh[2]. These mills were partially shielded drag driven machines used for grinding grain. Humanity has been aware of the naturally occurring energy sources which surround us every day and have been working to harness them to our benefit. Once the modern concept of aerodynamics began to be understood on a practical level the benefits of lift driven devices over drag were apparent, providing for both higher efficiency and less susceptibility to damage in high winds. With the advent of electricity and a more modern understanding of aerodynamics, the French aeronautical engineer George Jean Marie Darrieus patented the lift-driven VAWT in 1925. Several small models were built, but it wasn't until the 1950 s when the first electricity producing VAWTs were built, ranging up to 7 kW[3].

During the oil embargo of the 1970s, many western governments began looking for ways to minimize dependence on foreign energy sources and started to diversify their energy portfolios. Sandia National Laboratories, SNL, in the United States was given the task to study alternative sources of energy and quickly began

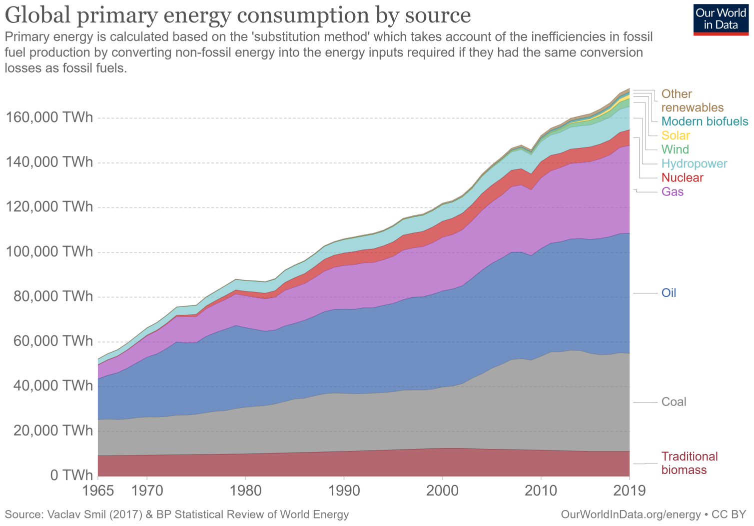

Source: Vaclav Smil (2017) & BP Statistical Review of World Energy

OurWorldInData.org/energy • CC BY

Figure 1.2: Worldwide energy usage with shading depicting energy source.[1]

work on vertical axis configuration wind turbines. Where research and development activities continued until the mid 1990s[4]. As part of this research several test machines were developed and deployed including both drag-driven Savonius turbines and lift-driven Darrieus. Troposkein shaped Darrieus turbines, where the blades approximate the curvature of a spinning rope in order to maximize structural efficiency, dominated the majority of development. SNL deployed a 2 m, 17 m, and 34 m test machines with the latter rated up to 500 kW. Throughout the research program many important aerodynamic and structural design codes were created and validated against a good amount of collected test data from the turbine. The data showed it was possible to achieve comparable power coefficients to horizontal axis turbines of the day, measuring over 40 %. These technologies were then shared with external private companies, namely FloWind corporation which was able to operate a fleet of over 500, 300 kW VAWTs in the Tehachapi pass in California[4]. While the company eventually faltered with the blades failing, generally due to a lack of understanding of high-cycle fatigue in chosen materials, the technology was demonstrated successfully and many excellent lessons were learned. The largest VAWT ever constructed was the 3.8 MW Eole machine, in Quebec in 1987 which was considered at the time to be the longest running, most reliable MW class wind turbine of any type[3]. Although it eventually was stopped from power production due to an uneconomical fix on the main bottom bearing, it still exists as a notable tourist attraction today.

About the same time as the demise of FloWind, the three-bladed up wind horizontal axis wind turbine was beginning to capture the relatively small wind market. Due to the relatively simple aerodynamics of the horizontal axis turbine, the loading was more completely understood with aerodynamic models like the actuator disk and blade element momentum theories of the day. The knowledge of the loading mechanism coupled with the use of composite materials for blade structures and a conservative design for the rotors, allowed the turbines to be more fatigue resistant delivering longer lifetimes. Due to these aerodynamics, higher power efficiencies were managed more consistently providing higher specific power, power per rotor area. At seeing this, most of the private and public research investments migrated to horizontal axis wind turbines leaving most vertical axis research being starved of funds.

1.2. Future Potential for the VAWT

Wind turbines have accelerated growth in size and market reach in the last decade. The next frontier of wind energy involves better utilization of the vast offshore resources that are available across the planet. In 2019, 60.4 GW of new wind turbines were installed, with 6.1 GW being in the offshore sector. This brings the share of offshore wind installations above 10 % of total installations for the first time. According to GWEC predictions, offshore wind is set to increase at an annual rate of 18.6 % until 2024 contributing more than 20 % of wind installations by 2025[5]. However, a significantly large portion of this available resource exists in areas with water too deep for conventional driven pile foundations. This has required designers to explore floating platform options. Beginning around 2025, the floating offshore wind installations are expected to ramp up as more technologies move from initial research into full commercialization. Traditionally, these floating platform designs incur high costs due to the large bending moments, and angular tilt requirements of a traditional Horizontal Axis Wind Turbine (HAWT). Due to the many differences in working with a floating platform compared to a land based turbine, it is useful to re-examine the concept of the wind turbine from the ground up and see if a design that varies from the traditional 3-bladed upwind HAWT is better for this new case.

Research into VAWTs has been progressing over the last few years due to this large shift in design constraints by leveraging tools and experience from research beginning in the 1970s and lasting until the HAWT established market dominance in the 1990s. The beginning studies looking into the feasibility of large VAWT turbines on offshore floating platforms have been largely positive and suggest a large cost savings potential when comparing to equivalent HAWT turbines[6–9]. The largest effects which contribute to the positive trend include in general a lower center of gravity, thereby reducing the overturning moment on the platform, as well as a greater tolerance for platform rotation. These savings assume certain platform cost reductions as well as ease of operations and maintenance due to certain systems being removed, like the active yaw system, and ease of access to significant components such as the gearbox and generator. It needs to be said however, that some of these cost decreases may be offset by an increased cost of the rotor. As the blades of a VAWT are typically longer than those of an equivalent HAWT. There may be some room for minimizing this increased cost due to blade length by simplifying the blade geometry, such as non-twisted constant cross-section blades, which would decrease the cost per blade length.

Another design constraint which begins to become dominant as wind turbines scale in size is cyclical gravitational loading which effects the horizontal axis turbine[10]. The blade weight increases with the turbine radius at a higher rate than do the aerodynamic loads, which means at a certain point depending upon the blade design, the oscillating blade loading due to gravity becomes one of the largest design drivers. Due to the VAWTs orientation, the gravitational loads are present, but do not oscillate with every rotation. This changes the large gravitational load into a quasi-static phenomena rather than a fatigue driving one. The orientation of the loading also changes from an edge-wise phenomena to a span-wise one changing the overall loading of the blades. For instance, edge-wise fatigue may be reduced due to gravity, but blade buckling instabilities may become more of a problem.

An exciting area of potential impact for the VAWT is in densely packing wind farms to increase the overall land use efficiency, and again work to minimize balance of plant costs. This may be possible based upon several factors. Due to the fact that each blade operates in its own wake on the downwind half of rotation, the turbulent mixing of the wake is accelerated, potentially shortening the overall length of the wake deficit[11,12]. Much more study needs to be done to provide more credence in this issue, but the possibility is present. Along the vane of wind farm and wake evolution leads to the possibility of deflecting the wake. This can be done vertically using pitched horizontal struts[13] in order to entrain higher speed flows from above the wind farm down into the farm, re-energizing the wake. It may also be performed with horizontal wake steering, discussed normally in the context of HAWTs[14,15], by utilizing circulation control methodologies to alter the thrust angle of the VAWT[16,17].

1.3. Challenges Facing VAWT Technology

By far the largest challenge when it comes to vertical axis based turbine projects is related to fatigue on practically all of the turbine components. The blades, even in ideal uniform wind loading conditions, undergo an inversion of the pressure and suction sides each rotation. This makes the structural design of not just the blades, but also of the support struts and connection points more complex. The fixed structure sees a load which oscillates in the direction of the wind about a mean thrust value, and a large load which oscillates about zero in the transverse direction which can have as large of an amplitude as the windward loading. This causes excessive wear on the bearing and foundation components of the turbine. The next challenge pertains to the tower based structural dynamics as will be discussed in further chapters. The rotor can enter into resonance with the whirling modes, depending upon the number of blades and the operating conditions these resonances can cause heavy damage, reducing usable lifetime, or sometimes leading to direct failure of the turbine.

Another difficulty lies with the ability to accurately model the aerodynamics in a way that can be properly used for design purposes. There are certain aerodynamic phenomena which are well known to occur, namely dynamic stall and blade vortex interaction, which can alter the loading behavior substantially. While some modeling techniques have been borrowed from other industries, such as helicopter design, the tuning of these parameters to better match the performance of a VAWT is not trivial. Any issue that mis-characterizes the experienced load within aeroelastic simulations may compound, leading to large errors in the design lifetime of the turbines. If the design safety factors aren't conservative enough, the turbine can fail in a much shorter time-frame than expected. This was demonstrated in past VAWT commercial attempts. However, large safety factors can lead to unrealistic turbine costs and prevent the machines from being built in the first place.

The effects of combined wind-wave loading for floating offshore structures will prove to be a difficult task to properly capture. The coupling of the rotor and platform dynamics may be difficult to correctly model with current engineering level solutions. Higher fidelity tools exist to study these effects, however the coupling still requires validation with real world utility scale experimental data. If these problems can be mitigated through research and thorough engineering, a new horizon in the world of large floating vertical axis turbines will become much more attainable.

1.4. Research Questions

With the research environment of wind energy and the VAWT in particular in mind, a series of research questions were formulated to guide work of this thesis.

The forcing function (aerodynamics) and the response function (structural dynamics) represent two major pillars of design for the VAWT. The mis-characterization of these effects have directly led to the failure of previous attempts to build VAWTs and will be the largest source of uncertainty moving into the future. This leads to two main research questions addressed by the thesis.

What are the dynamic characteristics of the load experienced by a VAWT?
and
Are current engineering models capable of representing experienced loading dynamics?

In order to answer these questions, a 2-Bladed H-type VAWT with individual pitch control capability was designed and manufactured. Finite element models and multi-body dynamics models of the turbine system are made and fully calibrated using multiple experimental techniques. The structural model is then coupled to aerodynamic simulations of the VAWT in several fixed pitch configurations from multiple fidelity aerodynamic models. Wind tunnel testing is then performed in the Open Jet Facility of TU Delft using sensors placed on the turbine to measure response dynamics as well as measurement of the flow with Particle Image Velocimetry. With these predictions and data direct comparisons can be made between simulation and experiment of both the aerodynamic flow fields and the structural response of the machine in multiple configurations. With these studies, a view of the aerodynamics, the structural dynamics, and the abilities of typical engineering models to capture them will be analyzed.

With the dynamics of the fixed pitch VAWT studied, the focus of the research is shifted toward actively performing circulation control on the VAWT. The following question is posed:

Can the wake of a VAWT be actively controlled by altering blade loading over a rotation?

The wake of a VAWT is a function of the average thrust loading on the flow over time. Using the simulation and experimental tools developed in the rest of the thesis, the average thrust vector of the turbine is actively varied using blade pitch for the purpose of deflecting the wake of the VAWT. The study acts as a proof of concept for wake steering on Vertical Axis Wind Turbines and opens the door to further optimization studies for wind farm optimization.

1.5. Thesis Layout

After the introduction, the rest of this thesis is presented in six major parts, each of which is shortly summarized herein, with a graphical representation given in figure 1.3.

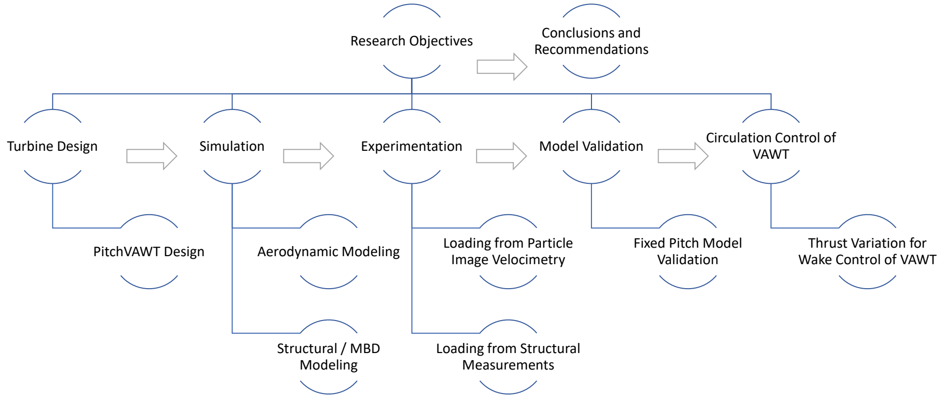

Figure 1.3: Graphical Thesis Layout

Part II: Turbine Design The thesis focuses around a vertical axis wind turbine test bed which was designed, built, simulated, and tested many times throughout the course of this work, referred to throughout as PitchVAWT. The first technical part of the thesis discusses the full design of the PitchVAWT turbine from impetus, to aerodynamics, structural design, and control system.

Part III: Simulation of VAWT Loading This section discusses in detail the simulation tools used to predict the response of the PitchVAWT turbine. First an introduction is given to aerodynamic modeling of wind turbines, with a focus on the VAWT. The models used throughout are then discussed, namely the implementation of the Actuator Cylinder, AC, model along with a Beddoes-Leishman dynamic stall model, and a quick discussion of the three-dimensional free wake vortex models.

A fully calibrated finite-element model and multi-body dynamics model are developed for the turbine in order to properly understand loading and dynamics of the operating system. The calibrated models are presented along with a study of dynamic excitation during loading ramps of the PitchVAWT turbine with expected aerodynamic loading.

Part IV: Experimental Demonstration of VAWT Loading Wind tunnel tests are performed on the PitchVAWT turbine with multiple pitching configurations in order to capture load shifting behavior of fixed pitch offsets. Data is collected using Particle Image Velocimetry to measure dynamic flow conditions and to estimate blade normal and tangential loading for the different pitch configurations. Due to the complex loading nature of the VAWT, phenomena such as dynamic stall, tower shadow, and blade vortex interaction are studied in detail. A similar set of tests were conducted using a strain-gage sensors mounted on the struts of the blades in order to estimate the normal force acting on the turbine in a completely independent way from the wind velocity measurements of PIV. Due to the sensors being integrated within the turbine controller, a much finer pitch and azimuthal resolution is possible. Providing for a different set of insights into the loading dynamics of the VAWT.

Part V: Experimental Validation of Modeling with Fixed Pitch Offsets The models discussed in part III are used to simulate the performance of the PitchVAWT turbine in the specific conditions present during the wind tunnel tests discussed in part IV. Each of the models, are compared with each other in multiple pitch conditions, as well as directly with the measurement data from the strain gage sensors and the load estimations from the PIV data. Insights are provided showing areas where the models perform well, and where there is substantial room for improvement.

Part VI: Circulation Control for Wake Deflection Lessons learned from the experimentation and model validation of parts IV and V are extended to a case of active circulation control with the goal of controlling the wake dynamics of the VAWT. Active sinusoidal pitch configurations are tested with the aim of shifting the directionality of the mean thrust vector of the VAWT. Simulations and experiment are compared showing good agreement between each method. The simulations are then used to extrapolate the experimental data to analyze the wake development of the VAWT. This demonstrates a proof of concept of actively controlling the evolution of the wake for an individually pitch controlled Vertical Axis Wind Turbine.

Part VII: Conclusions In this section, the work of the thesis is recapitulated, and main conclusions are drawn. The original research questions as proposed in this chapter are reviewed and addressed. As with most projects, many questions remain unanswered in the larger picture of Vertical Axis Wind Turbine development, and some next steps for research are proposed.

II

Turbine Design

2

PitchVAWT Design

Science can amuse and fascinate us all,
but it is engineering that changes the world

Isaac Asimov

Blade pitch has been proposed as a method to control circulation of the Vertical Axis Wind Turbine. Circulation (or load) control can potentially change the overall aerodynamic loading for multiple objectives, from power optimization to thrust direction control and wake control. The research in this thesis aims to experimentally demonstrate these phenomena with the use of a 1.5 m *diameter,* 1.5 m *height, two bladed H-Darrieus vertical axis wind turbine with individual blade pitch control. This chapter presents the aerodynamic, structural, controller, and instrumentation design of the PitchVAWT turbine. The resulting turbine will be used for collecting a wide array of experimental data of a VAWT in several loading conditions for the use of experimental demonstration and model validation.*

Parts of this chapter have been published in AIAA Conference Series [18]

2.1. Introduction

As discussed in chapter 3, a Vertical Axis Wind Turbine undergoes a variety of complex aerodynamic phenomena and loading fluctuations throughout each rotation. A few known examples are: large angle of attack swings, unsteady flow, dynamic stall, blade vortex interaction and tower shadow. This leads to many inherent difficulties for designers to properly characterize the loads and performance of these turbines, especially in understanding fatigue. An additional challenge for this work is that experimental research on VAWTs has mostly focused on fixed pitch turbines with the goal of understanding the complex nature of the aerodynamics.

One way of potentially improving the performance, limiting loading in high stress regimes, or even directing the mean thrust vector of the turbine during operation is to use active circulation control. This actively alters the aerodynamics of the turbine in real time in order to achieve a pre-defined goal, such as minimizing the effect of dynamic stall, aerodynamic braking, improving self-start capability, improving power capture, controlling the direction and shape of the wake, or minimizing loads during survival wind speed events at sea[8,17,19–21]. One method to control aerodynamic loads on the turbine is through varying the pitch of the turbine. With pitch control it will be possible to tailor the loading of the turbine as a function of azimuth.

There are two main categories of variable pitch VAWTs, the first is referred to as active pitch or 'forced-pitch', while the second is a passive pitch system. Active pitch VAWTs control the blade angle based upon a defined pitch schedule as a function of azimuth position relative to the wind direction, or based upon a closed loop control of local sensors. A passive system allows the airfoil to pivot on a pitch axis due to the natural moments acting on the airfoil from the wind conditions present. Passive systems have the ability to improve performance of smaller low TSR VAWTs by preventing stall,[22,23] however these systems are not suitable for testing the viability of potential pitch regimes. Active blade pitch systems have largely been limited to sinusoidal excitation with the use of mechanical devices such as cams or gears to prescribe a particular pitch motion[24]. These systems allow the capability to test certain sinusoidal pitch phenomena however are not able to meet the demands of the varying potential pitch schedules required for optimizing power production or limiting thrust loads in higher wind conditions. In order to verify the performance of potential pitch schemes for e.g. thrust magnitude and direction control, power control in multiple Tip Speed Ratios (TSRs) and self start ability, we require an independent pitch control system with the ability to function at a rate greater than once per revolution.

This chapter presents the current state of experimental validation for VAWT models and identifies a gap within the validated cases and the models. This is followed by the complete design and analysis of a new wind turbine used for the study of structural and aerodynamic loading of a VAWT with the capability of fully active variable pitch control.

2.2. Impetus for PitchVAWT Turbine Design

Scaled experimental campaigns, such as those conducted in wind tunnels, can be targeted to address a number of critical assumptions within the designing and modeling of systems. There are always sets of assumptions built into the various designs of a system such as a vertical axis wind turbine. These assumptions stem from the expected aerodynamic performance of the turbine, how much power is expected for a given wind condition, to calculation of loading for lifetime assessment of the mechanical components of the turbine. There are also unknowns as to how the larger system will perform and how the individual components will behave when coupled. It is possible that new flow physics could become relevant at specific areas of a rotation. For example, a dynamic stall event or a blade vortex interaction can lead to an unexpected excess loading causing a decrease in machine lifetime along with a reduction of power capture. The early models used to predict VAWT behavior, such as the Single and Multiple Stream Tube, models as discussed in chapter 3 focused almost exclusively on the power performance and torque produced by the rotor[25–29]. Namely because the power efficiency was the initial driving factor for many designs, and because it is the easiest to measure experimentally. It was known that due to the simplifying assumptions of the modeling that the actual blade loading would differ quite substantially from what was predicted in the Single and Multiple Streamtube models[30]. Therefore more complex models were derived in order to better predict these loads, namely the Double Multiple Streamtube, Actuator Cylinder, and vortex based methods. However these models were typically compared to published data for the VAWTs, which was mostly limited to power and torque coefficients for differing wind conditions[31–33]. During the development of the Actuator Cylinder model, experiments were performed also assessing the loading on the blades of the VAWT[34] in multiple pitched conditions showing variation of thrust with tip speed ratio and good agreement in principle with the actuator cylinder modeling approach. A tow tank experiment was performed during the development of the Sandia VDART vortex model showing very good agreement between measured normal and tangential forces measured during the tow-tank experiment and the model for specific tip speed ratios[35]. Sandia published another extensive dataset for the 34 m test turbine including strain gages on the blades, giving frequency content of loading as well as mean stresses[36]. This data is very valuable, however still misses information necessary for more complex model predictions, such as overall turbine thrust or blade loading over binned into azimuth position. There are also potential changes due to turbine pitch variations which have not had proper validation with experimental data.

A nice review of experimental results available for vertical axis wind turbines was published by Battisti et al.[37] which highlighted some gaps in the available literature on experimental campaigns and namely looked into the difference in Troposkien vs H-shaped vertical axis turbines. Mauri et. al[38] have designed an active variable pitch VAWT for use in external conditions for making power, and have adapted it for use in a wind tunnel. However, few published campaigns have measured the loading with a pitch controlled turbine in controlled conditions. There have also been measurements taken during the development of the Nenuphar offshore turbine[39], which are valuable, but are also very specific to the turbine in development and lack some crucial details which are needed for more generalization, such as more information of the turbine design. The data is also collected in the field, so the dataset is less controlled than is possible within a wind tunnel setting.

The construction of the PitchVAWT turbine is meant to address two objectives. First, to provide experimental validation for numerical models of VAWT loading and performance in varying pitching conditions. Second, to demonstrate the potential for active pitch mechanisms to vary the blade loading and influence the integrated thrust of the rotor and thus flow and wake control.

2.3. PitchVAWT Turbine Design Criteria

The main design objective is to develop a vertical axis wind turbine which can operate in controlled wind conditions of a wind tunnel in order to study the loading of a VAWT based upon various fixed and variable pitch strategies and its effect on the flow field. The results of the wind tunnel tests are used to demonstrate variable turbine loading scenarios and to validate turbine aerodynamic and structural models. Moving forward with the design requires a set of specific design goal criteria, these requirements are:

- Must be able to operate within the Open Jet Facility of TU Delft
- Must be oriented in a Vertical Axis Configuration
- Must be based upon the Darrieus lift based design
- Must be able to pitch the blades independently
- Must be able to pitch the blades ±10° per rotation of the turbine based upon azimuthal position
- Blade bending must be limited to 2.5 mm at blade center in all operating states

These design requirements are considered minimally restrictive in order to perform the stated goal of operating the turbine with variable loading configurations within the open jet wind tunnel shown in section 2.3.1. The design criterion of operating in the OJF puts an upper limit on the turbine cross-sectional area to prevent excessive tunnel blockage. Limiting the design to a lift-based VAWT is to align with potential future megawatt scale designs. The ability to pitch the blades independently allows for studying self-start capability as well as a wide variety of pitch combinations in operation, this is especially important in VAWT architectures as the aerodynamic loading changes dramatically with azimuth position as introduced in chapter 3. A pitch requirement of ±10° per rotation is chosen in order to provide substantial loading authority from the pitching of the airfoils. The vibration response of the turbine is crucial in the measurement of turbine loading as well as turbine operation, as will be discussed in chapter 4. Blade bending is limited in order to decrease uncertainty regarding blade shape through bend-twist coupling.

Satisfying the above requirements is completed by first understanding the expected turbine loading profile so that the components can be properly sized. This starts with a look at the expected aerodynamic loads, and required rotational speeds during testing profiles.

2.3.1. Open Jet Facility Overview

The Open Jet Facility (OJF) at Delft University of Technology, overview graphic shown in figure 2.1, is used for testing of the turbine model. It is capable of maintaining a steady flow field from approximately $4\,\mathrm{m\,s^{-1}}$ to $35\,\mathrm{m\,s^{-1}}$ wind speeds. It is powered by a 500 kW fan motor and has a cross section of $2.85\,\mathrm{m} \times 2.85\,\mathrm{m}$ hexagonal output jet. The test section has a cross section of 13 m wide and 8 m tall. The size of the output jet of the wind tunnel sets an upper limit to the potential size of the PitchVAWT turbine, as discussed later in section 2.4.2. The lower limit of the tunnel wind speed also places a bound to the maximum tip speed ratio capable for testing with active pitch control due to pitch rate limits for the turbine as discussed in section 2.5.2.

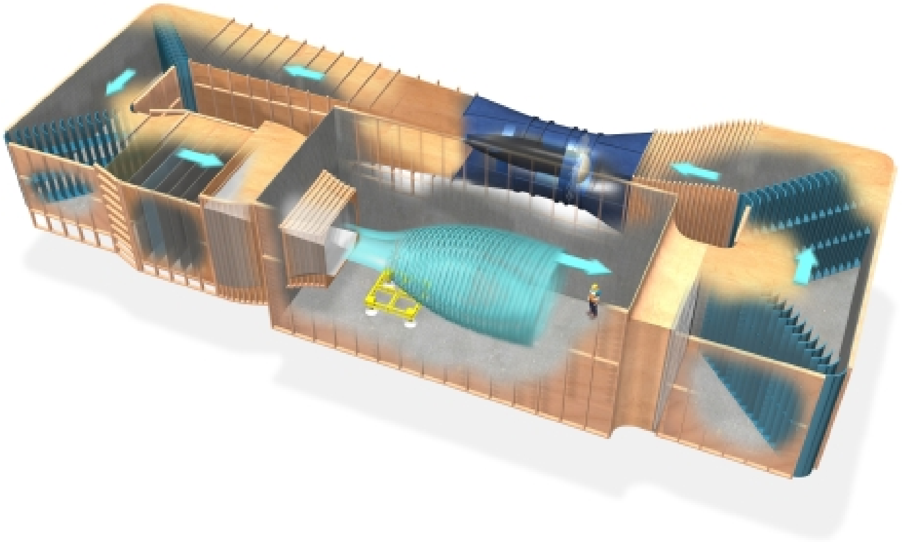

Figure 2.1: Overview graphic of the Open Jet Facility at TU Delft

2.4. Aerodynamics

In order to design the turbine properly, some initial design decisions and calculations need to be made. The rotor shape, size constraints, turbine solidity, blade count, and chord length will be discussed. Expected maximum operating loads will be calculated using the actuator cylinder model discussed in detail in Section 3.3 ;

2.4.1. Aerodynamic Planform

Past testing for lift driven VAWTs generally have one of two main geometries: that of a troposkein curve, which follows the natural arc of a rope spinning about a vertical axis, or a straight-bladed configuration. A lot of the data which has been used to validate the vortex method and engineering level models currently used in design have come from the Sandia National Laboratories (SNL) test machines[27,40,41] which are built with the troposkein geometry. The more recent Deepwind and SNL[7,9,42] projects have also used this geometry in order to minimize blade weight. However, due to the constant curvature of the blades, installing an active pitch system would become extremely complicated, if not impossible without drastic changes to the shape or active systems.

Straight bladed VAWTs which incorporate some version of variable pitch have been known as the Giromill concept and have been studied by McDonnell aircraft and Kirke, among others[43,44]. Current research projects for the multi-megawatt class have been designed using this geometry for manufacturing benefits of the blades as well as ability of easily mounting a pitch control mechanism[8,39,45,46]. Several other experiments have been performed on the aerodynamics of the straight bladed VAWT[12]. Due to the relevance of these projects to the aim of this work, as well as the relative ease of implementing an individual pitch control mechanism, a straight-bladed H type VAWT design was chosen.

2.4.2. Rotor Sizing

The sizing of the turbine is controlled by several factors. First, the pitch system needs to be able to respond at a frequency approximately four times that of the rotational rate of the turbine in order to match potential load distributions for the rotor. The larger the turbine, the slower the rotational rate required to achieve each TSR value for a given wind speed. The aspect ratio of the turbine is important for the characterization of two dimensional flow in the mid-plane of the rotor and should be as large as possible for comparison to two dimensional numerical models and PIV measurements. It is also important to ensure the area of the turbine is small enough in order to minimize the flow obstruction of the tunnel outlet. A straight bladed VAWT with a height and diameter of 1.5 m was chosen as the largest turbine cross-section without significantly restricting the flow of the tunnel causing blockage effects. The frontal area of the turbine is 2.25 m^2, however, since air flows through the turbine, the effective frontal area is less. The effective frontal area is calculated by comparing the expected thrust coefficient to that of a flat plate completely obstructing the flow, as shown in equation 2.1. The expected thrust coefficient of the turbine as calculated in section 2.5.4 is 0.9. While a flat plate at 90° orientation to the flow has a drag coefficient of 1.17. This gives an effective frontal area for the turbine to be 1.73 m^2. The OJF has an octagonal cross-section with an output area of 7.43 m^2. Therefore the effective blockage ratio for the turbine is 23 %. Based upon corrections for open jet wind tunnels presented in AGARD[47] the corrected tunnel velocity at the turbine is expected to vary by less than 1 % from the measured value.

$$A_{eff} = \frac{Ct_{turbine}}{Cd_{flatplate}} A_{turbine} \tag{2.1}$$

VAWT rotor design is primarily dependent upon both the solidity and the number of blades.

Solidity Turbine solidity is defined as the ratio of blade area to rotor frontal area. For a two dimensional analysis this breaks down to the ratio of chord length to rotor diameter for a given turbine height, given in equation 2.2. The solidity and the optimal tip speed ratio are inversely proportional. So in general for a given power, there is a design trade-off between torque and rotor speed based upon the solidity. The higher the solidity, the slower the rotation, and the higher the generated torque. The higher torque directly influences the cost of many of the drivetrain components of the turbine. So it is generally preferred to spin faster. However turbine struts act as parasitic drag, reducing efficiency at higher tip speed ratios. Therefore a compromise is needed based upon the desired operating conditions of the given turbine design. Most larger VAWT designs discussed above have a solidity of approximately 0.1. In the interest of maintaining similarity as much as possible this value was chosen for the PitchVAWT turbine as well.

$$\sigma = \frac{Nc}{2R} \tag{2.2}$$

Number of Blades Two blades were chosen in order to maximize the chord length per blade while maintaining rotor solidity. This allows the blade Reynolds numbers to approach 1.2×10^5 allowing better prediction of airfoil performance with available tools such as Xfoil[48]. The consequence of using two blades is a large oscillation in rotor thrust and torque on a twice per revolution, 2P frequency, from a fixed reference frame. Research of thrust measurement and control will have to take this oscillation into account. Loading of an individual blade in the rotational reference frame is unaffected by total number of blades.

Chord Length Given the turbine maximum diameter, rotor solidity, and number of blades, the chord length is fixed at 75 mm.

2.4.3. Airfoil

The airfoil was chosen to be the symmetrical NACA0021 due to its relative thickness for better structural performance and its prevalent use in other research turbines of this scale[38].

Reynolds number determination The chord Reynolds number during normal operation for the turbine varies with the local wind speed during the rotation. The Actuator Cylinder model described in chapter 3.3.1 was used with an inviscid polar to calculate the expected local velocity at a tip speed ratio of $\lambda = 4$, and free-stream wind speed of $U_\infty = 5\,\mathrm{m\,s^{-1}}$. Using the above chord length of 75 mm and typical values of air density, $\rho = 1.225\,\mathrm{kg\,m^{-3}}$, and dynamic viscosity $\mu = 1.85 \times 10^5\,\mathrm{Pa\,s}$, the local Reynolds number is calculated using equation 2.3. The resulting local Reynolds numbers, as shown in figure 2.2, cover a range from 0.6×10^5 to 1.0×10^5.

$$R_e = \frac{\rho U_{loc} c}{\mu} \tag{2.3}$$

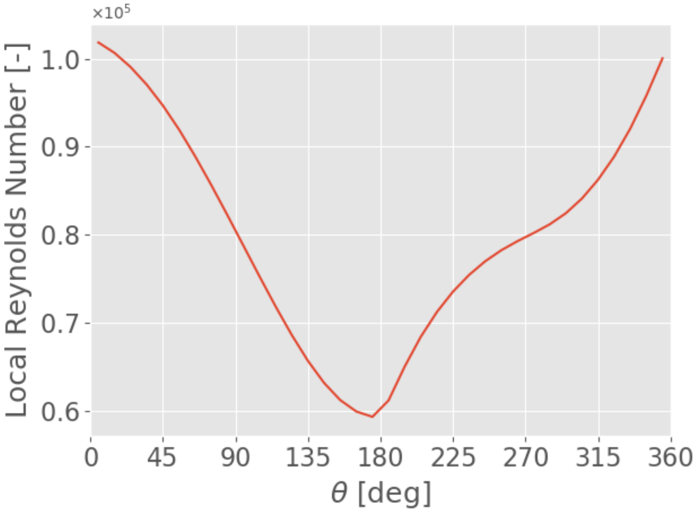

Figure 2.2: Local Reynolds number variation for PitchVAWT over a rotation

Viscous polars The difference in Reynolds number over the rotation is relatively large when taking into account that the airfoil performance in low Reynolds flows is more sensitive to Reynolds number than is typical for higher Re flows. The variation in C_L and C_D for a given set of Reynolds numbers is shown in figure 2.3. Within the current formulation of the AC model given above, only a single airfoil polar is used throughout the rotation. This can have an impact in the calculation of rotor loads and dynamic stall behavior, however the exact effect of this is considered out of scope in this design. Therefore, the polar at a Reynolds number of 0.9×10^5 is used in the analysis.

Airfoil Trip

It is difficult to predict the transition location from a laminar to turbulent boundary layer on the airfoil causing errors in the estimation of airfoil loading, especially in

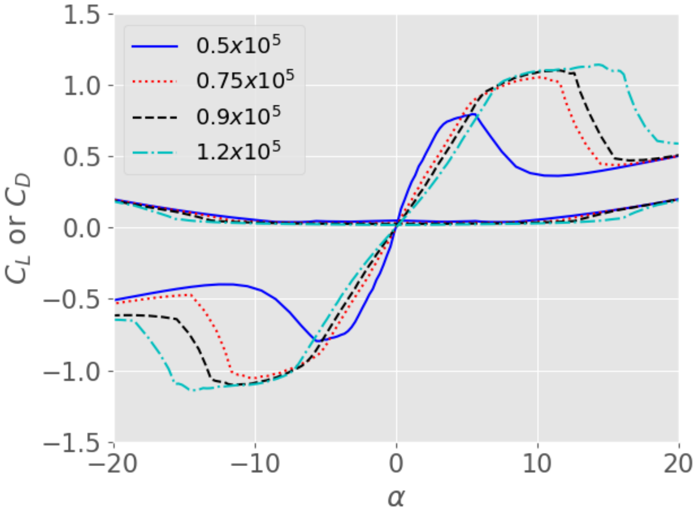

Figure 2.3: Viscous airfoil polar showing C_L and C_D for the NACA 0021 in relevant Re range, calculated in XFOIL

low Reynold's nubmers. In order to minimize this error, it is common practice in wind tunnel testing to force the transition to a turbulent boundary layer by applying a trip at a known location on the chord. For certain tests, this has been performed on the PitchVAWT turbine. A design for the trip including the location and height of the trip tape is performed based upon the work of Braslow et al.[49]. This design is given in Appendix A

2.5. Definition of Operational Loading

The operational loads of the wind turbine are dependent upon the wind speed, the tip speed ratio, and the pitch schedule being tested on the turbine. As a large variety of different pitch conditions are available with completely independent pitch control, we'll focus first on the effects of tip speed ratio and wind speed.

2.5.1. Tip Speed Ratio

The apparent wind velocity experienced by the blades is a combination of two vectors, the local wind velocity (U_{loc}) and the rotational velocity of the blade itself ($R\omega$). At low TSRs the relative value of the local wind is of comparable magnitude to the rotation of the blade. Therefore, the angle of attack change between upwind and downwind passes is large. As the TSR increases, the proportion of the total velocity attributed to the rotation increases. As this doesn't vary during the rotation, the angle of attack range experienced by the blade reduces. This is shown in figure 2.4. At a TSR of 4, the range of angle of attack drops to $-7.4°$ to $11.1°$ or a swing of $18.5°$. This effects the overall rotor thrust and power produced as shown in figure 2.5, with a continually increasing thrust coefficient and a maximum power coefficient at a TSR between 3 and 4. The actual maximum power, both magnitude and the TSR at which will occur, will be effected by any struts or external drag losses which are not modeled here, however this serves as a good baseline for the design. All TSRs up to 4 will be tested throughout the use of the turbine, however the maximum loads will be studied at a TSR of 4.

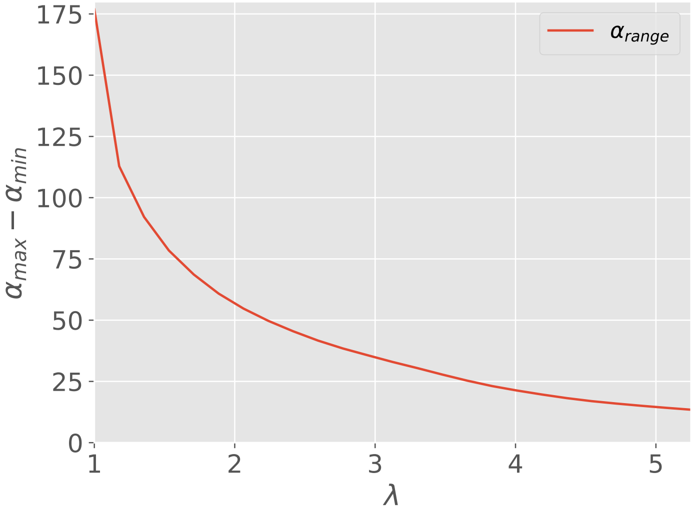

Figure 2.4: Extremes of α reduce with respect to tip speed ratio, λ.

2.5.2. Speed limitations

Wind speed alone is not a strict limit for the turbine in the OJF. However, the turbine rotational speed has a direct effect on the pitch rate of the turbine, and the structural loads of the rotating blades.

Fixed pitch operation

In fixed pitch operation, ignoring structural dynamics of the turbine and base structure, the only practical limit to rotational speed is the strength of the blades and connection with the struts. In order to keep centripetal accelerations within reason, limiting the blade deflection and loading on the struts, the maximum designed rotational speed is 350 $\mathrm{rev\,min^{-1}}$. This corresponds with a wind speed of 6 $\mathrm{m\,s^{-1}}$ at a tip speed ratio of 4.5. As is shown in section 2.6.8 on the structural dynamics and Campbell diagram of the built PitchVAWT the rotational speed is limited to less than this in the current design. However improvements to the base mechanism are possible allowing to reach higher rotational speeds in fixed pitch operation.

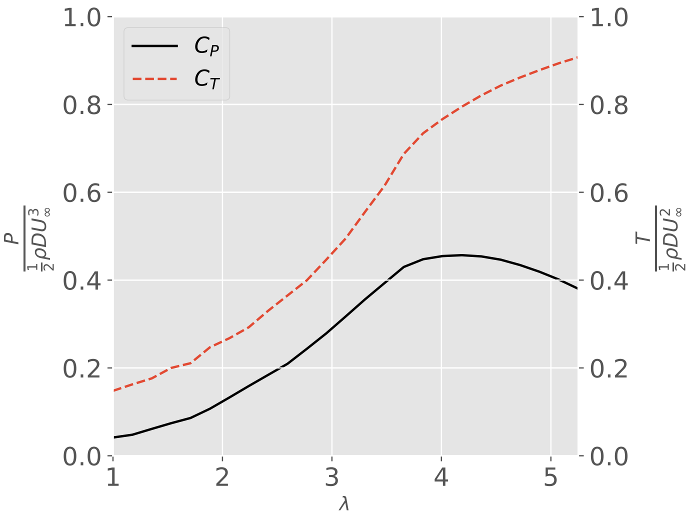

Figure 2.5: Power and thrust coefficients versus λ for PitchVAWT, calculated with dynamic stall and a viscous airfoil polar at $Re = 0.9x10^5$

Variable pitch operation

Variable pitch operation of the VAWT poses another limit on the rotational speed of the turbine as the pitch motors need to be able to react fast enough to prescribe the pitch motion as intended based upon either independent control signals or a pre-determined pitch schedule based upon azimuth position of the blades.

Pitch rate The desired pitch rate for individual pitch control is bound on the upper end by the ability to maximize power performance. This typically requires the airfoil pitch to cancel out the sinusoidal nature of the angle of attack over the rotation and instead jump between two fairly constant angles of attack, one up-wind and one down-wind with the intent to maximize the power conversion efficiency of the rotor by keeping the airfoil operating at a high efficiency over as much of the rotation as possible. An example of one such pitch trajectory is given in figure 2.6. In this figure, the angle of attack is given with no pitch action at all labeled as "α_0" in the solid line. This is the raw performance for the PitchVAWT turbine at a tip speed ratio of 4. The combination dash-dot line is the pitch setting at each azimuth position to achieve the maximum C_P for this model. The dashed line represents the experienced angle of attack due to the optimum pitch setting. At a wind speed of 4 m s^{-1} and a λ of 4, about 205 / min, the pitch rate already approaches 300 ° s^{-1}, as shown in figure 2.7.

Unsteady Effects

As discussed by Ferreira[11] due to the variation of local velocity with respect to azimuth position the reduced frequency of the VAWT can be approximated to equation

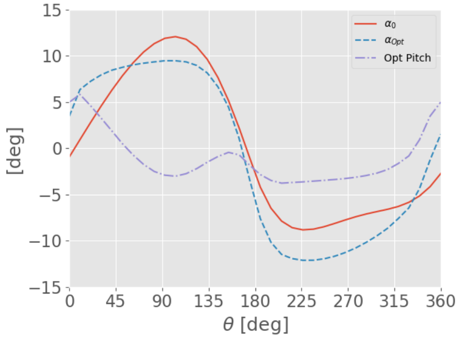

Figure 2.6: Optimal pitch setting for $C_{P_{max}}$ $\lambda = 4$

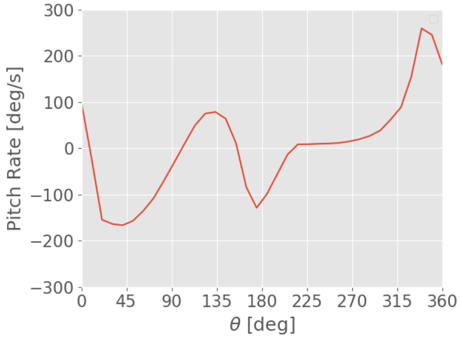

Figure 2.7: Pitch rate at $U_\infty = 4\,\mathrm{m\,s^{-1}}$

2.4. Given the turbine chord of 0.075 m and radius of 0.75 m, the reduced frequency of the PitchVAWT is 0.05. This puts the chord-wise flow right on the border of the unsteady regime as discussed by Leishman[50]. This has the effect that in most cases calculation of the loads can be considered quasi-steady. In most analysis situations however, a Beddoes-Leishman unsteady aerodynamics and dynamic stall model has been implemented which is described in detail in chapter 3.

$$k = \frac{\omega c}{2\lambda U_\infty} = \frac{\omega c}{2\omega R} = \frac{c}{2R} \tag{2.4}$$

2.5.3. Summary of turbine operational conditions

The above discussion is summarised in table 2.1 which presents the design specifications for the PitchVAWT turbine. A 1.5 m diameter H-VAWT turbine with two struts per blade. A NACA 0021 airfoil with a chord of 75 mm was chosen for the blades, and a NACA 0018 was chosen as the strut airfoil. The turbine has chord based solidity of 0.1 and a chord to radius ratio of the same. The maximum turbine rpm is limited to 350 $\mathrm{min^{-1}}$ to keep centripetal loads on the blade connections within reason of standard materials. Another limit on rotation rate of the turbine is dictated by structural dynamics of the full system which is discussed in Chapter 4.

2.5.4. Load Calculations

Given the above turbine specifications, models were run using the Actuator Cylinder model to calculate expected turbine loads in a fixed pitch configuration. These calculations are considered conservative from the aerodynamic side as things such as strut loss and three dimensional effects are neglected.

Power

Starting with the expected power, equation 2.5 gives the power for the turbine based upon the power coefficient, C_P. The above simulations in the shown figure 2.5 show this to be 0.34 for a given λ of 4. Substituting the other known variables of

Table 2.1: PitchVAWT Specifications Overview

Property	**Dimension**
NBlades	2
NStruts	4
Height	1.5 m
Diameter	1.5 m
Blade Chord	0.075 m
Strut Chord	0.060 m
Solidity	0.1
Blade Airfoil	NACA0021
Strut Airfoil	NACA0018
Operating TSR	1 to 4
Max RPM - Fixed Pitch	350 min^{-1}

the turbine the maximum expected aerodynamic power at a wind speed of $5\,\mathrm{m\,s^{-1}}$ is 63.7 W. This is before any losses due to bearing friction, or strut drag.

$$P = C_P(1/2\rho A U_\infty^3) \tag{2.5}$$

$$P = (0.34)(1/2(1.225\,\mathrm{kg\,m^{-3}})(2.25\,\mathrm{m^2})(5\,\mathrm{m\,s^{-1}})^3) \tag{2.6}$$

$$P = 59.3\,\mathrm{W} \tag{2.7}$$

Torque

The expected aerodynamic torque coefficient of the turbine can be calculated by dividing the power coefficient by the tip speed ratio. The aerodynamic torque at a wind speed of $5\,\mathrm{m\,s^{-1}}$ is then calculated to be 2.22 N m.

$$C_Q = \frac{C_P}{\lambda} = \frac{0.34}{4} = 0.085 \tag{2.8}$$

$$Q = C_Q(1/2\rho A R U_\infty^2) \tag{2.9}$$

$$Q = (0.085)(1/2(1.225\,\mathrm{kg\,m^{-3}})(2.25\,\mathrm{m^2})(0.75\,\mathrm{m})(5\,\mathrm{m\,s^{-1}})^2) \tag{2.10}$$

$$Q = 2.22\,\mathrm{N\,m} \tag{2.11}$$

Instantaneous torque Due to the aerodynamic nature of the VAWT, the average value isn't indicative of the actual experienced loading at any given period of time. Each blade contributes a majority of the aerodynamic torque in the upwind half of the rotation, leading to a torque ripple effect which has been documented in detail in past studies[51] and is very prominent with a two-bladed machine, as shown in figure 2.8 calculated with the AC model. The maximum torque expected during a rotation is 4.5 N m.

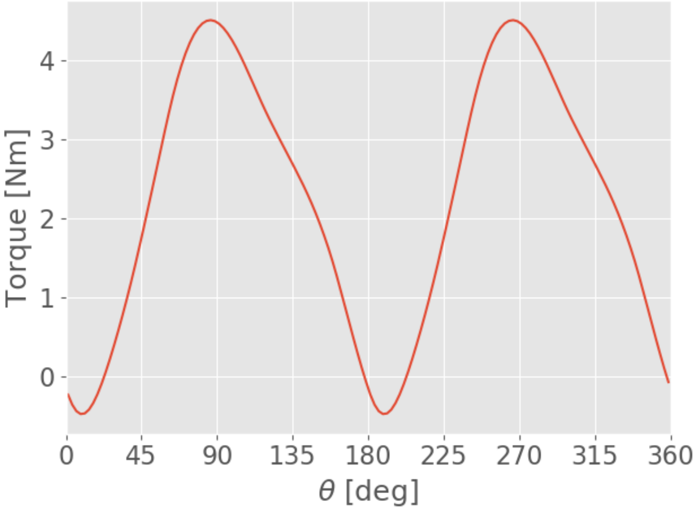

Figure 2.8: Instantaneous aerodynamic torque for PitchVAWT turbine at $U_\infty = 5\,\mathrm{m\,s^{-1}}$

Blades

There are two primary sources of loading for the turbine blades which need to be considered in the design. The first are the aerodynamic forces on the blades which can be modeled using the AC model described prior. The next set are the loads due to the rotation of the turbine itself. These are analyzed separately.

Aerodynamic forces The aerodynamic forces of the turbine are calculated using the above conditions of wind speed, $U_\infty = 5\,\mathrm{m\,s^{-1}}$ and tip speed ratio, $\lambda = 4$, with the Actuator Cylinder model representation. The above instantaneously varying torque load is directly due to the variation of loading on the rotor blades around the azimuth of the turbine. The aero-loading is shown resolved into normal and tangential directions relative to the surface swept by the blades in figure 2.9. The blade normal load oscillates in a 1P, once per rev, fashion between approximately 40 N in toward the center on the upwind section of the rotation and 30 N away from the center, shown as negative load, during the downwind pass. The tangential load is much smaller in magnitude compared with the normal load. It also exhibits cyclic behavior with the majority of torque being produced during the upwind pass, 0° to 180°.

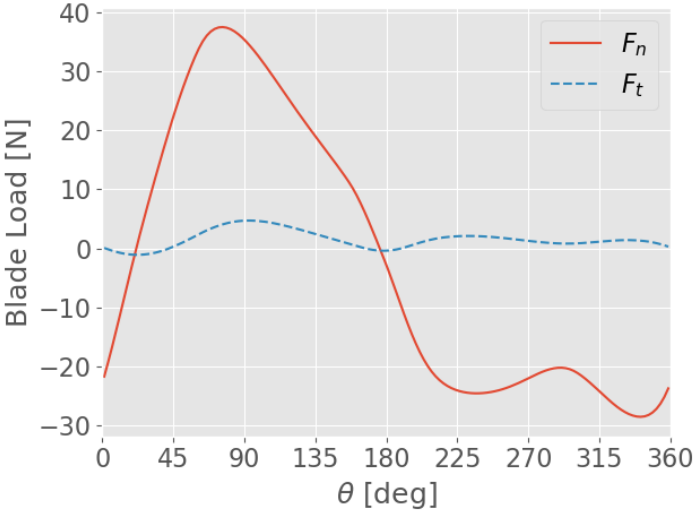

Figure 2.9: Instantaneous aerodynamic blade loading for PitchVAWT turbine at $U_\infty = 5\,\mathrm{m\,s^{-1}}$

Centripetal loading The blades experience an acceleration due to the rotation about the vertical tower which increases with the rotational speed squared. For a simplified model assuming a point mass for the blades and mounting hardware, m_{blade}, located at the radius of the turbine, R, and rotating with circular frequency, ω the acceleration is calculated as shown in equation 2.12, to be $533\,\mathrm{m\,s^{-2}}$, or 54.4 g. The force due to this acceleration cannot be directly calculated without having a complete design for the blades, so this will be revisited later in the chapter. However as a first pass assumption of 1 kg per blade, the centripetal force of 533 N is an order of magnitude larger than the aerodynamic forces. This ratio changes with larger turbines due to the required rotational speed to reach a given λ reducing with increasing radius.

$$a_{cent} = R\omega^2 = (0.75\,\mathrm{m})(26.67\,\mathrm{rad\,s^{-1}})^2 = 533.3\,\mathrm{m\,s^{-2}} = 54.4\,\mathrm{g} \tag{2.12}$$

$$F_{cent} = m_{blade} a_{cent} \tag{2.13}$$

Thrust

Like the above quantities, the thrust of the turbine varies with azimuthal position of the rotor, and has values both aligned with the flow, x, and perpendicular with the flow direction, y.

Average Thrust Using the AC model for the given operational condition, the axial thrust coefficient, C_{T_x} was calculated to be 0.9 for a λ of 4. This translates to an averaged thrust in the axial direction of 30.9 N.

$$T_x = C_{T_x}(1/2\rho A U_\infty^2) \tag{2.14}$$

$$T_x = (0.9)((1/2)(1.225\,\mathrm{kg\,m^{-3}})(2.25\,\mathrm{m^2})(5\,\mathrm{m\,s^{-1}})^2 \tag{2.15}$$

$$T_x = 30.9N \tag{2.16}$$

In the transverse direction, the C_{T_y} is calculated to be 0.13 yielding an average load of 4.56 N in the transverse direction.

$$T_y = C_{T_y}((1/2)\rho A U_\infty^2) \tag{2.17}$$

$$T_y = (0.13)(1/2(1.225\,\mathrm{kg\,m^{-3}})(2.25\,\mathrm{m^2})(5\,\mathrm{m\,s^{-1}})^2 \tag{2.18}$$

$$T_y = 4.56N \tag{2.19}$$

Instantaneous Thrust The instantaneous thrust of the turbine in the x and y, directions as calculated by the AC model is given in figure 2.10. The maximum thrust oscillates from 0 N to 60 N in the x direction and between −35 N to 35 N in the y direction.

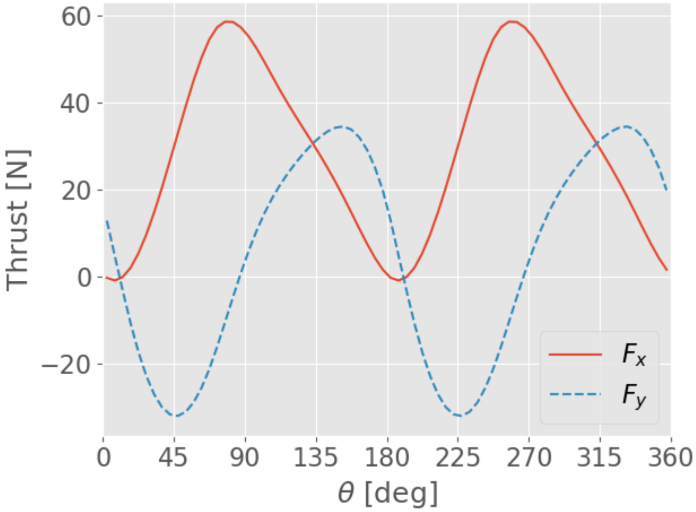

Figure 2.10: Instantaneous aerodynamic thrust in X and Y for PitchVAWT turbine at U_∞ = 5 m s^{-1}

Plotting the blade normal force over the azimuth of the turbine, figure 2.11, in a polar plot shows the distribution of loading in a clear way with the averaged thrust vector given as an arrow showing the resultant force on the flow from the turbine.

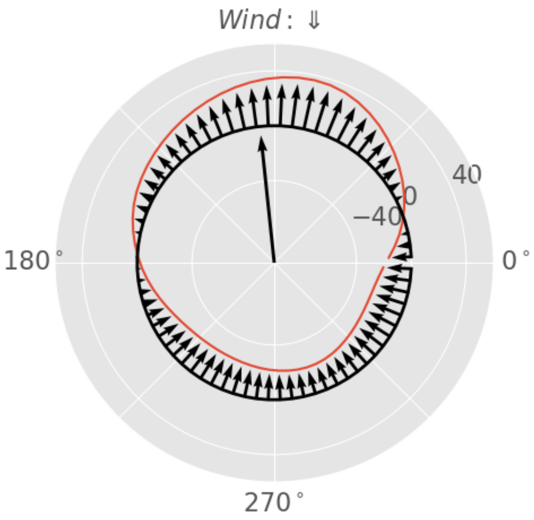

Figure 2.11: Polar plot of instantaneous normal force and resultant thrust for PitchVAWT turbine at $U_\infty = 5\,\mathrm{m\,s^{-1}}$

2.6. Mechanical Design

Using the loads and ultimate goals discussed above, the design of the turbine was completed. In the stress and deformation analyses for the rotor design, a maximum rotational acceleration of 100 g is used this provides a healthy safety factor of 1.84 on top of the already conservative 54.4 g calculated acceleration. This helps to take into account aerodynamic loading, as well as any additional dynamic loading due to the vibrations of the structure.

Overall dimensions for the full turbine are given in figure 2.12. The installed turbine in the Open Jet Facility is shown in figure 2.13. As shown in table 2.1 the PitchVAWT Turbine is a two bladed machine with a diameter of 1.5 m. The overall height of the machine is 2.8 m from the base to the top of the blades. The turbine has a set of clamp mounts in which the turbine can be bolted to or clamped down to a platform structure which is then positioned in the wind tunnel cross section appropriately. There are a set of leveling screws on the bottom of each leg to ensure level installation. The rotor is removable from the turbine base for the ability to swap out to a different rotor design in the future if required. This also provides for easier storage when not in use in the tunnel. An installation and operation manual for the turbine is provided in Appendix G.

This section will highlight the mechanical design for the main components of the turbine. Beginning with the motor/generator, transitioning into the rotor base, the main bearing set, and moving to the rotor design including the blades, struts, and pitching mechanisms.

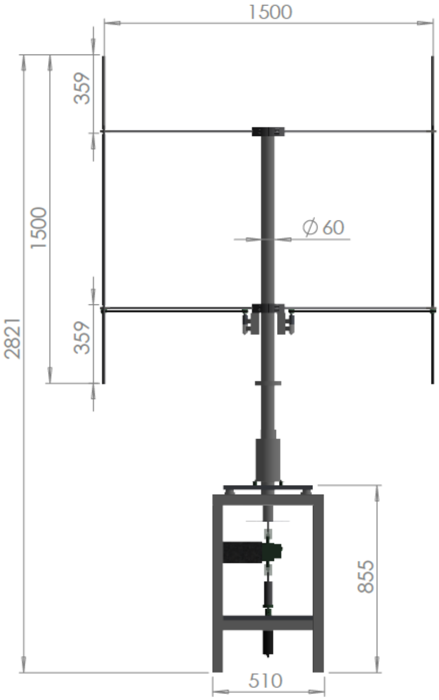

Figure 2.12: PitchVAWT model, dimensions in mm

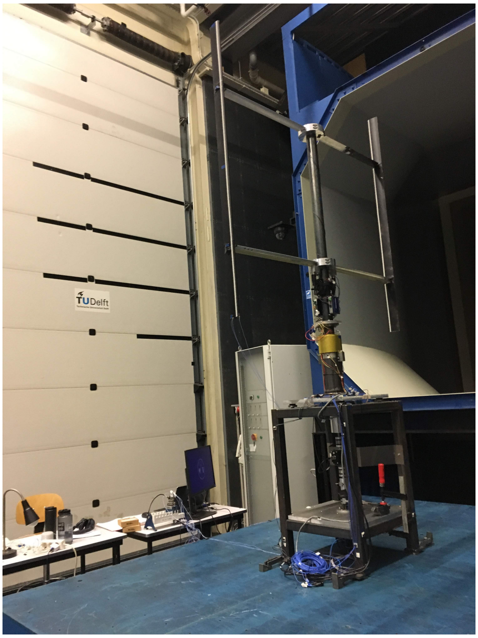

Figure 2.13: PitchVAWT installed in Open Jet Facility

2.6.1. Motor / Generator

The motor is designed only to handle the torque and power levels expected above for operation at low wind speed within a controlled wind tunnel environment. Therefore the motor is very undersized for operation outdoors or in high wind conditions. Based upon the expected maximum operational torque of 5 N m and a maximum power of approximately 60 W. A 200 W DC motor was chosen using a 12:1 gearbox. A Maxon motor controller is used to control the rotational speed of the turbine directly. This motor controller meets set-points provided through an analog voltage input which will be discussed in section 2.7.1. The specifications of the motor setup are given in table 2.2.

2.6.2. Base

The turbine base houses the drive-train and supports the rotor. The drive-train consists of the motor and gearbox, a torque and positioning sensor, and the connections to the lower section of the turbine tower. The drive-train is shown in figure

Table 2.2: Component information for PitchVAWT Maxon motor / generator

Item	**Model**	**Part Number**	**Notes**
Controller	ESCON 70/10	422969	10 A max
Motor	RE-50	370354	200 W DC Motor
Gearbox	GP 52 C	223083	12:1
Encoder	HEDL 5540	110518	500 count per turn

2.14. The base consists of 50 mm hollow tubes which have been welded together. Two aluminum platforms are installed on the base. The bottom platform is used as a mount for the motor and gearbox while the top platform serves as a mount for the main bearing system and supports the rotor. A detailed description and finite element model of the base is given in chapter 4.

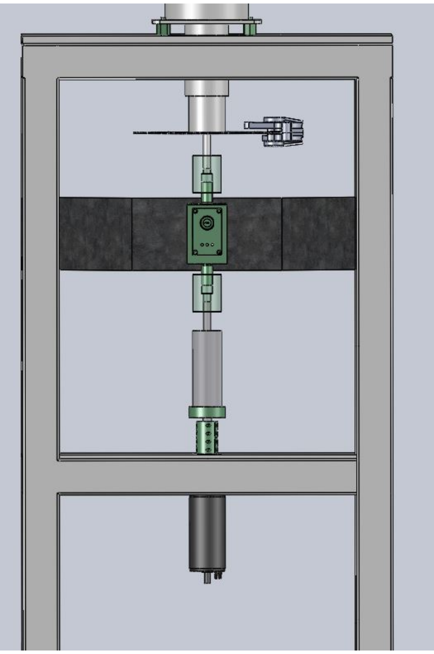

Figure 2.14: CAD model of PitchVAWT Drive-train showing torque sensor / encoder and base structure

Main Bearing

The main bearing transfers the weight and thrust forces of the rotor into the turbine base structure. It consists of two bearings and a load-bearing housing. It mounts to the top plate of the base with a set of load cells which measure the transferred load to the base. A CAD model of the assembly is featured in figure 2.15. The turbine tower has a step which sits on the top bearing. A height collet is then bolted to the tower to double the protection against vertical slippage in the bearing.

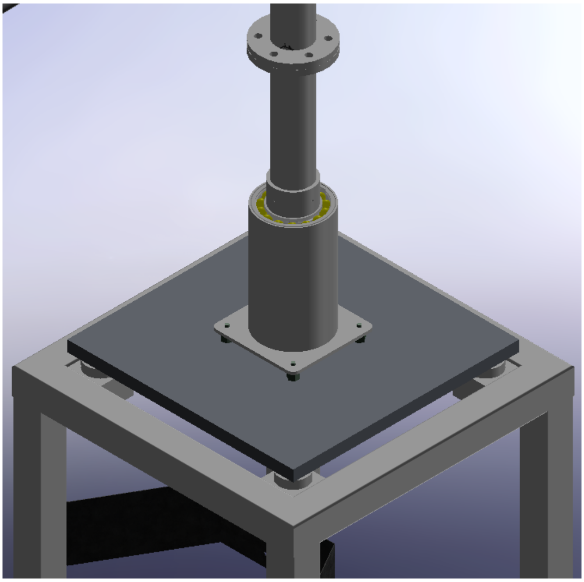

Figure 2.15: CAD model of main bearing assembly, showing top mounting plate, height collet, bearings, load cells, and tower segmenting flange

2.6.3. Tower

The tower is broken into two sections attached with a bolted flange. The lower section is permanently pressed into the main bearing and attached with a height collet. The rotor is mounted to the upper section of the tower. The main structure of the tower is a hollow steel tubular section with an outer diameter of 60 mm and a wall thickness of 5 mm. A detailed finite element model description is given in chapter 4.

2.6.4. Blades

The main design drivers for the turbine blade are as follows:

- Be able to be actively pitched by an independently controlled pitch mechanism
- Limit blade mid-plane deflection to 2.5 mm in maximum operation state
- Be relatively easy to model for digital twin capability

Location of Pitch Axis The pitch axis of the blade is located on the center of gravity of the airfoil. This is to minimize any rotational torque while rotating. Any of this load needs to be countered by the pitch mechanism, on top of any load dynamics due to accelerating the blade itself and the aerodynamic pitching moments. As the design is based upon a rotational acceleration of 100 g it is imperative to minimize this load. An initial model of the NACA0021 airfoil was made in Solidworks, with a reasonable wall thickness of 1.5 mm including corner fillets. The center of mass was then determined to be approximately 48 % of the chord length.

Blade Mounting A circular cutout was then included in the cross-section around this pitch axis where a 10 mm hardened steel pin is inserted in order to secure bearings for the pitching mechanism. Slots are made in the blade from the trailing edge of the airfoil giving access to the pitch axis. A manufacturing drawing of the turbine blade is given in figure 2.16.

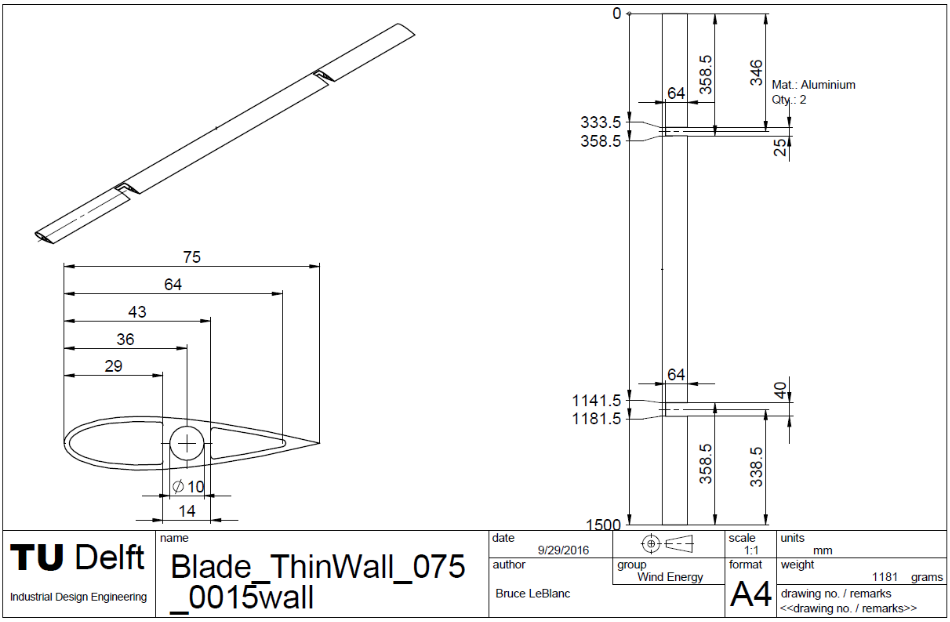

Figure 2.16: Drawing of PitchVAWT blades with cutouts

Load modeling Mechanical stresses and deformations of the turbine design were checked using Ansys. The blades were constrained in 6 DOFs at the location of the strut connections only on the steel inserts. The steel inserts into the extruded aluminum blade were modeled using contact elements to assure the pin would not tear out. A 100 g acceleration was imparted to the system. The resulting displacement and connection stress overlays are given in figures 2.17 and 2.18, respectively. Both criteria are met as the maximum expected deflection in the mid plane is calculated to be 2.3 mm and the maximum stress on the connection is approximately 400 MPa which gives a safety factor of 1.37 for high strength steel.

Revisiting Centripetal Load With the blade fully designed, the mass of the blades is approximately 1.2 kg each. Using the above equation 2.13 for centripetal load gives an outward load on the struts and connections of 639.6 N. However,

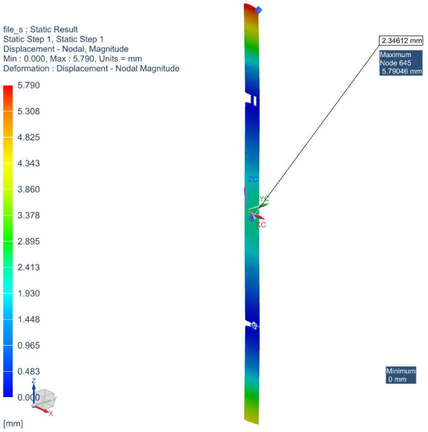

Figure 2.17: Maximum mid-plane deflection of 2.3 mm with 100 g outward acceleration, deformation shown in absolute scale

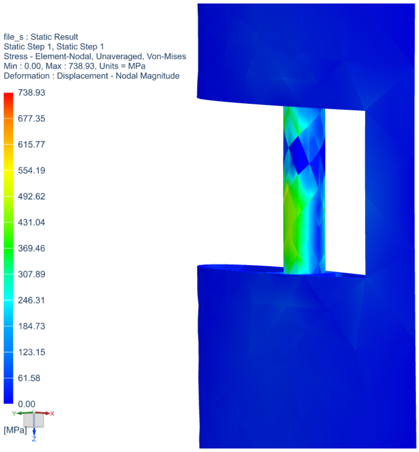

Figure 2.18: Stress in lower strut connection

as an extra safety factor, the loads were calculated with an acceleration of 100 g, therefore the following stress calculations are performed with an axial loading of 1.17 kN.

$$F_{cent} = m_{blade} a_{cent} = (1.2\,\text{kg})(533.3\,\text{m}\,\text{s}^{-2}) = 639.6\,\text{N} \tag{2.20}$$

2.6.5. Struts

The struts of the turbine are made from previously accrued stock of extruded aluminum airfoils. The cross-section is given in 2.19. The cross-sectional area of the strut is 143 mm^2. The axial stress on the strut is calculated analytically in equation 2.21 to be 8.18 MPa. This is well below the minimum yield strength of the material which is around 240 MPa.

$$\sigma = \frac{F_{axial}}{A_{strut}} = \frac{1.17\,\text{kN}}{143\,\text{mm}^2} = 8.18\,\text{MPa} \tag{2.21}$$

2.6.6. Connections

Steel transition pieces are fit inside the strut on each end, epoxied and pinned. The two main connections are between tower and the strut, and between the strut and the blade.

Tower to Strut Due to the connection being so close to the axis of rotation, the mass of the strut connection point is not a limiting factor. A large piece was designed that acts as a clamping collet around the tower. This is bolted together pinching the tower and securing its position. A slot is machined out of the block

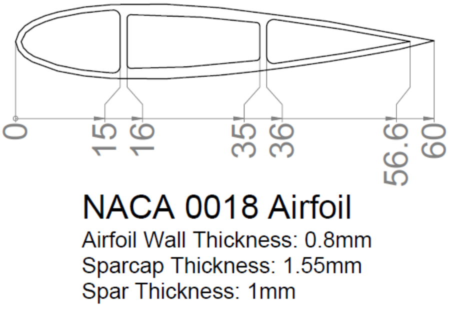

Figure 2.19: Cross-section of strut

where a connection adapter is inserted from the strut. A set of bolts locks this insert in place. The layout is given in figure 2.20.

To check the stress of the steel part in the high loading scenario described, a 2D finite element shell model was made in Ansys. The same axial load as above was imparted to the model, and the results are given in figure 2.23. With a maximum stress of approximately 90 MPa the safety factor for this part is about 6 based upon the same high strength steel used above.

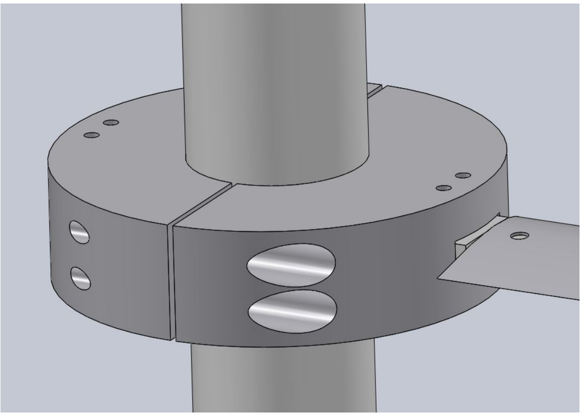

Figure 2.20: Tower to strut connection blocks from milled aluminum

Strut to Blade The strut to blade connection is more complicated than the inner connection due to the requirement of pitching the blades. Therefore the connection needs to house a bearing. The connection for the bottom strut, which also includes a pulley for the pitch actuation, and the top strut are given in figures 2.21 and 2.22, respectively. The strut to blade connections are mounted in the airfoil slots and the 10 mm steel pins are pressed into the pitch bearings from the outer ends of the blade. There are bushings used to maintain the offset between the airfoil cutouts and the bearing. Stress is calculated for the strut to blade connection in Ansys with a 3D model using the high load discussed. The results are given in figure 2.24. The load was applied as a bearing stress on the inner face of the cutout, and the internal pin was used as the sole constraint. The connection has a higher safety factor for this load than the internal strut connection. In the construction of the turbine, epoxy was added to these joints to stiffen them in addition to the connection pins.

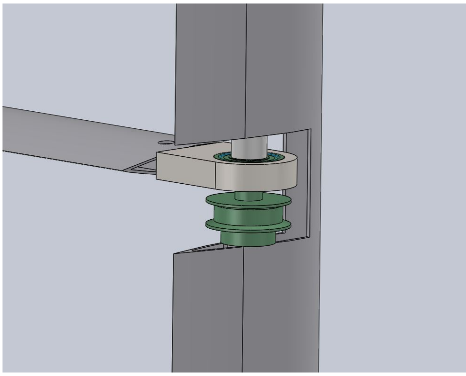

Figure 2.21: Blade to bottom strut connection with airfoil cutout and geared pulley for pitch system actuator

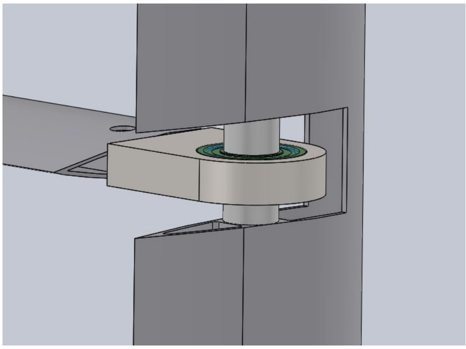

Figure 2.22: Blade to top strut connection, using freely rotating bearing

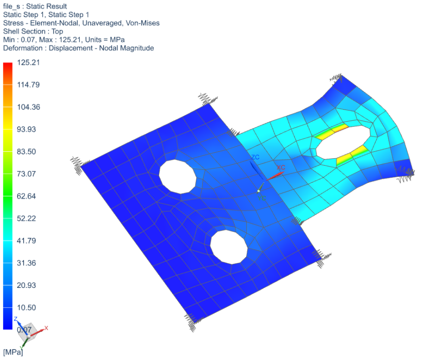

Figure 2.23: Tower connection to strut showing von-mises stress at 100g blade load

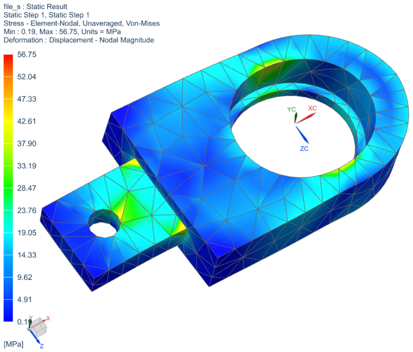

Figure 2.24: Strut connection to blade showing von-mises stress at 100g blade load

2.6.7. Pitch Mechanism

The turbine pitch mechanism consists of a DC micro-motor with a 60 to 1 gearbox mounted next to the turbine tower. When paired with a rotary encoder and a motor-position controller from Faulhaber, the exact position of the shaft can be controlled.

Each motor-position controller interprets an analog signal passed through a slip-ring from the SCADA system and converts it into the appropriate angular displacement required. A The controller monitors these set points and feeds back information to the turbine SCADA system about the ability for the motor to reach each intended position set-point. The details for the pitch actuation system are given in table 2.3.

Table 2.3: Component information for pitch actuation mechanism - Faulhaber

Item	**Model**	**Part Number**	**Notes**
Motor Controller	MC 5005	6500.01667	24 V 4 Quad PWM
Motor	2642-024 CR		28 W, 32 mN m
Gearbox	Series 26/1	2642.G0697	66:1 3 stage
Encoder	IE3-512L		512 count rev^{-1}

The pitch motor is attached to a geared pully which extends underneath the bottom strut airfoil to the blade where it is wrapped around a pulley of the same diameter. The blade pulley is attached to the blade pin insert with a shear-pin set-screw. The full arrangement mounted on the rotor is shown in figure 2.25. The pitch rate is limited by the ability for the servo-motors to respond to a given input command. This is limited in practice to the maximum rotational speed of the gearbox used on the motor. The limit provided for this design is $364\,°\,\text{s}^{-1}$.

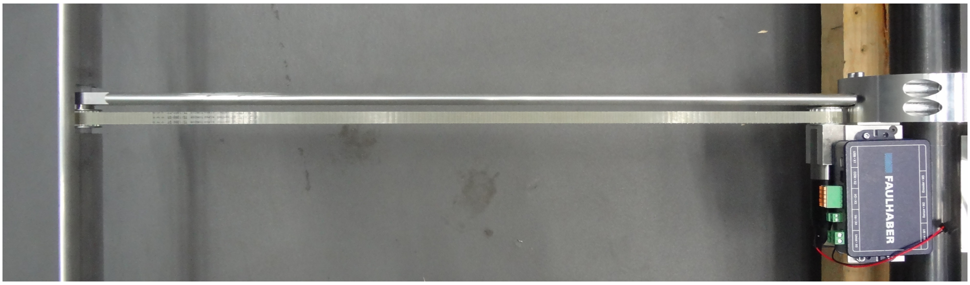

Figure 2.25: Pitch system installed on rotor

As the pitch system is based upon a relative measurement from a given starting point, calibration of the pitch setup needs to be performed prior to collecting data. This is by design so the turbine can be stored and the pitch manipulated when power is not applied. Procedures for performing this calibration are included in the installation and operation manual in Appendix G.

2.6.8. Campbell Diagram

A full structural finite element model of the turbine system has been made using Siemens Simcenter3D, and is discussed more in chapter 4, where full mode-shapes and frequencies are presented. A rotor dynamics solution was made in order to identify rotational effects on the mode shapes and frequencies of the turbine. These effects include tower whirling modes, both forward and backward, as well as rotational based stiffness changes. A view of the model is given in figure 2.26. Two Campbell diagrams are calculated for the turbine, the first including the dynamics of the large mounting platform which is generally used in the Open Jet Facility, and the second assumes a fixed base platform. This can be useful for understanding the effects of the platform dynamics on the rotor response, as well as for potentially coupling the model in a substructuring fashion to any other potential platform in the future. These Campbell diagrams are shown in figure 2.27.

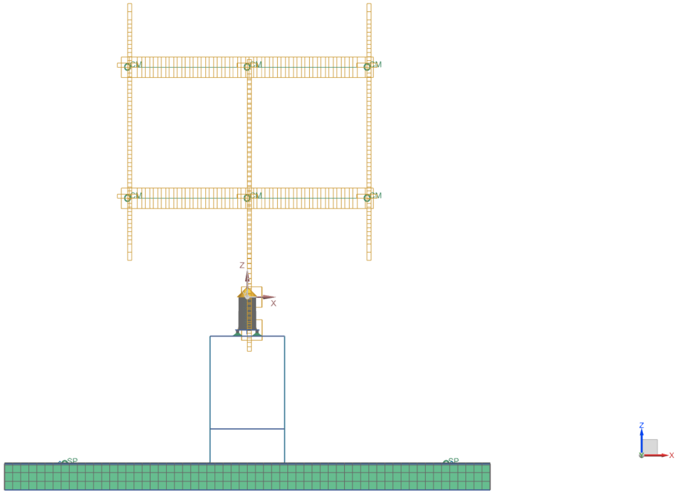

Figure 2.26: Rotor dynamics model of PitchVAWT turbine, orange boxes highlight rotational frame with local coordinate system, bearing elements are used to connect between the rotational and fixed frames

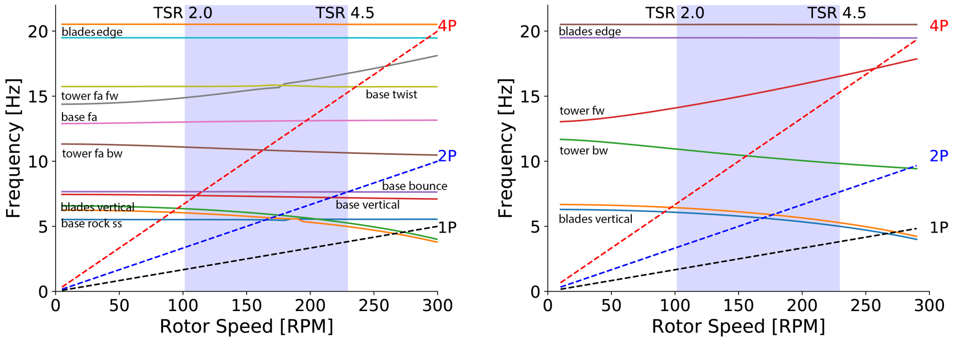

(a) ”Floating” platform base with grounding springs

(b) Fixed platform base

Figure 2.27: Campbell Diagram for PitchVAWT turbine modeled with complex modes at respective turbine rotational frequencies, λ of 2.5 and 4 at a wind speed of $4\,\mathrm{m\,s^{-1}}$ is highlighted in blue

As shown in the Campbell diagrams, the operating range for the turbine when in a $4\,\mathrm{m\,s^{-1}}$ wind speed shows potential mode crossings for the base modes and the vertical bounce modes of the struts. At a slightly higher rotational speed, issues with the tower backwards whirling mode can be encountered. Higher harmonics may be present depending on the aerodynamic loading of the turbine. Airfoil dynamic stall, may induce some higher frequency response due to vortex shedding, as well as blade vortex interaction on the downwind half of the rotor which may be several times the rotational frequency. These are important to keep in mind when reviewing the critical operating ranges for the turbine. Due to excitation of the tower whirling modes and the platform rocking modes, the turbine operation is practically restricted to about $210\,\mathrm{rev/min}$ for testing with the wind at $4\,\mathrm{m\,s^{-1}}$.

2.7. Supervisory Control and Data Acquisition

The turbine is operated by directly controlling the rotational speed and choosing a type of pitch control for the turbine. These pitch control options include fixed pitch offsets, sinusoidal pitch variations based upon azimuth position of the rotor, multi-frequency sinusoidal variations with tie to the azimuth position, or custom setups which operate by providing specific pitch schedules using an input file to the controller program. The system architecture will be discussed here.

2.7.1. System Architecture

The overall architecture of the turbine SCADA system is given in figure 2.28. The architecture is written in the program LabView with Real-Time support. There are two main Virtual Instruments, or VIs, which operate the turbine. The first runs on the turbine user PC which is situated in a safe place separate from the rotating turbine. In the case of operating in the OJF, this would be the main tunnel control room. The second runs on a National Instruments Compact RIO 9066 (cRIO) embedded controller running the LabView Real-Time operating system.

Queued Message Handler Both the host PC and the cRIO VIs use the concept of a Queued Message Handler (QMH)[52]. The concept has two loops running in parallel, the first responds to an event by the user such as requesting an RPM change for the turbine. In this case, the changing of the RPM request would trigger an event, the event handling loop then encodes a message of ”RPM” along with the requested value to a queue. The second loop is constantly running looking for messages in the queue, it receives the message from the event handling loop and transmits the message and the data to the embedded turbine controller via a network stream. It is similar to the well known ”state-machine” however the functions are in their own independent loop, which allows multiple independent tasks to be parallelized.

2.7.2. Functions of user PC

The user PC functions as the user interface with the turbine providing the abilities to control turbine run-state, change operational speed, or pitch settings. It also provides real-time feedback of turbine sensors including measured RPM, measured

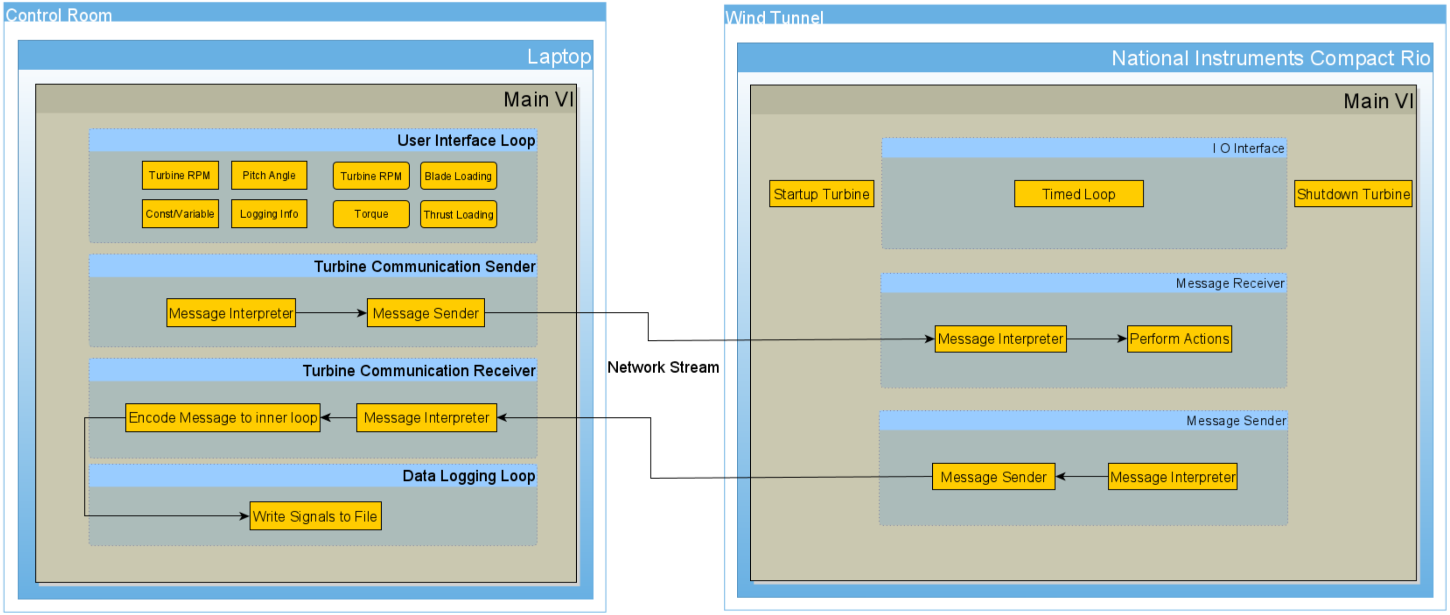

Figure 2.28: PitchVAWT controller architecture

shaft torque, turbine pitch, blade normal loading, and base acceleration. This PC also writes out all data to the specified log file in a tab-separated text file format. The specific data files and channels written are given in Appendix G.

2.7.3. Network stream

As shown in figure 2.28, a network stream connects the user PC to the embedded turbine controller using a TCP/IP connection. Communication between the RT target embedded controller and the host PC is non-deterministic. Therefore a queued network stream is used in order to ensure that each data packet is properly received in each of the two-way communications. Two independent network streams are used. The user requests of the turbine are pushed through the first stream to the target, where the target receives them and performs the requested actions. The turbine state and all collected data for each time-step is sent back to the user PC through the second independent network stream. Both streams are checked for missed packets and the cues are cleared prior to disconnecting in order to ensure that all data is properly transferred back to the user PC for logging. However, if in the event this connection is disrupted, such as a disconnected cable or user PC computer crash, the turbine controller will recognize this and bring the turbine to a controlled stop independent of the user PC. Due to limited storage on the embedded controller, this data is not stored locally at this time, meaning that the data would be lost after disconnection. This is a potential future upgrade if it is deemed necessary for a specific test.

2.7.4. Real-Time embedded target

The embedded target for the turbine controller, right half of the architecture diagram in figure 2.28, is responsible for directly interfacing with the turbine. In normal turbine operation there are three main functions for this VI. First is to receive, interpret, and implement all commands from the user PC through the first network stream, this is done using another QMH. The next is a precisely timed loop which sets the output pins to the required levels and reads in each sensor individually giving a time-stamp for the collected data. The final task is to communicate the turbine status and all collected data through the second network stream back to the user PC for logging and selected signals to be displayed on the main UI. The timed-loop is deterministic and is listed as top priority, while communications loops are more prone to jitter due to lower priority within operations, especially on the user PC. This can lead to issues and data-dropouts. This is avoided by using buffer variables to and from the timed-loop, ensuring that all data is properly transferred with the correct time-stamp from when the samples were actually collected.

2.8. Summary

The turbine design presented in this chapter is used to evaluate the loads and performance of vertical axis turbines based upon fixed pitch and variable pitch control schemes. The tools and sensors which are used to collect this data are presented in appendix B, which discusses in depth the measurement systems and baseline performance of the PitchVAWT. Aerodynamic simulations of the PitchVAWT turbine and the tools used to model them are discussed in chapter 3. In order to properly relate all of the turbine aerodynamic models to the measured turbine responses, especially the structural response measurements, a thorough understanding of the turbine structural response is required. A building of a calibrated finite element model and multibody dynamics solution for the installed PitchVAWT turbine is presented in chapter 4.

Bottom Line:

- In this chapter, the design of a Vertical Axis Wind Turbine with individual blade pitch control is presented.
- The operating range and expected performance of the turbine within the Open Jet Facility wind tunnel at TUDelft has been outlined.
- A manual for the installation and operation of the turbine is included as Appendix G.
- The modeling tools for analyzing the aerodynamic performance of the turbine are presented in chapter 3.
- The modeling tools for analyzing the turbine structural loading and dynamics are presented in chapter 4.
- This turbine platform is used throughout the rest of the thesis to explore various aerodynamic and structural dynamic phenomena in light of our stated research questions.

III

Simulation of VAWT Loading

3

Aerodynamic Modeling of VAWTs

This chapter overviews the different modeling techniques used within this thesis for design and performance assessment of Vertical Axis Wind Turbines. The implementation of the modeling tools used for further analysis is discussed. A series of simulations are conducted on the PitchVAWT turbine, highlighting the effects of turbine loading and wake development with changes in fixed pitch offsets between 2D and 3D modeling techniques.

3.1. Introduction

The aerodynamics of cross-flow or vertical axis wind turbines are generally less intuitive than their axial-flow, horizontal axis cousins. There are two families of vertical axis machines, drag driven and lift driven. The drag driven turbines, generally referred to as Savonius rotors after its inventor, are not used in this thesis and so will not be discussed in any detail. Most larger vertical axis wind turbines utilize the lift based, or Darrieus, wind turbine design.

This chapter gives a brief overview of the aerodynamics for the Darrieus, lift-driven VAWT. The momentary loading on each blade as the rotor rotates about its axis and the effects that may have on the machine design are discussed. These momentary loads are then integrated over the rotation to give average loading conditions on the rotor scale and how these may impact the development of the turbine wake. The major aerodynamic design variables are presented with these directly applied in chapter 2 for the design of a VAWT. The chapter moves to a discussion of the types of aerodynamic tools for analyzing the VAWT used within this thesis. The implementation of the 2D Actuator Cylinder (AC) model with a Beddoes Lieshman Dynamic stall model is detailed, which is compared to a free wake vortex based model. Studies are then presented comparing the wake evolution of the VAWT in two versus three dimensions, and the result of including airfoil viscous effects in the calculation of blade loads.

3.1.1. Introduction to VAWT Aerodynamics

The aerodynamics of a vertical axis wind turbine are distinct from their horizontal axis counterparts in several ways. Due to the orientation of the rotor with respect to the oncoming wind, there is no ”rotor plane” which can be collapsed to an infinitesimally small surface. This has impacts for understanding blade loading through modelling. Because the blades rotate around a vertical axis, each blade first operates in a clean air flow in what is called the ”upwind” pass. As the blade continues to rotate, the blade then cycles around and operates within its own wake on the ”downwind” pass. This is visualized with a reference wind direction and a given coordinate system for the two dimensional VAWT in figure 3.1. Due to the orientation change of the apparent wind speed, the pressure and suction sides of the airfoil flip. Essentially, what could be considered a ”mean” load for a horizontal axis turbine doesn’t exist for the VAWT.

The flow is inherently unsteady, which leads to difficulties in modeling rotor performance and blade loads. The shifting angle of attack over a single rotation is given in figure 3.2. This is calculated for a vertical axis turbine with a solidity, a ratio of covered blade area by the swept area of the rotor of $\sigma = 0.1$ operating at a tip speed ratio of $\lambda = 4$. Several things can be noticed in this figure. The angle of attack, α, of the upwind pass follows a sinusoidal curve with a maximum of about 12° as expected. On the downwind pass, the angle of attack switches negative, flipping the pressure and suction sides of the airfoil, and then the minimum angle of attack is cut off lower at only about $-8°$, before recovering to the starting position where $\theta = 360°$. This cutoff is due to the blade operating in the wake of the upwind pass. The energy that is removed during the upwind pass of the rotor is no longer

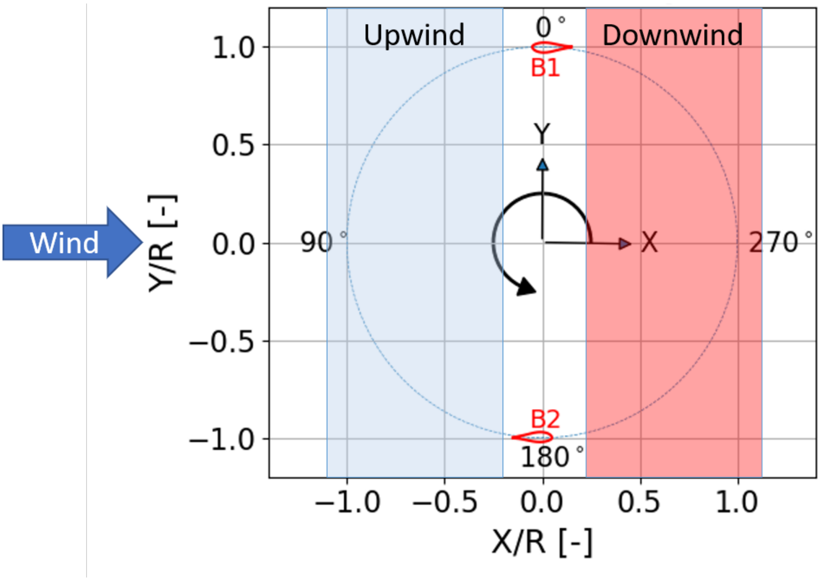

Figure 3.1: Coordinate System for 2D VAWT highlighting the upwind and downwind portions of the rotor pass. Wind in this example comes from the left side of the image.

present in the flow, slowing down the velocity of the wind. With the local airspeed reduced, a higher proportion of the resultant wind speed is due to the rotation of the airfoil itself, causing a lower relative angle of attack. In this downwind pass there are also issues of the blade interacting the vortex sheet which was previously shed in the upwind locations. This can add to local spikes in loading and a further increase in fatigue issues which are more difficult to model accurately. The model employed in the calculation of this angle of attack graph does not take into account these vortex interaction effects.

Another result of having the load consistently vary over the rotation is that the thrust in both the axial, x, and perpendicular, y, directions varies dynamically at a frequency which is a multiple of the number of blades on the turbine. For instance, the x and y thrust load for a two bladed VAWT is given in figure 3.3. The axial force oscillates between a maximum thrust value and zero twice each rotation, and the thrust perpendicular to the flow oscillates about zero with some amplitude. The exact amplitudes vary depending on the operating conditions, however the general curves will be consistent in all operating areas. These large oscillations also occur in the loading of the gearbox and fixed frame structure, leading to difficulties in fatigue failures which have been seen in past vertical axis wind turbine designs. Any mischaracterization in the experienced loads of the turbine due to modelling errors can lead to increased fatigue loading of the turbine rather than a fix offset which can be more easily dealt with in the mechanical design.

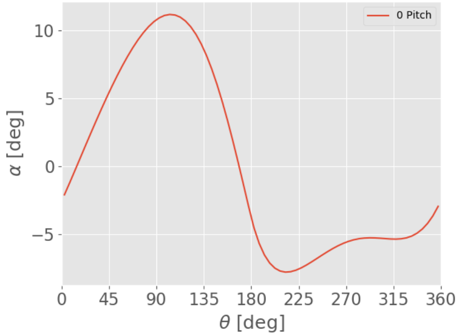

Figure 3.2: Angle of attack for $\sigma : 0.1 \ \lambda : 4$

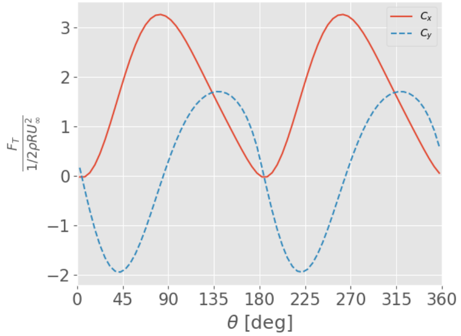

Figure 3.3: Rotor thrust for two bladed VAWT

3.2. VAWT Aerodynamic Models

There are a number of different types of models used while evaluating the aerodynamics of vertical axis wind turbines. In this thesis, four models are used regularly. Some main characteristics of each model are summarized in table 3.1. The table highlights whether the model is two or three dimensional; uses a blade element model formulation for calculating the blade loading; has an assumption of infinite number of blades or explicitly models the finite blades; uses a free-wake to account for induction effects on the blade loading. The first is known as the two dimensional Actuator Cylinder (AC) model, followed by a 2D free-wake vortex panel code by Ferreira referred to as U2Diva[11]. The next two models are 3D lifting line free wake vortex models. This section will quickly review each model. The actuator cylinder is the only of model to be directly implemented by the author and so the implementation of the AC model with a Beddoes-Leishman type dynamic stall model is discussed in detail along with a verification of the code implementation to the previously verified U2Diva model[53].

Table 3.1: Overview of Aerodynamic models used

Model	**2D v 3D**	**BEM**	**Dyn. Stall**	**∞ Blades**	**Free Wake**
AC	2D	Y	Y	Y	N
U2 Diva	2D	N	N	N	Y
CACTUS	3D	Y	Y	N	Y
Q-Blade	3D	Y	Y	N	Y

3.2.1. Actuator Cylinder Model

The version of the Actuator Cylinder (AC) used in this work is a linearized flow model developed in order to more realistically capture the loading behavior of the vertical axis turbine with respect to the streamtube models[54–56]. The concept was to extend the actuator disk to better follow the actual path traversed by the blades during a rotation. This was done by wrapping the actuator surface into a cylinder with normal and tangential components allowing for the inclusion of both axial and cross-flow induction terms to be taken into account. The wake of the turbine is explicitly modeled calculating the influence each element has on the other sections of the rotor. Due to this formulation, the induction of the downwind blade pass has an influence on the upwind pass providing a closer depiction of the actual physics. In most circumstances the non-linear influences are approximated with a modified linear approach, by applying a correction factor based upon the axial thrust coefficient of the rotor. The full non-linear solution is possible for higher rotor loading scenarios, though the benefits of a quick calculation time are somewhat compromised with the full solution. Blade loading is accounted for using a Blade Element Momentum (BEM) formulation using airfoil polars based upon the local angle of attack to calculate the appropriate lift and drag of the section. The limits of the model generally come from the assumption of an infinite number of blades, as well as the two-dimensional nature of the solution[53]. This model is used throughout the thesis and is discussed in greater detail along with a full implementation in section 3.3.

3.2.2. Vortex Models

Vortex models are a subset of Langrangian models which use vortex particles or elements to calculate the flow conditions at relevant locations, unlike Eularian models which are evaluated based upon a grid. The flow solution is calculated with potential flow theory as a linear combination of the solutions for each element or particle. Therefore for homogeneous flows, the full solution can be understood with relatively few key elements, reducing the required computational resource.

Unlike the engineering models above which are built upon time-averaged mean loading assumptions, vortex models explicitly calculate instantaneous loading in the time domain. Typically these models use a ”lifting line” formulation. In which a vortex line structure based upon the application of Helmholz theorem’s conservation of circulation is employed. This consists of a starting vortex, vortex lines at the tip and root of the blade, and a connecting bound vortex along the blade span as shown in figure 3.4 from[57]. Upon starting the simulation, what is known as a starting vortex is shed into the wake of the airfoil, its strength coinciding with the lift imparted into the flow, based on a BEM approach, through the Kutta-Joukowski theorem. As the flow advances into the next time step, the starting vortex then migrates into the wake of the wing at the local velocity. Tip vortices arrive due to the discontinuity of lift at the end of the wings, which connects to the starting vortex. Due to the Helmholz theorem that no vortex line can end in free-space of a fluid, a bound vortex along the wing develops. The flow field is then calculated for the given time step. At the next time step, a new vortex is shed, with its strength dependent upon the change in lift from the previous time step. For ”free-wake” vortex models, each vortex element in the fluid creates an induced velocity in the flow which influences the position and velocity of each other element in the flow, and finally inducing a velocity onto each element along the blade.

For ”fixed-wake” vortex models, the self-induction of the vortex elements onto themselves is ignored, meaning that the vortex elements are translated only with

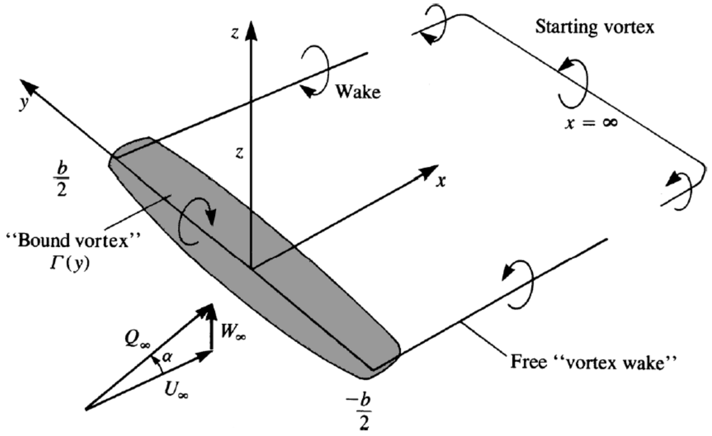

Figure 3.4: Horseshoe vortex definitions from Katz & Plotkin[57]

the mean flow velocity. Fixed wake models calculate much faster due to minimizing the number of interactions, however, are generally poor at capturing blade forces especially with higher loaded rotors where the induced velocity of the wake can have large impacts on the experienced velocity and angle of attack of the blades.

The two models most used within this work are QBlade by the Technical University of Berlin[58] and CACTUS by Sandia National Laboratories[59,60]. These models directly capture more of the physics than the actuator cylinder discussed above, however take approximately 2 orders of magnitude more CPU run-time (hours vs seconds) to complete. Some physics are difficult to capture tho, including effects such as Blade Vortex Interaction, or anything on the airfoil scale viscous effects such as dynamic stall. As lifting line models are reliant on airfoil polar data, either numerical or experimentally generated, the vortex models don't preclude the study of these phenomena, they just aren't inherently modeled.

U2Diva is a two dimensional potential-flow panel-model of the VAWT by Ferreira[11]. Unlike the above 3D lifting line models, U2Diva doesn't utilize the BEM approach with airfoil polars. Rather, the airfoils are represented by a 2D distribution of panels over the airfoil surface. The Kutta condition is forced at the trailing edge of the airfoil, and the strength of each panel, is calculated based upon the local incoming wind, and the induction from the wake of the turbine.

3.3. Actuator Cylinder Model Implementation with Dynamic Stall

Whereas other models used in this thesis are implemented and verified by a third party, generally the original author's of the model, the actuator cylinder flow model is directly implemented by the author. As such the way the model is implemented will be verified by comparing the model to expected results. The dynamic stall model will be first be introduced along with its independent verification, followed by the actuator cylinder model. Finally, a study of VAWT turbine behavior with fixed pitch offsets is studied with and without the implementation of the dynamic stall model in both two and three dimensions.

3.3.1. Actuator Cylinder Model Implementation

The actuator cylinder flow model has been incorporated into multiple performance models for the analysis of vertical axis wind turbines[56,61]. It was originally developed by Madsen[54,55] as a part of his doctoral research. It is essentially an extension to the Actuator Disk concept generally used in horizontal axis turbines to coincide with the swept area of a vertical axis turbine. The implemented model is two dimensional, which matches well with a straight bladed cylindrical turbine, such as PitchVAWT, excluding any three dimensional effects near the tips of the blades. The normal and tangential forces are applied onto the flow as body forces normal and tangential to the rotor surface, respectively and shown in figure 3.5 assuming an infinite number of blades. These are defined explicitly in terms of blade loading as per equations 3.1 and 3.2 where B is the number of turbine blades.

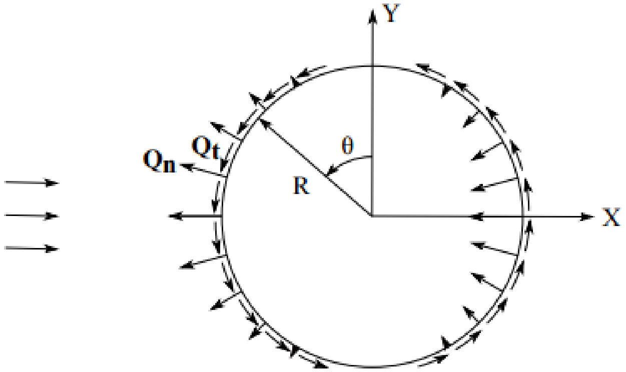

Figure 3.5: Q_n and Q_t reaction forces from blade loading as defined by Madsen[55]

$$Q_n(\theta) = \frac{BF_n(\theta)}{2\pi R\rho V_\infty^2} \tag{3.1}$$

$$Q_t(\theta) = -\frac{BF_t(\theta)}{2\pi R\rho V_\infty^2} \tag{3.2}$$

The blade loads are derived from given airfoil polars using the blade-element method, with the option of including the above dynamic stall model, or not. The output blade loads (C_{fn} and C_{tan}) are non-dimensionalized by the local dynamic pressure and the chord length. The implementation of the Actuator Cylinder Model in Python is given in appendix F.

The model is divided into two parts, a linear and a non-linear solution. Beginning with the linear solution, the induced velocities are modeled by dividing the cylinder into N elements with an azimuthal resolution of $\Delta\theta = \frac{360}{N} face$. Influence matrices for x and y velocities, equations 3.3 and 3.4 respectively, are calculated first. The loads are then calculated at each element in the cylinder, and the flow velocities are updated accordingly using equations 3.5 and 3.6.

$$R_{w_x}(i,j) = \int_{\theta_i - 1/2\Delta\theta}^{\theta_i + 1/2\Delta\theta} \frac{-(x_j + sin(\theta))sin(\theta) + (y_j - cos(\theta))cos(\theta))}{(x_j + sin(\theta))^2 + (y_j - cos(\theta))^2} d\theta \tag{3.3}$$

$$R_{w_y}(i,j) = \int_{\theta_i - 1/2\Delta\theta}^{\theta_i + 1/2\Delta\theta} \frac{-(x_j + sin(\theta))cos(\theta) - (y_j - cos(\theta))sin(\theta))}{(x_j + sin(\theta))^2 + (y_j - cos(\theta))^2} d\theta \tag{3.4}$$

where x_j and y_j are the evaluation points around the cylinder.

$$w_x(j) = \sum_{i=1}^{N} Q_{n_i} R_{w_x}(i,j) - Q^*_{n_j} + Q^*_{n_{N-j}} \tag{3.5}$$

where the starred terms are only added for the leeward part of the cylinder.

$$w_y(j) = \sum_{i=1}^{N} Q_{n_i} R_{w_y}(i,j) \tag{3.6}$$

In order to speed up computations, a modified-linear approach presented by Madsen in[54] allows for the modeling of the non-linear solution by applying a correction factor to the induced velocities from the linear version of the model derived from the expected thrust coefficient from the Blade Element Momentum model. The 'mod-lin' correction factor, k_a, is given in equation 3.7.

$$k_a = \frac{1}{1-a} \tag{3.7}$$

This scale factor is then applied to the linearly calculated velocities.

$$w_x = k_a w_{x_{lin}} \tag{3.8}$$

$$w_y = k_a w_{y_{lin}} \tag{3.9}$$

The blade loads and flow velocities are then updated iteratively until they converge to a minimum tolerance for the given analysis point.

3.3.2. Verification of Actuator Cylinder Model

The implementation of the AC model is compared with a 3D free wake vortex method within the open source design software Q-Blade[58]. The 3D model is run with a large aspect ratio of ten, and the results at the center horizontal plane of the rotor are used in order to have as close of a comparison with the two dimensional actuator cylinder as possible. Lift and drag for both models use the inviscid formulation of a NACA 0015 airfoil as was previously performed in[53], with the coefficients given in equation 3.10. Each model was run with azimuthal resolution of 5°, giving 72 points per rotation. Dynamic stall was disabled in both models to limit the scope of comparison to the AC model directly and to minimize differences between the two model types. The models are compared at a tip speed ratio of 4 and a rotor solidity of 0.1. Two blades are also assumed giving a chord to radius ratio of 0.1 as well.

$$C_L = 1.11 * 2\pi \sin(\theta), C_D = 0 \tag{3.10}$$

The angle of attack over the rotation given in figure 3.6a matches very well in the upwind half of the rotation, there is a small deviation from the 180° to 260° azimuth position, however this has been shown in previous comparison studies of the actuator cylinder[53] and does not seem to be emblematic of the model implementation. The blade relative velocity is given in figure 3.6b. There are small deviations in the velocity where the blades transition from leeward to windward facing 0° and 180° positions, however this doesn't translate into any substantial blade loading at these positions, and is more a function of the physics that are modeled rather than the implementation. The normal and tangential force coefficients, shown in figures 3.6c and 3.6d, match well, especially in the upwind section. Both the normal and tangential loads match the vortex model well, with a slight over prediction in both in the same area of deviation that was seen in the angle of attack, as is expected. With these close comparisons in model performance it can be assumed that the current implementation of the actuator cylinder model is performed correctly and that the behavior of the model is consistent with what has been documented in the past.

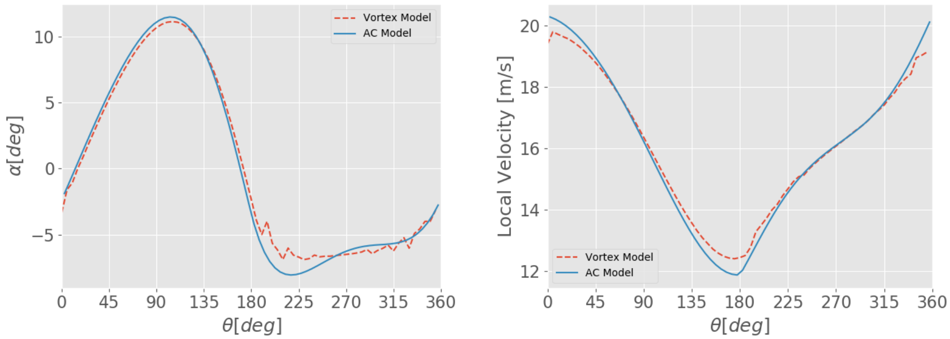

(a) α

(b) V_{local}

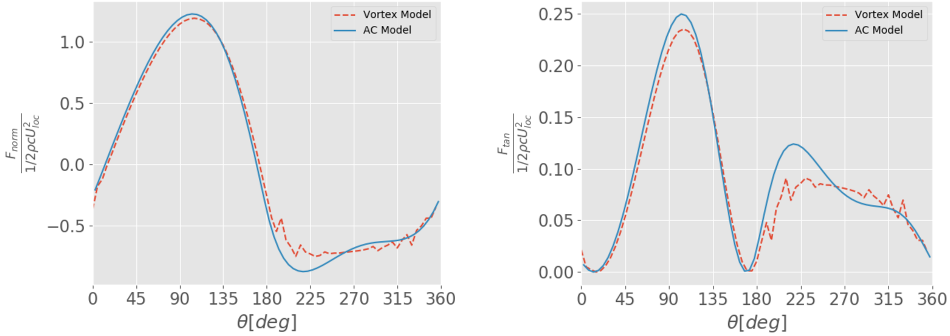

(c) C_{fn}

(d) C_{tan}, $\lambda = 4$ $\sigma = 0.1$

Figure 3.6: Comparison of implemented actuator cylinder model and a free-wake vortex model showing a) angle of attack, b) local velocity, c) non-dimensional normal force, d) non-dimensional tangential force

3.3.3. Dynamic Stall Model

There are several dynamic stall models which have been used in the load calculations of wind turbines. A study by Holierhoek[62] shows it is necessary to include dynamic stall effects in the calculation of loads in unsteady aerodynamics, however, due to the difficult nature of modeling the phenomena, none of the models implemented really outperforms the others in all situations. Given this understanding, the Beddoes-Leishman[63] dynamic stall model was chosen and is fairly common in the field. It is a semi-empirical model which models the physics of the unsteady effects inherent in pitching and plunging airfoils as well as the onset of leading edge separation leading to increased vortex lift and its decay over time. Originally developed for use in helicopters, the implementation has been adapted for use in wind turbines, in this case the Actuator Cylinder model specifically. One advantage of the model is that a relatively large percentage of the physics is modeled numerically, leaving only four main empirical constants which need to be supplied and the rest can be obtained using a static airfoil polar. The constants are defined in Table 3.2. The time constants are those used by Pereira while validating the model for wind turbine relevant analyses[64]. The exact time-constants to apply for vertical axis wind turbines remains an area of research that is outside the scope of this thesis. Due to the effects of the shed vortices traveling downstream with the rotor and interacting with the blade once again on the downstream pass may effect these time-constants.

The model is divided into four main modules:

- Attached flow model for linear unsteady forces
- Separated flow model for the leading edge pressure response
- Separated flow model for the trailing edge separation and pressure response
- Dynamic stall model with vortex lift from shed leading edge vortices

The modules are connected in series where the output of one serves as inputs to the next this also allows for slight modifications to each of the modules independently to better serve the purposes of the aerodynamics being modeled, hence the adoption to wind energy specific airfoils. Because the turbines being modeled have similar airfoils, symmetrical NACA 4-series, the original equations as given in[63] are used, these will be briefly described here. The actual python code for the implementation is given in Appendix D.

The scaling to non-dimensionalize time gives equation 3.11 for the parameter, S, which is the relative distance traveled by a semi-chord of the airfoil in time, t.

$$S = \frac{2Vt}{c} \tag{3.11}$$

Attached flow behavior The attached flow of the airfoil is modeled using a superposition of the circulatory and impulsive forces. The normal force due to circulation is calculated by multiplying the normal force slope of the static airfoil

Table 3.2: Beddoes-Leishman Constants from [63,64]

Constant	Definition	Value
T_p	Peak pressure lag	1.5
T_f	Boundary layer pressure lag	5
T_v	Vortex decay constant	6
T_{vl}	Vortex passage time-constant	5
A_1	Indicial lift coefficient	0.3
A_2	Indicial lift coefficient	0.7
b_1	Indicial lift coefficient	0.14
b_2	Indicial lift coefficient	0.53

polar with the effective angle of attack, equation 3.12. This effective angle of attack is comprised of the calculated α at the time step n corrected by two deficiency factors, X, and Y, given in equations 3.13 and 3.14. The original equations are given with corrections for Mach number, M, and compressibility β, where $\beta = \sqrt{1 - M^2}$, for completeness. In the current model implementation, the effects of compressibility are considered small and ignored.

$$C^C_{N_n} = C_{N_\alpha}(M)(\alpha_n - X_n - Y_n) = C_{N_\alpha}(M)\alpha_{E_n} \tag{3.12}$$

$$X_n = X_{n-1}e^{-b_1\beta^2\Delta S} + A_1\Delta\alpha_n e^{-b_1\beta^2\Delta S/2} \tag{3.13}$$

$$Y_n = Y_{n-1}e^{-b_2\beta^2\Delta S} + A_2\Delta\alpha_n e^{-b_2\beta^2\Delta S/2} \tag{3.14}$$

The impulsive terms are computed in equation 3.15 where $T_I = c/a$ and a is the speed of sound. The deficiency function for the impulsive term is given in equation 3.16.

$$C^I_{N_n} = \frac{4K_\alpha T_I}{M}\left(\frac{\Delta\alpha_n}{\Delta t} - D_n\right) \tag{3.15}$$

$$D_n = D_{n-1}e^{\frac{-\Delta t}{K_\alpha T_I}} + \left(\frac{\Delta\alpha_n - \Delta\alpha_{n-1}}{\Delta t}\right)e^{\frac{-\Delta t}{2K_\alpha T_I}} \tag{3.16}$$

where $K_\alpha = 0.75$ for low Mach number flows.

Total normal force in potential flow is the linear combination of the circulatory and impulsive force terms, given in equation 3.17

$$C^p_{N_n} = C^C_{N_n} + C^I_{N_n} \tag{3.17}$$

The chord-wise force, C_C is calculated with the equivalent angle of attack and the normal force slope, given in equation 3.18.

$$C_{C_n} = C_{N_n} tan(\alpha_{E_n}) = C_{N_\alpha}\alpha^2_{E_n} \tag{3.18}$$

Leading edge separation The onset of leading edge separation is a critical area for dynamic stall. The onset of separation on the leading edge has been discussed as due to reaching a critical pressure on the airfoil. This is approximated in the model by using a critical value of C_N, which can be computed from the static airfoil polar coinciding with the break in the chord force at stall. The critical pressure criterion is implemented by first applying a first order lag to the normal coefficient term. This is represented in equation 3.19, yielding C'_{N_n}. Similar to before, the deficiency function is given in equation 3.20. Using the pressure lag time-constant, T_p supplied in table 3.2.

$$C'_{N_n} = C_{N_n} - D_{P_n} \tag{3.19}$$

$$D_{P_n} = D_{P_{n-1}} e^{\frac{\Delta S}{T_p}} + (C^p_{N_n} - C^p_{N_{n-1}}) e^{\frac{\Delta S}{2T_p}} \tag{3.20}$$

Trailing edge separation Trailing edge separation is modeled using a modified version of separated Kirchoff flow on 2D bodies where the effective angle of attack is altered based upon the trailing edge separation location, f. First an effective angle of attack, α_f for the separated flow is calculated, equation 3.21.

$$\alpha_f(t) = \frac{C'_N(t)}{C_{N_\alpha}(M)} \tag{3.21}$$

The separation point for a steady-state flow on a flat plate for a given angle of attack is given in equation 3.22.

$$f^{st} = \left(2\sqrt{\frac{C_{N_{st}}}{C_{N_\alpha}\alpha_{st}}} - 1\right)^2 \tag{3.22}$$

The separation point, f^{st}, is then sampled at the effective angle of attack, α_f yielding an effective separation point, f'_n.

$$f'_n = f^{st}(\alpha_f) \tag{3.23}$$

This is corrected with a time delayed deficiency function D_{f_n} given in equation 3.25, with the parameter of pressure lag constant T_f, yielding the effective separation location at a given step of f''_n.

$$f''_n = f'_n - D_{f_n} \tag{3.24}$$

$$D_{f_n} = D_{f_{n-1}} e^{\frac{\Delta S}{T_f}} + (f'_n - f'_{n-1}) e^{\frac{\Delta S}{2T_f}} \tag{3.25}$$

The normal force including trailing edge separation is then given in equation 3.26, with the chord-wise load given in equation 3.27.

$$C^f_{N_n} = C_{N_\alpha}(M)\left(\frac{1+\sqrt{f''_n}}{2}\right)^2 \alpha_{E_n} + C^I_{N_n} \tag{3.26}$$

$$C^f_{C_n} = \eta C_{N_\alpha}\alpha^2_{E_n}\sqrt{f''_n} \tag{3.27}$$

where the recovery factor, η is 0.95.

Dynamic stall In the case where the leading edge pressure builds beyond the critical limit C_{N_I}, dynamic stall occurs. The dynamic stall phenomena is captured by modeling a vortex which grows on the leading edge of the airfoil, detaches and translates down the airfoil chord until it fully separates into the airfoil wake. The added circulation of this vortex adds to the phenomena of vortex lift on the airfoil, C^v_N. This is modeled by first calculating the increment in vortex lift, C_v, with the difference between circulatory loading and the unsteady nonlinear lift using a Kirchhoff approximation, equation 3.28, where K_{N_n} is given in equation 3.29.

$$C_{v_n} = C^C_{N_n}(1 - K_{N_n}) \tag{3.28}$$

$$K_{N_n} = \frac{(1+\sqrt{f''_n})^2}{4} \tag{3.29}$$

The vortex is allowed to decay in time, while adding in the response any new vortex lift from the current time step, shown in equation 3.30. As discussed in[63] a vortex time parameter, τ_v is tracked such that τ_v is zero at the separation condition and $\tau_v = T_{vl}$ when the vortex reaches the trailing edge of the airfoil.

$$C^v_{N_n} = C^v_{N_{n-1}}e^{\frac{\Delta S}{T_v}} + (C_{v_n} - C_{v_{n-1}})e^{\frac{\Delta S}{2T_v}} \tag{3.30}$$

The total normal loading is a linear combination of the vortex lift calculated, $C^v_{N_n}$, and the calculated lift from the previous module of separated flow behavior given in equation 3.26

$$C_{N_n}(t) = C^f_{N_n}(t) + C^v_{N_n}(t) \tag{3.31}$$

The unsteady pressure drag is then given by relating the normal and chord-wise forces through the pitch angle and given in equation 3.32.

$$C_{D_n} = C_{N_n}sin(\alpha_n) - C_{C_n}cos(\alpha_n) + C_{D_0} \tag{3.32}$$

where C_{D_0}, is the viscous drag at α_0

3.3.4. Verification of Dynamic Stall Implementation

To verify that the dynamic stall model has been implemented correctly, a comparison is made with the results given in the original Leishman paper[63]. This is done with a NACA0012 airfoil at a relatively high mach number of approximately 0.3. As the exact data used for the original comparison was experimental, the results here are to show the trends which are predicted by the authors and to show comparisons between the predictions in given unsteady conditions. This will be performed in three conditions. The first is the low reduced frequency response, the next is unsteady behavior in the non-stalled region of the airfoil, and finally is the behavior in dynamic stall. Code used for the verification is given in Appendix E.

One of the outcomes of the dynamic stall model is the dependence on the reduced frequency while modeling the unsteady aerodynamics. At low frequencies of oscillation the unsteady behavior of the model should be equivalent to the static polar. In order to test this, the dynamic stall model was run with a reduced frequency of $k = 0.001$. A 8.1° sinusoidal pitch oscillation with a mean value of 10.3° was applied to the airfoil. The results given in figure 3.7 show that the results of the dynamic model and the static polar properly overlay as expected.

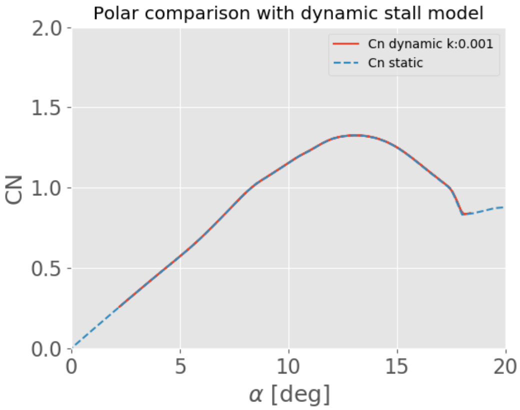

Figure 3.7: Normal Coefficient for $\alpha = 10.3° + 8.1° \sin(\omega t)$, $k = 0.001$

The unsteady aerodynamic model results as shown in figure 3.8a agree well with the original paper from Leishman. The results of which are given in figure 3.8b. This gives high confidence that the attached flow module is functioning as desired.

The response of the model in dynamic stall, along with the results from the Leishman paper are given in figure 3.9. The response of the model is very similar to the data in the previous works. The response varies from the Leishman response due to variations in the aerodynamic polar as well as a different set of constants, however the expected behavior of dynamic stall as shown is evident within the implemented model.

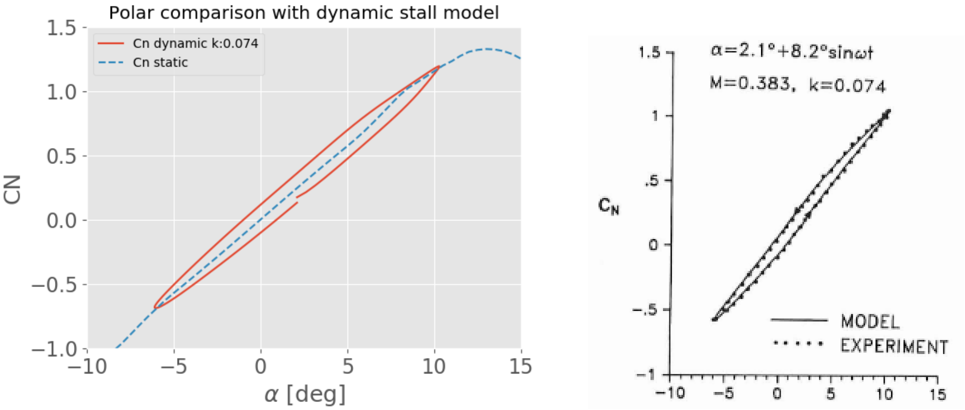

(a) Static polar and the unsteady dynamic model response

(b) Unsteady Response from Leishman

Figure 3.8: Comparison of implemented dynamic stall model with the results from Leishman's work[63], both models calculated at $\alpha = 2.1° + 8.2° \sin(\omega t)$, $k = 0.074$

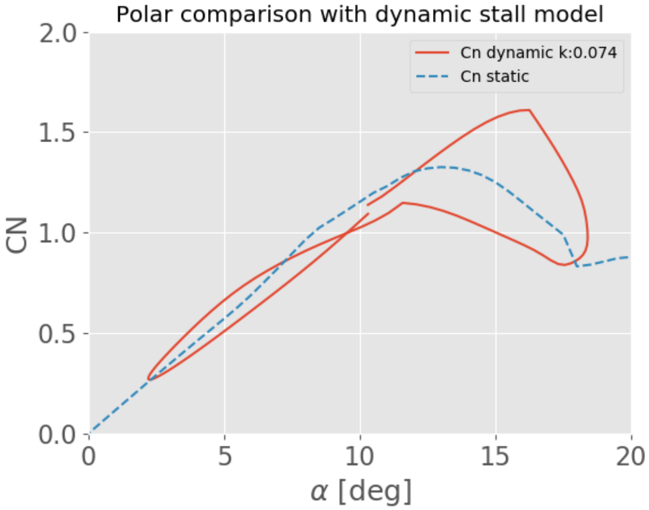

(a) Implemented dynamic stall model

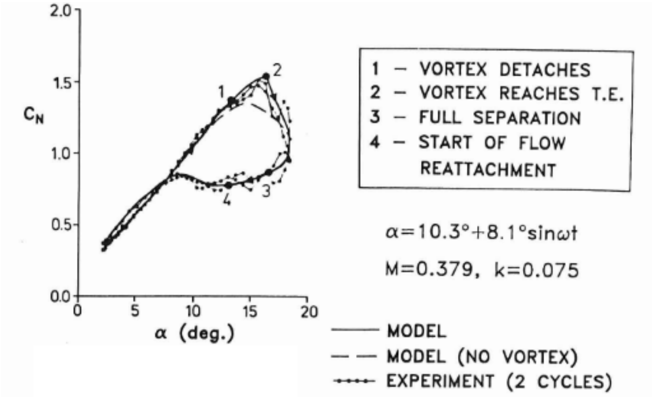

(b) Response from original Leisman implementation[63]

Figure 3.9: Normal Coefficient for $\alpha = 10.3° + 8.1° \sin(\omega t)$, $k = 0.075$

3.4. Virtual Camber Transformation

Flow curvature effects on Vertical Axis Wind Turbines result due to the continuous ”pitching” action of the airfoil as it rotates around the azimuth, causing a curvilinear flow[65–67]. Noting that this pitching motion is different from the ”active” pitch motion discussed in other areas of this thesis. This circular rotation of the airfoil functions by imparting a virtual camber to the airfoil resulting in a shift in the lift curve of the airfoil. The amount of the shift is a function of the chord to radius ratio and operating conditions of the wind turbine. Utilizing the functions presented out by Migliore et al[65], and implemented within the QBlade software package[58,68], the virtual camber was computed for NACA 0021 airfoil used on the PitchVAWT turbine as described in chapter 2. The shift in the airfoil profile is given in figure 3.10a. The polar was then calculated within XFoil. The comparison of the two polars showing the effect of the virtual camber is given in figure 3.10b.

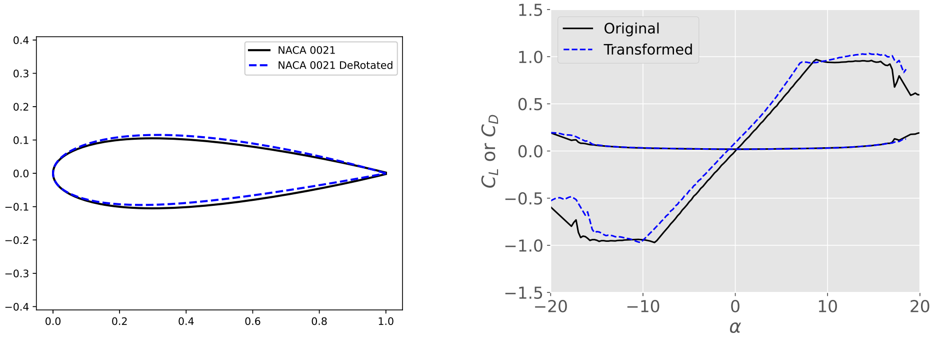

(a) Shape comparison

(b) Polar shift $R_e = 9 \times 10^5$

Figure 3.10: Effect of virtual camber transformation for NACA0021 Airfoil on PitchVAWT Turbine $\frac{c}{R} = 0.1$

3.5. Simulation of Fixed Pitch Offset, 2D and 3D

The blade pitch of a VAWT directly impacts the aerodynamic loading profile experienced by the rotor. The aim of the previous work by Ferreira[69] was to open the design space for potential airfoil optimization for the VAWT to include the possibility of shifting turbine azimuthal loading upwind or downwind as necessary with minimal impact to power performance. The shifting of the loading from upwind to downwind and vice versa results in shifting the operating range of the airfoil. For the potential flow idealized case this is of no consequence and is of use in assessing the feasibility of the idea. When viscous effects are taken into account this shift can have a large impact, especially in lower Reynolds number flows.

In potential flow the assumed airfoil polar used for the Actuator Cylinder model is: $C_l = 1.11 * 2 * \pi \sin(\alpha)$ with $C_d = 0$. As the angle of attack is shifted according to the pitch value, as shown in figure 3.11a the experienced normal load is shifted similarly, as shown in figure 3.11b. The normal load is shifted from slightly biased in favor of the upwind pass at $\beta = 0°$ to mostly downwind at a pitch of $-5°$ to almost completely upwind with a pitch of 5°. This is best visualized using a polar plot showing this normal load for each pitch condition in figure 3.12. The integrated thrust vector is shown emanating from the center of each polar plot. The magnitude of each thrust vector is generally constant at a $C_t = 0.85$ for a tip speed ratio of 4. However, due to the varying load distribution the overall thrust vector varies in direction.

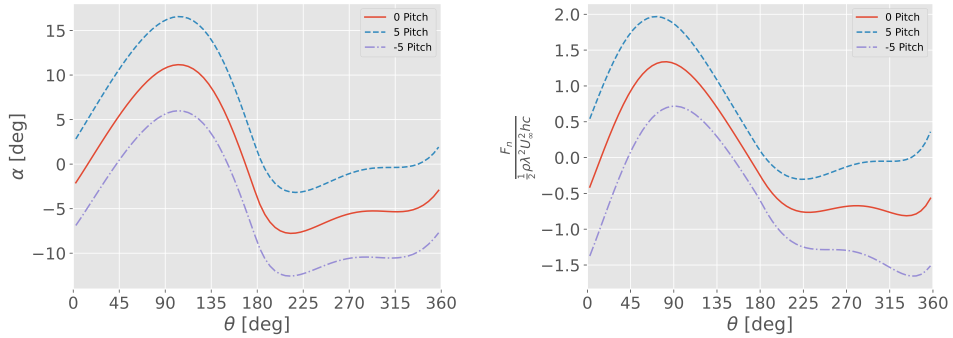

(a) α

(b) F_n

Figure 3.11: Angle of attack and normal force for each pitch offset with inviscid flow for a VAWT with a chord-radius ratio of 0.1 and $\lambda = 4$

The integrated loading of the VAWT is a function of the change in bound vorticity over time and the pitch angle change adds a constant bound vorticity over the rotation would thereby cancel out any effects in the wake development. In order to witness this, the study was conducted using the U2Diva 2D vortex panel code[11] to plot the wake development for 8 diameters downstream with each pitch configuration shown in figure 3.13. The wakes of all three pitch configurations are very similar until approximately 7D down stream when the coherent wake begins

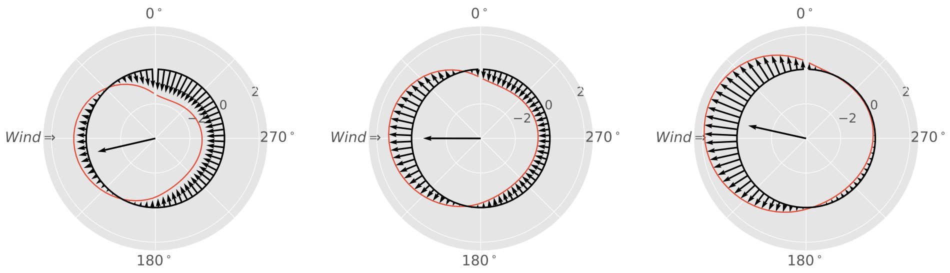

(a) β = −5°, C_T = .84 (b) β = 0°, C_T = .85 (c) β = 5°, C_T = .84

Figure 3.12: Polar plot showing effect of normal load shift with inviscid flow, calculated with AC model, normal force coefficient shown with integrated thrust magnitude as center arrow.

to meander a bit due to mostly numerical deviations. This behavior is consistent with the expected two dimensional behavior of wake evolution. Even with a varying thrust angle as shown in figure 3.12, the near wake evolution does not vary.

To understand the effect on the turbine wake evolution of a VAWT with an aspect ratio of $H/D = 1$ like the PitchVAWT, a 3D lifting line formulation of a vortex model is run using the software QBlade[58]. The same inviscid airfoil polar was used neglecting the role of drag. The evolution of the wake is shown in figure 3.14. The wakes begin to exhibit the appearance of a crescent shape to either side depending upon the average thrust vector. With a shift toward the positive y direction for the $\beta = 5°$ case, and the opposite for the $\beta = -5°$ scenario. The $\beta = 0°$ case remains neutral with the wake slowly expanding vertically and contracting horizontally as it evolves down stream. This suggests the possibility that not only are the instantaneous loads decoupled from the power and thrust integrated loading of the turbine, but the wake evolution in three dimensions is as well. There exist many possible azimuthal loading profiles which can extract similar power and thrust, which lead to varying wake evolution of the VAWT. This can potentially lead to large gains in the area of wake steering for wind farm scenarios.

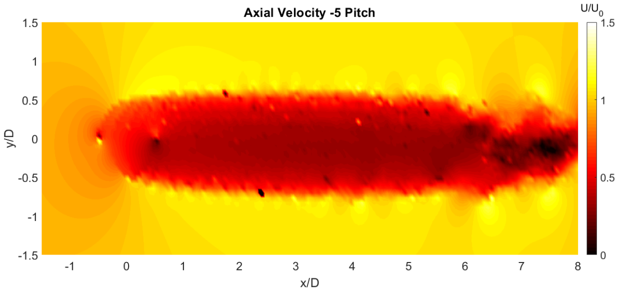

(a) $\beta = -5°$

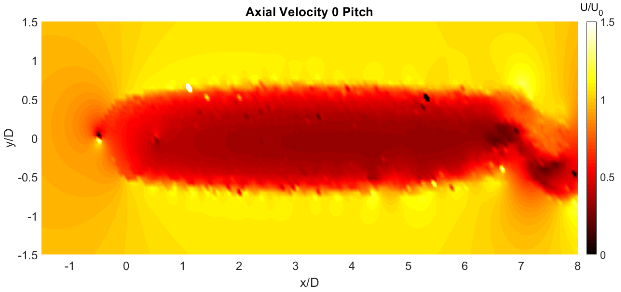

(b) $\beta = 0°$

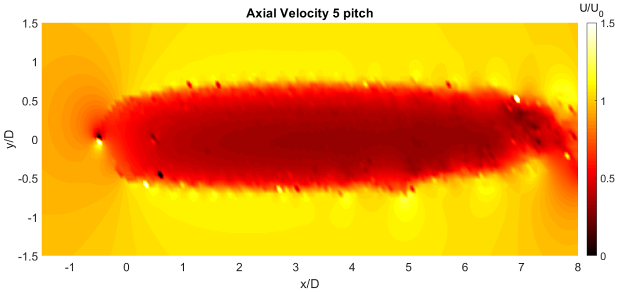

(c) $\beta = 5°$

Figure 3.13: Wake evolution of VAWT using 2D panel code U2DIVA, $C/R = 0.1$, $\lambda = 4$

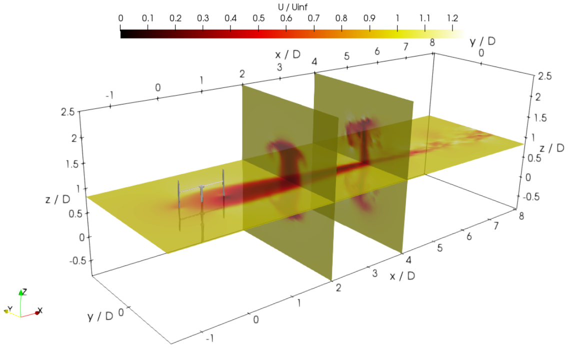

(a) $\beta = -5°$

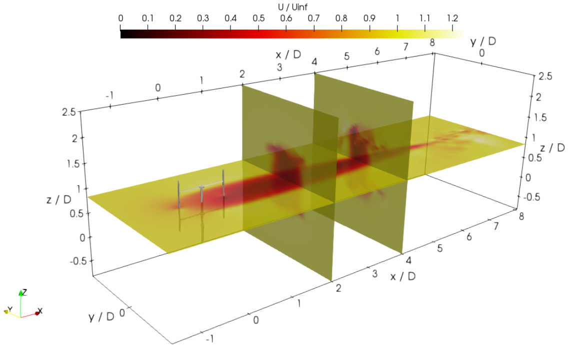

(b) $\beta = 0°$

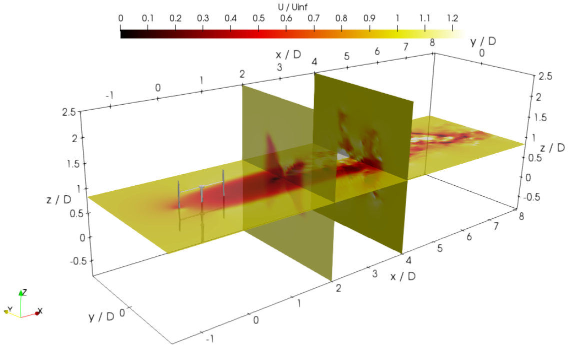

(c) $\beta = 5°$

Figure 3.14: Wake evolution of 3D VAWT using from lifting line vortex model with varying pitch angle, $C/R = 0.1$, $\lambda = 4$

In order to properly understand the effects of varying the pitch angle in practical application, and for comparison to wind tunnel test data of the PitchVAWT turbine, viscous effects of the airfoil need to be accounted for. Unlike in the potential flow examples above, the shift in angle of attack over the azimuth makes a large difference in the behavior of the airfoil. The added pitch causes a shift in the operating region of the airfoil, which can lead to stall. As an example of this phenomena the airfoil used for the PitchVAWT turbine and expected results are given. First, a virtual camber transformation was performed on the once symmetrical airfoil in order to compensate for flow curvature. The lift and drag polar were then calculated using XFoil for an operating Reynolds number of 9×10^4. Due to the surface condition of the manufactured airfoil including a spray painted exterior, a $N_{crit} = 5$ was used. The resultant polar is given in figure 3.15a. The Beddoes-Leishman dynamic stall model which is described in section 3.3 is used during the analysis. The lift coefficient versus the experienced angle of attack around the azimuth is plotted in figure 3.15b. The effects of the shift in α due to pitching are visible noting how the solid black line of zero pitch oscillates from approximately $-9°$ to $12°$ and each case is offset by approximate $5°$. The airfoil subsequently enters dynamic stall on the upwind pass for the positive pitch case and on the downwind pass in the negative pitch case. Therefore the understanding of the stall phenomena in these cases is critical for predicting the expected loading of the offset pitch cases.

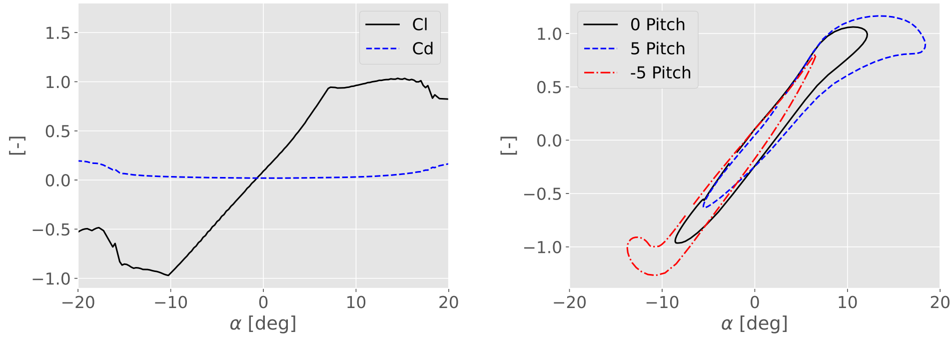

(a) Static polar

(b) Lift with DS model for each pitch

Figure 3.15: Airfoil polar with correction for flow curvature static and dynamic stall during operation. $Re = 9 \times 10^4$, $N_{crit} = 5$ Calculated with XFoil[48]

The results showing the viscous effects on both the experienced angle of attack and the normal force coefficient are given in figure 3.16. The dynamic stall in both the upwind and downwind location of the rotor complicate the expected normal load profile, as there is no longer a clear shift from upwind to downwind loading across the whole rotation. This violates the assumptions made of the addition of a constant bound vorticity over the rotation. Therefore the expectation of a consistent thrust over the rotation is also violated. This is shown in the resultant model as the values of thrust coefficient vary from 0.64 to 0.78 for the 2D actuator cylinder model with dynamic stall at a Reynolds number of 9×10^4. The polar plot of the normal loads in figure 3.17 do show a shifting in the load profile between upwind and downwind, but it is much less pronounced than seen in the potential flow case.

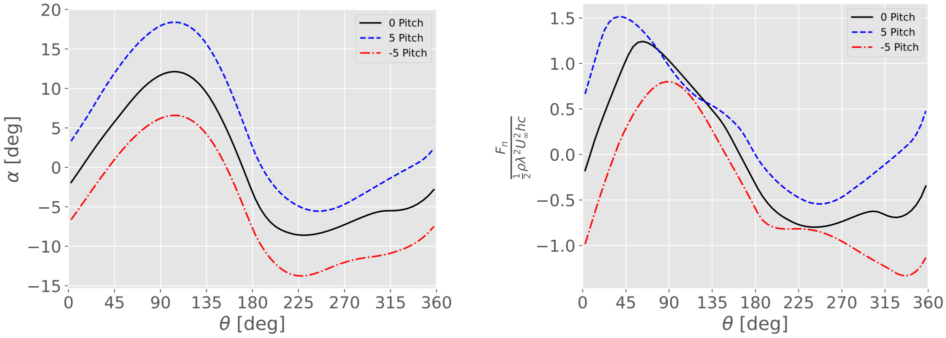

(a) α

(b) F_n

Figure 3.16: Expected α and F_N for each pitch offset with viscous flow for PitchVAWT turbine. $R_e = 9 \times 10^4$ $\lambda = 4$

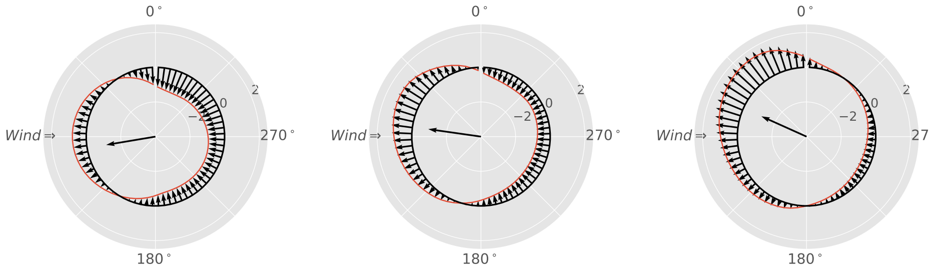

(a) $\beta = -5$, $C_T = .74$

(b) $\beta = 0$, $C_T = .78$

(c) $\beta = 5$, $C_T = .64$

Figure 3.17: Polar plot showing effect of normal load shift with $R_e = 9 \times 10^4$ flow, calculated with AC model with dynamic stall, normal force coefficient shown with integrated thrust magnitude as center arrow. $\frac{F_n}{\frac{1}{2}\rho\lambda^2 U_\infty^2 hc}$

With these model predictions, during experiments it is expected to see a higher loading of the five pitch case at the start of the rotation which would quickly stall before recovering on the downwind half of the rotation with a spike in load. The negative pitch case should have lower loading in the start of the rotation, before entering into stall on the downwind half of the rotation.

3.6. Summary

In this chapter, the tools and techniques for modeling the aerodynamic performance and loading of Vertical Axis Wind Turbines is discussed. The Actuator Cylinder flow model with a Beddoes-Leishman type dynamic stall model was discussed in detail, and each were verified with previous results. These tools were then used to simulate the response of the PitchVAWT turbine under fixed pitch offset conditions. This simulation outlined the difference in turbine behavior assuming a completely inviscid solution, and one expected in wind tunnel conditions in the Open Jet Facility. The evolution of the turbine wake was studied in two and three dimensional simulations with fixed pitch offsets highlighting the potential for influencing the wake evolution of the VAWT by modifying blade pitch.

Bottom Line:

- Aerodynamic modelling tools used within the thesis are presented. These tools are summarized in table 3.1:
    - Actuator Cylinder Model with Beddoes Leishman Dynamic Stall model
    - U2Diva: 2D inviscid vortex panel method
    - CACTUS: 3D Lifting Line free wake vortex model
    - Q-Blade: 3D Lifting Line free wake vortex model
- Aerodynamic behavior is highly dependent upon airfoil viscous effects at the low Reynold's number flow of 9×10^5 and below.
- Changing circulation distribution over the turbine azimuth effects the evolution of the 3D wake
- Fixed pitch offset changes of the turbine shifts the loading upwind or downwind corresponding to the pitch offset. In 3D, this loading change alters the expected development of the wake as it progresses downstream.

4

Structural Modeling and Multibody Dynamics

A digital twin can be described as a digital replica of a physical asset. The use of such models is key to understanding complex loading phenomena experienced during testing of vertical axis wind turbines. Unsteady aerodynamic and structural effects such as dynamic stall and dynamically changing thrust and blade loading are difficult to predict with certainty. This leads to inefficient turbine designs or worse yet premature failures. Many of these phenomena can be better understood through experimental testing. The analysis of these test results is greatly improved by having a well calibrated digital twin model of the turbine. This chapter discusses the methodologies used in the development of the model for a H style vertical axis wind turbine. This includes physical measurements of the as built system, updates to the models based upon experimental testing and a final correlation between test and model on a component by component as well as fully assembled system. A multibody dynamics model is then built based upon the results of the calibrated finite element model allowing for efficient simulation of loading phenomena in the time domain.

Parts of this chapter have been published in ”Experimental characterization of H-VAWT turbine for development of a digital twin.”[70]

4.1. Introduction

A finite element model of the turbine was made to understand the effect of changes in aerodynamic loading on the thrust and blade reaction loads. It is also used as a check to properly design tests in order to operate the turbine in stable conditions. To be confident what is predicted by the models correctly matches the test data, it is important to make sure the model is as representative of reality as much as possible. It has been shown that modal test data is a good way of estimating the uncertain material parameters used in modeling[71] and has been used for many years on wind energy systems[72–77]. Modal testing provides a way of validating the models such that the overall mass, stiffness, and boundary conditions of the system can be accurately captured. Whereas traditional static testing such as 3 point bend tests and overall weight measurements will not properly provide all necessary detail.

Therefore a series of tests were performed on the PitchVAWT turbine in order to ensure the digital twin finite element models correctly match reality. Each major component of the turbine, the blades, the struts, the mounting platform and the fully assembled system are checked for consistency with the corresponding digital model.

4.2. Finite Element Model

The finite element models of the turbine system are composed of a mix of beam and shell elements. The initial turbine modeling, as well as the comparison and correlation to the modal test data was performed using Siemens Simcenter3D software package. The turbine blades and struts were modeled using 1D beam elements with the measured cross sectional properties discussed above. The simple nature of the constant cross section and no blade curvature aided in the modeling process. The tower was also modeled as a constant tubular cross section beam. For the full turbine system, point masses were added to simulate the effect of the mounting hardware for the blades and struts and rigid connections were made between adjacent nodes to tie the model together. The platform is modeled in three major components, the steel top-sheet is modeled with shell elements, the support frame is modeled with constant cross section beam elements, and the lower scissor support is modeled with grounding springs in each DOF tied to the frame where the lift mounts were located during the testing. A more in-depth discussion of each of the models is described here.

4.2.1. Platform

The platform is a 2 m × 3 m platform lift consisting of two steel flat plates bolted to a steel beam frame of a scissor lift. The table top height is set to 72.5 cm for this testing. This positions the table so that the platform is ”floating” on the lift and not settled in its lowest position where it contacts the base. This is to avoid the nonlinear effects of contacting the base structure without being properly fixed in place. It also coincides with the position used in testing of the PitchVAWT vertical axis wind turbine. A photo of the platform is given in figure 4.1 and a CAD model showing the elevated table with respect to the Open Jet Facility outlet is given in figure 4.2.

Due to the ”floating” nature of the platform top, it was decided to physically model the top platform and represent the lifting structure as a series of springs connected at the locations of contact for the pin / rollers of the scissor lift. The turbine model is based upon three major components, the grounding springs, the beam sub-frame and the top steel platform. Each independent mesh uses an element size of 50 mm. The full finite model is shown in figure 4.3.

Grounding Springs

A translational spring is added to each direction at the four connection point nodes, yielding twelve translational springs in total. A spring constant of $500\,\mathrm{N\,mm^{-1}}$ was assigned to each spring as a starting point assumption. The value of each spring will be updated through an optimization process based upon the measured data acquired during modal testing.

Sub-frame

The platform sub-frame consists of a set of constant cross section square beams welded together. The cross section is shown in figure 4.4. The layout of the beams is based upon cross-referencing the provided solid cad model pictured in figure 4.2 with physical measurements of the system. The layout is given in figure 4.5.

Platform surface

The top surface of the platform consists of two 15 mm thick steel plates. These are modeled as a single 2D shell mesh. The side skirts are modeled with 3 mm thick steel 2D shells. Nodes along each edge are shared between the element meshes tying them together. Mass-less rigid body elements, RBE, are used to tie the 2D shell meshes to the 1D beam elements of the sub-frame.

4.2.2. Base

The base structure houses all of the electronic and drive-train components for the turbine. Structurally it is made up of three sections, a tubular steel structure, aluminum mounting plates, and a main bearing housing which supports the rotor and takes all of the thrust loading. The base is shown in figure 4.6.

Tubular Structure

The base of the turbine consists of a set of square tubular sections welded together. The cross section of the tubes are 50 mm square with 3 mm wall thickness. These are modeled with 1D beam elements. All connections are made by directly merging intersecting nodes, resulting in fixing all 6 DOF to the neighboring elements.

Mounting plates

Shell elements are used to model the horizontal platforms where the motor and main bearing housing are mounted. The top plate is 20 mm thick, while the bottom plate is 30 mm. Both are made of Aluminum.

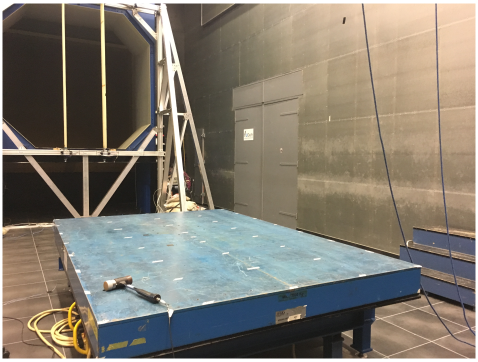

Figure 4.1: Photo of platform

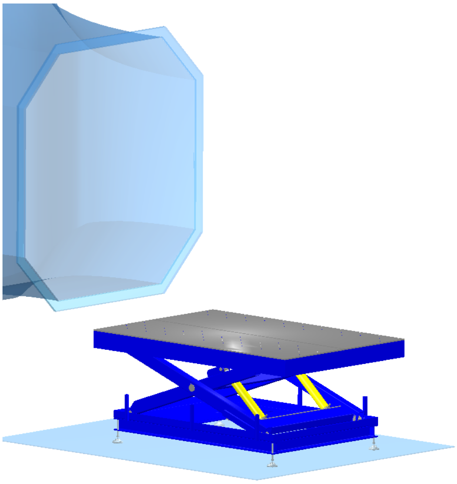

Figure 4.2: CAD model of platform

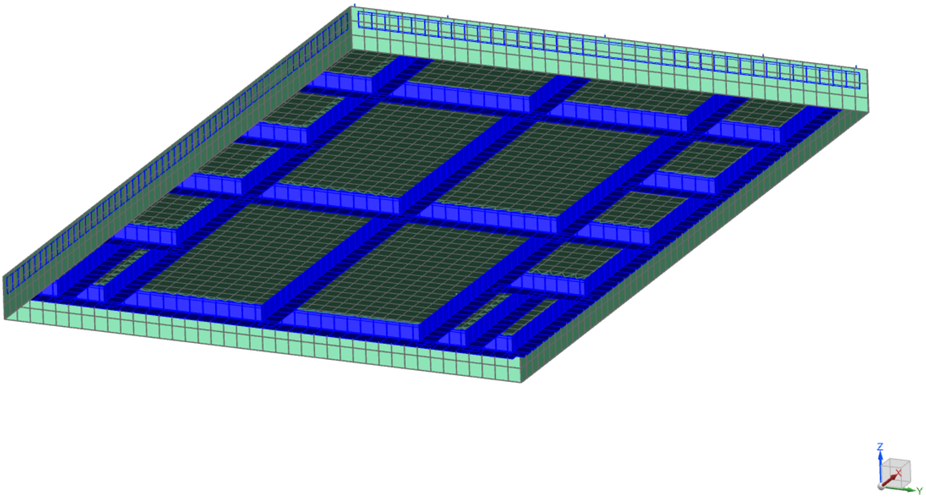

Figure 4.3: Finite Element Model of platform showing base sub-frame beams and shells for the deck and side-skirts

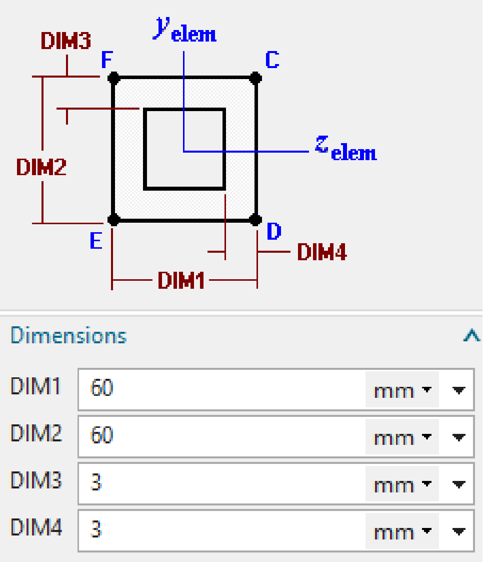

DIM1 60 mm

DIM2 60 mm

DIM3 3 mm

DIM4 3 mm

Figure 4.4: Cross-Section of beams used in platform sub-frame

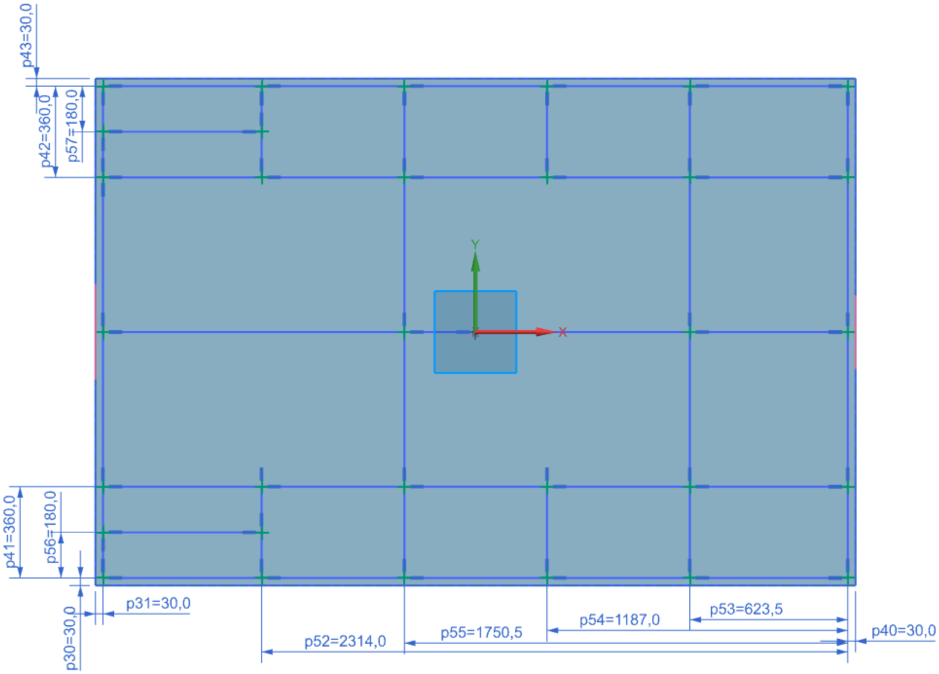

Figure 4.5: Layout of beams used in platform sub-frame dimensions in mm

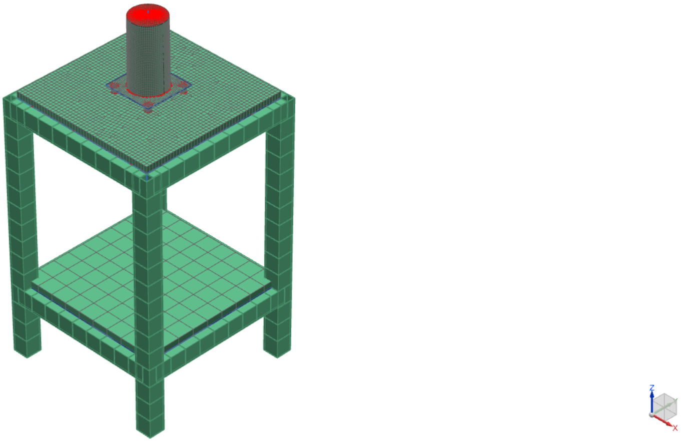

Figure 4.6: Turbine base structure using beam and shell elements with cross-sections represented

Main Bearing Housing

The main bearing housing is modeled using using 5 mm thick steel shells. Rigid body elements are connected to a central node representing both bearings. The load cells are modeled with 3D steel elements and mated to the base top plate and the housing using RBEs.

4.2.3. Rotor

The rotor consists of a main tower, with two blades, and two struts per blade. The rotor model is a collection of 1D beam elements for the blades and tower and point masses with rotational inertia representing the relevant connection hardware. Each sub-model is connected with RBEs to neighboring nodes.

Tower The tower is a hollow steel tube with a 60 mm outside diameter and a 5 mm wall thickness. The tower is designed to split for the easy removal of the rotor. This is accomplished with a flange 54 cm from the base of the tower, which is mounted to the main-bearing. The tower is modeled with 1D beam elements. The mass and inertia of the connections for the main flange and the strut connection blocks are modeled using point mass elements.

Blades and Struts The blades and struts are constant cross-section extruded aluminum. The cross-section of the blades are a NACA0021 airfoil with 75 mm chord length, shown in figure 2.16. The external shape of the struts is a NACA0018 airfoil and a chord length of 60 mm, but they are of a different alloy and are thus tested and modeled with different material properties. The cross section is given in figure 2.19. Both blades and struts are modeled with beam elements. The connections between them are modeled with point-masses with rotational inertia for each of the connections.

4.2.4. Full Assembly

For the full-turbine assembly, each of the turbine sub-components are mated based upon realistic mounting conditions. The base is assembled to the platform using the mass-less RBE elements coinciding with the clamp-attachments on the base of the turbine. The rotor is then assembled with spider nodes corresponding to the upper and lower main bearings. These allow for rotation about the vertical axis, so only 5 DOF are constrained.

4.3. Testing Methods

Individual tests are performed to measure:

- As-built dimensions of components and full turbine
- material properties of blades and struts
- Frequencies and mode shapes of turbine and components
- representative grounding spring stiffness values for flexible blue platform

The approach is to verify as many physical properties as possible through independent measurements. For example, in going from the design concept of the blade to a calibrated finite element model there are several unknowns which need to be verified: the actual material density and elastic modulus, the as produced geometry, and the boundary conditions which support the said blade on the turbine. The length of the blades are verified using a tape measure. The profile of the blade is measured with a Coordinate Measurement Machine and used to calculate the cross sectional area and moment of inertia about each axis. The weight of the blades is then measured with a Kern 16K0.1 platform scale reproducible to the nearest 0.1 g. Knowing the length, cross sectional area, and weight of the blades allowed the calculation of the material density. The two properties left to verify are the material stiffness and the boundary conditions of the blade on the turbine. A free-free modal test removes the effect of boundary condition, thereby allowing the stiffness of the material to be altered to match the natural frequencies of the blade. With a calibrated free-free model, the full turbine modal test is used to identify the boundary conditions of the attachments. This procedure was also performed for the struts.

The platform dimensions were measured with standard tape measures and was tested with EMA prior to turbine installation in the height configuration used for the testing. Standard material models for steel were used as initial guesses. The 6 rigid body modes are used to tune the support springs, and the flexible modes are used to tune the material stiffness of the beam elements. These tests are used to update the finite element model properties of each component independently.

The full turbine is then tested while mounted to the platform in the open jet facility wind tunnel to verify the boundary conditions of the connections between each component.

Experimental Modal Analysis with impact testing was performed for each structure in a Single Input Multiple Output (SIMO) format. EMA consists of measuring a series of excitation and response between degrees of freedom of the structure. Traditionally a force transducer is used to measure the force excitation imparted into the structure at a given degree of freedom, DOF, and an accelerometer is used to measure the response of the structure. A transfer function is calculated between the excited and the measured DOF, this is known as the Frequency Response Function or FRF. A transfer function is required between each DOF in order to understand the global motion of the structure due to a given input. The collection of FRFs relating each output DOF and response DOF is referred to as the FRF matrix. Each FRF is then curve fit with a specific polynomial which has been designed to extract dynamic characteristics of the response including magnitude and phase of the DOF motion as well as the natural frequency and damping characteristics of each mode, this is referred to as Modal Parameter Estimation or MPE. This test takes advantage of the concept of reciprocity, which means that the transfer function between the force and response degrees of freedom is independent of direction. Which in practice means that it is not necessary to measure both response and force at each DOF. A response measurement is required so that each mode can be visualized independent of other modes, but is not necessary at every DOF. The force measurement is ”roved” between all test DOF. In this manner, the full FRF matrix can be assembled.

The blade and strut, referred to for simplicity as ”beam”, component tests used a single accelerometer located at the end of the beam and the hammer was roved to each measurement point. This was completed for both flap-wise and edgewise modes. Measurements were taken with the beam hung horizontally from an overhead support using two long strings. The strings were aligned with the expected location of the nodes for the first bending mode so as to minimize the effects of the supports on the measured modes. The beam is rotated in the supports so that the axis which is being measured is normal to the support. Thus providing minimal support effects in the measured direction. The blade was measured with 22 measurement locations evenly distributed across the blades, while the struts were measured with 5 evenly distributed locations. Figures 4.7 and 4.8 show the test setup and accelerometer mounting for the blade / strut free-free modal tests.

After initial modeling of the platform showed several modes of interest in the frequency range of interest, it was decided to perform a more detailed modal survey of the platform. The testing geometry composed 52 measurement locations in X, Y, and Z directions across the turbine with ten averages at each point. For certain locations it is not possible to physically impact the point in each dimension (like impacting inside the plane of the platform), for these locations slave degrees of freedom to proper adjacent points were used in order to correctly visualize the mode shapes. Three tear-drop IEPE based accelerometers were placed in the X, Y, and Z directions of point 1 located on the top corner of the plate. This corresponds

Figure 4.7: Accelerometer blade flapwise test

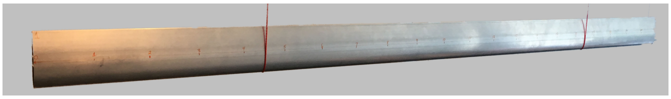

Figure 4.8: Blade Free-Free boundary condition setup

to 73 impact locations and three response measurements with ten impacts per location. Figures 4.9 and 4.10 show the test setup and accelerometers mounted for the platform modal test.

The test geometry of the full turbine is shown in figure 4.11. Impacts are made at 42 locations in X, Y, and Z directions distributed across the turbine system with five averages at each measurement location. The response of the turbine is measured by a set of six tear drop accelerometers placed in the X, Y, and Z directions of the corner of the platform, and the X, Y, and Z directions on the bottom of the first blade. The locations are chosen in order to properly capture modal dynamics in the three translational directions within the frequency range of interest. In total 6 reference measurements are made from 100 impact locations with 5 averages for each location.

4.3.1. Data Collection and Processing

Data was collected using National Instruments™CDAQ hardware and LabView at a sampling rate of 2560 Hz. Each data block lasts 10 s. No windows have been used in the collection of the data. The averaged autopowers for the platform drive-point impact measurement during the full turbine testing are shown with the X, Y,

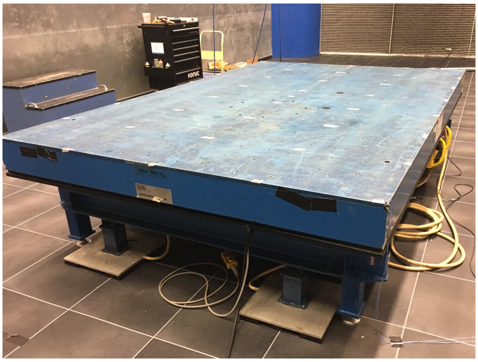

Figure 4.9: Platform modal setup

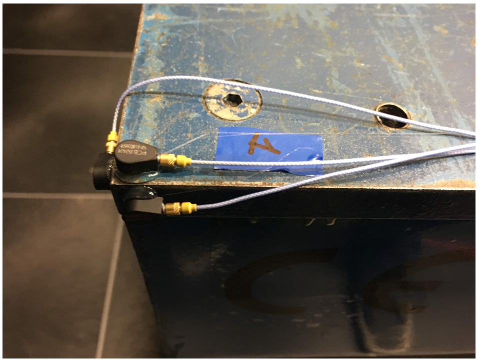

Figure 4.10: Accelerometers on platform

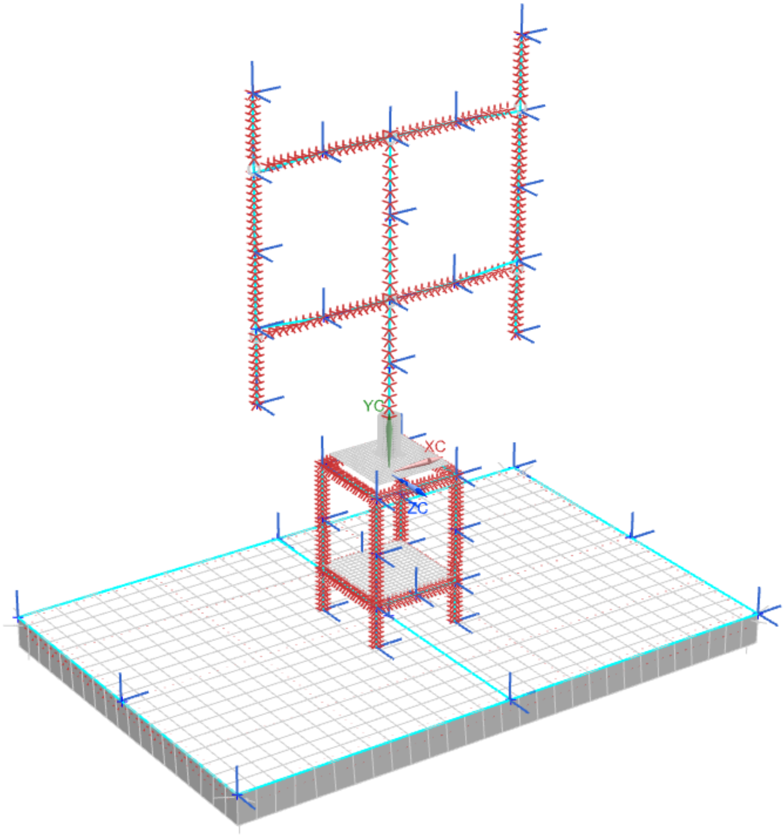

Figure 4.11: Experimental test geometry with impact directions shown as long blue arrows overlaid on the finite element model including all 42 test impact locations

Z response in figure 4.12. This shows the frequency range excitation of the impact is relatively flat throughout the range of interest, meaning the modes should be properly excited.

The three reference accelerometers on the platform were shown to be sufficient to properly capture the dynamics of the full system in the lower frequency range up to 40 Hz. The sum of all FRFs for all three directions from the platform reference accelerometers is shown in figure 4.13. This measurement gives insight into just how many modes the full structure has between 5 Hz to 18 Hz. Data post-processing and Modal Parameter Estimation, MPE is performed within Siemens™Test.lab software using the Polymax curve-fitter. After calculation of the mode shapes individual FRFs are then synthesized based on the fit modes. The synthesized FRFs should compare well with each measured FRF if the modes have been properly characterized. An example of one of these comparisons is given in figure 4.14. Modes have been fit in this case up to a frequency of 40 Hz. Each vertical line represents the frequency where a mode was found. The magnitude and phase of the synthesized FRF matches the measurement closely throughout the range of interest. This process is performed on all EMA tests of the individual components as well as the full turbine system.

4.3.2. Model Correlation

The model is compared with test data on two major criteria, the natural frequency of the modes and the similarity of the mode shape vectors themselves. The correlation between mode shape vectors will be made using the Modal Assurance Criterion, MAC[78,79], shown in equation 4.1. MAC is a correlation tool which compares each modal vector. A MAC value of 1 corresponds to a perfectly correlated mode shape pair, meaning mode shape vectors are exactly the same, while a MAC value of 0 implies no correlation between the shapes. While not a comprehensive measure, it provides good insight into the behavior of the model with respect to the test data.

$$MAC = \frac{[[U]^T[E]]^2}{[[U]^T[U]][[E]^T[E]]} \tag{4.1}$$

Where:
U = Mode shape vectors of FEA
E = Mode shape vectors from EMA
T = Transpose

4.4. Testing Results

The blades, struts, and platform have been each measured using a variety of techniques in order to verify the assumptions of the finite element models. The full system was then tested in-situ at the Open Jet Facility wind tunnel in Delft. The results of these tests are given here.

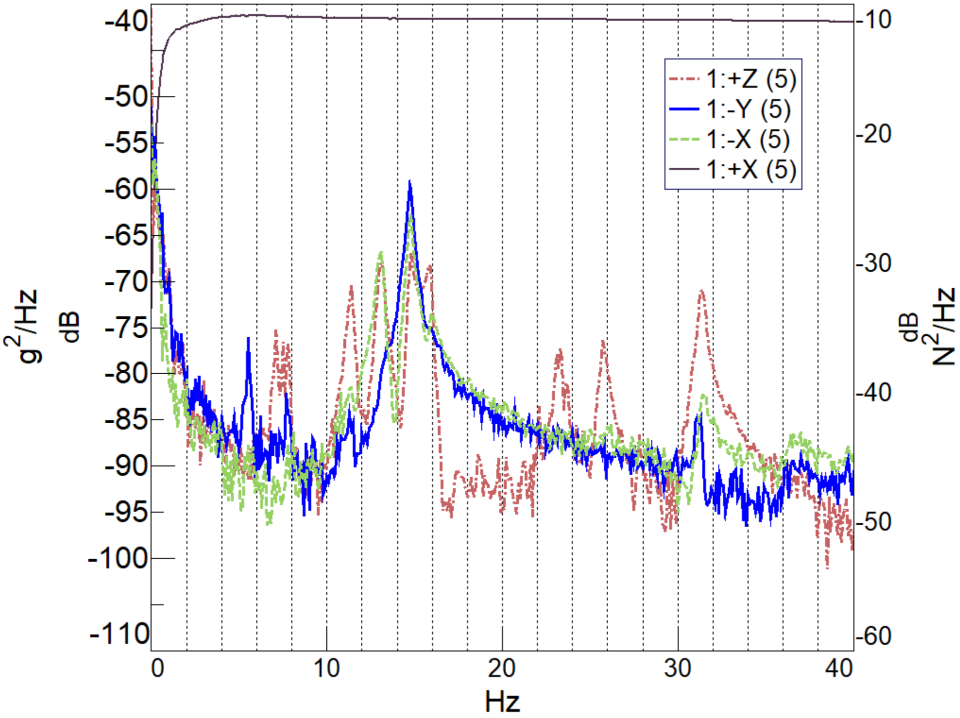

Figure 4.12: Averaged autopowers of impact (right axis, solid black line) and response (left axis) at drive-point location on platform

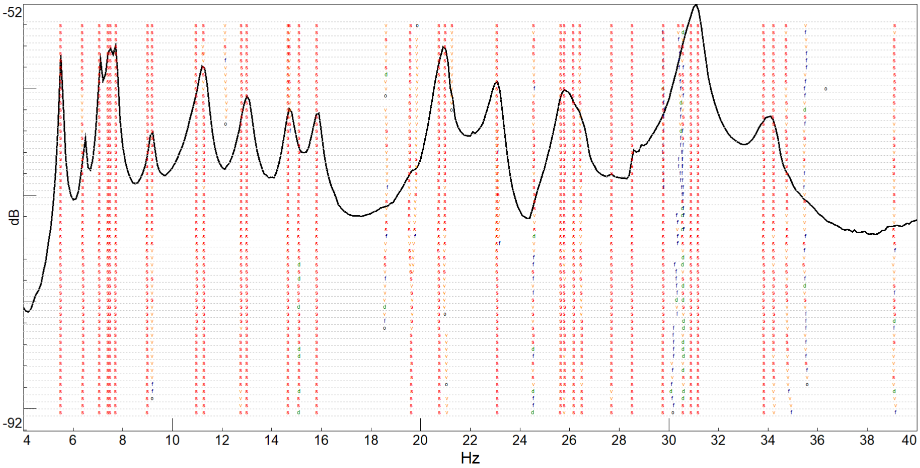

Figure 4.13: Sum of included FRFs on the full turbine system from platform mounted accelerometers with overlaid stabilization diagram, each red ”s” represents a stable pole

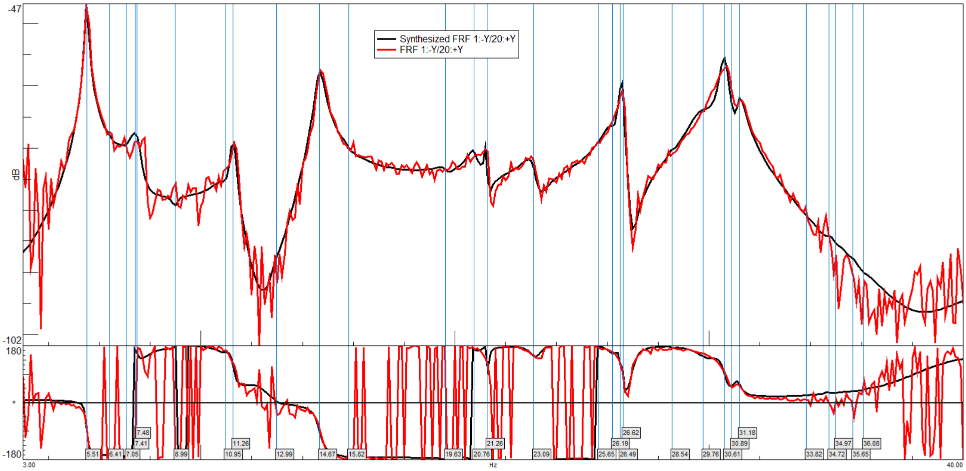

Figure 4.14: Example of a synthesized FRF (black) with a measured FRF (red) from the fit mode shapes(blue vertical lines).

4.4.1. Blades and struts

A set of measurements have been carried out in order to determine the actual length and mass of the blades. Three blades were measured to understand the variability of the manufacturing process for the blades. These measurements together with the previously measured cross sectional properties of the blade, allowed the density of the material to be calculated. Results of the three individually tested blades are shown in table 4.1. The average values of the three blades were used to update the blade length to 1.508 m and density to 2707 kg m^{-3} in the model. The density of the strut material was measured directly to be 2620 kg m^{-3} by measuring a small sample of the material with a DeltaRange AG204 analytical balance.

The first five flexible modes of two independent blades were extracted from measurement data. The natural frequency and damping values for each mode are shown in table 4.2. The values for each blade are very similar, with the largest % difference in frequency being 0.18 %. The conclusion from this is that the two blades are very consistent from the manufacturing process with minimal variation between each blade.

The first four flexible modes for the blades and struts are given in table 4.3.

Table 4.1: Measurements of Blade Properties

Blade	**Length**(m)	**Area** (mm^3)	**Mass**(kg)	**Density**(kg m^{-3})
1	1.508	303	1.2332	2699
2	1.508	303	1.2400	2713
3	1.508	303	1.2380	2709
Average	1.508	303	1.2371	2707

Table 4.2: Variability in Modes Between Blades

Mode	**B1 F**(Hz)	**B1 Damp**(%)	**B2 F**(Hz)	**B2 Damp**(%)	% **Diff Freq**
1	38.10	0.11	38.12	0.38	0.06
2	104.79	0.14	104.98	0.14	0.18
3	204.80	0.06	204.99	0.06	0.09
4	336.83	0.07	337.20	0.08	0.11
5	499.95	0.05	500.60	0.04	0.13

As to be expected based upon the geometry of the airfoils, the flapwise modes are substantially lower in frequency than the edgewise and the structural damping values are all very low due to being Aluminum extrusions. The frequency ranges for the free-free blades are very high with respect to the turbine operating frequencies (up to 3 Hz). This is a by-product of being designed for minimal displacement during rotation at high speeds for use with laser and photographic imaging systems like Particle Image Velocimetry.

4.4.2. Platform Structure

The platform where the turbine is mounted in the tunnel plays a critical role in the overall system dynamics. It is made of a 2 m × 3 m × 0.015 m steel sheet supported by a scissor lift frame. The rigid body modes of the ”floating” support structure can be close to the 2-P excitation frequency of the turbine during operation and needs to be studied in detail. The first flexible modes of the full platform begin to occur in the 20 Hz range. The mode shapes for the first rigid body mode and first flexible mode are given in figures 4.15 and 4.16 respectfully. The natural frequencies and damping values for the modes of interest are given in table 4.4.

Table 4.3: Natural Frequency and Damping Values of Flexible Modes for Blades and Struts

Mode	**Description**	**Freq**(Hz)	**Damp**(%)
	Blade		
1	first flap-wise	38.10	0.11
2	second flap-wise	104.79	0.14
3	first edge-wise	144.25	0.09
4	third flap-wise	204.80	0.06
	Strut		
1	first flap-wise	116.19	0.04
2	second flap-wise	317.87	0.05
3	first edge-wise	471.28	0.03
4	second edge-wise	1257.22	0.04

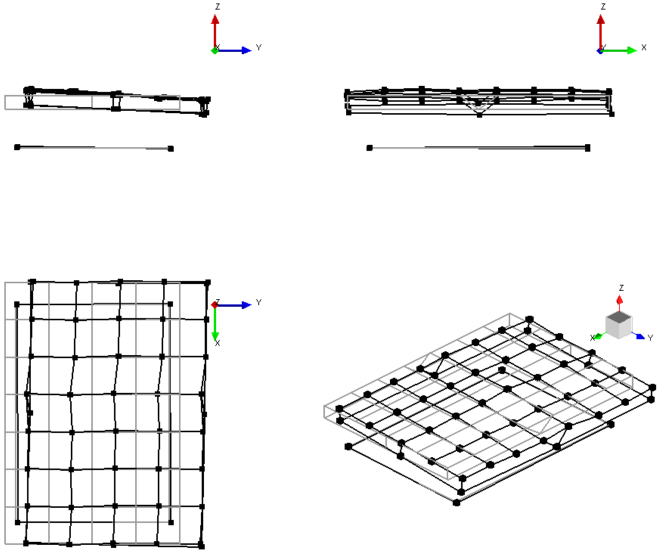

Figure 4.15: First side-side Rigid Body Mode of platform at 5.8 Hz

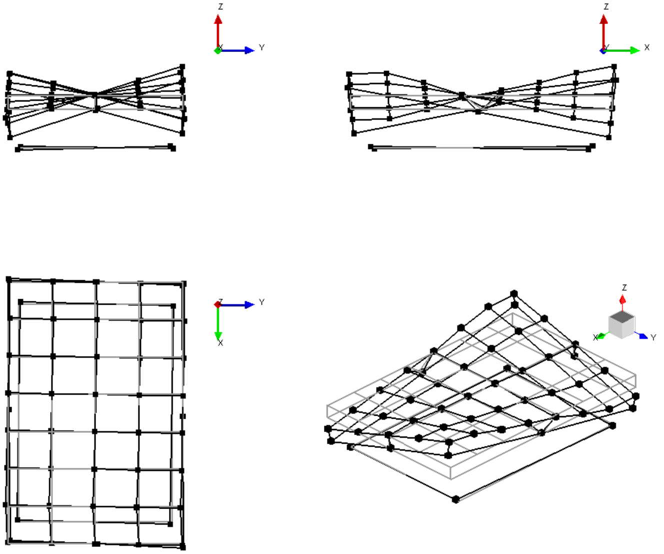

Figure 4.16: First torsion flexible mode of platform at 22.9 Hz

Table 4.4: Natural Frequency and Damping Values of Platform Structure

Mode	**Description**	**Freq**(Hz)	**Damp**(%)
1	side-side rigid	5.81	1.47
2	vertical bounce rigid	7.28	1.6
3	rotation about x-axis rigid	9.78	2.06
4	fore-aft rigid with rocking	12.71	2.4
5	rotation about z-axis rigid	15.68	2.27
6	rotation about y-axis rigid	16.294	1.68
7	first torsion	22.915	0.93
8	first bending with drum	28.84	1.46

4.4.3. Full Turbine

The natural frequency and damping values for each mode are shown in table 4.5. As some of the mode shapes are non-standard, the description of them can be difficult to relate, however, an attempt has been made. Sixteen modes were fit in this frequency range showing a varied set of both rigid body and flexible motion from the platform as well as several flexible rotor modes. These modes were then used to re-synthesize the FRFs. These give a measure of how well the modes were fit. An example of the synthesized FRFs are shown in figure 4.14. The synthesized FRFs fit the data well for the given responses, and is mostly consistent throughout the measurement range. At higher frequencies the sparsity of the test geometry prevents properly tracking modes with large amounts of curvature. An example of the first platform side to side rigid body mode is shown in figure 4.17

Table 4.5: List of Modes of Full Turbine Installed in OJF

Mode	**Description**	**Freq** (Hz)	**Damp** (%)
1	table side-side	5.51	0.97
2	strut vert blades out of phase	6.41	1
3	strut vert blades in phase table in phase	7.06	0.71
4	strut vert blades in phase table out phase	7.41	0.9
5	platform rock in phase with tower side side	7.48	3.16
6	platform rock out phase with tower side side	7.71	0.63
7	tower fore-aft	9.05	1.19
8	tower side-side table rock out of phase	11.00	3.42
9	platform rock side-side flex at bearing	11.29	1.03
10	platform rock fore-aft flexible struts	12.96	1.12
11	platform twist	14.68	1.08
12	platform rock fore-aft	15.82	1.02
13	rotor strut rock out of phase	19.65	0.75
14	rotor strut rock in phase	20.77	0.97
15	platform torsion	23.088	1.17
16	platform vertical drum mode	25.65	1.1

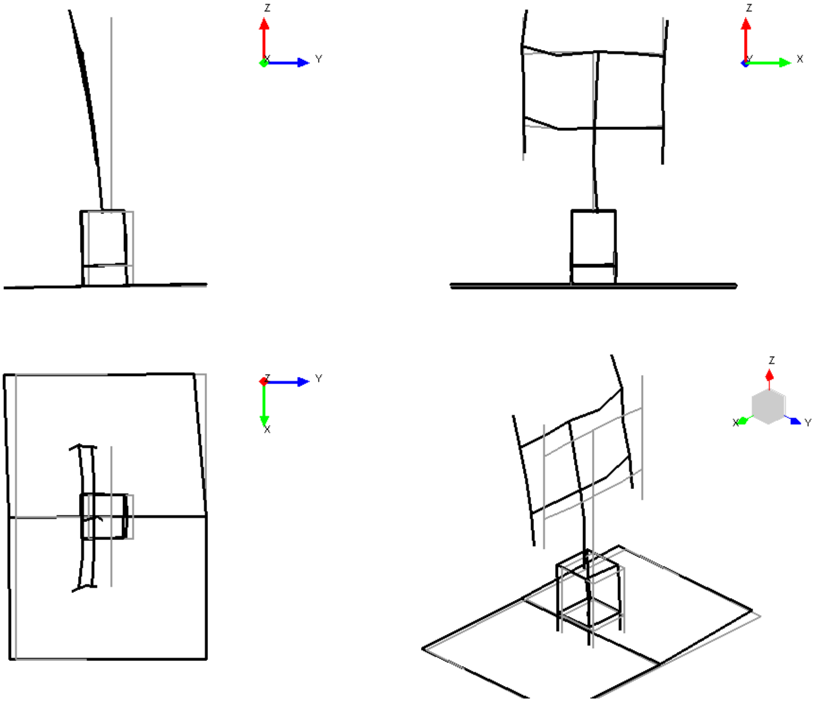

Figure 4.17: First mode of platform rocking at 5.5 Hz

4.5. Correlation and Updating

As stated above, the goal of the updating process is to independently verify the assumptions used in the modeling of the turbine with various measurement techniques on the as built system. These changes are propagated to the models of each component and compared with reality using the correlation of mode shapes and the values of the predicted natural frequencies.

4.5.1. Blades and Struts

The measurements of the lengths, cross sectional areas, and densities of the blades and struts are directly applied to the representative beam models. The material stiffness of the blades and struts are then tuned to match the measured natural frequencies. The updated material properties for the blades and struts are given in table 4.6. The blades and struts are relatively simple to model and the results of the free-free modal tests compare very closely with the expected natural frequencies and MAC values for each mode. The correlation results are shown in table 4.7. The first four flap-wise bending modes of the blades show shown in figure 4.18. The finite element model overlays well with measured mode shapes for each mode.

4.5.2. Platform

As discussed above, the platform consists of a frame structure composed of square tubular steel with a steel plate bolted on top. An under view of the fem model is shown in figure 4.3 giving a view of the frame construction. The scissor-lift structure is approximated by attaching grounding springs in the X, Y, and Z translational directions at each location where the scissor lift mates to the frame. Figure 4.19 shows the layout of the spring attachments from a top down view. The platform dimensions were measured with standard tape measures and input directly into the model. It was not possible to measure the mass of the entire platform due to its size so standard material models for steel were used. The important take away for the model of the table is a representative boundary condition for the turbine, so as long as the equivalent dynamics of the frame and support match the measured data, the model is considered accurate enough for this purpose. The rigid body modes of the platform are used to tune the support springs. The tuning of the springs was achieved through a multi-objective genetic algorithm optimization of each spring stiffness with the target being to maximize the MAC value and minimizing the difference in frequency between each mode pair. The results of the optimization for each spring stiffness is given in table 4.8.

Table 4.6: Updated Material Properties for Blades and Struts

Property	**Dimension**
ρ_{Blade}	2707 kg m^{-3}
ρ_{Strut}	2620 kg m^{-3}
E_{Blade}	69 GPa
E_{Strut}	55 GPa

Table 4.7: Blade and strut free-free EMA vs FEA updated properties

Mode	**EMA Freq**(Hz)	**FEA Freq**(Hz)	% **Diff**	**MAC**
		Blade		
1	38.10	37.97	−0.33	0.996
2	104.79	104.66	−0.12	0.997
3	204.80	205.19	0.18	0.997
4	336.83	339.21	0.71	0.995
		Strut		
1	116.19	117.75	1.34	0.999
2	317.87	323.05	1.62	0.995
3	471.28	424.19	−9.99	0.995
4	616.04	628.22	1.98	0.998

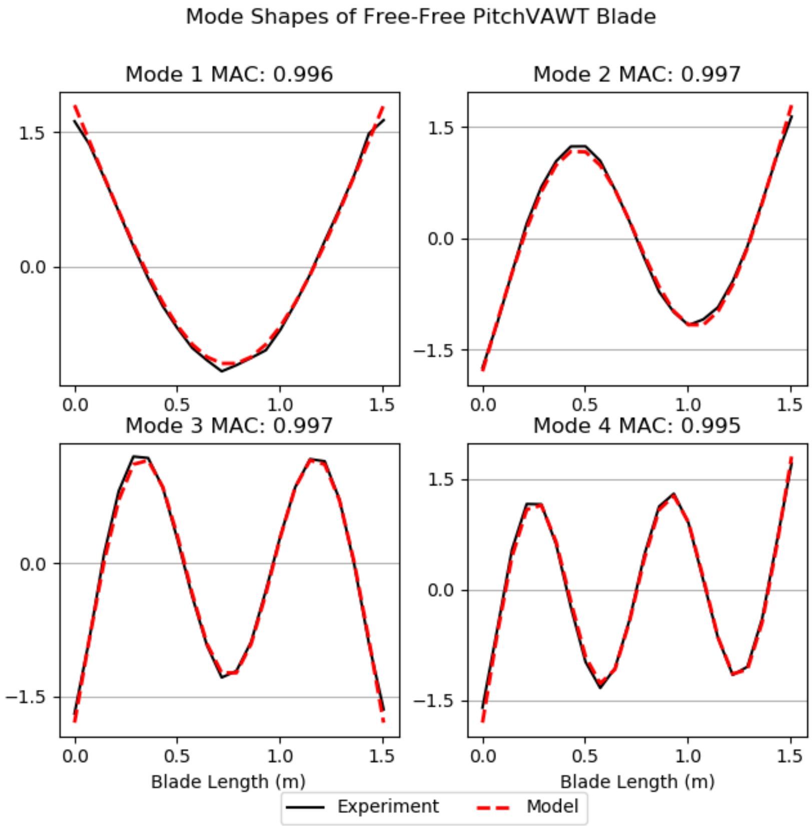

Figure 4.18: Overlay of first four flexible modes of turbine blade, Unit Modal Mass scaling

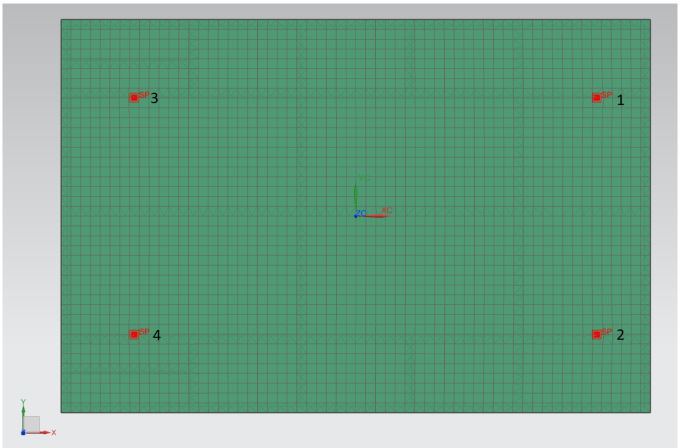

Figure 4.19: Layout of spring connections for platform

The correlation of the rigid body modes and first two flexible modes for the platform are given in table 4.9. The rigid body mode frequencies and mode shapes align fairly well which points to the tuning of the mounting spring constants and the general accuracy of the layout of the frame structure. However, not all modes are matched perfectly, such as the twisting of the platform, and this can be seen as a limitation of replacing the actual scissor lift structure with this set of simple springs. For the purposes of being a boundary condition to the overall turbine performance, the results are considered valid.

4.5.3. Full Turbine Assembly

For the fully assembled turbine, the independently calibrated finite element models of the platform, blades, and struts are mated together along with models of the turbine base and tower which were described above. The flexible dynamics of the tower and base structure are much higher in frequency range than the operating range of the turbine, so standard material models and measurements were used for these parts. Point masses of 200 g were added to simulate the effect of the mounting hardware for the blades and struts. Mass-less rigid connections were made between adjacent nodes to tie the model together. There was no additional model tuning in the fully assembled system.

The correlation of a subset of modes of the full turbine system is given in table 4.10. Overall the model is able to capture the turbine dynamics well. The first rigid body modes of the system match well in frequency and shape especially the side-side and vertical bounce modes. The turbine based flexible modes are also represented well matching frequency to within 0.6 % and accurately in mode shape with a MAC value of up to 0.918. The fact that these modes match so well is evidence that the assumptions used in the connecting of the independent models are valid in the domain of interest. Figure 4.20 shows the EMA and FEA mode shapes side by side.

Table 4.8: Updated platform grounding spring stiffness

Spring	**Stiffness** (N mm^{-1})
$Spring1_X$	20 387.6
$Spring1_Y$	567.2
$Spring1_Z$	2343.7
$Spring2_X$	8637.6
$Spring2_Y$	601.6
$Spring2_Z$	1888.5
$Spring3_X$	8254.5
$Spring3_Y$	329.6
$Spring3_Z$	892.4
$Spring4_X$	11 755.6
$Spring4_Y$	811.1
$Spring4_Z$	935.5

Table 4.9: Platform EMA vs FEA updated modal properties

Mode	**Description**	**EMA Freq**(Hz)	**FEA Freq**(Hz)	% **Diff**	**MAC**
1	side-side	5.82	5.76	−0.89	0.909
2	bounce	7.28	7.60	4.31	0.900
3	rock side-side	9.78	8.81	−9.86	0.975
4	rock fore-aft	12.71	13.10	3.01	0.733
5	twist	15.69	15.75	0.40	0.693
6	first torsion	22.92	28.99	26.5	0.963
4	first bending	28.85	32.09	11.25	0.676

Table 4.10: Full turbine EMA vs FEA

Mode-pair	**EMA Freq**(Hz)	**FEA Freq**(Hz)	% **Diff**	**MAC**
1	5.50	5.64	2.54	0.869
2	6.41	6.44	0.51	0.820
3	7.06	6.65	−5.74	0.844
4	7.71	8.11	5.15	0.839
5	11.29	12.99	15.03	0.611
6	12.96	14.45	11.44	0.658
7	19.65	19.68	0.16	0.859
8	20.77	20.63	−0.65	0.918
9	26.16	28.93	10.58	0.806

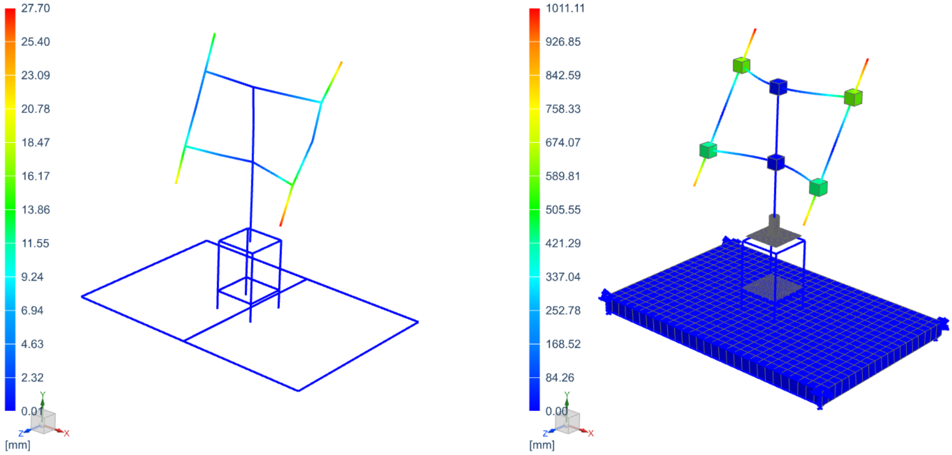

Figure 4.20: Rotor rocking in phase left: EMA 20.77 Hz right: FEA 20.56 Hz MAC: 0.89

4.5.4. Rotational analysis and Campbell Diagram

This calibrated finite element model was then used to compute a Campbell diagram of the turbine in order to identify potential areas of resonance during operation. A complex modal solution was performed using Simcenter Nastran on the turbine every 5 rev min^{-1} up to 300 rev/ min with mode tracking enabled, results shown in figure 4.21. The frequency of the first eleven modes are plotted along with a text label indicating the type of mode shape. The first four fundamental frequencies of rotation are plotted as well to show frequency crossings of interest. An important crossing occurs with the 2P excitation frequency crossing the base side-side mode and the two blade vertical bouncing modes (in-phase and out-phase) at about 160 rev/ min and another important crossing of the base fore-aft and vertical bounce modes at about 230 rev/ min. The 2P excitation frequency is very important due to the fact that the turbine has two blades, therefore the turbine thrust will constantly act at the 2P frequency. Whereas other aerodynamic loads may excite higher per rev harmonics. Many of the tests to be conducted on the turbine occur at $\lambda = 4$, so in order to place the typical operating rotational speed between these two crossings, a wind speed of 4 m s^{-1} was selected. The shaded region represents the potential operational range of the turbine at that wind speed.

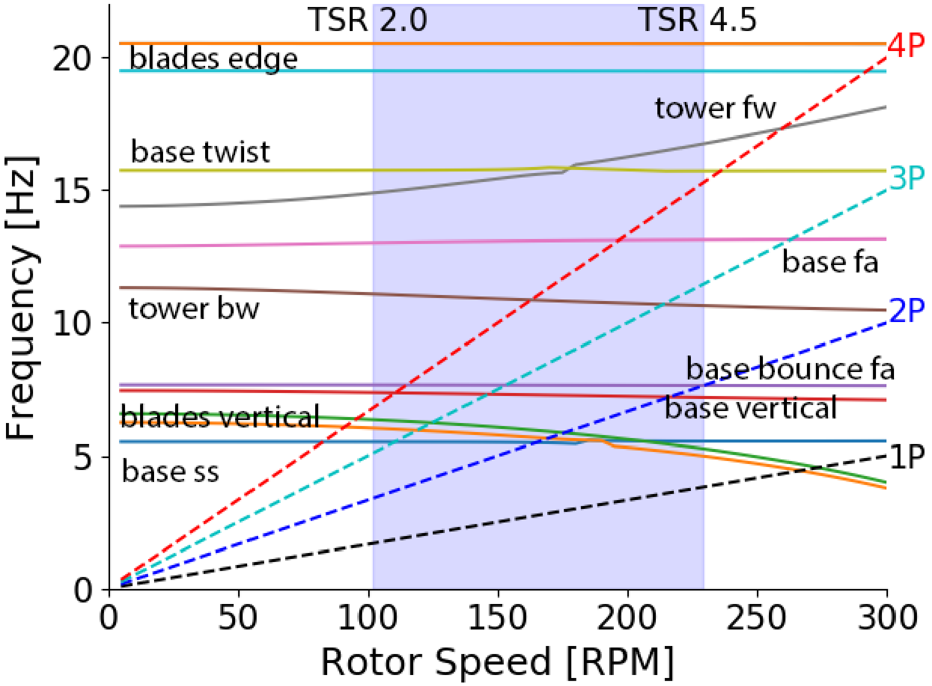

Figure 4.21: Campbell diagram of PitchVAWT turbine with operating ranges outlined from $\lambda = 2.5$ to $\lambda = 4.5$ for a wind speed of $4\,\mathrm{m\,s^{-1}}$

4.6. Multibody Dynamics Simulation

The updated finite element model provides a calibrated base line which can be used to simulate any number of loading and operational dynamics that are of interest. However in order to capture long term dynamic events in the time domain the computational time for the full structural model is very costly. The most efficient way to simulate long duration loading events is to use a multibody dynamics (MBD) simulation. The Siemens Simcenter Motion environment is used which can incorporate rigid motion bodies to understand general loading dynamics, or incorporate flexible motion for bodies where internal stresses or displacements are of importance, for instance blade motion and deformation. The flexible dynamics are modeled using a modal space representation of the component.

4.6.1. Model summary

The finite element model was separated into three distinct components, as done previously. The first body is the rotor, consisting of the blades, struts, tower, and added non-structural masses representing the connection components. The second is the turbine base, made up from the steel beam support structure and holding the main bearing housing and drive-line. The third component is the blue mounting platform. Each motion body is shown with a label in figure 4.22.

Each body is connected together with a series of joints. The rotor is connected to the base at the location of the top and bottom rotor bearings, the top bearing consisting of a fixed joint in the x and y directions, while allowing all other DOF’s to remain free. The bottom of the bearing is defined as a revolute joint and is used to control the rotational speed of the turbine. For the case where the forces in x and y directions are shown at the bearings, these two loads are summed. This only comes into play when the rotor is considered flexible, as the rigid body would only result in a loading at the revolute joint. The base is then rigidly connected to the platform at the nearest element node in all six DOFs. As the real turbine is rigidly clamped using machining clamps, at each leg this is considered a viable assumption. The blue platform is then connected to the ground with the same springs as described in the previous section. It is also possible to fix the platform to the ground in a rigid condition as a control study when required.

The included modes for each flexible body determine the available combinations which can be processed in the response. Therefore it is important to include as many modes as necessary to properly capture the dynamics, however every included mode increases the computational time, so there is a tradeoff. It is deemed important to include the major flexible modes of the platform, which includes the first 2 bending and torsion modes, whereas many modes involve only the platform skirt vibrating, which will not have a large effect on the turbine dynamics, so they are deactivated in the solution. The first 25 flexible modes of the base structure were included, as well as the first 30 rotor modes.

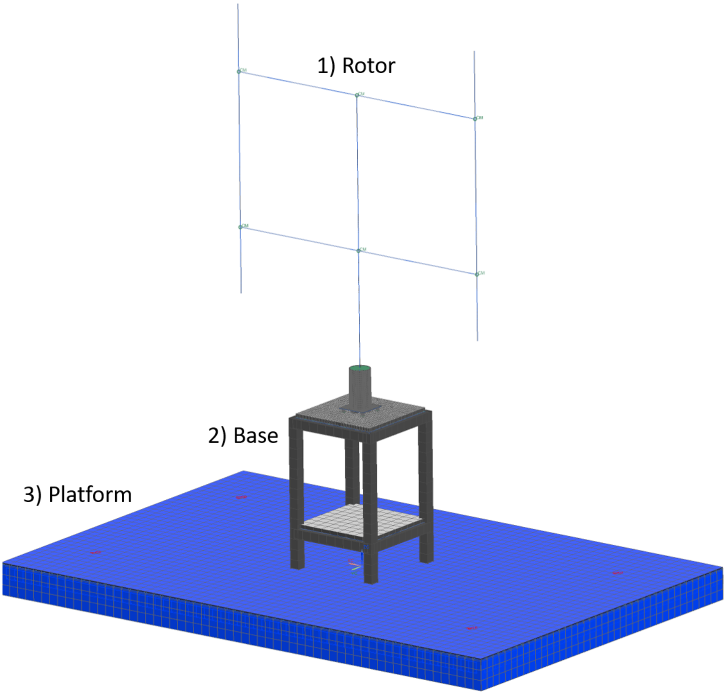

Figure 4.22: Flexible PitchVAWT model with motion bodies identified. 1) Main rotor, 2) Base structure, 3) Grounding platform

4.6.2. Applied Loading

As a test case for the MBD simulation, a speed ramp up to 400 rev min^{-1} and a dwell at an operating speed of 205 rev min^{-1}, both with a simulated aerodynamic load are performed. The normal and tangential loading is first calculated with the Actuator Cylinder model introduced in section 3.3 for a tip speed ratio of 4. Using the local flow velocity and the normal and tangential coefficients from the AC model, the 2 dimensional load for each azimuthal position is calculated. The load is then multiplied by the height of the blades, giving the expected full 3D load over the rotation. The nromal and tangential load over a rotation is shown in figure 4.23. During this step, the turbine is considered rigid, so there are no relative blade velocities introduced in the calculation. This is considered a fair assumption given how stiff the turbine rotor is, however, this may not be true in large deformable VAWTs. A simulation is then programmed in python to simulate the rotation of the turbine through a predefined rotational speed ramp. The speed ramp for the dwell at 205 rev min^{-1} is shown in figure 4.24. A time delay is added to the rpm ramp to allow the flexible bodies to come to a rest after an initial transient period of about 3 s when the simulations initial conditions, such as gravity, are implemented. The azimuth position of each blade is then calculated for every time step, and the appropriate loads are applied to the blades. A representative loading curve over time for each blade is shown in figure 4.25. Vector loads are applied on the appropriate blade in the corresponding normal and tangential directions within the MBD model in Simcenter Motion. The time step for each simulation is 0.001 s.

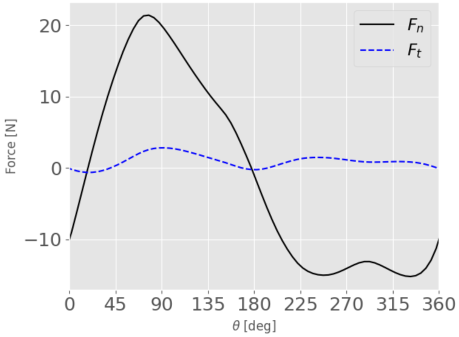

Figure 4.23: Normal and tangential loading versus azimuth position from Actuator Cylinder Model

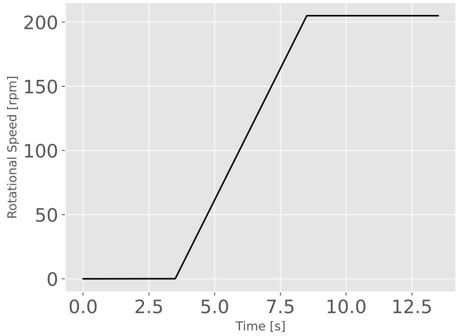

Figure 4.24: Rotational speed ramp to an operational rpm of 205

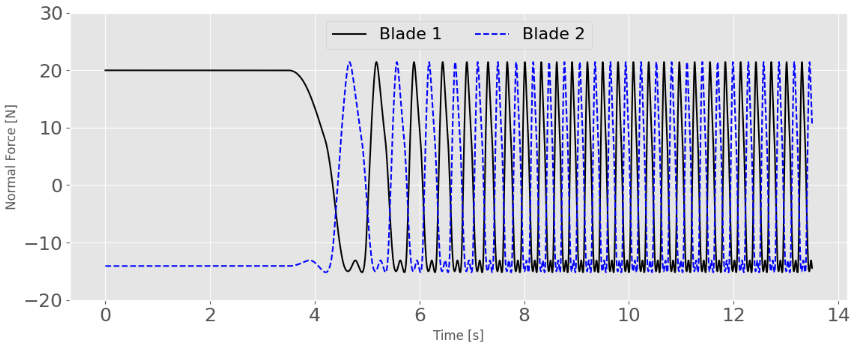

Figure 4.25: Applied normal loading for each blade over time.

4.6.3. Transient response at TSR 4

The transient response of the turbine while rotating at 205 rev min^{-1}, corresponding to a tip speed ratio of 4, was calculated with both flexible and rigid bodies in order to explore the effects of the flexible body response on the loads experienced by the turbine. The total loads measured at the bearing locations over one second of operation are shown in figure 4.26. The solid black line shows the load for the full flexible body, where the blue dashed curve shows the expected load with all rigid bodies. The first check is to make sure that the loads are applied correctly to the model. The x direction thrust force oscillates around a mean which is offset from zero pushing back against the wind, while the thrust perpendicular to the wind direction, y, oscillates around zero as expected. The torque also oscillates with the 2P response frequency and has a sign which is consistent with needing to resist the rotor from accelerating. These all give the correct feedback to say that the normal and tangential rotor loads are applied properly to the model.

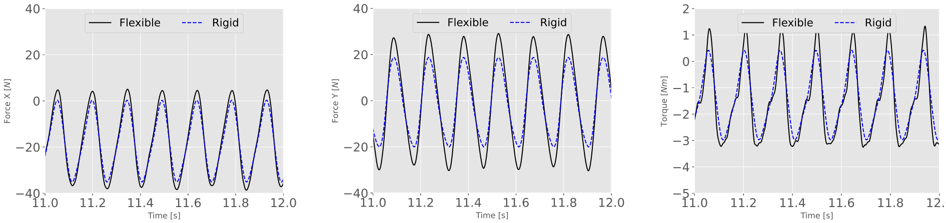

(a) F_x (b) F_y (c) Torque

Figure 4.26: Response forces for 1 s at the main bearing for $\lambda = 4$ at a speed of 205 rev min^{-1}, comparison between rigid model and flexible motion model shows increased loading due to inertial response.

As shown in the comparison of the loading between the solutions, the inertial dynamics of the flexible bodies, particularly the spring support system for the platform have a large impact on the experienced loads of the rotor base. The amplitude of each loading in the x and y directions is shown in table 4.11 along with the % difference from the rigid body to the flexible solution. This shows that for the Pitch-VAWT, the experienced loads of the turbine at the base are over 50 % greater in the y-direction due to the side-side motion of the platform suspended on the springs and the inertial loading of the turbine in response. This is an important take-away which is vital in the design of platform systems, to make sure that the natural frequencies of oscillation of the platform structures don't interact unfavorably with the rotor dynamics and to ensure that the platform stiffnesses are properly taken into consideration in the design.

Load	**Rigid [N]**	**Flexible [N]**	% **difference**
F_x	35	45	28.6 %
F_y	39	59	51.3 %

Table 4.11: Comparison of load oscillation amplitude for rigid and flexible bodies at the bearing mount location

Gravity is also included in the simulation, and has the largest effect on the rotor deformation. The least stiff portion of the turbine model are the struts in the vertical direction. This is shown in figure 4.27 showing the rotor deformation, scaled to 5 % of model size for effect, while rotating at the 205 rev min^{-1}. As to be expected, there is a radial displacement of less than a millimeter in the rotor plane, whereas the tips have a slightly higher displacement due to their cantilevered nature. The gravitational load is the most pronounced in deformation, however has minimal effect on overall rotor loading, as the vertical position of the blades doesn't directly effect the aerodynamics. This would however be a potential driving factor for much larger turbines as the gravitational load grows with turbine size, whereas the centrifugal loads reduce.

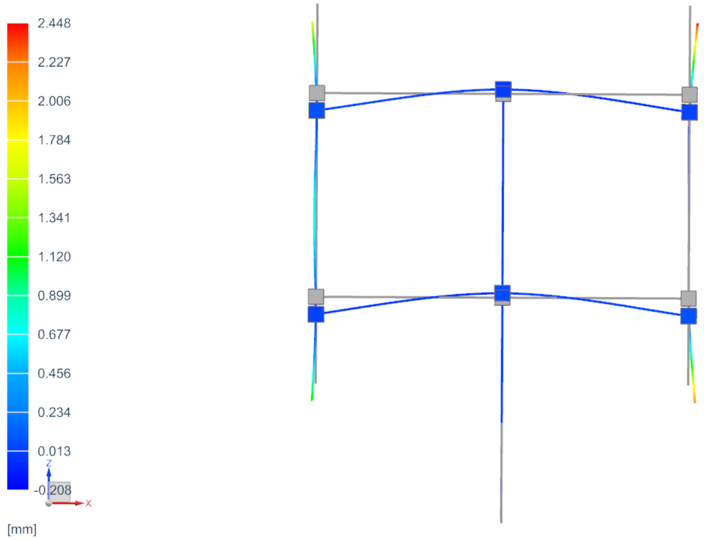

Figure 4.27: Rotor deformation including gravity and blade loading at $\lambda = 4$ scaled to 5 % of model to make shape visible, coloring shows radial deformation.

4.6.4. Transient response due to speed ramp

The transient response to the above aerodynamic loading is dependent upon the excitation frequency of the loading, thereby the turbine rpm. In order to showcase this, a linear speed ramp up to 400 rev min^{-1} is simulated with the MBD model. After the settling time for the initial transients due to gravity, the duration of the ramp is 10 s. The time step was kept at 0.001 s. The bearing loads in x and y direction are given in figure 4.28. The loads are graphed versus the rotational speed so the dependence on rotor speed can be easily observed. There is a large transient due to the startup of the speed ramp, which requires a relatively large torque to be applied to the rotor, visible until approximately 100 rev min^{-1}. However, the response then begins to follow what is expected from the applied aero-loading.

As the rotational speed nears the first major 2P crossing at 160 rev min^{-1}, with respect to the Campbell diagram in figure 4.21, the side-side motion of the platform begins to be excited, showing an increasing load amplitude in the y direction, which begins to die off by 200 rev min^{-1}. Beginning about 250 rev min^{-1} the turbine begins operating in resonance in both the x and y directions. This corresponds to the 2P crossing of the tower backward whirling mode. In order to verify this assumption, the modal displacement participation factor for the tower bending free-free mode is given in figure 4.29. Showing the resonance of this mode at the appropriate rotational speed. The full finite-element-model solution of the tower backward whirling

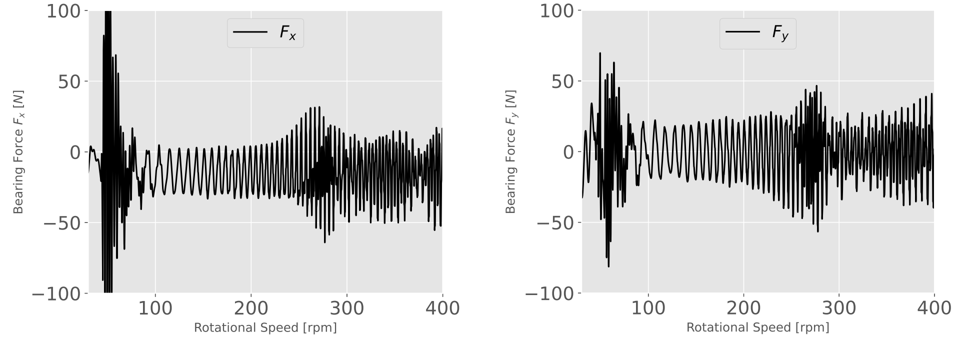

(a) F_x (b) F_y

Figure 4.28: Bearing loading in X and Y direction as rotational speed increases with consistently applied aerodynamic loading during a linear speed ramp to 400 $\mathrm{rev\,min^{-1}}$

mode is given in figure 4.30. This mode shape was computed at 200 $\mathrm{rev\,min^{-1}}$, so the frequency is a bit higher than expected at the actual operating frequency, however the mode shape will remain consistent.

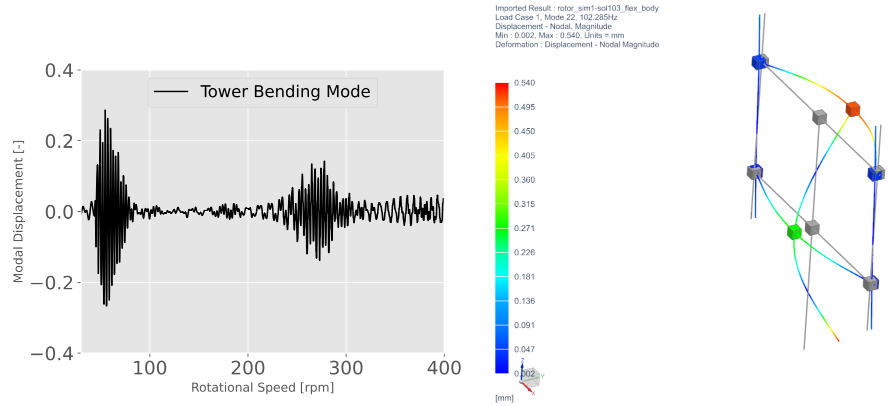

(a) Modal displacement of tower bending mode. (b) Free-free mode shape of excited mode

Figure 4.29: Mode excitation during whirling event.

As the ramp continues through the whirling mode, the resonance abates, however other modes begin to be excited. For example, the fore-aft platform mode begins to be excited by the 2P frequency, as the 1P crosses the rocking mode about the y-axis of the platform leading to a complex dynamic scenario with much higher loads than the simple rigid body aerodynamics.

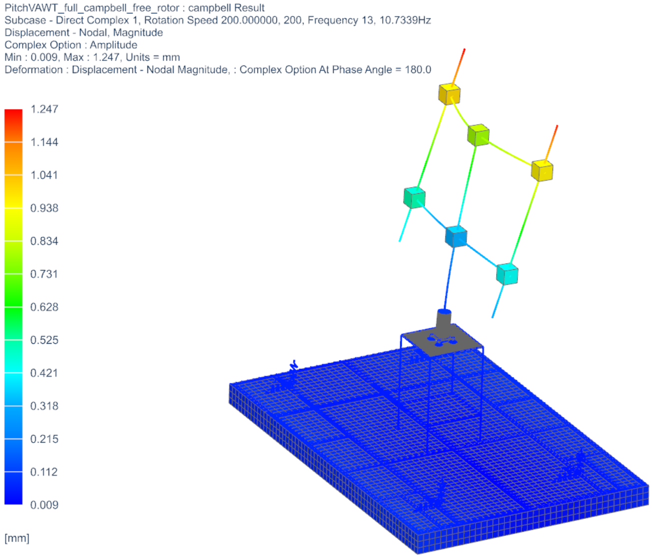

Figure 4.30: Tower backward whirling mode calculated at a rotor speed of 200 rev min^{-1} at a frequency of 10.7 Hz.

4.7. Summary

In conclusion, a set of characterization tests were performed on the PitchVAWT turbine and components. These data were used to update finite element models of the turbine at multiple levels of fidelity. Results of the individual component tests were as to be expected from initial finite element modeling. The specific cross sectional areas and material quantities required only slight adjustments from the expected values in the as-built condition. However, in the full system configuration the dynamics of the platform structure play a significant role in the turbine response at specific frequencies of interest. Therefore the model has been updated to reflect these results and the platform dynamics are considered in the turbine response. Several insights were gained into the structural behavior of the system including the large effects of the flexible platform structure on the mode shapes and frequencies of the overall turbine. The updated finite element and multibody dynamics models are able to properly capture all dynamics of interest and will be used to predict turbine response due to dynamic pitching and base excitation during operational measurements in the Open Jet Facility.

Bottom Line:

- In this chapter a detailed finite element model of the PitchVAWT turbine was presented.
- An experimental modal analysis and material characterization of each major sub-component in the turbine was conducted and used to update the model of each component independently.
- A full experimental modal analysis was performed on the installed turbine, and used to update the mounting stiffness and boundary conditions for the mating of each component into a full system calibrated finite element model.
- This finite element model was then used to generate a linearized modal based Multi-body dynamics model within the Siemens Sim-Center software.
- Coupling this multi-body dynamics model to the aerodynamic output from external models presented in chapter 3 allows the prediction of time-domain response of loading and dynamics on the PitchVAWT Turbine.
- Platform stiffness has a large influence in the dynamic excitation of the turbine, altering the Campbell diagram, and therefore the reaction loads experienced by the turbine, including areas of resonance.
- Whirling mode dynamics are consistently of concern within the operating range for the 2-bladed H-VAWT analysed in this thesis.
- Inclusion of flexibility in the multi-body dynamics model greatly increase reaction loads due to response of inertial structural motion.

IV

Experimental Demonstration of VAWT Loading

5

Estimation of Blade Loading of VAWT with Fixed Pitch Offsets from Particle Image Velocimetry

This chapter presents the flow fields and aerodynamic loading of the PitchVAWT turbine with active variable pitch for load control. Particle Image Velocimetry is used to capture flow fields at six azimuthal positions of the blades during operation, three upwind and three downwind. Flow phenomena such as dynamic stall and tower shadow are captured in the flow fields. The phase-averaged velocity fields and their time and spatial derivatives are used to calculate the normal and tangential loading at each position for each pitching configuration using the Noca formulation of the flux equations. The results show the effect of load shifting from the upwind to downwind region of the actuator using pitch and the effects of dynamic stall on the blades. The results also provide an unique database for model validation.

Parts of this chapter have been published in ”Estimation of blade loads for a vertical axis wind turbine from particle image velocimetry”[80]

5.1. Introduction

The blades of a Vertical Axis Wind Turbine undergo a variety of complex aerodynamic loading fluctuations throughout each rotation. Large angle of attack swings, unsteady flow, dynamic stall, blade vortex interaction and tower shadow to name a few known examples. This leads to many inherent difficulties for designers to properly characterize the loads and performance of these turbines, especially in understanding fatigue over the lifetime of an asset. In order to provide better insight into these phenomena, a set of flow field measurements through Particle Image Velocimetry were conducted using the PitchVAWT active pitch turbine. This chapter presents these flow fields as well as a technique for estimating the aerodynamic forces acting on the VAWT blade mid-span section for several upwind and downwind azimuthal positions.

There is a lack of high quality experimental data for both flow fields and loading phenomena in operation of VAWTs which can be used for calibration and validation of computational models. A set of studies was performed by Ferreira[11], which presented an array of simulations and Particle Image Velocimetry measurements which focused on the near wake of the turbine, but also characterized dynamic stall and blade loading with studies using the velocity data captured through both CFD and PIV. Castelein et al. studied VAWT loading in dynamic stall using a similar PIV technique along with calculation of loads using the Noca flux method[81,82]. Greenblatt et.al[83] looked into dynamic stall specifically with a goal to control the stall behaviour with the use of plasma actuators. Other works have focused on the behavior of small VAWTs specifically while looking into the differing stall behavior at multiple tip speed ratios[84]. A detailed study was also performed on the wake of a fixed pitch VAWT in operation by Tescione[12], which provides insight into the wake behavior of the VAWT, but doesn't look into the blade level loading phenomena. There were other works using PIV for loads measurement as well including for horizontal axis wind turbines in uniform and yawed flow by del Campo[85,86]. These previous works show that collection of this type of data is indeed possible in a dedicated setting and can prove useful for characterizing complex flow.

This work looks to add to the available datasets further by providing a set of data with multiple pitch configurations for the same operating turbine, with a rotor solidity matching larger scale turbine designs[8] conducted in the same tunnel allowing for the study of several phenomena with a consistent data set.

5.2. Methods

5.2.1. Definition of Coordinate System

For reference the coordinate system is given in figure 5.1. The turbine is mounted in the wind tunnel such that the incoming flow consistently comes from the 90° azimuth position, with the x-direction following the direction of the wind. The turbine rotates counter-clockwise as viewed from the top, and the y-direction is defined using the right-hand rule.

The blade pitch, β, sign convention is given in figure 5.2. The path of the airfoil is shown with a dashed line. Positive turbine pitch is defined as pitching the leading edge towards the center of rotation, which corresponds to an increase in angle of attack for each azimuth position. Negative blade pitch therefore corresponds to a more negative α, decreasing upwind and increasing in the downwind portion of the rotor sweep.

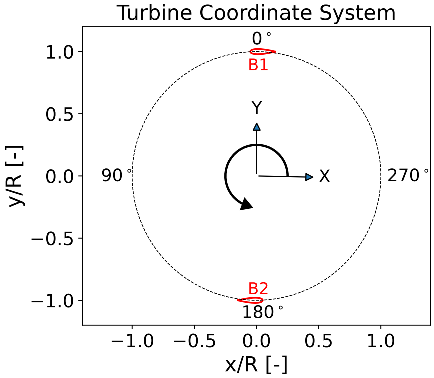

Figure 5.1: Turbine coordinate system, wind from 90°

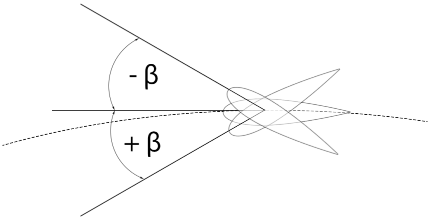

Figure 5.2: Blade pitch convention

5.2.2. Description of Test Campaign

Testing of the turbine was conducted in the open jet facility at TU Delft, referred to as OJF. A large blue lifting base is available in the tunnel for mounting test hardware. The turbine is mounted to this platform and placed to align in the center of the jet, with the center of the turbine 2 m from the outlet face. A view of the turbine installed in the facility along with the PIV system is given in figure 5.3.

The wind speed was held to $4\,\mathrm{m\,s^{-1}}$ using the wind tunnel control system, and the turbine rotational speed was controlled via a DC motor controller to be 208 rev/min, for a constant tip speed ratio of 4. Images were taken using two planar PIV fields overlapping around the airfoil in order to capture a complete velocity field surrounding the blades at each position. A 5 V TTL trigger pulse is output by the turbine each rotation at $\theta = 0$. Using this signal, and the measured rotational speed, a phase locked delay can be calculated. This delay is added to the triggering mechanism in order to capture the data with blade 1 at the correct azimuth position. In order to prevent the effect of laser shadow blocking half of the field of view, two lasers were used to light the area and are synchronized by splitting the TTL trigger pulse. The images are taken at the mid-plane of the rotor in order to minimize any three-dimensional effects by the blade tip vortices or the struts. The cameras are mounted to a computer controlled traverse system which allows the measurement field of view, FOV, to be properly aligned to capture a series of positions in the x-y plane. The traverse system monitors the general positioning of the local measurement FOV in the global coordinate system. Any small deviations which can be accumulated due to runout of the traverse system or any other unaccounted for motion are corrected for by aligning the expected airfoil position

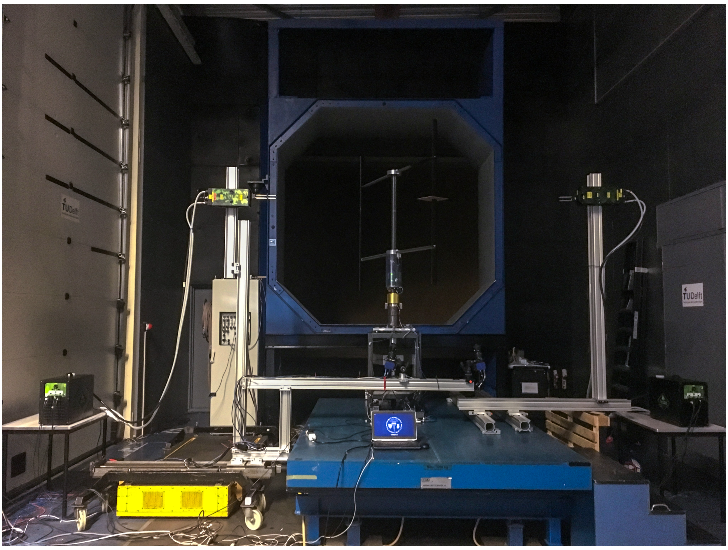

Figure 5.3: PitchVAWT mounted in the Open Jet Facility with opposing synchronized PIV lasers, cameras, and traversing system.

in the global coordinate frame with the measured trailing edge of the airfoil during operation.

The cameras used are LAVision 16 Mpix cameras with 60 mm Nikon Micro-Nikkor lenses using a 2x multiplier zoom lens, giving an overall focal length of 120 mm and an F-Stop of 5.6. Two Evergreen dual pulse PIV lasers were used with the Δt offset between each laser pulse as 0.2 s. A set of 75 images were taken by each camera at each measurement position. A mask is applied to each image to minimize effects of laser reflection on the blade surface as well areas of the blade which obstruct the view of the flow. The raw images are then filtered to remove background noise and enhance the particles. Vectors are calculated using sequential PIV within LAVision's Davis software. An average and standard deviation of each measurement field is calculated for each position. The calculated fields are then filtered to remove any excessive standard deviation in the measurement vector, usually due to insufficient particles or excessive background noise.

Six azimuths are measured in this experiment, three upwind, and three downwind. All data presented here is in the global reference frame. For each local station around the azimuth, three sets of images are taken. A nominal θ position and two neighboring points with an offset of about $\pm\Delta\theta = 5°$. As the camera system is triggered by a time-delay, any minor deviations in the rotational speed or triggering delays causes a slight deviation in actual angle of measurement. This is accounted for by fitting the transformed raw images with a representation of the airfoil overlaid numerically. The measured azimuth position is then used as the reference location. This is necessary for the calculation of the aerodynamic load as discussed in section 5.2.3. Data is collected in three fixed-pitch configurations for the turbine, 0°, 5°, and −5°. The azimuth positions of each local measurement is given table 5.1.

Table 5.1: Azimuth of the blade for each case. The cases are labelled by an approximate azimuth. Nine azimuth positions are acquired for each case, three for each of the three pitch angle cases. The results use the case label and the pitch angle to identify the case and sub-case.

Case Label	**Aft [°]**	**Mid [°]**	**Fore [°]**
$\beta = -5°$			
$\theta = 60°$	55	61.5	64.5
$\theta = 90°$	85	90	95
$\theta = 120°$	122	124.5	128.5
$\theta = 240°$	239.5	243.5	248.5
$\theta = 270°$	269.8	274	278
$\theta = 300°$	293.4	299.5	301.7
$\beta = 0°$			
$\theta = 60°$	55	60	65
$\theta = 90°$	85	91	95
$\theta = 120°$	122	125	129
$\theta = 240°$	239.5	243.5	248.5
$\theta = 270°$	270	274	278
$\theta = 300°$	294.5	299	303
$\beta = +5°$			
$\theta = 60°$	56.5	61	64.5
$\theta = 90°$	86	91	95.5
$\theta = 120°$	122.1	124.6	128.6
$\theta = 240°$	239.5	243.5	248.5
$\theta = 270°$	269.5	274.5	278
$\theta = 300°$	295	299.5	303.5

The velocity fields are measured at the mid-plane of the rotor disk in order to minimize any three-dimensional effects of the flow. Figure 5.4 shows a model of the rotor with velocity fields measured for cases $\theta = 90°$ and $\theta = 270°$.

5.2.3. Estimation of Loading with Noca Method

The experimental velocity fields are used to calculate the blade normal and tangential loading for each measurement position. This is done in order to gain an understanding of the complex loading on the blades in these notoriously difficult to predict flow regimes. The loads are calculated using the flux formulation described by Noca.[87,88] Originally derived from the conservation of momentum, the method allows for the calculation of body forces in the flow using only the velocity fields and their derivatives. Ferreira used this technique with simulated PIV data[89] discussing the accuracy of the method along with routine issues that are encountered when performing the measurements in the wind tunnel, such as overlapping flow fields from multiple cameras. It was also implemented by Castelein[81] on a VAWT for the study of loading in dynamic stall, and by Del Campo et.al while studying loading on a HAWT.[85,86] This section discusses the implementation of the flux equation, and the corrections made for the acceleration of the airfoil body due to rotation. A quick study is shown documenting the sensitivity of the load calculation to the selection of

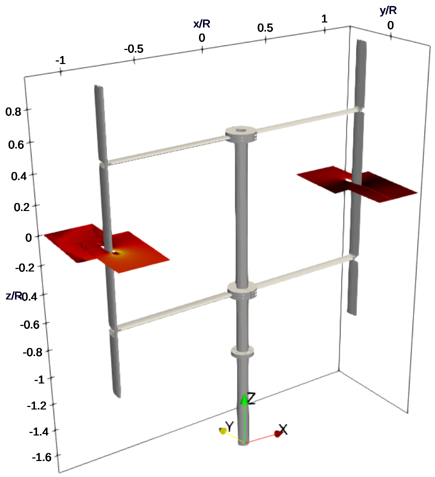

Figure 5.4: PitchVAWT turbine showing the measurement planes at locations $\theta = 90$ and $\theta = 270$.

the control surface boundary, including when it doesn't encompass the airfoil, and the specifics of the velocity, acceleration, and vorticity fields used for a calculation for the normal and tangential loading is given for the $\theta = 120°$ azimuthal position.

Noca proposed the following formulation for the fluid dynamic force per density F/ρ acting on the body using a flux equation formulation given in equation 5.1, with the goal of analysing time dependent loads on bodies using only the velocity fields and their derivatives:

$$\frac{F}{\rho} = \oint_{S(t)} \hat{n} \cdot \gamma_{flux}\, dS - \oint_{S_{b(t)}} \hat{n} \cdot [(u - u_S)u]\ dS - \frac{d}{dt} \oint_{S_{b(t)}} \hat{n} \cdot (ux)\, dS \tag{5.1}$$

where T is the viscous stress tensor

$$T = \mu(\nabla u + \nabla u^T) \tag{5.2}$$

and with γ_{flux}:

$$\begin{aligned} \gamma_{flux} =& \frac{1}{2}u^2 I - uu - \frac{1}{N-1}u(x \cdot \Omega) + \frac{1}{N-1}\Omega(x \cdot u) \\ & - \frac{1}{N-1}\left[\left(x \cdot \frac{\delta u}{\delta t}\right)I - x\frac{\delta u}{\delta t} + (N-1)\frac{\delta u}{\delta t}x\right] \\ & + \frac{1}{N-1}[x \cdot (\nabla \cdot T)I - x(\nabla \cdot T)] + T \end{aligned} \tag{5.3}$$

As the data from the PIV measurements has been taken using phase locked averaging, the equations have been transformed to use changes in azimuthal position to calculate the time dependent forces. The phase averaged flux equation given in equation 5.4 consists of three major terms. The first is the flux over the boundary surface surrounding the airfoil, this is the major target of the analysis. The next two are corrections for the inner boundary of the control volume surface. The second term has to do with flow through the boundary surface of the airfoil, as the airfoil is a solid body, this force goes to zero. The third term is due to the change of the internal boundary surface over time mainly due to the rotation of the airfoil through the control volume.

$$\begin{aligned}\frac{\langle F\rangle}{\rho} &= \left\langle \oint_{S(t)} \hat{n}\cdot\gamma_{flux}\,dS \right\rangle_{\theta_1} - \\ &\left\langle \oint_{S_{b(t)}} \hat{n}\cdot[(u-u_S)u]\,dS + \frac{d}{dt}\oint_{S_{b(t)}} \hat{n}\cdot(ux)\,dS \right\rangle_{\theta_1}\end{aligned} \tag{5.4}$$

The phase-locked average of the flux term $\langle \gamma_{flux}\rangle_{\theta_1}$ is:

$$\begin{aligned}\left\langle \oint_S \hat{n}\cdot\gamma_{flux}\,dS\right\rangle_{\theta_1} &= \left\langle \oint_S \hat{n}\cdot\left[\frac{1}{2}u^2 I - uu - \frac{1}{N-1}u(x\cdot\Omega) + \frac{1}{N-1}\Omega(x\cdot u)\right] dS\right\rangle_{\theta_1} \\ &- \frac{1}{N-1}\left\langle \oint_S \hat{n}\cdot\left[\left(x\cdot\frac{\delta u}{\delta t}\right)I - x\frac{\delta u}{\delta t} + (N-1)\frac{\delta u}{\delta t}x\right] dS\right\rangle_{\theta_1} \\ &+ \left\langle \oint_S \hat{n}\cdot\left[\frac{1}{N-1}\left[x\cdot(\nabla\cdot T)I - x(\nabla\cdot T)\right] + T\right] dS\right\rangle_{\theta_1}\end{aligned} \tag{5.5}$$

The instantaneous time derivative of the velocity field is approximated using multiple phase-locked azimuthal positions offset by a $\Delta\theta$. This approximation is as follows.

$$\frac{\delta u}{\delta t} = \frac{\Delta u}{\Delta t} + O(\Delta t) = \frac{u_{\theta+\Delta\theta} - u_\theta}{\Delta/\omega} + O(\Delta\theta) \tag{5.6}$$

The full flow acceleration term can then be approximated by a numerical differentiation between nearby ($\Delta\theta$) azimuth positions.

$$
\begin{aligned}
&\frac{1}{N-1}\left\langle \oint_S \hat{n}\cdot\left[\left(x\cdot\frac{\delta u}{\delta t}\right)I - x\frac{\delta u}{\delta t} + (N-1)\frac{\delta u}{\delta t}x\right] dS\right\rangle_{\theta_1} \\
&\qquad = \frac{1}{N-1}\left\langle \oint_{S(t)} \hat{n}\cdot\left[\left(x\cdot\left(\frac{u_{\theta+\Delta\theta}-u_\theta}{\Delta\theta/\omega}\right)\right)I\right] + \right. \\
&\left. \hat{n}\cdot\left[-x\left(\frac{u_{\theta+\Delta\theta}-u_\theta}{\Delta\theta/\omega}\right) + (N-1)\left(\frac{u_{\theta+\Delta\theta}-u_\theta}{\Delta\theta/\omega}\right)\right] dS\right\rangle_{\theta_1} + O(\Delta\theta) \\
&= \frac{1}{N-1}\frac{1}{\Delta\theta/\omega}\left\langle \oint_{S(t)} \hat{n}\cdot\left[(x\cdot u_\theta)I - xu_\theta + (N-1)u_\theta x\right] dS\right\rangle_{\theta_1+\Delta\theta} \\
&-\frac{1}{N-1}\frac{1}{\Delta\theta/\omega}\left\langle \oint_{S(t)} \hat{n}\cdot\left[(x\cdot u_\theta)I - xu_\theta + (N-1)u_\theta x\right] dS\right\rangle_{\theta_1} + O(\Delta\theta)
\end{aligned}
\tag{5.7}
$$

During the experiments, the turbine was operated with a constant rotational speed of 21.6 rad/s. Therefore, the term associated with the acceleration of the non-porous airfoil (third term in equation 5.4 and shown explicitly in equation 5.8) remains constant throughout the rotation in the frame of the airfoil. Therefore, the calculation of this term is independent of the azimuth position of the turbine. The force is a function of rotational velocity, the airfoil geometry, and pitch. Given the NACA0021 airfoil and the constant ω of 21.6 rad/s the 2D load due to the body rotation is $F_{n_b} = 0.023$ and $F_{t_b} = 0.007$, with the load non-dimensionalized by $\frac{1}{2}\rho\lambda^2 U_\infty^2 c$. An in depth calculation of this term is given in appendix C along with all codes used.

$$
\frac{d}{dt}\oint_{S_{b(t)}} \hat{n}\cdot(ux)\, dS \tag{5.8}
$$

5.2.4. Example of Velocity Fields in Noca Calculation

As an example of the flux calculation, the azimuthal position 120° with a pitch of 0° is detailed. Each velocity field is given for $\theta = 122°$, $\theta = 125°$, $\theta = 129°$ in figure 5.5. The boundary surface, S, is shown in black for each figure. The placement of the boundary surface is based upon two criteria. The surface must be large enough to encompass the airfoil position for all three measurement locations, and there must be sufficient velocity information with accurate PIV measurement to properly calculate the terms, constricting the size of the surface. The velocities at the surfaces of $\theta = 122°$ and $\theta = 129°$, shown in figures 5.5a and 5.5c, are used to determine the flow acceleration term given in equation 5.7 by numerical differentiation over the boundary surface. The velocity, acceleration, and vorticity in term 1 of equation 5.5 are given in figures 5.6, 5.7, and 5.8, in nondimensional form, respectively. The terms are plotted against the distance around the boundary surface nondimensionalized by the chord length. The sharp peaks in each figure located at approximately $Sc^{-1} = 2$ correspond to the wake of the airfoil crossing the boundary ellipse. In the first term of equation 5.5, the vorticity is multiplied by a positional vector of the integration over the boundary. In order to minimize the error associated with this moment of vorticity, the x positional vector is set to the location on the surface with the maximum vorticity. After subtracting out the body forces discussed in equation 5.8, the load vector is calculated.

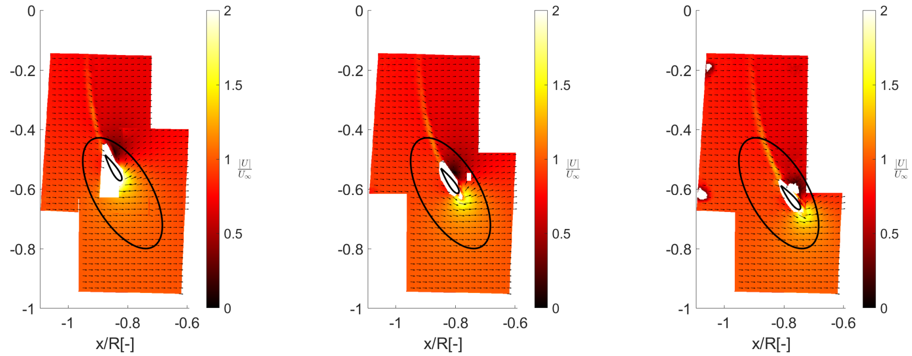

(a) θ = 122°   (b) θ = 125°   (c) θ = 129°

Figure 5.5: Velocity magnitude of each measurement section, the boundary surface shown as the blue oval envelopes each azimuthal position.

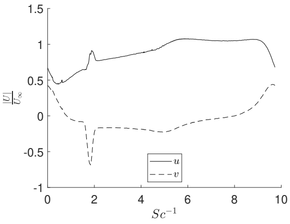

Figure 5.6: Velocity vs distance over boundary surface.

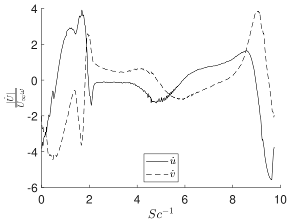

Figure 5.7: Acceleration vs distance over boundary surface.

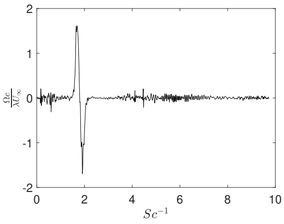

Figure 5.8: Vorticity vs distance over boundary surface.

5.2.5. Sensitivity of Flux Term to Boundary Surface

As a verification for the flux calculations detailed above, the same calculations are conducted over a variety of surfaces for the same airfoil position. One boundary surface of measured data that does not overlap the airfoil body and a series of independent surfaces which do encompass the body. The boundary surface without the body is given in figure 5.9. The calculated normal and tangential force are both near0 which is to be expected. The series of other surfaces is shown in figure 5.10. The normal and tangential load was calculated for each surface. The goal is to understand the variability of calculated load based upon the boundary surface choice. The calculated loads are given in table 5.2. The mean and standard deviation of the measurements is also given. For the normal load, the standard deviation is 1.6 % of the mean load, where as the tangential load is more sensitive, with a standard deviation of 16.67 % of the mean load. The error likely stems from difficulty in measuring the exact momentum deficit and vorticity within the thin wake of the airfoil due to averaging over many rotations with slight phase offsets in the PIV measurements. This also explains the larger error for the tangential loading, as the loading in this direction is highly dependent upon the characterization of the wake.

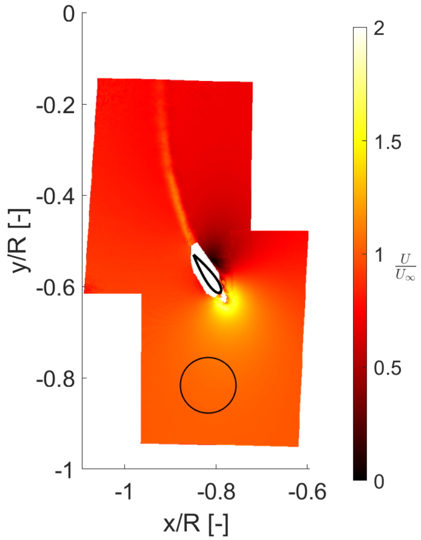

Figure 5.9: Velocity magnitude at $\theta = 125°$ with a test boundary surface not encompassing the airfoil. $F_n = 1.8 \times 10^{-3}$, $F_t = 3.48 \times 10^{-4}$.

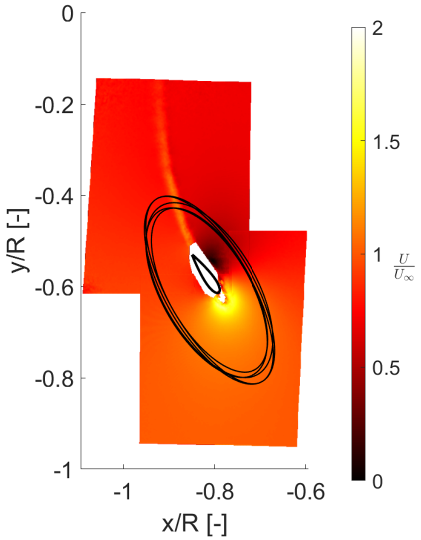

Figure 5.10: Various surface boundaries encompassing the airfoil positions. Results given in table 5.2.

Table 5.2: Sensitivity to flux surface nondimensionalized by $1/2\rho\lambda^2 U_\infty^2 c$

Surface	$F_{n_{flux}}$ **[-]**	$F_{t_{flux}}$ **[-]**
0	1.8×10^{-3}	3.48×10^{-4}
1	0.791	0.135
2	0.801	0.095
3	0.783	0.128
4	0.766	0.130
5	0.774	0.154
mean	0.783	0.128
σ	0.014	0.021

5.3. Results and Discussion

5.3.1. PIV Velocity Profiles

In this section, flow fields are displayed for each of the measurement stations with fixed pitch configurations of, $\beta = 0$, $\beta = 5$, $\beta = -5$. The flow fields are presented in two sections. First, composite images showing the velocity magnitude and vorticity are given for each pitch condition at each measurement location on the rotor. Second, a closer view of the velocity magnitude and each component will be given for a subset of rotational positions.

Zero Pitch

The velocity fields at each azimuthal position for the zero pitch configuration are given in figure 5.11. The airfoils are also plotted for reference at each position. The wind comes from the 90° position, or the left of the image, and flows in the direction of the arrow. There are several things to note in these velocity fields, starting with the overall effect of the turbine thrust slowing the flow in the downwind half of the turbine. When the blade is at a position of 270°, the effect of tower shadow is evident. On the airfoil scale, as is expected, the wake of the blade pass is evident in each of the measurement positions, as is the flow acceleration over the airfoil surface. The wake is most easily seen while looking at the vorticity of each measurement given in figure 5.12. As can be verified, in the velocity fields as well, there may be some small laminar flow separation due to the low Reynolds number effects, but there is no clear deep stall present in this operational configuration.

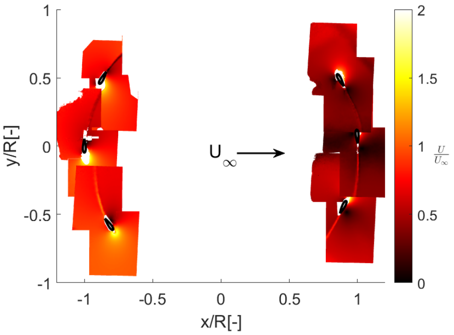

Figure 5.11: Velocity magnitude, $\lambda = 4$, $\beta = 0$.

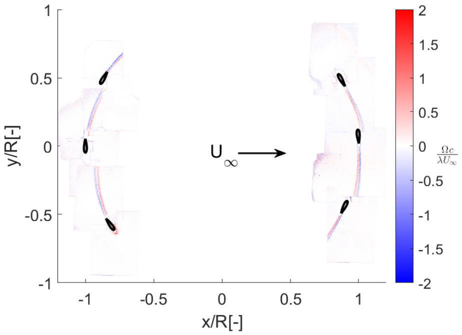

Figure 5.12: Vorticity, $\lambda = 4$, $\beta = 0$.

Five Pitch

The pitch of the turbine was then commanded to 5°, toe-in, on each blade and the PIV data was collected once again. The effect of pitching the blades in this manner causes a positive angle of attack shift which while neglecting airfoil viscous effects, means a shifting of the load from the downwind to the upwind half of the rotor sweep. However, due to the airfoil stalling, a case of dynamic stall is captured. Figures 5.13 and 5.14 show the velocity and vorticity of the measurement views.

Starting at the 60° position, there is a much greater flow acceleration over the airfoil as compared to the 0° pitch case, as the blade progresses to the 90° position the flow begins to separate, and by the 120° position a large bubble has been shed into the wake of the blade. The overall velocities on the downwind half of the rotor pass are greater in the 5° pitch case than was exhibited in the 0° case. This is likely due to stall on the upwind pass leading to less induction than in the 0° case, decreasing energy extraction from the blade and leading to a higher wind speed in the downwind half of the rotor. The vorticity in the airfoil wake at each position is also less intense due to the effective angle of attack in the downwind half being reduced.

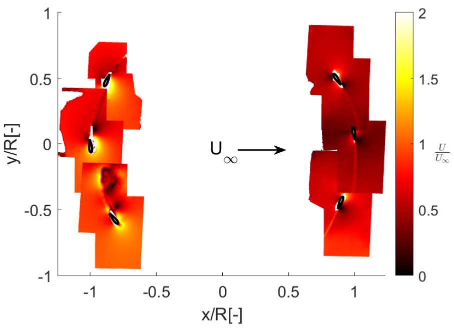

Figure 5.13: Velocity magnitude, $\lambda = 4$, $\beta = 5$.

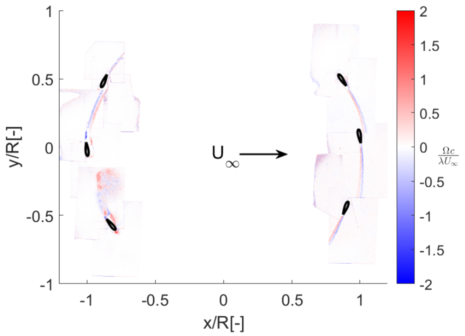

Figure 5.14: Vorticity, $\lambda = 4$, $\beta = 5$.

Minus Five Pitch

In the −5° pitch case, the loading is shifted opposite from that in the 5° case discussed in the previous section. The loading tends to shift to the downwind half of the rotor. Thereby decreasing the effective angle of attack and energy extraction in the upwind half, and increasing it in the downwind half. As can be seen in the velocity profiles in figure 5.15, the overall wind speed entering the rotor in the upwind pass is closer to that of the incoming free stream velocity, as the angle of attack in the upwind pass is much less. The flow remains attached as can be expected. However, once the airfoil reaches the 240° position, the airfoil begins to enter into a deep stall, which continues through the rest of the downwind positions. The flow then reattaches between the measured 300° section and the 60° section of the next pass. The displayed vorticity in figure 5.16 exhibits the stall in the downwind section. When determining the proper operating pitch position for the VAWT it is crucial to take into account the limits of the airfoil in both positive and negative angles of attack to minimize these dynamic stall phenomena. As the load is shifted between from upwind to downwind passes, or vice versa, multiple effects can be exacerbated. For example, the blade vortex interaction occurring in the downwind pass will depend on the strength of the shed vorticity of the upwind pass.

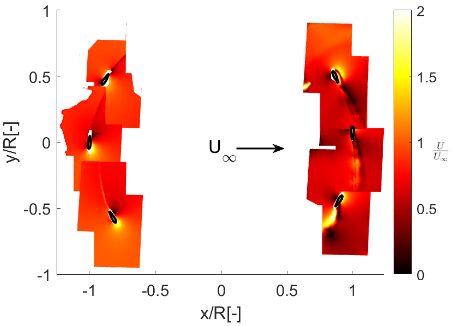

Figure 5.15: Velocity magnitude, $\lambda = 4$, $\beta = -5$.

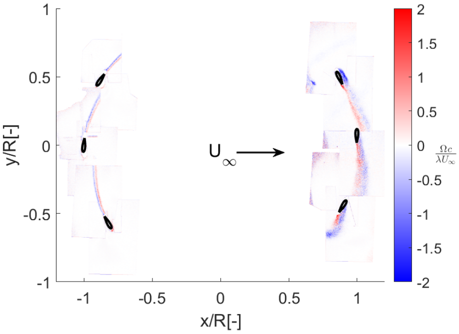

Figure 5.16: Vorticity, $\lambda = 4$, $\beta = -5$.

Direct Comparison of Pitch Value on Flow Fields

The velocity fields in figures 5.17, 5.18, and 5.19, give a direct comparison for the changes in flow over the surface depending on the pitch conditions for the 90°, 120° and 270° positions. The first row of each figure gives the overall velocity magnitude along with the overlay of the vector field, the second row provides the nondimensional velocity in the flow wise, or x-direction, and the last row shows the flow perpendicular to the oncoming wind. Each column represents a pitch configuration in order from left to right of $\beta = -5°$, $\beta = 0°$, and $\beta = 5°$. These azimuth positions were chosen in order to highlight the effect of loading in the most upwind condition, the stall that sets in at the 120° position for the 5° pitch orientation, and its effect on the behavior of the downwind pass. The less the loading on the upwind half of the rotation, for instance, the $-5°$ pitch case, the greater the flow velocity on the downwind half, increasing the relative angle of attack and exacerbating the stall, causing an overall much lower rotor thrust compared to the 0° pitching case. This is also exhibited in the dynamic stall seen in the 5° pitch case, causing a slightly higher velocity downwind at the 240° azimuth condition than is seen for the same pitch case at 300° azimuth.

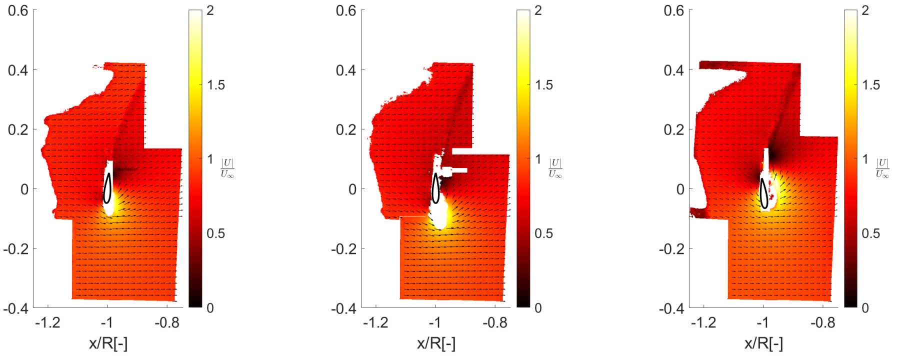

(a) $|U|$ for $\beta = -5°$, $\theta = 90°$ (b) $|U|$ for $\beta = 0°$, $\theta = 90°$ (c) $|U|$ for $\beta = 5°$, $\theta = 91°$

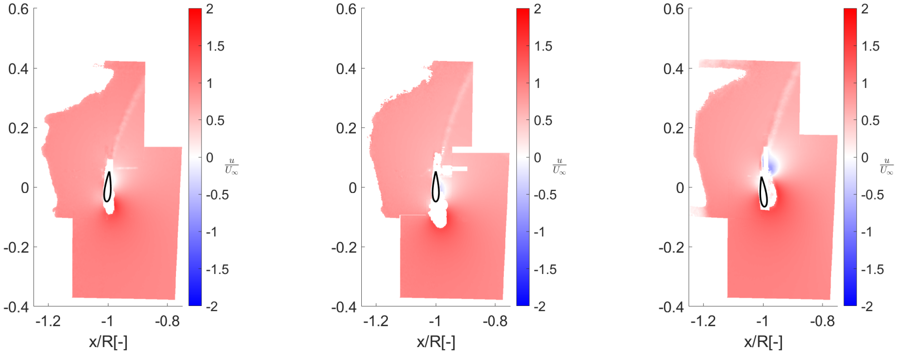

(d) U_x for $\beta = -5°$, $\theta = 90°$ (e) U_x for $\beta = 0°$, $\theta = 90°$ (f) U_x for $\beta = 5°$, $\theta = 91°$

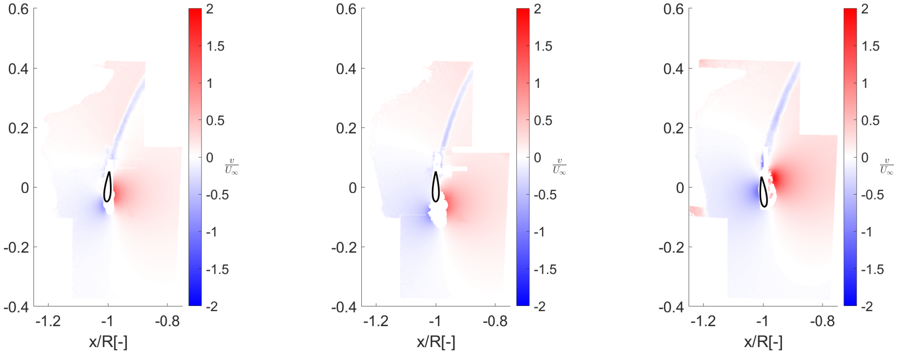

(g) U_y for $\beta = -5°$, $\theta = 90°$ (h) U_y for $\beta = 0°$, $\theta = 90°$ (i) U_y for $\beta = 5°$, $\theta = 91°$

Figure 5.17: Quiver and color plot of the velocity magnitude, velocity in x-direction and velocity in y-direction for $\theta = 90°$ position.

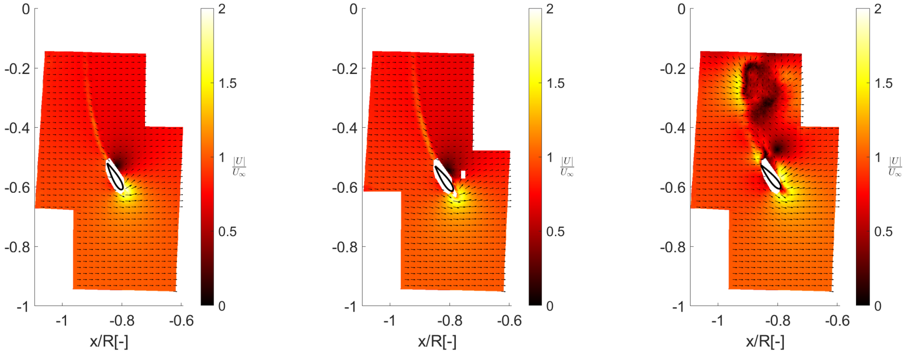

(a) $|U|$ for $\beta = -5°$, $\theta = 124.5°$ (b) $|U|$ for $\beta = 0°$, $\theta = 125°$ (c) $|U|$ for $\beta = 5°$, $\theta = 124.6°$

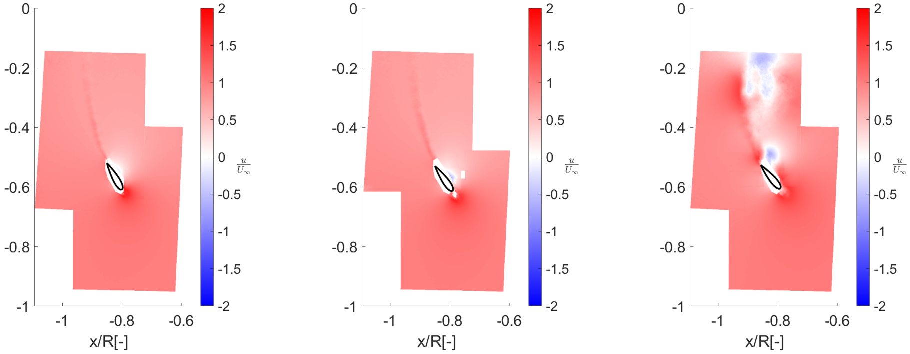

(d) U_x for $\beta = -5°$, $\theta = 124.5°$ (e) U_x for $\beta = 0°$, $\theta = 125°$ (f) U_x for $\beta = 5°$, $\theta = 124.6°$

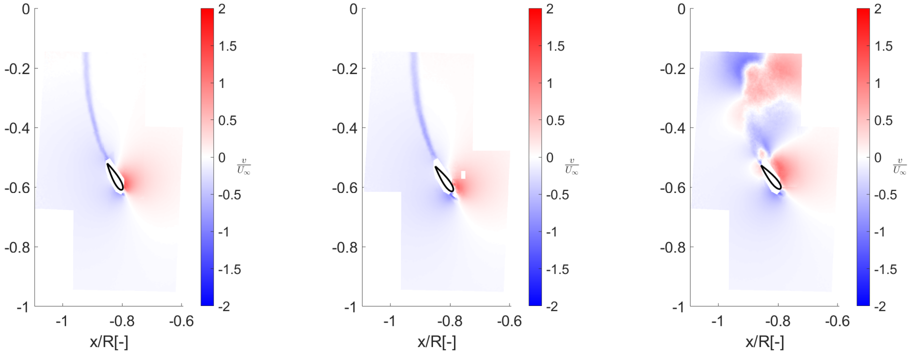

(g) U_y for $\beta = -5°$, $\theta = 124.5°$ (h) U_y for $\beta = 0°$, $\theta = 125°$ (i) U_y for $\beta = 5°$, $\theta = 124.6°$

Figure 5.18: Quiver and color plot of the velocity magnitude, velocity in x-direction and velocity in y-direction for $\theta = 120°$ position.

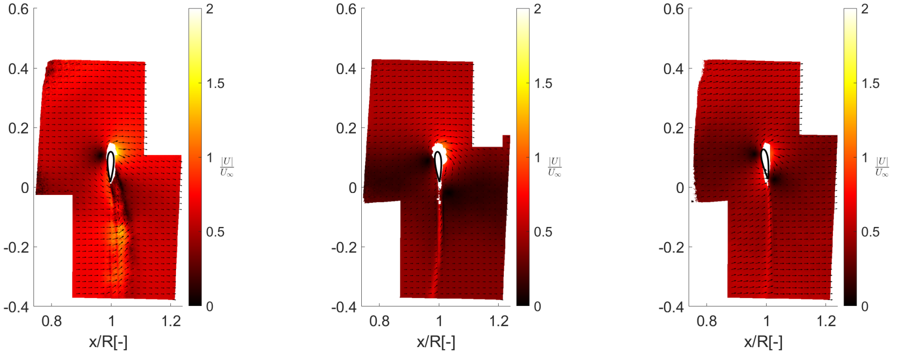

(a) $|U|$ for $\beta = -5°$, $\theta = 274°$ (b) $|U|$ for $\beta = 0°$, $\theta = 273.5°$ (c) $|U|$ for $\beta = 5°$, $\theta = 274.5°$

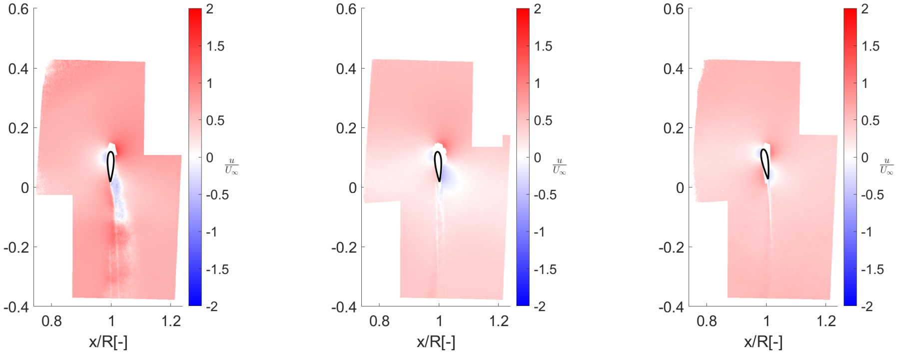

(d) U_x for $\beta = -5°$, $\theta = 274°$ (e) U_x for $\beta = 0°$, $\theta = 274°$ (f) U_x for $\beta = 5°$, $\theta = 274.5°$

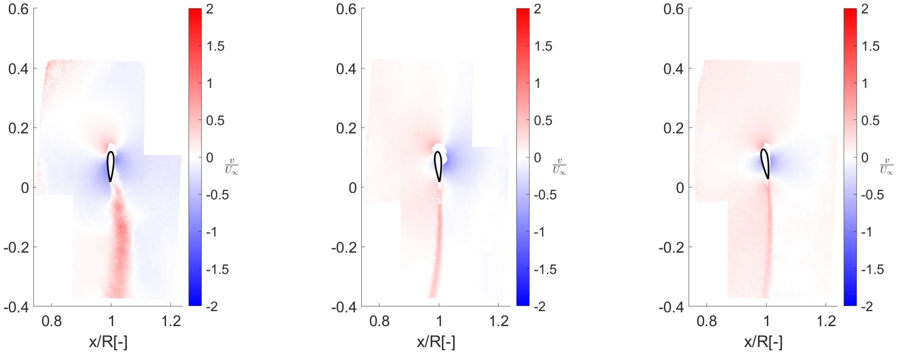

(g) U_y for $\beta = -5°$, $\theta = 274°$ (h) U_y for $\beta = 0°$, $\theta = 274°$ (i) U_y for $\beta = 5°$, $\theta = 274.5°$

Figure 5.19: Quiver and color plot of the velocity magnitude, velocity in x-direction and velocity in y-direction for $\theta = 270°$ position.

5.3.2. Load Measurements from PIV

Results for the normal and tangential loading for the six azimuthal positions and the three constant pitch orientations are given in table 5.3. These same results are then plotted versus the azimuth position. Figure 5.20 shows the normal loading, while figure 5.21 gives the tangential loads at each position. A positive normal load indicates the blade reaction forces are pushing out from the normal plane of the rotor rotation, while a negative load is the opposite. Therefore, the expected upwind load is positive while the downwind normal load is negative. For tangential forces, a positive load would work to accelerate the rotor in the direction of rotation, while a negative load would work to slow the rotor. As a continuity check, the calculations were also performed from the rotating reference frame of the airfoil. This was performed by adding the local tangential velocity of the airfoil to the velocity fields and then moving the boundary surface with the airfoil as shown in figure 5.22. The normal load calculation for each position for each reference frame is given in figure 5.23. As can be seen, the two methods match well in the calculation. Each of the terms in the flux equation discussed in equation 5.5, the inviscid loading term, the acceleration term, and the viscous term, can have a varying effect on the overall loading depending upon the relative values of the flow fields. The slight difference in the calculation depending on the reference frame highlights the shifting emphasis from the flow acceleration term in the fixed reference frame, to the inviscid loading term in the rotating reference frame.

Table 5.3: Aerodynamic loading for each pitch configuration. The 2D loads are non-dimensionalized by $\frac{1}{2}\rho\lambda^2 U_\infty^2 c$

(a) $\beta = 0$

θ[°]	F_n[-]	F_t[-]
60	1.114	0.032
90	1.194	0.195
125	0.791	0.135
243.5	-0.666	0.106
274	-0.667	0.069
299	-0.740	0.074

(b) $\beta = 5$

θ[°]	F_n[-]	F_t[-]
61	1.672	0.122
91	1.538	0.120
124.6	0.324	-0.208
243.5	-0.379	0.018
274.5	-0.071	0.027
299.5	-0.246	0.018

(c) $\beta = -5$

θ[°]	F_n[-]	F_t[-]
61.5	0.401	0.046
90	1.00	0.123
124.5	0.803	0.107
243.5	-0.358	-0.035
274	-0.256	-0.019
299.5	-0.953	0.105

Data for the $\beta = 0°$ pitch configuration indicates the performance of the turbine is as to be expected based upon the velocity profiles discussed above. The upwind pass shows a positive normal load and smaller torque at the 60° position peaking near 90° before declining again as the angle of attack lowers, the blade begins to move away from the oncoming wind and head to the downwind pass. At the 240° position, the loading has flipped to the other side of the airfoil, flipping the direction of the normal load. The overall loading is lower than the upwind pass due to the relative velocity in the back half of the rotor being lower. The rotor load is fairly consistent across the downwind pass, at least at this relatively coarse resolution, which has been seen in previous modeling studies of the VAWT.

With the blades pitched to $\beta = 5°$ the loading becomes very interesting. As expected the normal loading is much greater at the $\theta = 60°$, and $\theta = 90°$ positions

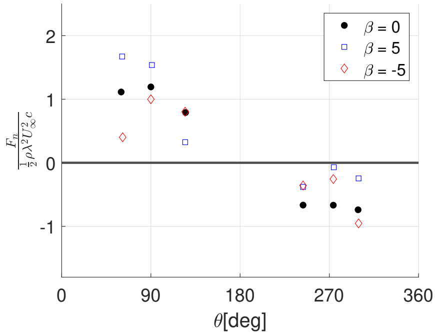

Figure 5.20: Normal load for each fixed pitch.

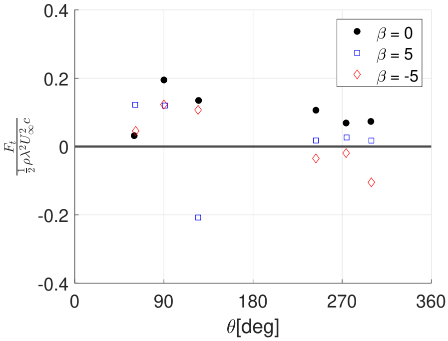

Figure 5.21: Tangential load for each fixed pitch.

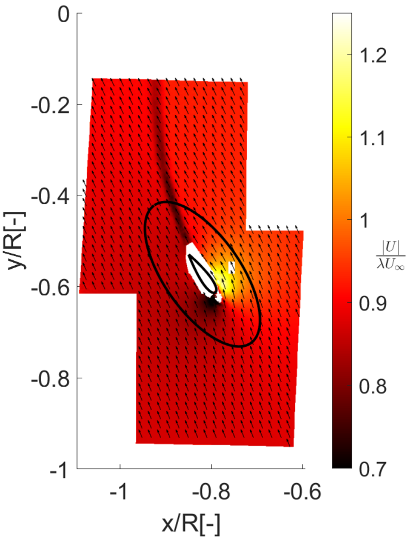

Figure 5.22: Velocity field in the airfoil reference frame at the 120° position.

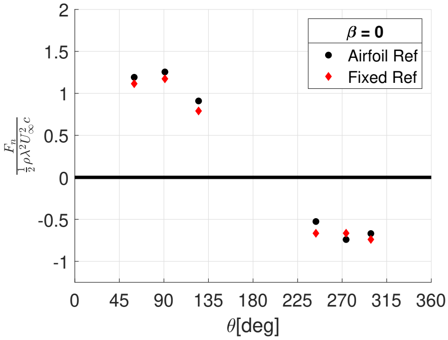

Figure 5.23: Comparison of normal load calculation in fixed and rotating reference frames.

due to the greater angle of attack, however, at 90° both the normal and tangential loads drop relative to the $\theta = 60°$ position, indicating the onset of stall behavior. By $\theta = 120°$, the airfoil has completely stalled, with the normal force dropping substantially and the tangential force dropping further from the 90° position, becoming negative. This of course follows with the massive separation event as shown in figure 5.13. On the downwind half of the rotor pass, the normal load is negative, and the tangential load goes slightly positive, however the angle of attack is decreased in magnitude from the $\beta = 0°$ case causing lower overall loading. The loading for the 240° case is relatively greater than for the other downwind locations, most likely due to the flow velocity being higher there as the airfoil was stalled directly upwind of the location.

At a pitch of $\beta = -5°$ the behavior is opposite of that experienced with the blades pitched positively. With a lower angle of attack on the upwind pass, the normal load is lower than the previous pitch scenarios. However, on the downwind pass, where the angle of attack is a greater magnitude, the blade goes into a deep stall, as shown in the loading by the lower magnitude normal load, and the negative tangential load. This is confirmed with the velocity field shown in figure 5.15. The stall cancels out what would be expected to be a greater magnitude normal load on the downwind pass for the negative pitch value. At the $\theta = 300°$ position, the flow begins to reattach, causing a spike in the normal and tangential loading.

5.4. Conclusions

Experiments were conducted on a Vertical Axis Wind Turbine in multiple pitch configurations testing the effect of shifting load between upwind and downwind passes. Particle Image Velocimetry was deployed on the rotating turbine in each pitch configuration to capture velocity fields for 18 independent measurements using 54 individual velocity fields. A phase-locked averaging interpretation of the Noca method for calculation of fluid forces on a body using velocity fields and their derivatives to successfully calculate the normal and tangential loads on the blades. These measurements were consistent in two reference frames, a fixed global frame, and a reference frame rotating with the blades. The measurements highlight the effect of dynamic stall on the loading profile of the VAWT in both the upwind and downwind sections of the rotation, depending on the pitch angle. The measurements show, prior to stall, the load is shifted upwind with increasing pitch angle as to be expected, however once the airfoil enters stall, the benefit of this increased load vanishes, resulting in loss of thrust and decreased overall torque generation. The effects of stall in the upwind section of rotation cause an increased wind velocity in the downwind section, leading to higher loading in the position directly downwind of the stall. Despite the increased velocity in the downwind section, the loss of torque is not completely made up for and the end result is a loss in overall performance. For cases of negative pitch, which shifts the load to the downwind side, the upwind pass removes little energy from the flow, leading to a higher perceived angle of attack on the downwind pass. This caused the airfoil to enter deep stall and to experience a spike of loading later in the rotation when the flow reattaches. The presented data gives insight into 2D aerodynamic loading, tower shadow, and dynamic stall behavior of the VAWT in multiple pitch configurations and can function as a benchmark to validate numerical models of the phenomena.

Bottom Line:

- Particle Image Velocimetry was deployed on the rotating PitchVAWT turbine for three pitch configurations to capture velocity fields for 18 independent measurements using 54 individual velocity fields.
- A phase-locked averaging interpretation of the Noca method for calculation of fluid forces on a body using velocity fields and their derivatives was used to successfully calculate the normal and tangential loads on the blades for six azimuthal positions.
- The PIV velocity fields show the presence of dynamic stall on both the upwind and downwind sections of the rotation.
- Blade vortex interaction and tower shadow are prevalent in all pitch configurations.
- Shifting blade pitch corresponds to shifting load between upwind and downwind locations only where dynamic stall is not present.
- Blade stall in the upwind half of the rotation results in a lower induction for the upwind half, thereby contributing to a higher velocity on the downwind half of the rotation, leading to deeper stall in that region.
- Normal and tangential loading calculated from the velocity fields demonstrates the harsh effect of dynamic stall in both the upwind and downwind rotations depending upon pitch configuration. These loads would lead to less rotor performance and potentially much higher fatigue loading cycles for the VAWT.

6

Estimation of Blade Loading of VAWT with Fixed Pitch Offsets using Strain Gages

The blade pitch of a Vertical Axis Wind Turbine can have a profound impact on the aerodynamic loading experienced by the turbine. This in turn impacts the structural loads and the performance of the machine. In order to characterize the effects of changing pitch, studies are conducted with fixed pitch offsets from a neutral pitch position in the open jet wind tunnel of TU Delft. Measurements with strain gages bonded to the turbine struts are used to estimate the normal loading of the blades. The measured behavior gives insights into the sensitivity of the turbine loading to the blade pitch angle. Aerodynamic phenomena associated with VAWTs are evident in the data including dynamic stall and blade vortex interaction. Shifting of turbine blade pitch is shown to alter the azimuthally varying normal loading, causing changes in magnitude and direction of rotor thrust. Frequency responses of the turbine and platform mounting structure are presented for rotating and fixed reference frames, respectfully. The effects of stall due to high pitch offsets is shown to excite higher per rev frequencies in both the rotor normal measurements and platform accelerations. The data sets are made available for validation of numerical models.

Parts of this chapter have been published in ”Estimation of blade loads for a vertical axis wind turbine with strain gage measurements”[90]

6.1. Introduction

The blades of a Vertical Axis Wind Turbine experience complex loading every rotation, including swapping pressure and suction sides, unsteady aerodynamics, dynamic stall, blade vortex interaction, and tower shadow. Each of these phenomena can be difficult to simulate, especially at the fidelity of an engineering model, which is generally used in design and lifetime assessment. The blade pitch of the VAWT has a profound impact on the azimuthally varying loading of the blades. As shown by Ferreira[69] and discussed in chapter 5, for a 2D VAWT in potential flow, the power extracted by the turbine can be viewed independently of the azimuthal blade loading by applying fixed pitch offsets which have the effect of shifting the loading between the upwind and downwind passes of the blades. However, in practice, this shifting causes the operation point on the airfoil polar to change corresponding to the pitch angle shifts. With real airfoils dynamic stall is encountered altering the energy extraction from the flow and leading to complex loading scenarios which are difficult to model.

Few data sources exist in the literature for calibration and validation of numerical models with blade loading on an azimuthal level. Typically models are calibrated based upon overall rotor integrated loads such as power and thrust coefficients. For instance the effects of blade preset pitch on power coefficient versus tip speed ratio were studied by Klimas et al.[91]. While useful as a baseline, these comparisons can miss many things that are crucial for the design and development of Vertical Axis Wind Turbines. Especially in situations where individual blade pitch is considered. As part of the validation campaign for the development of a vortex model for the Darrieus turbine (DART), Strickland et al.[35] published a dataset from a drag tank facility for a straight bladed VAWT at multiple tip speed ratios. Data was also collected in a wind tunnel test by Vittecoq et al.[92] showing normal and tangential load data for a VAWT with a chord to radius solidity ratio of 0.2. While collected at a handful of locations around the azimuth, it provides excellent detail of the potential presence of dynamic stall at tip speed ratios lower than 3.5 for said solidity ratio. More recently measurements have been made using flow analysis techniques such as described in chapter 5, previously used by Ferreira[11], while very useful, these measurements are limited in resolution and are expensive to conduct. Force measurements were made by Uppsala University[93–95] using load cells between the strut connection points and the tower for parked conditions. These measurements were made in both parked and operating conditions for a larger 12 kW machine in the field. The data is very useful as a real-world check. However due to being field measurements, the wind conditions are not controlled, which adds a level of difficulty for comparison to models for validation. The datasets provided herein look to extend these data sources to include a higher azimuthal resolution in a controlled wind tunnel environment allowing the detailed exploration of the effects of variable blade pitch on the load experienced by the blades.

As shown in the detailed flow fields in chapter 5 the pitch angle of the VAWT has a profound impact on the azimuthally varying loading of the blades. Experimental data with a high degree of azimuthal resolution is required in order to assess the performance of the simulations at capturing the above mentioned aerodynamic phenomena. With this in mind, a sensor system was designed for a 2-Bladed variable pitch H-type vertical axis turbine at TU Delft to discern blade normal loading and azimuth position in multiple blade pitch configurations. The design of this turbine is discussed in detail in chapter 2. Data is presented for 7 fixed pitch cases establishing loading trends of the turbine based upon pitch configuration. The strain gage measurement system allows a high resolution of test cases to be performed.

6.2. Methods

This section describes the information pertinent to the specific data presented in this chapter. For a more complete list of sensors and data processing incorporated on the PitchVAWT Turbine see appendix B.

6.2.1. Definition of Coordinate System

For reference the coordinate system is given in figure 6.1. The turbine is mounted in the Wind tunnel such that the incoming flow consistently comes from the 90° azimuth position, with the x-direction following the direction of the wind. The turbine rotates counter-clockwise, and the y-direction is defined using the right-hand rule.

The blade pitch, β, sign convention is given in figure 6.2. The path of the airfoil is shown with a dashed line. Positive turbine pitch is defined as pitching the leading edge towards the center of rotation, which corresponds to an increase in angle of attack for each azimuth position. Negative blade pitch therefore corresponds to a decrease in α. The pitch axis for the PitchVAWT turbine is located at 48 % of the chord in order to minimize loading on the pitch mechanism at high rotational speeds.

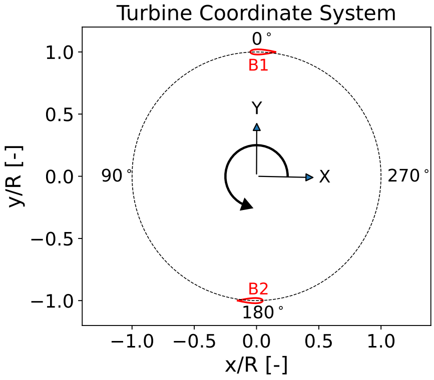

Figure 6.1: Turbine coordinate system, wind from 90°

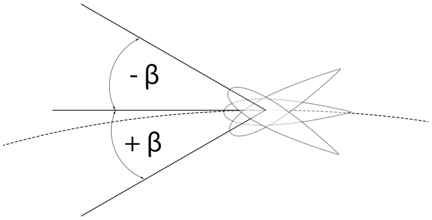

Figure 6.2: Blade pitch convention

6.2.2. Measurement of Rotor Speed and Azimuth Position

The rotor position is measured using a torque transducer with embedded digital incremental optical rotary encoder mounted in the drive-line between the gearbox and the turbine tower. It is shown installed in figure 6.3. The encoder has a 1600 count rev^{-1} or an angular resolution of 0.225°. The encoder is incremental, meaning the zero position needs to be set each time the turbine is powered on. The $\theta = 0°$ position is defined as the angle between the center of the tower and the pitch axis of the machine ($.48c$) being parallel to the tunnel outlet. A laser alignment system is used to set the zero position of the turbine relative to the opening of the wind tunnel outlet, see procedure given in appendix G. The digital output from the encoder is wired to a DIO module on the PitchVAWT DAQ system. A Field Programmable Gate Array, FPGA, device is then used to convert this signal set to a rotation count and speed. The controller converts the counts from the sensor into azimuth position and the rotation rate of counts per second into revolutions per minute.

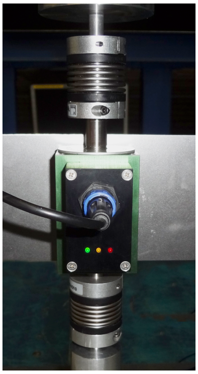

Figure 6.3: Rotary encoder / torque sensor installed on PitchVAWT

6.2.3. Measurement of Normal Load

Blade normal loading is measured utilizing the horizontal extruded aluminum struts used to mount each blade. The struts are a constant cross-section and have the profile of a NACA 0018 symmetrical airfoil. The cross sectional dimensions are given in figure 2.19. Through work performed creating a calibrated finite element model of the turbine, discussed in section 4.5.1, the material properties of the struts have been measured experimentally, and are given in table 6.1. This information is required to transform measured strain to applied normal loading on the strut.

Table 6.1: Strut Material Properties

Property	**Dimension**
ρ_{strut}	2620 kg m^{-3}
E_{strut}	55 GPa
$A_{cross-section}$	143 mm^2

Measurement and Signal Conditioning

The normal load is measured using a set of strain gages on the top strut of the first blade of the turbine. A full-bridge strain gage setup is utilized in an axial configuration in order to compensate for any vertical bending or temperature fluctuations which can occur while testing.

In principle, electrical resistance strain gages measure a small change in resistance of a wire due to its elongation ($\epsilon = \delta l / l_0$.) Generally, the strains which occur in materials due to a generic load are very small, on the order of 1×10^{-6}. In order to measure these very small changes, a wheatstone bridge is used, see figure 6.4. Each resistor shown in the figure is a strain gage mounted on the structure. Due to each strain gage having approximately the same resistance, when no load is applied to the structure, the bridge is said to be "balanced" and no voltage difference is measured across V_{out}. If the resistance changes on any of the legs due to an applied strain, the circuit will go unbalanced and a voltage will be output to V_{out}. When the gages are applied in a specific way, shown in figure 6.5, only the axial strain is measured. This is because any bending load will stretch one gage and compress the gage oppositely positioned on the beam the same amount (assuming a symmetrical beam cross-section), therefore keeping the two legs of the wheatstone bridge in balance. This is also true for transverse loading due to Poisson effects and for temperature fluctuations.

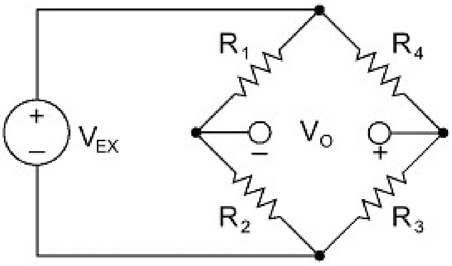

Figure 6.4: Wheatstone Bridge.

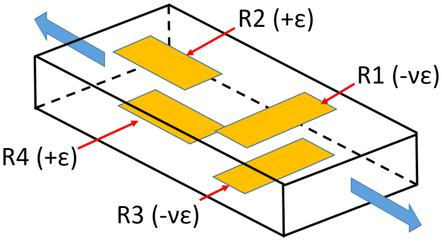

Figure 6.5: Strain gage configuration for axial load.

The measured voltage out corresponds to the change in resistance of each strain gage as shown in equation6.1.

$$V_{out} = \frac{V_{ex} R_2 R_3}{(R_2 + R_3)^2} \left(\frac{\Delta R_3}{R_3} + \frac{\Delta R_1}{R_1} - \frac{\Delta R_2}{R_2} - \frac{\Delta R_4}{R_4} \right) \tag{6.1}$$

The voltage due to the strain response is a relative voltage measurement of the measured voltage difference in the wheatstone bridge versus the excitation voltage between strained and un-strained states shown in equation 6.2.

$$V_r = \left(\frac{V_{out}}{V_{ex}} \right)_{strained} - \left(\frac{V_{out}}{V_{ex}} \right)_{un-strained} \tag{6.2}$$

The axial strain can then be attained using the known ”strain-gage factor”, provided by the manufacturer, the response voltage, and the Poisson’s Ratio for the material of the strut (0.33 for aluminum) by using equation 6.3.

$$\epsilon_n = \frac{-2V_r}{GF[(\nu+1) - V_r(\nu-1)]} \tag{6.3}$$

Data is collected directly within the PitchVAWT Controller based upon the National Instruments Compact-Rio platform. The strain gage set is wired to a NI 9237 strain gage module. The wires pass through a slip ring up to the top strut for blade 1 of the rotor. A shunt calibration is performed in order to calculate the equivalent voltage drop due to the wiring of the strain gage bridge. However, because a full bridge configuration is used and the gages are placed close together, the local effects of wire resistance is considered negligible. Data is collected within the controller at a rate of 500 Hz. This rate allows capturing the effects of airfoil dynamics directly in the time domain as well as capturing higher frequency content which may be of interest.

Normal Load Calculation

First, a calculation is performed to transform the measured strain into a stress. This is performed using Hooke’s Law given in equation 6.4. The measured strain is multiplied by the known Elastic modulus of the material (given in table 6.1. For axial loading the stress on a cross section is the force on that section divided by the area, equation 6.5. For this calculation, the force has only been measured on one of the two struts and is therefore doubled, equation 6.6. Due to the symmetrical design of the blades and struts, the assumption that the normal loading is equally distributed among the struts is considered valid.

$$\sigma_n = E\epsilon_n \tag{6.4}$$

$$F_{n_{strut}} = \sigma A_{cross-section} \tag{6.5}$$

$$F_{n_{blade}} = 2F_{n_{strut}} \tag{6.6}$$

A correction is then performed to remove the large load due to the rotation of the turbine around the vertical axis. The mass of the blades and struts are located at a radius removed from the rotational axis. This causes a substantial centrifugal load which corresponds to the suspended mass having an acceleration proportional to the square of the rotational frequency. For a point mass this can be simplified to $F_{cent} = mr\omega^2$. However for the turbine, this is a fairly complex phenomenon to perfectly correct for with such an assumption. For the processing here a second order polynomial was fit to the normal load data with respect to the rotational frequency. This accounts for any non-linearities built into the system, as well as the exact sprung mass outboard of the strain gage placement. This correction is given in figure 6.6. The polynomial is then used to relate a given measurement point to the load offset based upon the rotational speed. This offset is subtracted from the measurement to give the corrected normal load without the rotational effect.

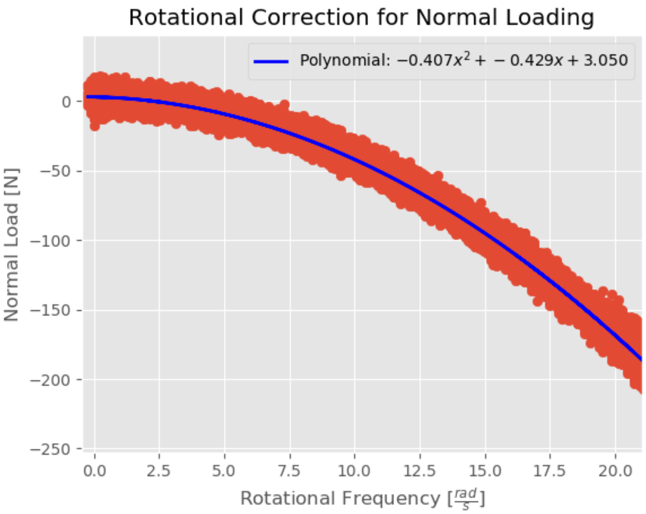

Figure 6.6: Rotation correction for Normal loading

6.2.4. Calculation of Thrust from Normal Load

The most direct way to measure the aerodynamic thrust for the PitchVAWT is to convert the blade normal loading as measured above into x and y components. If each rotor blade had a set of strain gage measurements, this would entail simply summing up the loads over each blade as a function of azimuth position. However, due to channel limitations in the slip-ring of the PitchVAWT, the normal load is only measured for a single rotor blade. As the second rotor blade is designed to mirror the first blade, and the rotor is balanced, the assumption can reasonably be made that it behaves like that of the first. So by sampling the azimuthal load distribution of the first blade with a 180° offset, it is possible to estimate the experienced aerodynamic thrust load for both blades over the rotation of the turbine. The x and y loads from the measured normal load are given first for the individual blade measurement, and then for the assumption of both blades in figure 6.7.

6.2.5. Normal Load Assumption

Due to inherent difficulties with directly measuring the tangential loads on each blade, an assumption is made that measuring the normal loading at each azimuth position provides a good representation of the total turbine loading. In order to verify this assumption, turbine thrust is calculated from the AC Model, see chapter 3.3.1, both with and without inclusion of the tangential force vector. Figure 6.8 and table 6.2 highlight the effect of ignoring the tangential component of the blade forces on the calculated thrust magnitude and direction. In the direction of the wind, the difference is negligible, however there is a slight underestimation of the cross-flow thrust. This underestimation leads to a offset in calculated thrust direction of approximately ±2.5° for the current model. This error is considered acceptable for

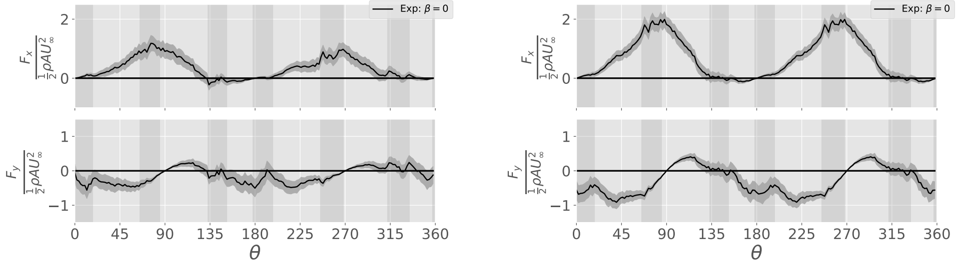

(a) Thrust from Blade 1

(b) Total thrust assuming both blades

Figure 6.7: Thrust from blade normal loads

the current analysis. However, depending on the purpose of the study, this may need to be taken into account.

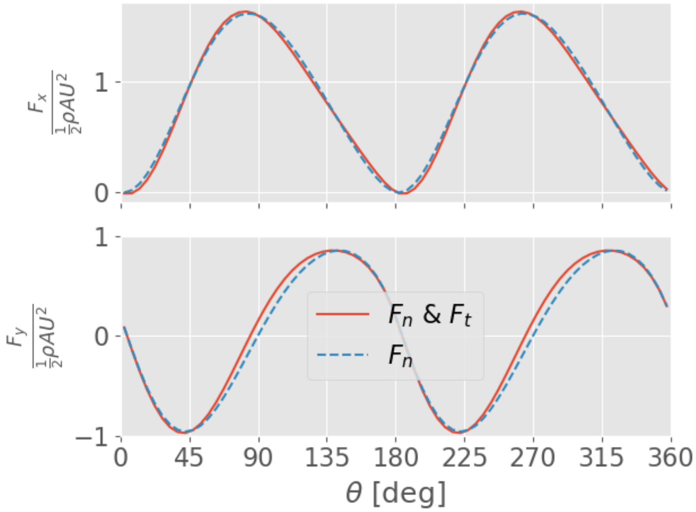

Figure 6.8: Thrust with and without tangential load, from Actuator Cylinder Model

Table 6.2: Effects of including tangential force on thrust calculation.

Pitch	Param	Mag	Dir
0°	F_n, F_t	0.843	89.93°
	F_n	0.848	92.58

6.2.6. Experimental Setup

Testing is conducted with the PitchVAWT turbine as described in detail in chapter 2 in the Open Jet Facility of TU Delft. The wind speed was held constant throughout testing at $4\,\mathrm{m\,s^{-1}}$. The turbine was operated at a constant tip speed ratio of $\lambda = 4$, for an average rotational speed of about 205 RPM. These speeds are chosen due to a resonance which occurs at roughly 215RPM due to crossing with the backward whirling mode of the tower. At a $\lambda = 4$ most of the deleterious effects of dynamic stall are minimized, allowing the loading changes due to small pitch angle deltas to be measured. Therefore the wind speed was lowered in order to allow this tip speed ratio at the upper limit of RPM without initiating the resonance with the tower backward whirling mode. For more details see the description of the dynamic characterization and model development of the PitchVAWT in chapter 4.

The loading over time are binned into azimuthal buckets for understanding the loading over the rotation. The turbine is divided into 180 azimuthal bins of 2°. Each measurement is binned based upon the azimuth position at the time the measurement was taken. The mean and standard deviation are then calculated for each azimuthal bin. Due to the sampling, each measurement bin has a potentially different number of counts. The range of counts per bin was 178 to 216 for testing at the zero pitch, $\beta = 0°$ position. With similar counts for each pitch configuration.

The strain signals are passed through a slip ring in order to transfer the data from the rotating frame of the rotor to the fixed frame of the turbine base. In this process, noise was introduced into the signal at several distinct points along the azimuth position giving a higher uncertainty in these measurements. Data has been collected with no turbine loading in order to quantify the effect of the slip ring in these areas and to remove any localized bias, however some dynamics exist which are not considered representative of the aerodynamic flow such as sharp inflection points, and therefore should be treated with care. A vertical shaded region in the plots highlights these sections of the data. As there are ample sections of high quality data for comparison from test to test and from test to model, there is minimal information lost. Other potential sources of uncertainty include: strain gage placement, as it is necessary to align the gages with the axial direction any deviation will cause cosine losses of voltage change; Material properties, stiffness and density were directly measured experimentally several times on a spare turbine strut to minimize any deviation, however there is a small error associated with all data collection; Poisson's ratio for the strut material is assumed on best practice with aluminum however has not been directly measured with this turbine. These sources of error are generally much smaller than the overall standard deviation for each measurement bin, and are considered to be within the accepted error margin for the measurements.

The mean normal load coefficient ($\frac{F_n}{\frac{1}{2}\rho\lambda^2 U_\infty^2 hc}$) of each azimuthal bin is plotted as a line, with $\pm\sigma$ given as a shaded region. In order to establish trends in both the positive and negative pitch directions data is presented for cases where $\beta = 0°, \pm 2°, \pm 3°, \pm 5°$.

6.3. Results and Discussion

6.3.1. Azimuthally Varying Normal Load

The baseline loading for neutral pitch with $\beta = 0°$, at the operating tip speed ratio of $\lambda = 4$ is given in figure 6.9. The data is presented in two formats, first in the Cartesian x-y manner, and then in polar form to better visualize the effects of the normal loading on the flow of the turbine. Figure 6.9a displays a graph of the normal force coefficient as a function of azimuth position. The standard deviation of each measurement bin, relayed by the shaded area around the curve, remains consistent over the rotation reflecting a general noise level on the strain measurement. This provides a view of the consistency of the measured load at each azimuth position, as well as the continuity in the turbine loading between each azimuth bin, as no other filters have been applied to the data. The next presentation in figure 6.9b shows the same data in a polar format. This plot shows the normal force on the flow around the azimuth position as if viewing the turbine from a top down vantage point, with the wind incoming from the left of the image. The thick black line represents the zero load condition with the red line representing the normal load coefficient at the given azimuth position. Normal load vectors are used to further enhance the observation of the loading. Total turbine thrust is represented by a large vector stemming from the center of the plot. The normal load is transformed to thrust in x and y directions using the method discussed in section 6.2.4. A trapezoidal integration is then performed over the azimuth for each component of thrust. The components are then used to generate the integrated thrust vector.

Investigating the normal loading for this $\beta = 0°$ condition, the upwind load response between 0° to 90° increases with angle of attack as expected based upon the sinusoidal nature of VAWT aerodynamics of both the apparent wind speed and the expected angle of attack. After the peak loading, as the blade begins to retreat from the wind, between 90° to 180° the load drops quickly to zero, going negative before the 180° position. This drop is likely due to a reduction in both the angle of attack, and the apparent velocity with the blade retreating from the oncoming wind. And potentially due to flow separation behavior at the low Reynold's numbers for the relatively thick NACA0021 airfoil. The downwind half of the rotor pass shows greater jumps in load than the upwind pass possibly indicating the effect of blade vortex interaction and tower shadow. The resultant thrust vector shows that due to this load collapse in the receding blade after 90° there is a substantial cross-flow thrust term.

Moving to the variation of loading due to fixed pitch offset cases, the normal loading for each pitch case is provided in polar plot form in figure 6.10. The overall trend in the change of load magnitude and direction due to the offset pitch is readily visible. As the pitch increases, the loading shifts earlier in the rotation with the load decreasing post peak at a greater rate. Potentially indicating airfoil stalling behavior due to the increasing angle of attack. The opposite occurs for cases with negative pitch offset, with the negative pitch angles reducing the amount of cross-flow thrust experienced by the turbine. Indicating a lower angle of attack delaying the onset of any stall behavior in the upwind portion of the rotation.

The normal load responses for each pitch are directly compared in figure 6.11.

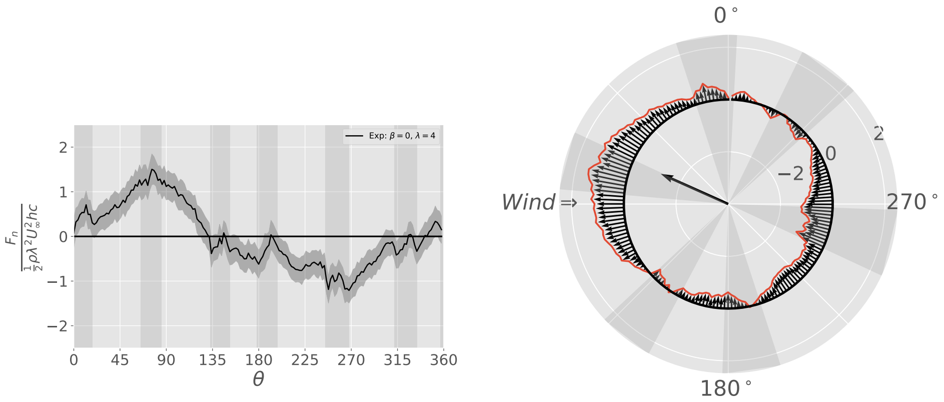

(a) Normal load over azimuth

(b) Polar plot highlight normal load and resultant thrust

Figure 6.9: Normal load coefficient with $\beta = 0°, \lambda = 4$

The neutral pitch of zero degrees appears to be partially stalled due to the rapid drop off of normal load after the peak. As the blade pitch is increased, this effect is exaggerated, forcing the load higher earlier in the rotation, however also stalling deeper and earlier. With the negative pitch angle, a different response is witnessed. The loading begins the rotation below the neutral pitch case, and then continues to increase in loading beyond where the zero pitch case does, perhaps due to less stall on the upwind half. This however also reaches a maximum, and the effect is not seen to increase after $\beta = -3°$ pitch case. The behavior is mirrored in the downwind half of the rotor, as to be expected with the inversion of the pressure and suction sides of the airfoil on the downwind half. The direct comparison between the extremes of the pitch angles highlight the above analysis more directly.

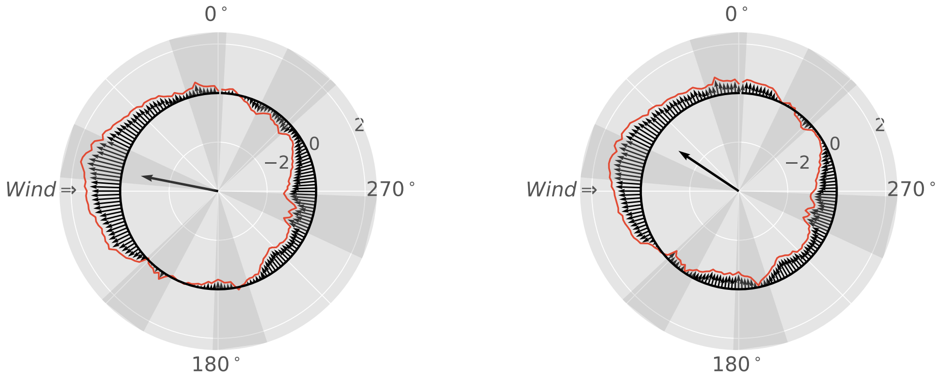

(a) $\beta = -2°$

(b) $\beta = 2°$

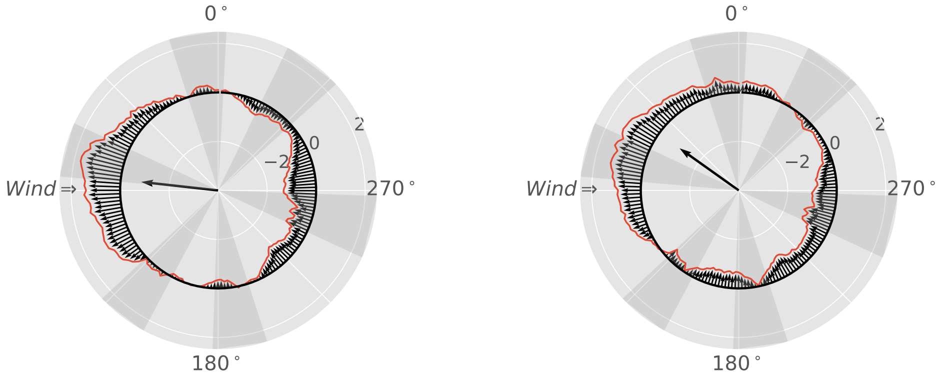

(c) $\beta = -3°$

(d) $\beta = 3°$

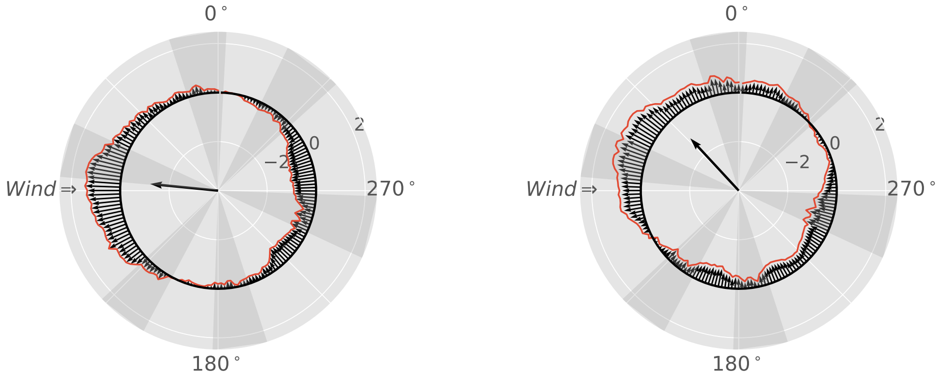

(e) $\beta = -5°$

(f) $\beta = 5°$

Figure 6.10: Normal load coefficient with fixed pitch offset of PitchVAWT with the integrated thrust vector, $\frac{F_n}{\frac{1}{2}\rho\lambda^2 U_\infty^2 hc}$

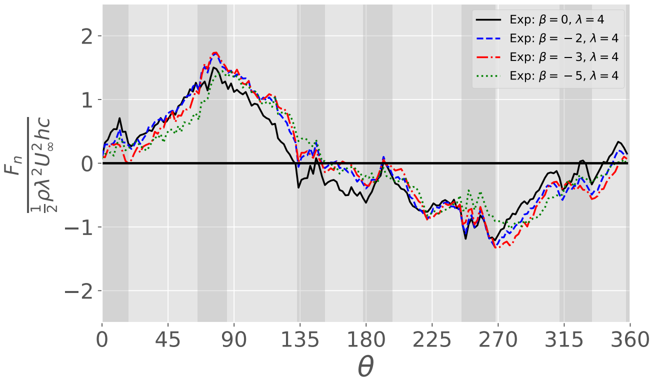

(a) Negative pitch offsets

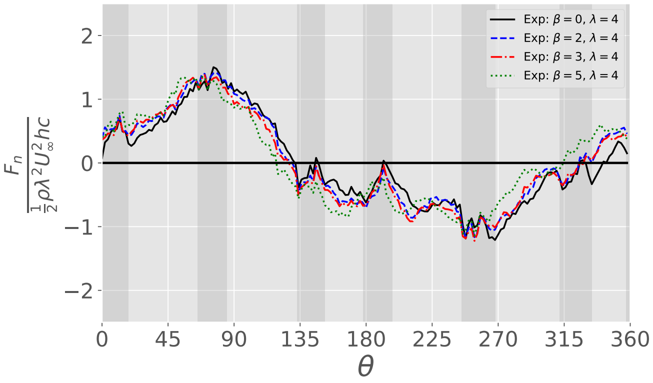

(b) Positive pitch offsets

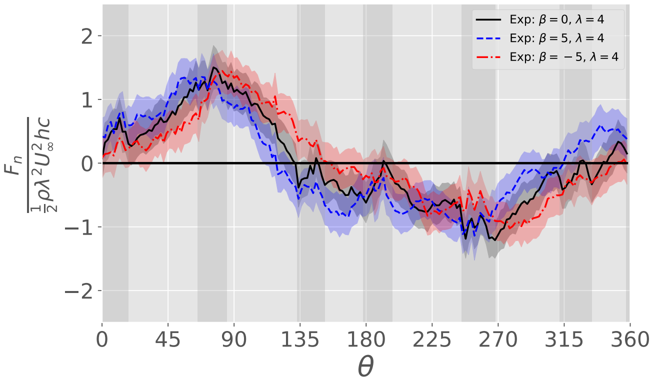

(c) Comparison $\beta = 0°, \pm 5°$

Figure 6.11: Experimental normal load coefficient for negative and positive pitch offsets measured using the PitchVAWT strain gage data

Thrust coefficients are calculated using the normal load distribution as described in section 6.2.4. These are given for both the oncoming wind direction, x, and the cross-flow direction, y, in table 6.3. The thrust magnitude and direction relates more clearly the above stated relationship with pitch angle. The $\beta = 0°$ case represents the minimum in the magnitude of the thrust vector. Increasing the pitch any further causes a more drastic shift in the direction of the thrust while having a minimal effect on the magnitude, this is most likely due to the airfoil already being partially separated in the upwind half of the rotation at the zero pitch condition. With the pitch slightly negative at the $\beta = -2°$ and $-3°$ positions, the magnitude of the thrust is much greater, and more directly aligned with the flow direction. At a pitch of $-5°$ the thrust magnitude decreases due to a lack of loading on the downwind half of the rotor, most likely due to stall on that half.

Table 6.3: Thrust coefficients from normal load data in axial and cross flow directions for fixed pitch cases.

β[°]	C_{Tx}	C_{Ty}	Magnitude	Direction [°]
0	.68	-.28	.73	-22.3
2	.63	-.42	.76	-33.5
3	.63	-.45	.78	-35.9
5	.52	-.55	.75	-46.9
-2	.84	-.14	.86	-9.7
-3	.85	-.05	.85	-3.6
-5	.78	-.05	.78	-3.5

6.3.2. Frequency Response in Fixed and Rotating Reference Frames

The frequency content of the loading provides insight into the data from a different perspective. Especially when categorizing important information for fatigue estimation. This section presents the frequency response of the normal load measurement for the extremes in turbine pitch compared to the baseline of $\beta = 0°$. The frequency response of the platform is also measured, giving a comparison of the response between the fixed and rotating reference frames. Finally, a comparison is made between multiple tip speed ratios for the $\beta = 0°$ case highlighting the effect of changing rotational speed on the response.

The power spectral densities of the normal loading for $\beta = -5°, 0° and 5°$ are plotted against the nondimensional frequency of cycles per revolution in figure 6.12. As the normal load is measured in the rotating reference frame, the major response corresponds to the frequency of rotation at 1P. All three pitch cases show the same behavior with the 1P frequency response. As to be expected with the sinusoidal nature of the loading discussed in previous sections. The area of interest occurs in the higher order harmonics, where differing blade loading characteristics such as dynamic stall or blade vortex interaction can take place. With the first three harmonics, the behavior of each pitch condition is consistent with the baseline. However, there is a greater response in the pitched conditions than the zero pitch baseline where greater stall exists in the 3p, 4P, 8P, and 10P frequencies. Meaning the stall exacerbates loading at higher per rev frequencies than is seen in the zero pitch case.

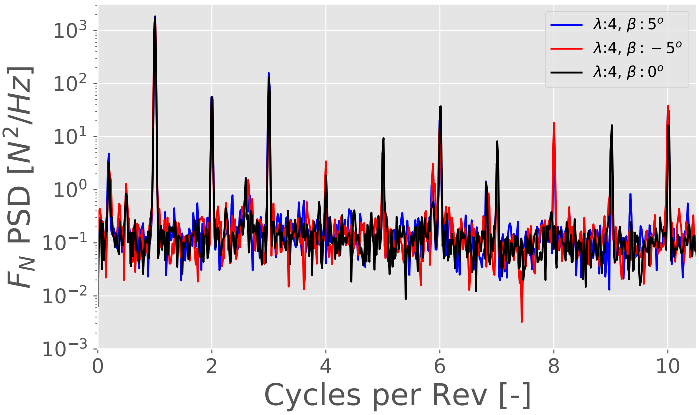

Figure 6.12: Power Spectral Density vs Cycle per Revolution for Normal Force, comparing pitch angles

A set of single axis PCB 352A24 100 mV/g accelerometers are mounted to the large blue base as discussed in chapter 2 measuring the platform motion in the X, Y, and Z directions. The accelerometers were mounted on the corner of the platform in order to properly capture the motion for all frequencies of interest by avoiding any vibration node locations. The accelerometers and corresponding directions are shown in figure 6.13. As a reminder, the x-axis is aligned with the incoming flow, the y-axis is perpendicular to the flow, and the z-axis is vertical.

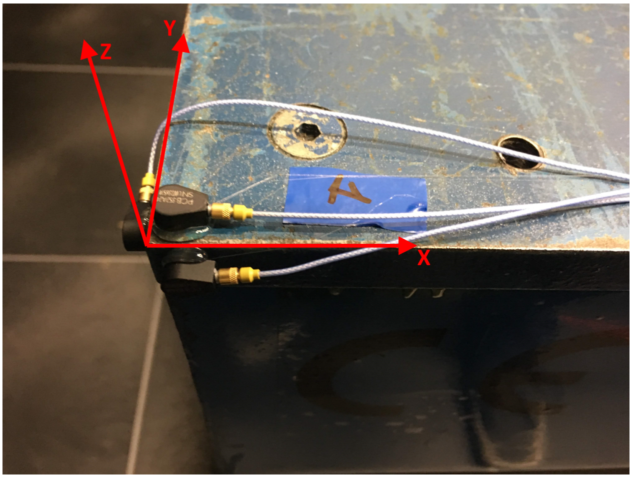

Figure 6.13: Accelerometers mounted to platform with turbine coordinate system

The platform motion as measured by the accelerometers is given in figure 6.14. The stiffness of the platform is quite different in each direction, with the X-direction being stiffest followed by the Y-direction, with the vertical stiffness relatively free in comparison. This is due to the general construction of the scissor lift based system, and the relative geometry, with the x-direction aligning with the longest side. This is proven out by the relative responses in each of the directions for all pitch cases. The fixed reference frame shows the fundamental excitation frequency for each direction to coincide with the 2P frequency as expected with the two blades of the turbine. The x-direction response shows both 2P and 4P excitation with very little in response at higher frequencies. There is very little difference in response with respect to changing pitch. The y-direction response is heavily dominated by the 2P side-side effect. There is more excitation for the 3P and 4P side loads with both the positive and negative pitch offsets. This may be due to the increased side-loading experienced with the offsets due to earlier onset stall. The most excitation in the higher frequencies occurs in the vertical direction. As the platform is effectively ″floating on springs″ due to the nature of the scissor lift operation, there is less stiffness in the vertical direction (discussed in detail in chapter 4). The moment-arm from the thrust loading will also cause a rotation about the turbine base which is measured by the acceleration on the corner of the platform. Each pitch case is consistent with response at the 2P, 3P, and 4P peaks, however begin to diverge in the higher frequencies. The loading at 6P, 7P, and 8P is substantially higher with the effect of pitching. This is potentially due to the effects measured in the 3P, 4P, and 8P frequencies measured in the rotating frame from figure 6.12. These results show that it may be important to keep in mind the effects of higher per rev frequencies when evaluating structural loading in conditions where dynamic stall can occur.

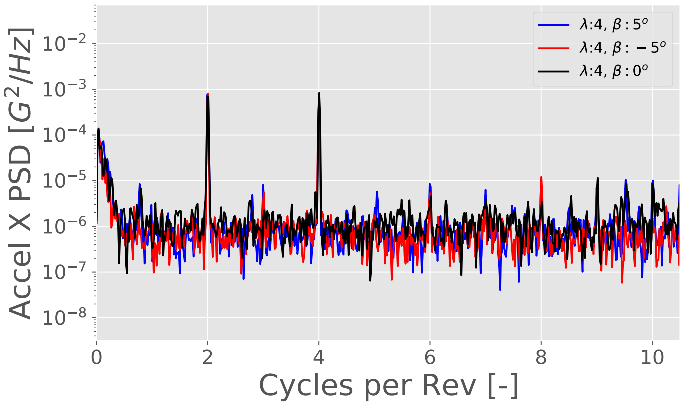

(a) Acceleration X

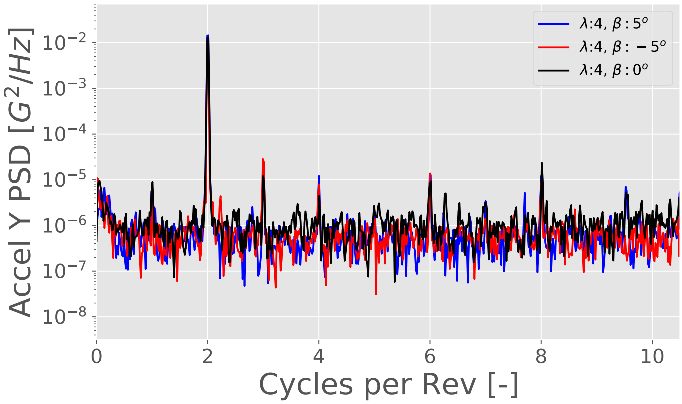

(b) Acceleration Y

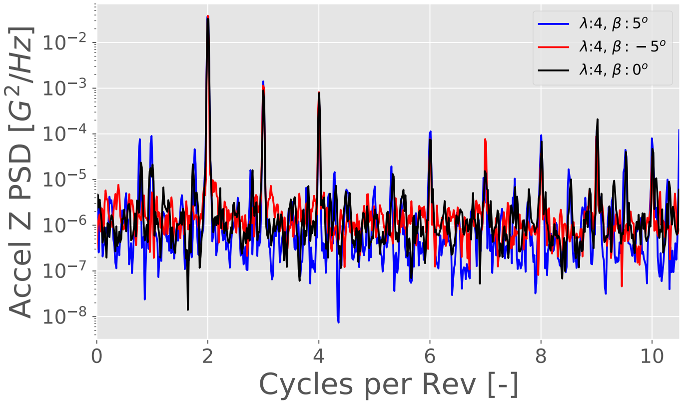

(c) Acceleration Z

Figure 6.14: Power Spectral Density of platform acceleration

6.4. Conclusion

A series of experiments have been conducted in the Open Jet Facility of TU Delft with the PitchVAWT 2-Bladed H-type Vertical Axis Wind Turbine comparing the effects of blade pitch offsets on normal loading at each azimuth position. A technique for measuring the normal loading of the turbine based upon axial strain gage measurements of the turbine struts was presented.

The measured blade loads generally behave in the manner expected for Vertical Axis Wind Turbines with the suction and pressure sides flipping each rotation. The loading in the upwind half for each blade pitch is fairly smooth indicating a clean inflow behavior, while the downwind pass for each blade pitch condition is considerably more turbulent, showing potential behavior of blade vortex interaction and tower shadow. For positive pitch angles, the loading increases with pitch in the first quarter of the turbine rotation. However, this inverts between $\theta = 90° to 180°$ most likely due to increasing effects of stall behavior. The opposite happens with negative pitch angles, as is consistent with the expected stall behavior in the upwind half of the rotation. In the third quarter of the rotation between $\theta = 180° to 270°$ the trends continue from the upwind half, where stalled behavior continues as the pressure and suction sides reverse. By the 270° position, the flow has recovered for each pitch case, with the positive pitch angles giving a more positive load, and the negative pitch angles more negative. This tendency leads to a trend of turbine thrust having a greater cross flow component in positive pitch angles, and being more aligned with the flow direction for negative pitch angles.

Measurements presented are for a given wind condition and tip speed ratio to restrict the analysis to varying pitch angles. Operating at lower tip speed ratios would further increase the relative effects of dynamic stall than those already exhibited within the data and would complicate the analysis further. Operation in different wind speed ranges would have an effect on the chord-wise Reynold's numbers, thereby affecting the local airfoil loading and dynamic stall. However, the relative changes experienced due to shifting blade pitch should remain consistent across Reynold's number scales.

The frequency response of both the normal loading and platform motion were studied. The results indicate the effect of changing pitch conditions excites loading in higher cycles per rev. This is potentially due to the much increased stall behavior for the turbine with bigger fixed pitch offsets. These results warrant more study in lower tip speed ratio operating regions where the turbine may have to operate above rated wind speed when loading is also higher. The dataset can be used as a benchmark to validate numerical models of Vertical Axis Wind Turbines experiencing an array of complex flow phenomena.

Bottom Line:

- A technique for measuring the normal loading of the PitchVAWT turbine based upon axial strain gage measurements of the struts was presented.
- More resolution in azimuthal position and pitch setting provided by the strain gage measurement system confirm trends witnessed in PIV measurement data of chapter 5.
- The loading in the upwind half of the rotation is fairly smooth indicating a clean inflow behavior, while the downwind pass for each blade pitch condition is considerably more dynamic, showing potential behavior of blade vortex interaction and tower shadow.
- Shifting pitch effects the dynamic stall experienced by the machine changing the azimuth position of onset, and the magnitude of the stall.
- The changing load profiles effect the integrated thrust of the machine, changing both the axial and cross-flow terms of the thrust.
- Frequency response of both the normal load and platform accelerations show higher per rev excitation when dynamic stall is present.

V

Experimental Validation of Modeling with Fixed Pitch Offsets

7

Rotor Loading with Fixed Pitch Offsets Model to Experiment Comparison

Accurate simulation results for the performance and loading of a Vertical Axis Wind Turbine are critical in the design and life cycle assessment for the machine. In order to have confidence in the simulated loading of the turbines, it is crucial to have quality experimental data in which to compare and calibrate simulation results. This chapter presents the comparison of normal loading estimated by two independent experimental techniques taken simultaneously on the PitchVAWT wind turbine with simulations conducted using 2D and 3D numerical models. Data for zero pitch offsets compare very well between all methods. Multiple turbine fixed pitch angles are compared, showing the limits of the models to capture deep stall regimes.

7.1. Introduction

Accurate simulation results for the performance and loading of a Vertical Axis Wind Turbine are critical in the design and life cycle assessment for the machine. In order to have confidence in the simulated loading of the turbines, it is crucial to have quality experimental data in which to compare and calibrate simulation results.

Experiments performed on the PitchVAWT turbine in the Open Jet Facility as discussed in chapters 5 and 6 measured the normal loading of the turbine in completely independent manners. The first technique in chapter 5 measured the velocity fields around the airfoil at the turbine mid-span at multiple azimuthal positions using Particle Image Velocimetry. These flow fields were then used within the Noca flux formulation to calculate the normal and tangential loading at each position. The second technique, presented in chapter 6, estimated the normal load by measuring the strain response of a strut during operation. Each of these tests were conducted at several fixed pitch operational positions in order to witness the behavior in several configurations. Trends were measured highlighting the effects of dynamic stall in both the upwind and downwind locations of each experiment.

This chapter presents the comparison of normal loading estimated by these two independent experimental techniques taken simultaneously on the PitchVAWT wind turbine with simulations conducted using 2D and 3D numerical models.

7.2. Methods

The models and experiments are all based upon the PitchVAWT wind turbine. The test conditions are determined based upon operating limits of the wind turbine in the Open Jet Facility at TU Delft. This section gives a brief overview of the turbine parameters relative to the chapter, for a more detailed description of the turbine along with design constraints see chapter 2.

7.2.1. PitchVAWT Turbine Overview

The PitchVAWT turbine is a two bladed H-shaped Vertical Axis Wind Turbine with individual pitch control. General turbine specifications are given in table 7.1. The as built diameter of the turbine is 1.48 m and the NACA0021 blade airfoils have a chord length of 0.075 m giving a chord to radius ratio of approximately 0.1.

Each blade pitches about the center of mass of the built airfoil at $0.48c$ in order to minimize torque from the centripetal acceleration of the blades on the pitch control motors. The pitch of each blade of the turbine is controlled by an independent motor and can therefore be configured to test most conceivable pitch schemes in the relatively controlled environment of the OJF. Calibration of blade pitch position is performed with a laser alignment system prior to each test. This ensures alignment of zero position for blade pitch and turbine azimuth with reference to the opening of the wind tunnel.

7.2.2. Definition of Coordinate Systems

The coordinate system used for the study is given in figure 7.1. The turbine was mounted in the wind tunnel such that the incoming flow comes from the 90° azimuth

Table 7.1: PitchVAWT Design Specifications

Property	Dimension
NBlades	2
NStruts	4
Rotor Height	1.508 m
Diameter	1.48 m
Blade Chord	0.075 m
Strut Chord	0.060 m
Solidity	0.1
Blade Airfoil	NACA0021
Strut Airfoil	NACA0018
Blade Pitch Axis	48 % c
Operating λ at U=4 $\mathrm{m\,s^{-1}}$	1 to 4

position, with the x-direction following the direction of the wind. The turbine rotates counter-clockwise, and the y-direction is defined using the right-hand rule. Forces are defined from the perspective of the force acting on the flow. Therefore, a force acting on the flow in the outward facing normal from the surface of rotation is defined as positive.

The blade pitch, β, sign convention is given in figure 7.2. The path of the airfoil is shown with a dashed line. Positive turbine pitch is defined as pitching the leading edge towards the center of rotation, which corresponds to an increase in angle of attack for each azimuth position. Negative blade pitch therefore corresponds to a decrease in α.

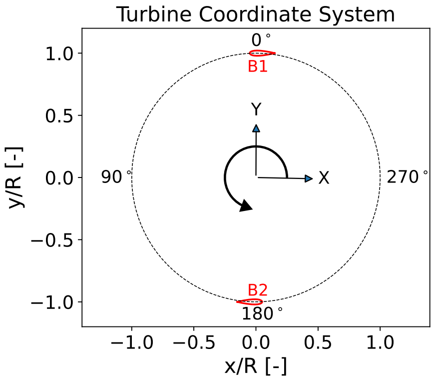

Figure 7.1: Turbine coordinate system, wind from 90°

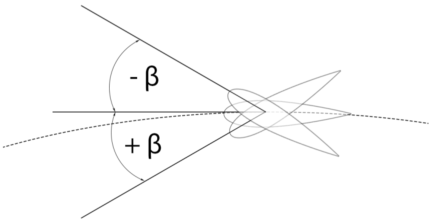

Figure 7.2: Blade pitch convention

7.2.3. Test Conditions

The experiments were conducted in the OJF at TUDelft. Due to rotational speed limitations of the wind turbine and a desired tip speed ratio of operation, wind speeds were limited to $4\,\mathrm{m\,s^{-1}}$ during testing. A large blue lifting base is available in the tunnel for mounting test hardware. The turbine is mounted to this platform and placed to align in the center of the jet, with the center of the turbine 2 m from the outlet face.

7.2.4. Simulations

Simulations were performed with three independent models; the Actuator Cylinder model as discussed in section 3.3; the nonlinear lifting line free-wake vortex model implemented within QBlade[58]; and CACTUS the free-wake vortex model developed by Sandia National Laboratories[59]. The vortex models are both three dimensional, and the blades are divided into 11 elements sinusoidally distributed across the blade height, shown in detail in figure 7.3. Each vortex model was run for a minimum of 15 revolutions and then a convergence criteria of 0.0005 on the power coefficient to determine the final output. For all three models, the azimuthal resolution was 5° corresponding to 72 calculations per rotation.

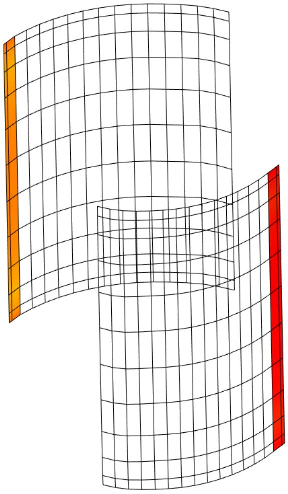

Figure 7.3: Sinusoidal element distribution across blade height for free-wake vortex models, exhibited in QBlade. 125° of azimuth rotation is shown with a resolution of 5°

In order to properly compare each simulation to wind tunnel test data of the PitchVAWT turbine, viscous effects of the airfoil need to be accounted for. First, a virtual camber transformation was performed on the symmetrical NACA0021 airfoil in order to compensate for flow curvature, see section 3.4. The lift and drag polar were then calculated using XFoil for an operating Reynolds number of 9×10^4. Due to the surface condition of the manufactured airfoil including a spray painted exterior, a $N_{crit} = 5$ was used. The resultant polar is given in figure 7.4. A Beddoes

Leishman type dynamic stall model was implemented for each simulation. Specifics of the time-constants used in the model may vary between the vortex models due to implementations being performed by third parties. Where able, the dynamic stall model time-constants are set to be the same, however both QBlade and CACTUS have an internal implementation of these models which has not been altered. For instance, in QBlade only two of the four time-constants are available to alter, and in Cactus, the coefficients are calculated off of the given polar directly, so no constants are directly changed. The implementation of dynamic stall within the actuator cylinder model and its verification to prior results are provided in appendices D and E, respectively.

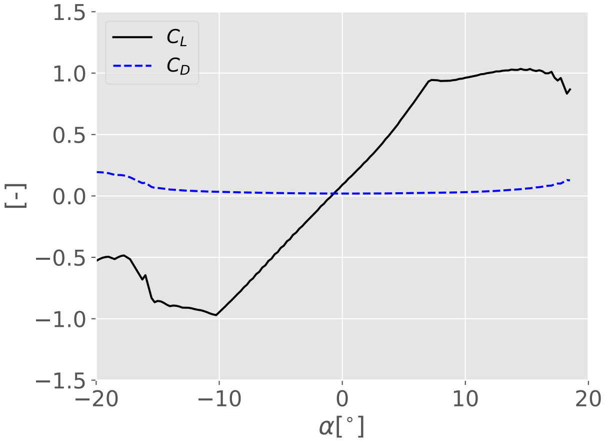

Figure 7.4: Airfoil polar used in simulations $Re = 9 \times 10^4$, virtual camber transformation as described in section 3.4

Data is compared for three fixed pitch settings, $\beta = 0°$, $\beta = 5°$, and $\beta = -5°$. All testing and models are compared at a free stream wind speed of $U_\infty = 4\,\mathrm{m\,s^{-1}}$ and a tip speed ratio of $\lambda = 4$.

7.3. Results and Discussion

The data is presented in two ways. First, data is presented comparing the normal load at each pitch configuration for each measurement technique and simulation type. Next all models and simulations are compared directly to each other for each pitch position.

7.3.1. Particle Image Velocimetry Data

Normal loading for the test conditions were estimated at 6 azimuthal positions using the Noca method based upon flow field velocity measurements taken with PIV. See chapter 5 for a full formulation and analysis of the technique. A direct comparison of the estimated normal load for each pitch position from PIV measurements is given in figure 7.5.

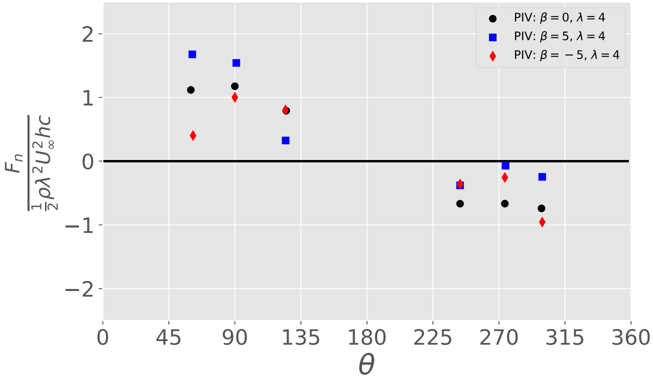

Figure 7.5: Estimated normal load coefficient from Particle Image Velocimetry measurements on Pitch-VAWT at $U_\infty = 4\,\mathrm{m\,s^{-1}}$, $\lambda = 4$.

7.3.2. Strain Gage Data

Normal loading for the turbine was also measured using strain gages mounted to the struts of the turbine during operation. The procedure and analysis of the measurements are given in chapter 6. Due to the relative ease of capturing the strain gage data compared to that of PIV, a higher resolution of experiments were collected showing gradually increasing and decreasing pitch values. For this chapter, only the extremes of $beta = \pm 5°$ are compared. The normal load coefficient from the strain gage measurements for each pitch are given in figure 7.6.

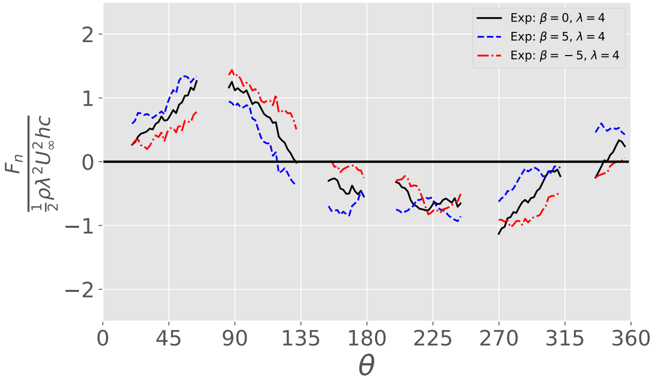

Figure 7.6: Normal load coefficient as measured from strain gages on turbine struts at $U_\infty = 4\,\mathrm{m\,s^{-1}}$, $\lambda = 4$.

7.3.3. Simulation Results

Normal loading from each simulation at each pitch condition is given in figure 7.7. All of the simulations have similar results as is expected. The largest differences appear in the areas associated with deeper airfoil stall behavior.

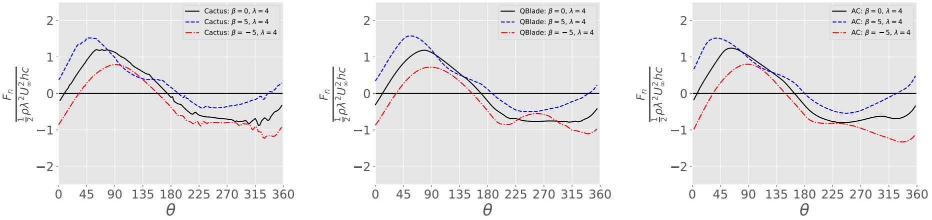

(a) CACTUS (b) QBlade (c) Actuator Cylinder

Figure 7.7: Simulation results for each pitch configuration.

7.3.4. Model validation

The normal load from the three models are compared with the experimental strain gage and Particle Image Velocimetry measurements in figure 7.8.

Beginning with the $\beta = 0°$ pitch configuration in figure 7.8b all of the models and data match very well in the $\theta = 0° to 90°$ azimuthal range. The AC model tends to predict slightly more load than the vortex models. As the blade passes $\theta = 90°$ the effects of the various dynamic stall models begin to separate the predictions of the models. The strain gage data diverges from the PIV data and the model predictions in this area as well. It is not immediately apparent why this is the case. It is possible that there are three dimensional effects in stall related to the nearby blade-strut interface above and below the PIV measurement plane which is not included in the three dimensional lifting line models. However, this has not been studied in detail. On the downwind half of the rotor, the models, PIV, and strain gage measurements all converge again until $\theta = 270°$ where the strain gage data deviates. This may be due to tower pass effects which are not modeled in the numerical comparisons.

Both the 5° and −5° pitch tests show greater deviations between all models and measurement results compared to the neutral 0° pitch condition. For the $\beta = -5°$ case, the three models are fairly close for the upwind half. The PIV matches the model calculations at the $\theta = 60°$ and $\theta = 120°$ locations, but measures a higher loading in the 90° position, potentially due to the onset of dynamic stall. This trend is more characteristic in the strain gage data as the jump is profound until the $\theta = 180°$ position. On the downwind side the differences in the models is prevalent, with the QBlade model predicting a much deeper drop in load due to stall, as is measured with the PIV. The strain gage data shows a steep drop in load after the spike around the 300° position. The $\beta = 5°$ data again shows the deviations between the models and experimental data highlighted in areas of deeper stall. Both vortex models do a better job matching the pattern of the PIV data in the upwind pass, although the dynamic stall is more severe than predicted in the models. The strain gage data has a large negative load through the rest of the retreating azimuth position section. After the $\theta = 270°$ location, the models and data re-converge showing good agreement.

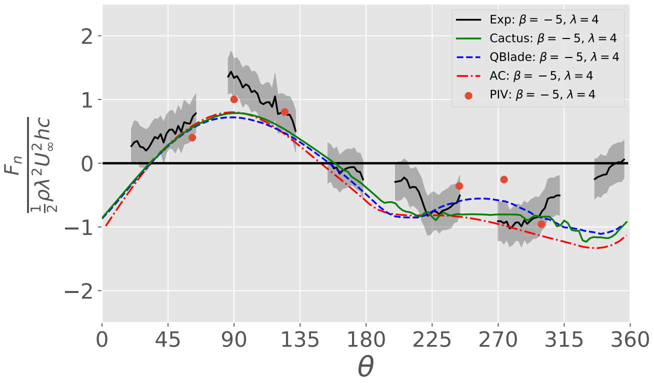

(a) β = −5°

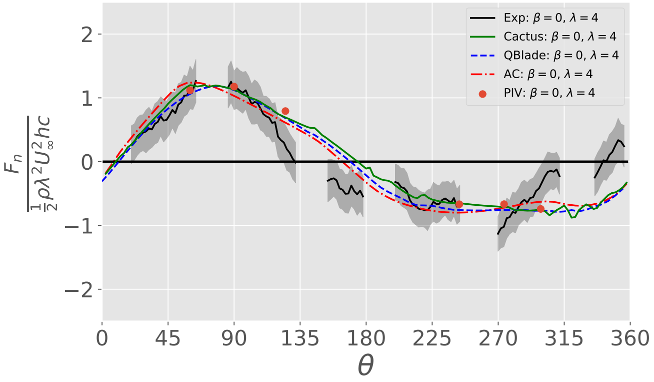

(b) β = 0°

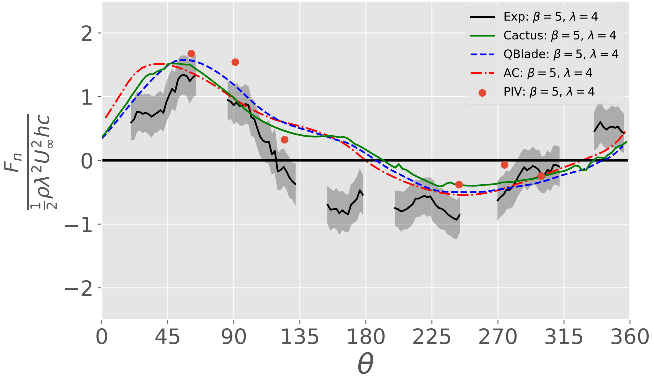

(c) β = 5°

Figure 7.8: Measured normal load comparing PitchVAWT Strain Gage Data, PIV measurement, AC model, 3D Lifting Line Models prediction

7.3.5. Thrust Variation with Tip Speed Ratio

The integrated loading of the turbine gives an overall idea of the performance. Each of the models is used to calculate the average thrust force in line with the incoming flow for tip speed ratios from 1 to 4. The models were run with a single consistent polar as used above. The experiment however was conducted with a constant wind speed, therefore varying the tip speed ratio, meant slowing the rotor to each required rotational speed, resulting in a much lower chord Reynold's number. As shown in figure 7.9, each of the models over estimates the measured thrust force by a consistently high margin. Once the rotor speed begins to pick up, there is a large gain in performance from the experimental turbine to be much more in line with the predictions from the model. The experiment also has a larger load in the off-axis direction as was studied in chapter 6. The effect of the load dropping in the rotation post $\theta = 90°$ leads to a greater side load, this side load is not accounted for in the axial thrust coefficient. The overall thrust magnitude as given in table 6.3 shows values which are in line with the predicted values from the Actuator Cylinder, Cactus and Q-Blade at $\lambda = 4$.

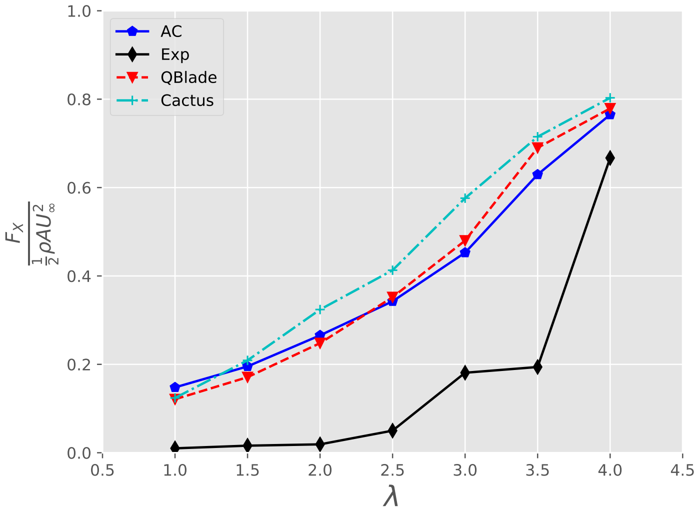

Figure 7.9: $\beta = 0°$, C_T - λ curve for each model using the $Re = 9e5$ polar versus experimentally derived thrust from normal measurement.

7.4. Conclusions

Experimental and numerical results for the PitchVAWT wind turbine have been compared with the goal of assessing the ability of models with different levels of fidelity to capture turbine loading at several fixed pitch offsets. Independent experimental techniques matched well with each other in the overall normal loading for the turbine. Particle Image Velocimetry was deployed on the rotating turbine in each pitch configuration to capture velocity fields surrounding the airfoil at 18 azimuthal positions while a phase-locked averaging interpretation of the Noca method for calculation of fluid forces on a body using velocity fields and their derivatives to successfully calculate the normal and tangential loads on the blades for 6 azimuth positions. A comparison of strain gage data collected on the struts of the turbine, matches well with the PIV and all model predictions for the 0° pitch case. The measurements highlight the effect of dynamic stall on the loading profile of the VAWT in both the upwind and downwind sections of the rotation, depending on the pitch angle. The simulations had difficulty capturing the loads in the pitched cases where effects of dynamic stall are most pronounced. It is probable that the fault largely lies with the calculation of the airfoil polar with a relatively thick airfoil at a low Reynold’s number. The measurements show, prior to stall, the load is shifted upwind with increasing pitch angle as to be expected, however once the airfoil enters stall, this increased load vanishes resulting in loss of thrust. The effects of stall in the upwind section of rotation cause an increased wind velocity in the downwind section, leading to higher loading in the position directly downwind of the stall azimuth. For cases of negative pitch, which shifts the load to the downwind side, the upwind pass removes little energy from the flow, leading to a higher perceived angle of attack on the downwind pass. This causes the airfoil to enter deep stall and to experience a spike of loading later in the rotation when the flow reattaches. The presented data and comparisons give insight into the aerodynamic loading, tower shadow, and dynamic stall behavior of the VAWT in multiple pitch configurations.

Bottom Line:

- The simulation results discussed in chapter 3 are compared to experimental normal measurements using the Particle Image Velocity data presented in chapter 5 and the strain gage data from chapter 6 for pitch cases with $\beta = -5°, 0° and 5°$.
- PIV measurements and strain gage based measurements agree well for each pitch configuration, albeit with offsets for the extreme pitch configurations most likely due to three dimensional effects not captured by the planar PIV.
- Models agree well with both experimental datasets for $\beta = 0°$.
- The Actuator Cylinder model and the vortex based models generally agree with each other for each configuration.
- While the general trends and magnitude of the loading is captured well with the models (especially the 3D vortex based methods) the inability to properly capture dynamic stall behavior, exacerbated by the low Reynold's number operating range on the 21 % thick airfoils of the PitchVAWT, leads to a fundamental difficulty in predicting accurate loading of the VAWT to a fine precision.
- The comparison of C_T versus λ highlights the difficulty in capturing the loading at low Reynold's numbers and low tip speed ratios where high angles of attack are present. At higher tip speed ratios, the airfoil performance is better captured by the models, coming closer to the measured C_T values derived from the normal load strain gage measurements.

VI

Circulation Control with Variable Pitch for Wake Deflection

8

Thrust Variation for Wake Control of a VAWT: Simulation and Experiment

The aerodynamic loading of a VAWT varies with the azimuth position of the blades. The thrust of the VAWT can be estimated as a decomposition of the normal force on each of the blades. By varying the blade loading as a function of turbine azimuth, it is possible to vary the direction of the average thrust of the turbine. An experiment is performed using an active pitch controlled H-VAWT turbine in the Open Jet Facility at TU Delft demonstrating the ability to actively vary the rotor aerodynamic loading and as a result the average thrust vector. The experimental loading results are then compared with simulations performed with a three dimensional free wake vortex model. The effects of the active pitch variation on the loads experienced by the wind turbine and on the downwind evolution of the wake are studied using simulation results. By applying a sinusoidal pitch actuation with phase offsets, a directional change in the average thrust vector of over 78° was demonstrated experimentally. The results serve as a proof of concept for the active control of the thrust vector of the rotor of a VAWT for purposes such as wake steering.

Parts of this chapter have been published in ”Experimental Demonstration of Thrust Vectoring with a Vertical Axis Wind Turbine using Normal Load Measurements.”[17]

8.1. Introduction

The Vertical Axis Wind Turbine has been proposed as a potential solution for lowering the overall costs of turbine installations, especially in large floating offshore concepts[8,9]. This potential can be achieved through a lower center of gravity and a greater tolerance to platform motions than an equivalent horizontal axis machine. The cost of the platform system is related to the overturn moment of the turbine in crucial operational states. The largest contribution to this moment is the rotor thrust. It has been shown that the orientation of the thrust vector for a VAWT can be directed by varying the blade normal loads as a function of azimuth in specific ways[16]. The ability to change the thrust vector dynamically without having to yaw the machine may have many positive benefits in the field of wind farm control. The integrated thrust vector is a summation of blade loading acting over the rotation. The experienced loading of each blade is a function of both the incident resultant wind vector and the blade pitch orientation. Therefore it is conceivable to have a degree of control over the rotor averaged thrust vector by manipulating the blade pitch as a function of turbine azimuth, altering the axial and side thrust forces over the rotation.

A proof of concept for this capability is tested numerically and experimentally utilizing the PitchVAWT turbine described in detail in chapter 2. A series of sinusoidal variable pitch studies using phase offsets from the rotational position of the turbine are tested in the Open Jet Facility. The measured normal loading of the turbine in each pitch scenario is then compared to numerical simulations using the 2D Actuator Cylinder model and a 3D lifting line free wake vortex model as described in chapter 3. The results from the free wake vortex model are then used to extrapolate the turbine performance to the evolution of the wake downstream for a uniform inflow condition.

8.2. Methods

8.2.1. Pitch Schedule Definition

Before one can perform pitch optimization for a given integrated thrust vector or wake evolution, it is first necessary to demonstrate control authority of the blade pitch on the overall thrust of the turbine. The geometric angle of attack for the VAWT follows a sinusoidal pattern with respect to the azimuth position of the blades. As was discussed in chapter 3 for an inviscid turbine, adding a fixed pitch offset to the turbine shifts this entire curve up or down by the amount of the blade pitch. Effectively shifting the loading between the upwind and downwind blade passes. While there is a small shift in the cross-wind thrust component due to this shift, the thrust is still predominantly aligned with the oncoming flow. Shifting primarily the cross-flow thrust component requires altering the phase relationship between the blade loading and the azimuth position. A proposed way of achieving this is to add a sinusoidal pitch offset with a 90° phase shift leading and lagging the turbine rotation. An amplitude of 10° was chosen to be assuredly large enough to effect the turbine loading while remaining within the limits of the pitch capability for the PitchVAWT turbine as discussed in chapter 2.5.2. Equation 8.1 is used to define blade pitch as a function of azimuth angle θ, phase offset ϕ, and a fixed pitch offset β_0. For this study, β_0 is kept at a constant 0°.

$$\beta = A\sin(\theta + \phi) + \beta_0 \tag{8.1}$$

Figure 8.1 gives a representation of the applied pitch as the rotor revolves for each case. The thicker black line represents the zero pitch point. As shown, the $\beta = 10^\circ\sin(\theta + 90^\circ)$ or ”leading” case, will tend to increase the angle of attack in the region from $\theta =$ 270°to90°, with the blade advancing toward the flow, and decrease the angle of attack on the other side, with the blade retreating from the flow direction. The $\beta = 10^\circ\sin(\theta - 90^\circ)$ would have the opposite effect on the experienced angle of attack.

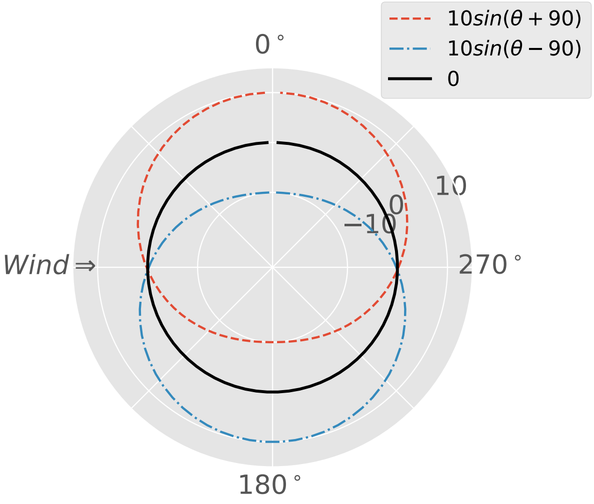

Figure 8.1: Pitch setting with respect to azimuth position for each pitch case with $\beta = 0$ for the baseline.

8.2.2. Simulations

Simulations matching the experimental conditions were calculated with the two-dimensional Actuator Cylinder Model and the three-dimensional free wake vortex lifting line models as discussed in detail in chapter 3. As many characteristics as possible were held constant between each model. Each model was broken into 72 azimuthal steps per rotation, coincident with an azimuthal resolution of 5°. The airfoil polar was calculated at a Reynold’s number of 9×10^4 with a virtual camber transformation to capture the effect of flow curvature as described in detail in section 3.4. A Beddoes-Leishman unsteady aerodynamics and dynamic stall model was implemented for both the 2D AC model and the 3D free wake vortex model. For the vortex model specifically, each blade was divided into 11 elements sinusoidally distributed across the blade height. The vortex model for each case was run for 25 rotations to ensure a fully developed wake, as checked by a converging average power coefficient to within 0.001.

8.2.3. Experimental Setup

Experimental data for the comparison of the sinusoidal pitch offsets was collected in the Open Jet Facility with the PitchVAWT turbine. The 2-bladed H-type VAWT has a diameter of 1.48 m, a height of 1.5 m. A chord length of 0.075 m is constant over the height for each blade. The pitch of each blade is actively controlled independently using a pair of DC motors. All details of the turbine and performance can be seen in the full turbine design which is described in detail in chapter 2.

The sensors used to measure the normal force on the blades and rotor position, used in this analysis are described in chapter 6. A greater detailed breakdown of each turbine sensor is provided in appendix B. The integrated turbine thrust is calculated from the normal load measured on the turbine as a function of azimuth position. This assumption ignores any contribution to the thrust force from the tangential component of the blade loads. The effect of this is relatively small, however it is present, and is discussed in detail in section 6.2.3.

For all normal force data presented in this thesis the measured loads are separated into 180 2° azimuthal bins where the mean and standard deviation of the bin are calculated. The mean of each bin is then plotted with the shaded region around each line showing $\pm\sigma$ or one standard deviation of the measurement bin. The estimation of normal load for fixed pitch cases using strain gages mounted on the struts has been validated using loads calculated from Particle Image Velocity measurements as given in chapters 5 and 7. All testing is performed at a tip speed ratio of $\lambda = 4$ and a free-stream wind speed of $U_\infty = 4\,\mathrm{m\,s^{-1}}$.

8.3. Results and Discussion

The experimental results for each pitch case are presented first showing the effect of the pitch with phase offsets. These are followed by the comparison of the experimental data with the results of the two simulations. Lastly, the predicted wake evolution from the 3D free wake vortex model are compared to show the effect of the shifting thrust vector from each pitch case.

The blade loads discussed herein are non-dimensionalized by $\frac{1}{2}\rho\lambda^2 U_\infty^2 hc$. In the experiment as well as the simulations, two types of normal load are presented. For the case of both the Actuator Cylinder model and the loads estimated from Particle Image Velocimetry, the techniques are two dimensional in nature at the mid-plane of the rotor. For the experimental data measured using strain gages on the strut and for the lifting line vortex model, the full blade load is measured or calculated, respectively. In order to compare these measurements directly, the strain gage derived loads and the lifting line model loads have been non-dimensionalized by the height of the turbine, or 1.508 m. These loads will inherently have effects such as tip-loss from 3D behavior which is not present in the inherently two dimensional models.

8.3.1. Experimental Results

The most direct measurement of the blade load available on the PitchVAWT turbine is the normal force measured on the struts. The overlay of each normal load distribution versus the azimuth position of the turbine is given in figure 8.2. The drop-outs in data from the strain gage measurements are from an abundance of caution due to potential slip-ring effects as noted in section B.4.2. The baseline of $\beta = 0$ case is shown as a control with the solid black curve. Due to the addition of the sinusoidal blade pitch with the phase offsets the normal loads for each case have been shifted with respect to the azimuth position of the rotor. The $10^{\circ}\sin(\theta + 90^{\circ})$ pitch setting causes the peak load to occur earlier in the rotation as the positive pitch setting adds to the increasing angle of attack as the blade enters the upwind rotor position. The $10^{\circ}\sin(\theta - 90^{\circ})$ pitch follows behind the $\beta = 0°$ load case as the pitching causes the maximum load to occur later in the rotation. The loads are rotated into X and Y components from the normal load and plotted in figure 8.3. For this comparison, the expected total thrust load is plotted. This is calculated by sampling the normal loading measured by blade 1 as it would be experienced by blade 2 operating 180° out of phase. This assumes that blade 1 and blade 2 are exactly the same in performance. The procedure is described in more detail in section B.5. The peaks in the X direction are offset in azimuth position as expected. Although the vertical shift in the Y direction shows the effect of offsetting the pitch phase the clearest.

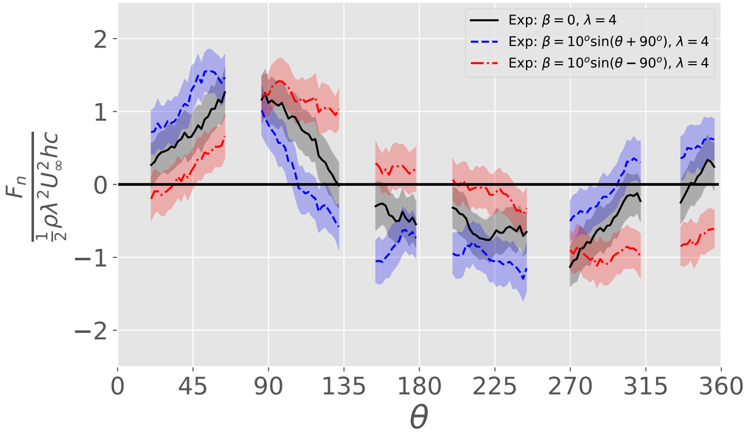

Figure 8.2: F_n vs θ phased sinusoidal pitch input and zero pitch response from strain gage data.

Figures, 8.4a, and 8.4b show a polar plot of the normal force coefficient with respect to azimuth position of the blade for each pitch scheme. The oncoming wind is from the 90° position as depicted in the figures. The integrated magnitude and direction of the normal force is given as an arrow from the origin of each polar plot. As shown, the integrated thrust vector changes substantially from the zero pitch response position by the inclusion of both phases for sinusoidal pitch actions showing a swing of 78.9°.

A summary of the turbine thrust loading is given in table 8.1. The direction vector given is in the coordinate system of the turbine, in the direction of the thrust

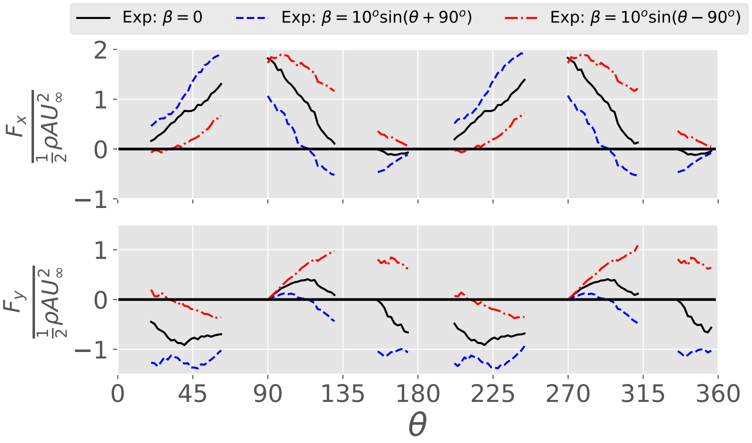

Figure 8.3: Total X and Y load computed from normal measurement

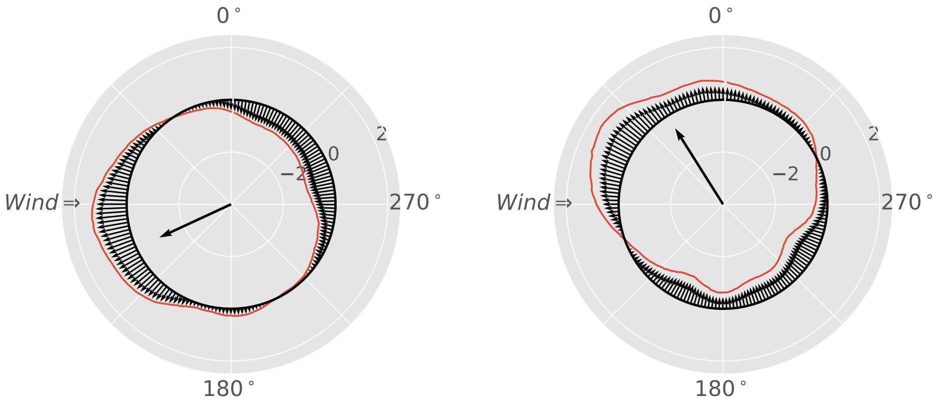

(a) $\beta = 10°sin(\theta - 90°)$ (b) $\beta = 10°sin(\theta + 90°)$

Figure 8.4: Comparison of experimental integrated thrust vectors for sinusoidal pitch offsets leading and lagging the azimuthal position.

load onto the flow. With the wind coming out of the 90° azimuth position, the zero pitch thrust response has an offset of about 18° this is most likely due to viscous airfoil effects and the large change in Reynolds number between the upwind and downwind passes. There is also a strong likelihood of unsteady effects and dynamic stall happening after the 90° position. The angular change in thrust position can be seen with a shift from this 72° zero pitch response to 117° with the lagging pitch and 38° with leading pitch. The swing represents a change of 78°. The overall magnitude of the thrust vector increased for both the pitching conditions suggesting there is a price to pay in blade and thrust loading for deflecting the thrust from the zero pitch position. A study of closed loop control of blade pitch for the purpose of directing this thrust vector would have significant benefits in limiting loading not directly contributing either to power generation or deflecting the wake.

Table 8.1: Summary of experimental turbine thrust computed from normal force measurements on PitchVAWT

β	C_{T_X}	C_{T_Y}	**Mag**	**Dir**
0	0.73	0.24	0.76	71.8°
$10^{\circ} sin(\theta + 90^{\circ})$	0.54	0.70	0.88	37.7°
$10^{\circ} sin(\theta - 90^{\circ})$	0.76	−0.38	0.85	116.6°

8.3.2. Simulation Results

Results of the simulations conducted with both the AC flow model and the 3D free wake vortex model compare favorably with the acquired experimental results. The simulated data for each pitch case are compared with the experimental results presented above in figure 8.5. The $\beta = 0°$ case presented in figure 8.5b overlays the measured and predicted results for the baseline case. Data was collected experimentally using both the strain gage measurements over the whole azimuth and estimated at 6 azimuthal locations with loads derived from PIV as described in section 5.2.3. As discussed in detail in chapter 7 the fixed pitch data compares favorably between these experiments, and all simulations presented. The magnitude of the loading in both the upwind and downwind positions is captured fairly well by each model. The load from the strain gage drops off significantly faster after $\theta = 110°$ most likely due to lower Reynold's number effects altering the flow of the airfoil in higher angles of attack which are not easily captured in the models.

For each of the dynamic pitch cases, the overall shift in azimuth of the loading is captured, however, some differences in the response can be seen between the experiment and the models. For the case of the leading pitch phase offset in figure 8.5a both models predict a much higher normal force than is measured in the experimental data. The higher normal loads are never quite reached in the measurement. A spike in load from the experiment is seen between 45° to 90° as would be expected during a dynamic stall condition. With the load then reducing in the same range as was seen for the $\beta = 0°$ scenario. However, by the downwind half of the rotor after $\theta = 270°$ both models match the experimental loads. The lagging pitch case shown in figure 8.5c has excellent agreement between $\theta = 45°$ and $\theta = 300°$, where both models do a much better job of tracking the loading compared to the leading pitch case. After $\theta = 300°$ the experimental airfoil loses lift where the models predict an increasingly negative load. This is most likely due to the inability of capturing the dynamic stall onset properly in the low Reynold's number flow of the relatively thick airfoil.

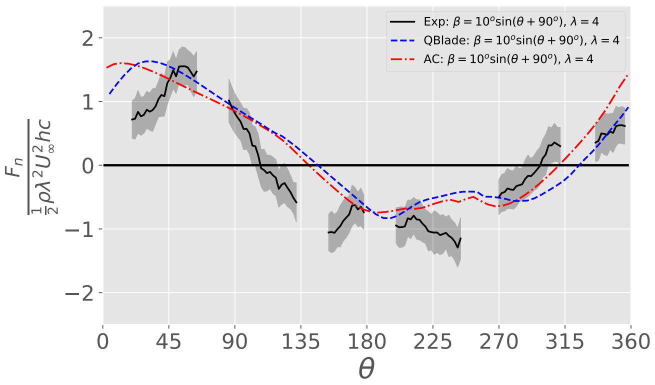

(a) $\beta = 10° \sin(\theta + 90°)$

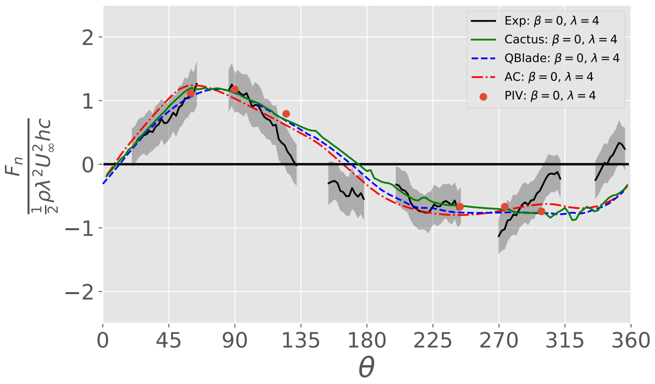

(b) $\beta = 0$

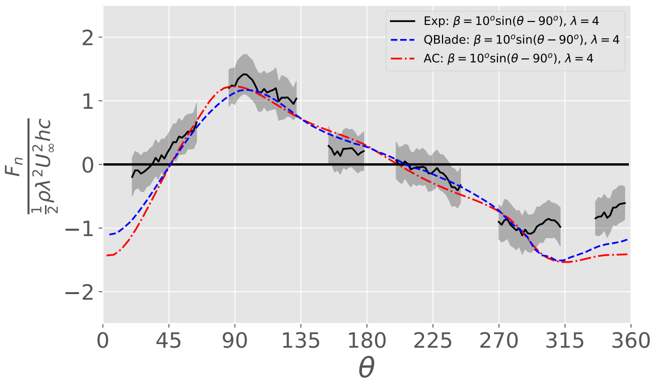

(c) $\beta = 10° \sin(\theta - 90°)$

Figure 8.5: Direct comparison of simulated normal force and measured normal force for sinusoidal pitch cases $\lambda = 4$, $U_\infty = 4$, shaded region represents $\pm\sigma$ of measurement bin.

8.3.3. Wake Evolution

The wake for each case is simulated using the three-dimensional lifting line free-wake vortex model. Wind velocities were calculated along five planes within the flow field of each simulation; A XY-plane at the mid-plane of the rotor, and YZ-planes at four downstream locations corresponding to 1D, 2D, 3D, and 5D in order to show the three dimensional evolution of the wake. All of the models are run at the same tip speed ratio and the same free-stream wind speed. Due to the variable nature of the loading between cases, the axial turbine thrust is not held constant. This trade-off is to remain consistent with the measurements of the PitchVAWT turbine in the wind tunnel. However, it limits a rigorous comparison of wake deflection versus thrust and turbine power. This is considered outside the scope of the presented work. The goal was to demonstrate the control authority of the integrated thrust direction, not to optimize for specific wake deviation.

The top-down view of the rotor mid-plane shows the evolution of the wake for each pitch case. The axial velocity U_X is given in figure 8.6 and the transverse velocity for each case is shown in figure 8.7. The $\beta = 0°$ wake as shown in figure 8.6a is a typical wake for the H-VAWT with a fairly symmetrical wake expansion aft of the rotor, followed by a contraction in the mid plane and a breaking down after about 5 rotor diameters, $\frac{x}{R} = 10$. The phase shifted pitch cases show a quite different result with the off-axis thrust component causing the wake to deviate side to side. As shown by the red color just above the rotor in figure 8.6b and just below the rotor in figure 8.6c the flow accelerates in order to compensate for the rotor blockage effect, but also as a consequence of the added cross flow term from the rotor pitching, leading to the wake deviation. The transverse velocity, V_Y plotted in figure 8.7a where $\beta = 0°$ shows the expansion and contraction of the wake further down stream, yet the response is symmetric. The phased pitching shown in figures 8.7b and 8.7c demonstrate the consistent transverse velocities to the negative and positive Y direction, respectively.

The evolution of the wake for the VAWT is predominately a three dimensional effect, as has been demonstrated by De Tavernier and others previously[11,12,96]. For a H-VAWT turbine with a square cross-sectional area in uniform flow the wake first expands horizontally and then vertically as counter-rotating vortices begin to interact. Eventually diffusing outward and breaking down. This is demonstrated for the baseline $\beta = 0°$ wake in figure 8.8 shown at four wake cross-sections. There are no ground effects modeled, and the rotor vertical position ranges from $\frac{z}{R} = 1.3 to 3.3$.

The additional transverse force added to the flow due to the sinusoidal pitching acts much like a lift device causing a ”down wash”, but in this case in the transverse direction, with counter rotating tip vortices. This is shown in figures 8.9 and 8.10 as the wake evolves downstream. In both cases the wake is moved from the centerline. Due to the effects of dynamic stall and changing overall thrust load between the pitch cases, the wakes are not expected to be inverses of each other. At a downstream position of 5D the wake of the $\beta = 10° \sin(\theta + 90°)$ case has been offset by approximately half a radius. The $\beta = 10° \sin(\theta - 90°)$ case at the same downwind distance of 5D, has a more coherent wake still with a side translation

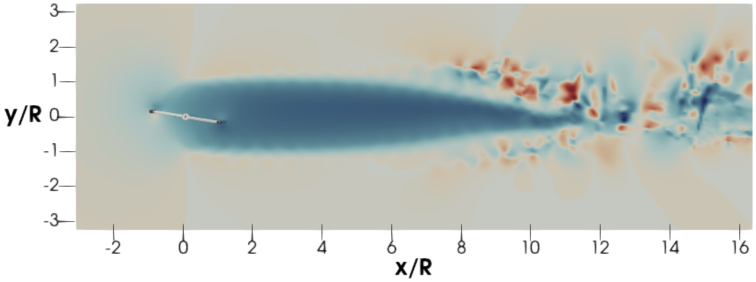

(a) $\beta = 0°$

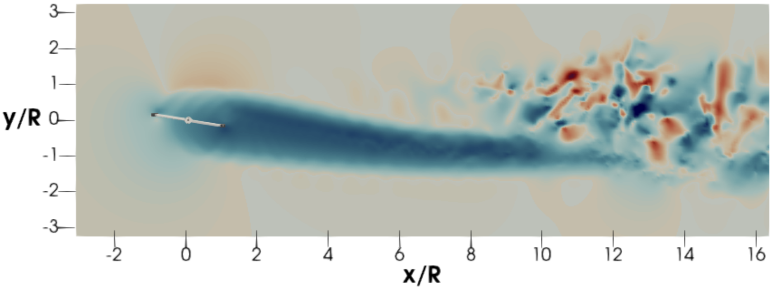

(b) $\beta = 10° \sin(\theta + 90°)$

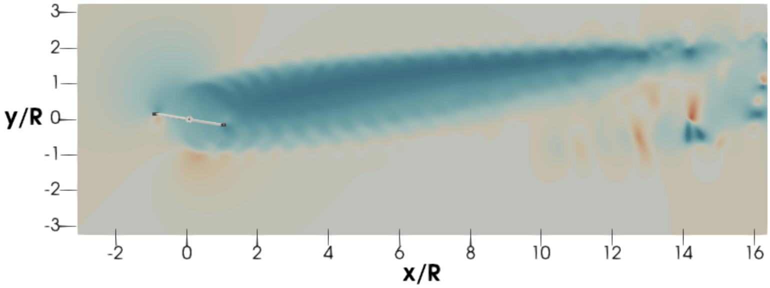

(c) $\beta = 10° \sin(\theta - 90°)$

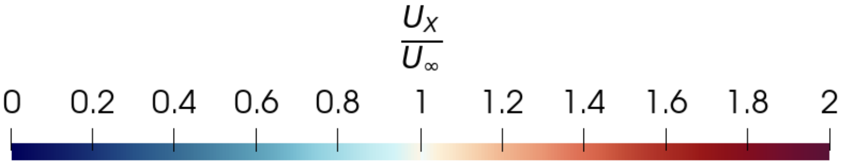

Figure 8.6: Wake development behind PitchVAWT showing axial wind speed U_X as modeled using 3D lifting line model. $\lambda = 4$, $U_\infty = 4\,\mathrm{m\,s^{-1}}$

of a full rotor radius. This is most likely due to the varying axial thrust coefficient between the cases.

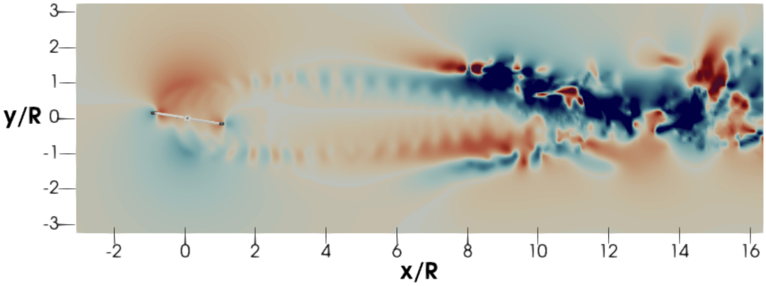

(a) $\beta = 0°$

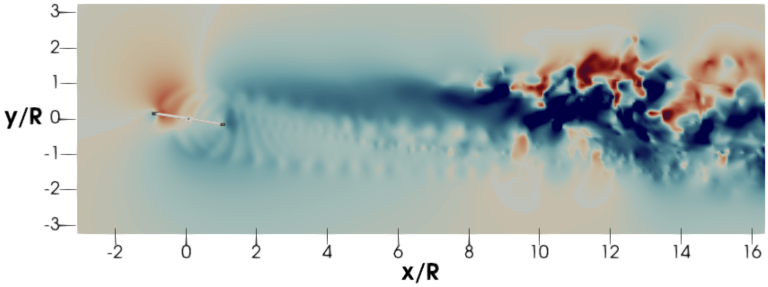

(b) $\beta = 10° \sin(\theta + 90°)$

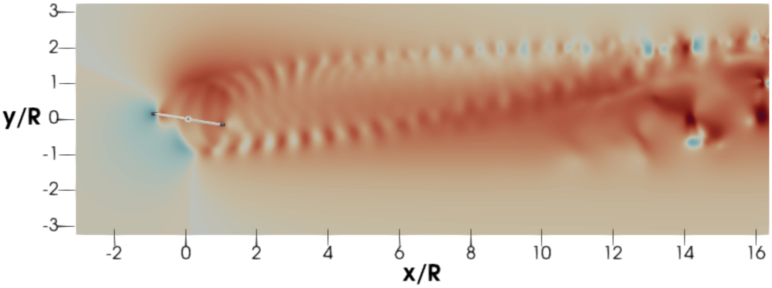

(c) $\beta = 10° \sin(\theta - 90°)$

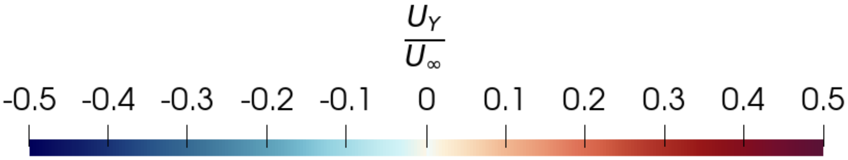

Figure 8.7: Wake development behind PitchVAWT showing transverse wind speed U_Y as modeled using 3D lifting line model. $\lambda = 4$, $U_\infty = 4\,\mathrm{m\,s^{-1}}$

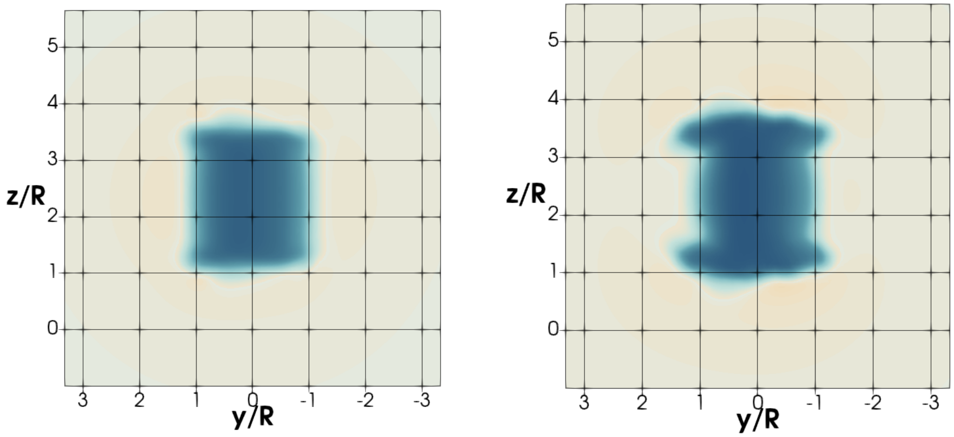

(a) 1D

(b) 2D

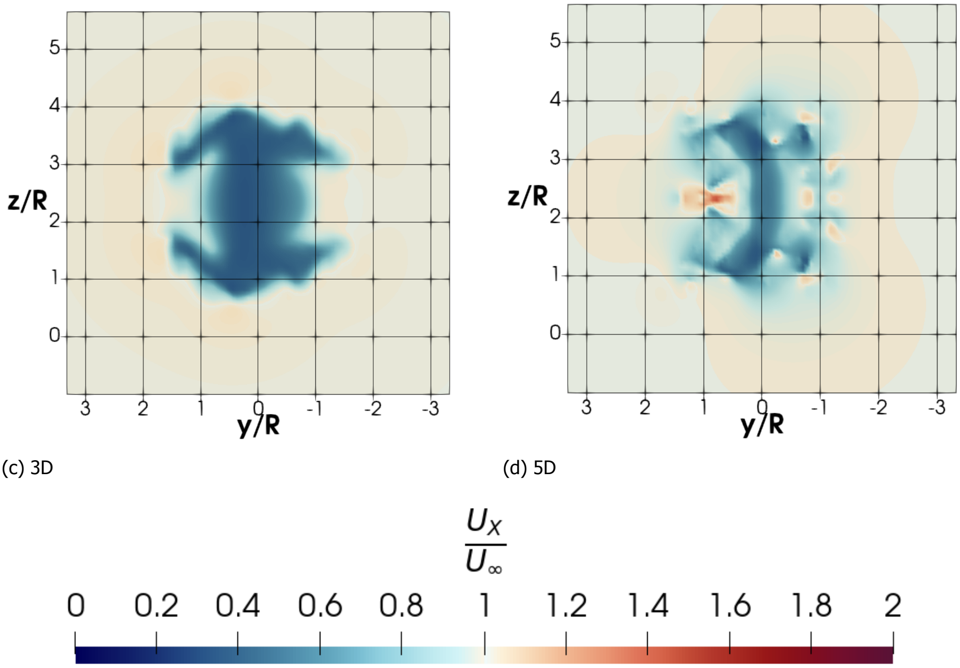

(c) 3D

(d) 5D

Figure 8.8: Wake evolution at four downstream positions, (a) 1D (b) 2D (c) 3D (d) 5D $\beta = 0$, $\lambda = 4$, $U_\infty = 4$

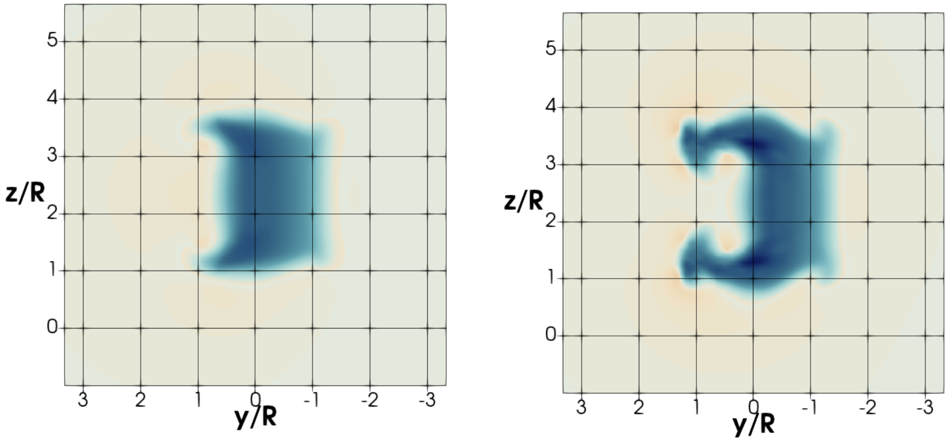

(a) 1D

(b) 2D

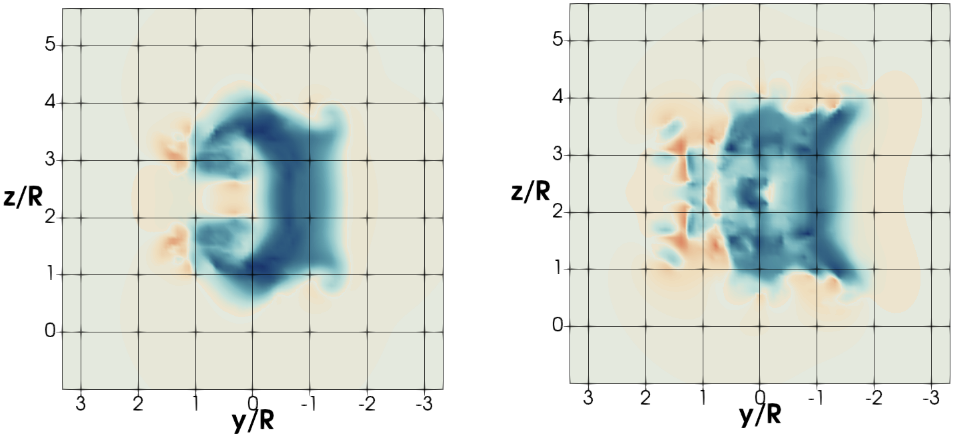

(c) 3D

(d) 5D

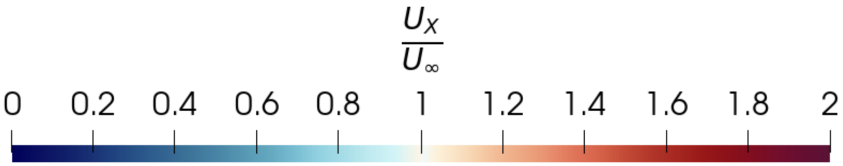

Figure 8.9: Wake evolution at four downstream positions, (a) 1D (b) 2D (c) 3D (d) 5D $\beta = 10° \sin(\theta + 90°)$, $\lambda = 4$, $U_\infty = 4$

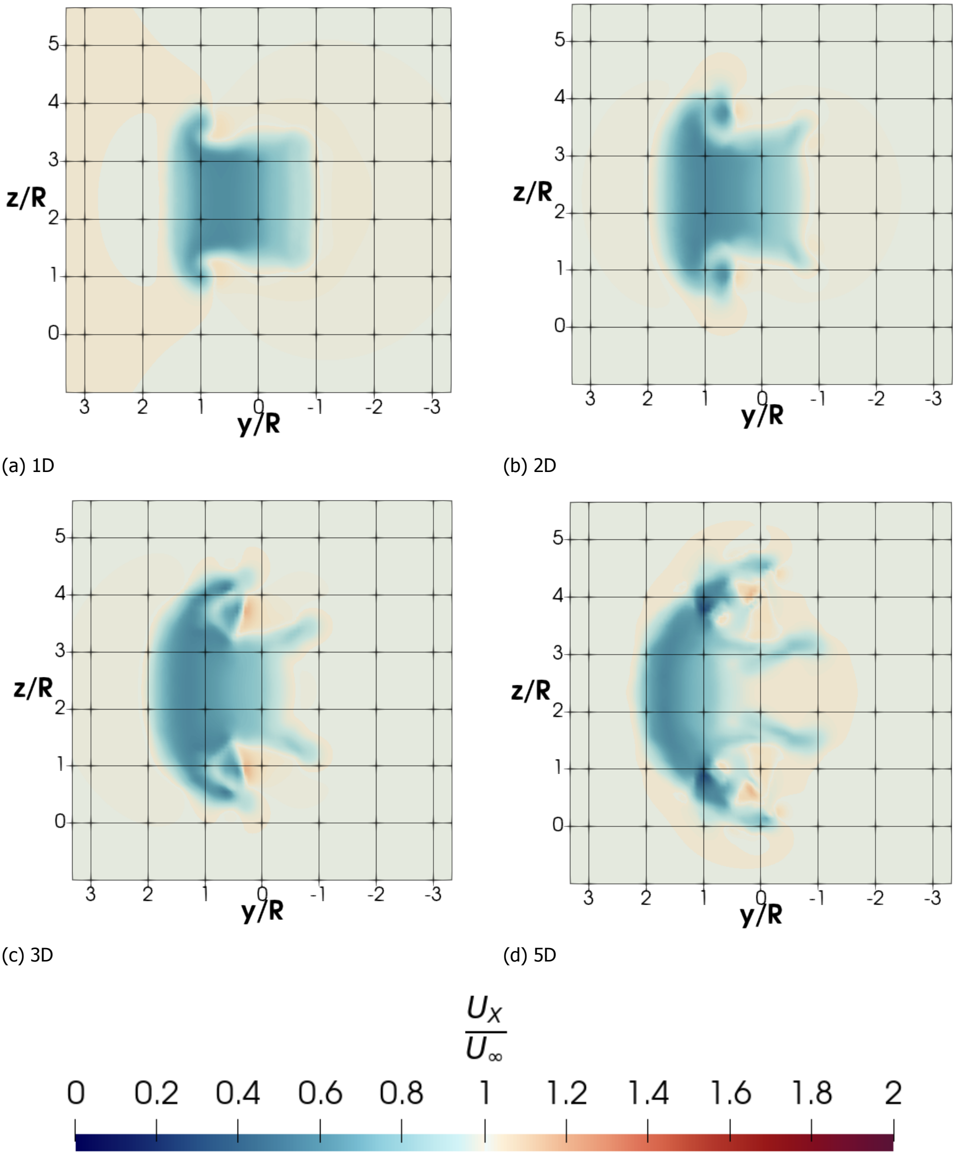

(a) 1D

(b) 2D

(c) 3D

(d) 5D

Figure 8.10: Wake evolution at four downstream positions, (a) 1D (b) 2D (c) 3D (d) 5D $\beta = 10° \sin(\theta - 90°)$, $\lambda = 4$, $U_\infty = 4$

8.4. Conclusion

A test case was put forward to vary the thrust direction of the integrated blade loads for a Vertical Axis Wind Turbine using sinusoidal blade pitch with phase offsets from the azimuth position. Simulations and testing of this phenomena were conducted on a two-bladed H-VAWT wind turbine with actively controlled variable pitch in order to demonstrate the control authority for varying the thrust vector with turbine pitch. Predetermined sinusoidal pitch schedules of $10^{\circ} sin(\theta \pm 90^{\circ})$ were prescribed to the turbine while operating at a tip speed ratio of $\lambda = 4$. The normal force of the turbine was measured and used to determine an approximation of the overall aerodynamic thrust in X and Y directions of the turbine. The overall magnitude of the thrust vector increased from the zero pitch performance while the direction of the thrust was altered by up to 78° in experimental testing. Simulation of the active pitch cases matched the general performance of the experimental turbine fairly accurately. However, limitations exist in the region of higher angles of attack in predicting dynamic stall impacting the overall agreement with the models on the airfoil scale. The three dimensional free-wake vortex model simulations show the wake development of the VAWT is dependent upon the rotor averaged thrust loading. The introduction of a transverse loading component causes the rotor itself to act like a lifting body, causing a side-side ”down-wash” effect leading to counter-rotating vortices at the bottom and top of the rotor. This effect causes the wake to translate in the direction of the cross-flow term of the integrated transverse loading vector. These results are considered a proof of concept for the ability to control the wake of a variable pitch VAWT. Exact power and load trade-off studies should be completed with a more detailed and optimized pitch control system to minimize effects such as deep stall or excessive loading which does not contribute either to turbine power extraction or to deflection of the wake.

Bottom Line:

- A test case was put forward to vary the thrust direction of the integrated blade loads for a Vertical Axis Wind Turbine using sinusoidal blade pitch with phase offsets from the azimuth position.
- This case was simulated with each of the aerodynamic models discussed in chapter 3 and then tested in the Open Jet Facility at TU Delft with the PitchVAWT platform.
- The models are able to capture the normal loading of the turbine well when compared to strain gage measurements on the struts of the PitchVAWT in spite of the already documented difficulties of predicting the low Reynold's number behavior of the thick airfoils.
- Extrapolating the normal loading behavior of the blades validated by the strain gage measurements on the turbine with 3D Lifting line free wake vortex models allows a prediction of the resultant turbine wake
- The variation in thrust direction causes the wake to deflect in the opposite direction of the thrust vector, as is expected from previous work on Horizontal Axis Wind Turbine wake steering.
- The concept of using active blade pitch to control the integrated rotor thrust magnitude and direction is shown to be feasible and worthy of a more dedicated controls based study.

VII

Conclusions

9

Conclusions and Future Research

The research presented in this thesis was guided by three major research questions: What are the dynamic characteristics of the load experienced by a VAWT? Are current engineering models capable of capturing the experienced dynamics? Can the wake of a VAWT be actively controlled by altering blade loading over a rotation? This final chapter will briefly summarize the work performed, review the key results in light of these research questions, and present several areas in which the research may be expanded in the future.

9.1. Summary and Conclusions

This thesis was presented in five main sections. The first being the design and fabrication of a new two bladed Vertical Axis Wind Turbine with individual active blade pitch capability referred to as PitchVAWT where the detailed aerodynamic and structural designs for the turbine were described. The following section discussed the simulation of the turbine along with the theory and methods behind the tools used in the analyses. The third section discussed in detail a set of experimental campaigns testing the structural response and aerodynamic performance of the wind turbine when in operation for a range of tip speed ratios and blade pitch configurations. The next section discusses the validation of the turbine simulations using the experimental campaigns by focusing on the normal load predictions of the models and the measured response using particle image velocimetry and strain gage based structural measurements. In the final section, a proof of concept demonstration is given of open-loop wake control for a vertical axis wind turbine by use of continuously variable blade pitch.

9.1.1. Turbine Design

There are several difficulties which are encountered in the design of a vertical axis wind turbine, especially one with only two blades. This stems from the large periodic variation in thrust load from twice the nominal value to zero at a frequency twice that of rotation. This along with the side-side thrust load variation leads to the excitation of several vibration modes which were in the frequency range of interest due to flexibility of the support platform, as discussed in detail in chapter 4. This fact happened to limit the operational regime of the turbine within the Open Jet Facility at TU Delft, forcing a limitation to wind speed in order to reach desired tip speed ratio values. Nevertheless, a turbine capable of performing fully active variable pitch, with a rotor solidity on par with expected large offshore machines, and operating at typical tip speed ratios of around 4 was successfully designed and fabricated.

9.1.2. Simulation

Aerodynamic Tools

- Aerodynamic modeling tools used within this thesis included the two-dimensional linearized Actuator Cylinder flow model, a two dimensional inviscid free wake vortex panel code (U2DIVA), and two independent three-dimensional lifting line free wake vortex models, one from TU Berlin (Q-Blade), and the other from Sandia National Laboratories (CACTUS). Derivations for the Actuator Cylinder model along with a Beddoes Leishman dynamic stall model were given.

- Predicted aerodynamic performance for fixed pitch configurations with various offsets were compared between the models generally showing good agreement in predicted angle of attack and normal force distribution.

- Wake development was studied with the free-wake vortex methods in two and three-dimensional models. The changing circulation distribution brought on by changing pitch offsets lead to varying wake evolution shown in the three-dimensional models. These variations are not visible with two dimensional models that assume an infinite length blade.

- One of the inherent drawbacks of testing at a reduced size scale is dealing with low Reynold's number flow regimes. The local chord-Reynold's number varies greatly over the blade, causing potentially differing stall characteristics and lift slopes for upwind, downwind, leeward, and windward positions over the azimuth. In most cases these deviations are ignored, choosing a representative airfoil polar.

Structural / Multibody Dynamics

- Siemens Simcenter3D was used to develop detailed finite element models of each structural component of the wind turbine. Each of these components were individually experimentally verified for material properties and stiffness characteristics using a combination of density measurements and experimental modal analysis. These components were then assembled into an overall finite element model for the PitchVAWT turbine including the platform. Experimental modal analysis for the full turbine system validated the behavior of the model and was used to optimize the stiffness of ground springs and dampers for the system.

- A modal-based multibody dynamics model was assembled from the individually validated structural components and coupled to the output of the aerodynamic simulations to predict the full turbine and platform dynamic loading.

- Flexible platform dynamics had a large influence on the mode shapes and frequencies of the combined system, leading to a large number of frequency crossings within the range of operation as exhibited with a Campbell Diagram. In particular the excitation of a backwards tower whirling mode was evident in multibody simulations when coupled to the aerodynamic loads output from simulation.

- Inclusion of flexibility in the multibody dynamics model greatly increases reaction loads due to response of the inertial structural motion. Therefore rigid aerodynamic analysis is insufficient for determination of structural loading phenomena.

9.1.3. Experimentation

Particle Image Velocimetry

- An experimental campaign was performed in the Open Jet Facility at TU Delft operating the PitchVAWT Turbine at a tip speed ratio of 4 with a mean wind of $4\,\mathrm{m\,s^{-1}}$. Particle Image Velocimetry with a pair of synchronized lasers was used to capture two-dimensional velocity fields at mid-span of the rotor surrounding the operating blades at 18 azimuthal positions.

- The measured velocity fields capture the presence of tower shadow and blade vortex interaction for all pitch configurations on the downwind half of the rotation.

- A phase-locked averaging interpretation of the Noca method for calculation of fluid forces on a body using velocity fields and their derivatives was used to successfully calculate the normal and tangential loads on the blades for six positions around the azimuth of rotation, for each pitch configuration.

- Shifting of the blade pitch positive or negative corresponds to shifting the load between upwind and downwind locations respectively prior to the onset of dynamic stall.

- Blade stall in the upwind section of the rotation results in a lower induction over the upwind half, thereby contributing to a higher velocity on the downwind half of the rotation. This would lead to a lower local tip speed ratio, higher angle of attack, and deeper stall in the downwind half, which is indeed observed.

- Normal and tangential loading calculated from the velocity fields demonstrates the harsh effect of dynamic stall in both the upwind and downwind portions of the rotation, depending on the pitch configuration. These loads lead to less rotor efficiency and much higher fatigue loading cycles for the VAWT.

Strain Gage Measurements

- A technique for measuring the normal loading of the PitchVAWT turbine based on axial strain gage measurements on struts of the turbine was presented. Experimental data was collected in increments of 1° pitch from $\mathrm{B} = -5° to 5°$, overlapping with the data collected from particle image velocimetry. Higher resolution of these data in both azimuthal position and pitch offset confirms the trends witnessed with PIV.

- In general, the loading in the upwind half of the rotation is fairly smooth indicating the expected clean inflow behavior, while the downwind pass for each pitch condition is considerably more variable, showing potential behavior of blade vortex interaction and tower shadow.

- Shifting pitch effects the dynamic stall experienced by the machine changing the azimuth position of onset and the depth of the stall.

- The changing load profiles effect the integrated thrust experienced by the machine, changing both the axial and cross-flow terms of the thrust.

- Frequency response of both the normal load on the blades and platform accelerations show higher per rev load excitation when dynamic stall is present.

9.1.4. Model Validation

- The simulation results discussed in chapter 3 are compared to experimental normal measurements using the Particle Image Velocity data presented in chapter 5 and the strain gage data from chapter 6 for pitch cases with $\beta = -5°, 0° and 5°$.

- PIV measurements and strain gage based measurements agree well for each pitch configuration, albeit with offsets for the extreme pitch configurations most likely due to three dimensional effects not captured by the planar PIV taken at mid-span.

- Models agree well with both experimental datasets for zero pitch, $\beta = 0°$.

- The Actuator Cylinder model and the vortex based models generally agree with each other for each configuration.

- While the general trends and magnitude of the loading is captured well with the models (especially the 3D vortex based methods) the inability to properly capture dynamic stall behavior, exacerbated by the low Reynold's number operating range on the 21 % thick airfoils of the PitchVAWT, leads to a fundamental difficulty in predicting accurate loading of the VAWT to a fine precision.

- The comparison of C_T versus λ highlights the difficulty in capturing the loading at low Reynold's numbers and low tip speed ratios where high angles of attack are present. At higher tip speed ratios, the airfoil performance is better captured by the models, coming closer to the measured C_T values derived from the normal load strain gage measurements.

9.1.5. Circulation Control for Wake Deflection

- A test case was put forward to vary the thrust direction of the integrated blade loads for a Vertical Axis Wind Turbine using sinusoidal blade pitch with phase offsets from the azimuth position.
- This case was simulated with each of the aerodynamic models discussed in chapter 3 and then tested in the Open Jet Facility at TU Delft with the PitchVAWT platform.
- The models are able to capture the normal loading of the turbine well when compared to strain gage measurements on the struts of the PitchVAWT in spite of the already documented difficulties of predicting the low Reynold's number behavior of the thick airfoils.
- Extrapolating the normal loading behavior of the blades validated by the strain gage measurements on the turbine with 3D Lifting line free wake vortex models allows a prediction of the resultant turbine wake
- The variation in thrust direction causes the wake to deflect in the direction of the cross flow component of the thrust vector, as is expected from previous work on Horizontal Axis Wind Turbine wake steering.
- The concept of using active blade pitch to control the integrated rotor thrust magnitude and direction is shown to be feasible and worthy of a more dedicated controls based study.

9.2. Discussion of the Research Questions

Following the statement of the key findings from the research, the original research questions are revisited.

What are the dynamic characteristics of the load experienced by the VAWT?
This question is addressed in detail with chapter 4 of modeling the structural dynamic response of the PitchVAWT, and in chapter 6 with the experimental measurement of blade loading and platform dynamic response for multiple pitch configurations and tip speed ratios. The governing dynamic characteristics of the VAWT stem mainly from the oscillatory nature of the aerodynamic loading. Beginning with the pressure and suction sides of the blades alternating once every rotation, this load is transferred to the support structure with large temporal variability of the turbine thrust acting at varying azimuth angles. This leads to complex bearing and support structure design requirements. As a first order estimation for turbine

loading, these have been previously modeled. However, several second order dynamic loads have been highlighted in this research which have could have large consequences for turbine fatigue design calculations. Namely the extent to which blade vortex interaction, tower shadow, and the difficulties of capturing temporal dynamic stall loading information affect both the temporal and azimuthally averaged thrust dynamics. It was also shown that in operation where dynamic stall is present, higher per rev frequencies were excited, perhaps leading to consequences in turbine blade, support structure, and controller designs.

Are current engineering models capable of capturing the experienced dynamics? As demonstrated in chapter 7, all of the models are able to capture the global first order behavior of the blade loading. However, the dynamics associated with higher frequency phenomena such as blade vortex interaction, and tower shadow are not captured by this implementation of the 2D actuator cylinder engineering level model. These may excite higher order modes within structural design and could be of high importance when studying system level interactions, for instance with platform or mooring structures. A level of Vortex based model or CFD may be required in order to capture these. Three dimensional effects of stalled blades were not captured well by the two dimensional AC model. Three dimensional versions of this flow model were not implemented at the time of this thesis, but may better track these effects.

Can the wake of a VAWT be actively controlled by altering blade loading over a rotation? As demonstrated in chapter 8, three dimensional free wake vortex models were used in conjunction with active variable pitching of the blades to vary the direction of the integrated thrust vector of the PitchVAWT. The azimuthally varying normal load for both fixed and variable pitch was validated against wind tunnel measurements on the PitchVAWT. In said models, the variation in thrust direction causes the wake to deflect in the direction of the load being imparted on the fluid, as is to be expected. Given the magnitude and direction of the applied thrust vector can be actively controlled using the blade pitch, it is considered feasible to in turn control the evolution of the turbine wake.

9.3. Recommendations

9.3.1. PitchVAWT Improvements

There are a few improvements which if made to the PitchVAWT Turbine will improve the quality of the data and expand the operating region to allow for higher wind speeds, improving signal to noise ratio.

The first would be to modify the mounting structure within the tunnel. Currently the blue lift platform used for mounting the turbine has a major side-side vibration mode at 5 Hz which directly influences the turbine dynamics leading to resonances with the machine limiting the possible wind speed. It is possible to either create a new stiffer dedicated platform, or to modify the current one to move this side-side platform frequency away from the operating range of the turbine.

The next update for the turbine would be to the instrumentation package. Currently the normal load measurements are extrapolated from measuring the strain on a single strut through a set of slip rings. This leads to drop outs in data where the slip ring is accumulating damage, and potential uncertainties due to the assumptions made in the method. While it is believed that these assumptions are valid, including additional strain measurements on each strut would cut down on any sources of uncertainty in the measurements. A wireless system which communicates with the rotor to read in sensor data from the strain gages and pitch response would eliminate any uncertainties due to the raw data connection over the slip ring.

9.3.2. VAWT Research Direction

A major area of concern when it comes to vertical axis wind turbines at large scales are the aeroelastic effects of the oscillating blade loads. This comes down to having fundamental knowledge in two distinct areas, and the design tools adequate to address them in a fast iteration environment. I believe the fundamental knowledge gaps for VAWTs at the moment are the non-linear aeroelastic response in blade deformation for calculation of loading and rotor performance (aero-elastic twist over the blades), and the calibration of dynamic stall models for use within VAWTs where the series of constants may need to vary depending upon the azimuth position of the rotor. For instance, where the shed vortices travel with the blade while moving leeward, and away from the blade while moving windward. Any serious effort at designing a large scale VAWT will require a design tool package capable of running coupled aerodynamic simulations on the order of tens of thousands per day. Requiring fast aerodynamic calculation, but including enough detail to simulate the system dynamics properly. As was shown in this thesis, that includes higher order phenomena such as blade vortex interaction, tower shadow, as well as structural base influences. These would need to be able to model sufficiently the floating platform dynamics as well as any interaction with the mooring system in a chaotic wind-wave scenario.

One of the potential advantages to moving toward a vertical axis configuration for floating offshore wind farms lies in the optimization of the full wind farm. The fact that VAWTs interact with their own wake on the downwind pass may cause the coherent wake structure to break down sooner in the wake evolution compared to the horizontal axis turbine. This would allow wind farm designers to place VAWTs closer in spatial distance to each other, reducing overall balance of plant costs. This would however require the creation and calibration of a reduced order wake model for VAWTs similar to what has been used in the horizontal wind turbine plant design which can be used in larger multidisciplinary optimization tools utilized by the industry.

Once the general benefits of VAWTs in wind farm arrays can be understood, the benefits of closed loop wake steering may be explored to greater effect. As was demonstrated in this thesis, it is feasible to direct the evolution of the wake using active blade pitching on the VAWT. This research can be furthered by using a closed loop controller monitoring the overall thrust direction of the turbine over a rotation to control the pitch of the blades. This would greatly improve the efficiency of the action compared to the blind open-loop prescribed pitch used within chapter 8 of this thesis. In addition to using active pitching on the blades to deflect the wake side to side, it is also possible to control the lift of the turbine struts to deflect the wake vertically, potentially pulling flow from above the turbines into the farm, re-energizing the wake much sooner and reducing farm losses.

9.4. Parting thought

The Vertical Axis Wind Turbine was introduced as a potential alternative energy source in the early 1970s. The concept had undergone a variety of early successes and failures prior to the dominance of the wind energy market by the three bladed upwind horizontal axis turbines commonplace today. With the new dawn of floating offshore wind, the vertical axis turbine has a potential market in which finally compete again and a slim chance to make a comeback in the future energy mix.

VIII

Appendices

A

Airfoil Trip Design

Design of Boundary Layer Transition Elements for Use in PitchVAWT Wind Tunnel Testing

Bruce LeBlanc[1]

[1]Wind Energy Research Group, Department of Aerospace Engineering, Delft
University of Technology, Kluyverweg 1, Delft, The Netherlands

March 2019

1 Introduction

Due to the low Reynold's numbers experienced during wind tunnel testing of the PitchVAWT turbine, large laminar separation occurs in much of the operating regime of the airfoil. This leads to high levels of drag, a relatively low stall angle, and most importantly, difficult to model behavior leading to uncertainties in model validation. If the airfoil boundary layer is sufficiently tripped ahead of the natural separation of the airfoil, the performance is more consistently modeled. This report discusses the general operating conditions for the turbine and airfoil, discusses the choice of tripping location, and the calculation of required height of the roughness element which performs the trip.

2 Test Conditions

The PitchVAWT Turbine has been designed to measure dynamic rotor and blade loads across an array of tip speed ratios, TSRs, including the use of active pitch control. Due to limitations in required pitch rate, the wind speed used for testing is kept low in order to reach high tip speed ratios. For the following calculations a wind speed of 4 meters per second is used as a low end of wind speeds. In order to reduce effects of dynamic stall as much as possible, most measurements will be performed at a TSR of 4. This will also be used for deciding where to trip the airfoil.

2.1 Turbine Layout

The wind turbine is a 1.5 m square, H-type VAWT. Detailed discussion of the design and previous testing campaigns can be seen in previous papers by LeBlanc and Ferreira [4, 3]. For reference the turbine dimensions are listed in Table 2.

2.2 Airfoil

The airfoil selected for the turbine is a NACA 0021. This symmetric airfoil has been used by several previous experimental studies of vertical axis turbines, and has a large literature

Table 1: PitchVAWT Design Specifications

Property	Dimension
NBlades	2
Height	1.5 m
Diameter	1.48 m
Load Cells to Rotor Center	1.15 m
Chord	0.075 m
Solidity	0.1
Blade Airfoil	NACA0021
Strut Airfoil	NACA0018

available as to its performance in lower Reynold's number flows. The nature of the VAWT requires an airfoil that can perform well in both positive and negative angles of attack, fitting nicely with the symmetric geometry of the airfoil. It also has the benefit of being a relatively simple geometry to model structurally. Blade stiffness was a high priority in the design of the turbine in order to limit aeroelastic effects and to minimize deflection at the midpoint of the blade for use during PIV measurements of airflow around the blades.

2.3 Operating Range

A 3D Free wake vortex lifting line model was used to calculte turbine performance at the expected operation point with a wind speed of 4 m/s and a TSR of 4. The calculated Reynold's number and angle of attack at the midplane of the rotor is shown in Figure 1. The expected Reynold's number for this operating condition ranges from approximately 60000 to 90000. The angle of attack ranges between $+12$ and -10 degrees for the zero pitch configuration. While pitching, the action typically reduces the maximum angle of attack experienced by the blades, therefore this is considered conservative for this tip speed ratio case.

3 Modeling Airfoil Performance

Airfoil performance is modelled using XFOIL 6.99[2]. Viscous solutions were performed with M=0.0 and the given Reynold's numbers specified. No dynamic stall models or other effects were taken into account in the solutions presented. Airfoil polars were calculated within an angle of attack range of $\pm 15^o$.

3.1 Location of airfoil trip

To calculate the position of the airfoil trip, a free transition polar was first calculated. In these low Reynold's numbers, the flow around consists of large laminar separation at small angles of attack. Figure 2 shows the pressure distribution for the untripped airfoil at $Re = 55000$ and $\alpha = 9$. The calculated free transition location for this configuration is 36% of the airfoil chord. Therefore, the trip location should be placed sufficiently upstream of this location in order to ensure forced transition.

Polars were calculated with free transition, forced transition at 20% of chord on both upper and lower surfaces, as well as 15% on both surfaces. The polars are shown in Figure 3. It is

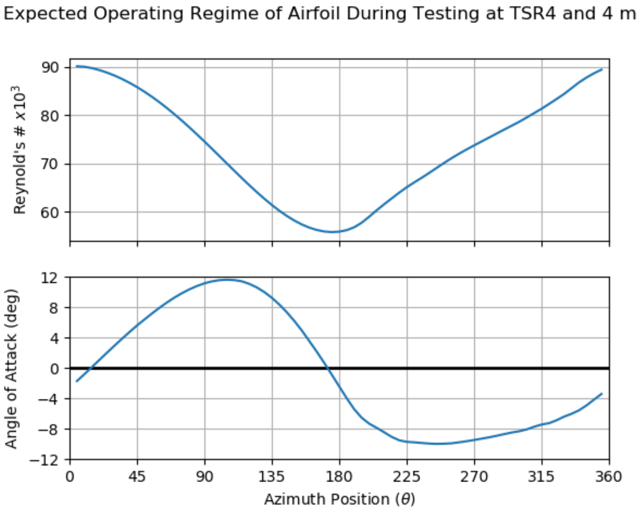

Figure 1: Reynold's Number and Angle of Attack for PitchVawt at TSR: 4 and wind speed: $4\frac{m}{s}$

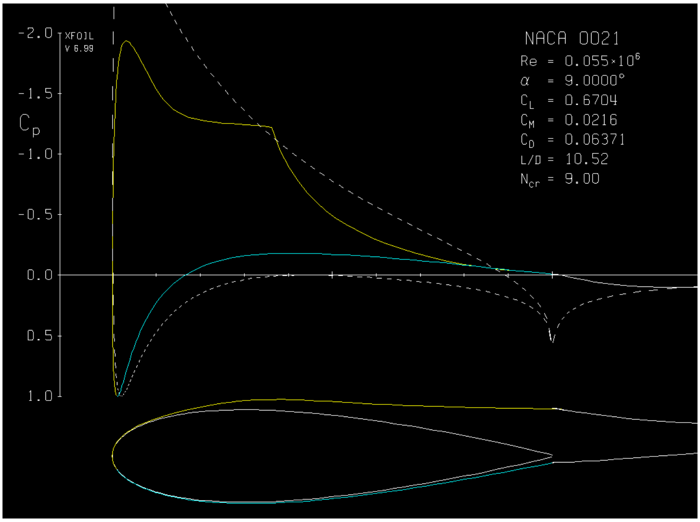

Figure 2: Cp - x distribution of NACA0021 airfoil with $Re = 55000$ and $\alpha = 9^o$

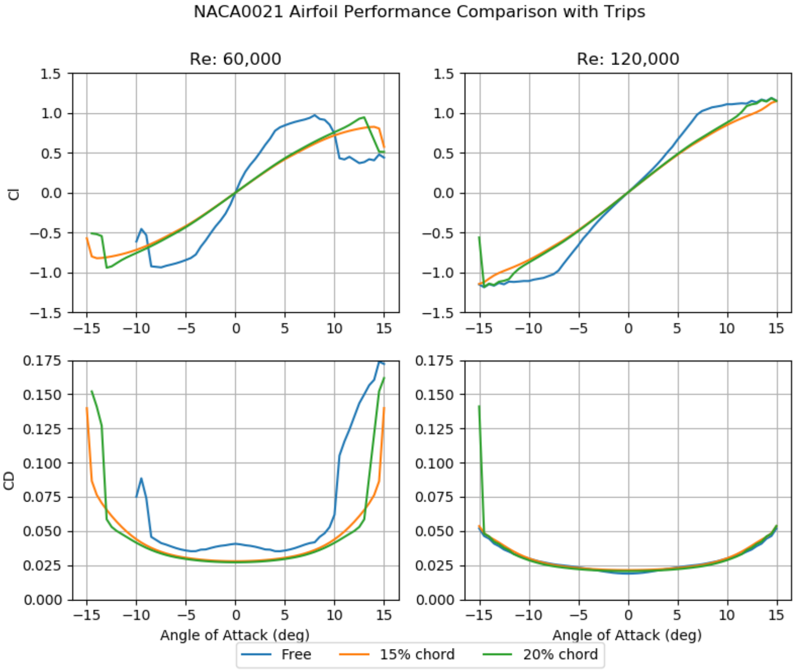

Figure 3: Comparison of airfoil polars bridging the expected angle of attack and reynold's number ranges during operation of PitchVAWT

shown that moving the trip location to a position of 15% chord delays stall to approximately 14 degrees even at the low reynold's number. Due to the large laminar separation of the free-transition airfoil creating a large drag, the trip substantially reduces overall drag at this Reynold's number throughout the operating angles of attack.

4 Height of Roughness Element

In order to physically trip the flow to achieve the above results, a roughness element needs to be chosen, and a minimum height of said element needs to be calculated. This section overviews the chosen element and describes the calculation of the critical height of the element.

4.1 Roughness Type

For this work, a ZigZag tape turbulator will be used to trip the flow. This tape has been used extensively in wind tunnel and flight testing environments of aircraft in order to force transition to turbulent flow. (reference). An example of this tape is shown in Figure 4

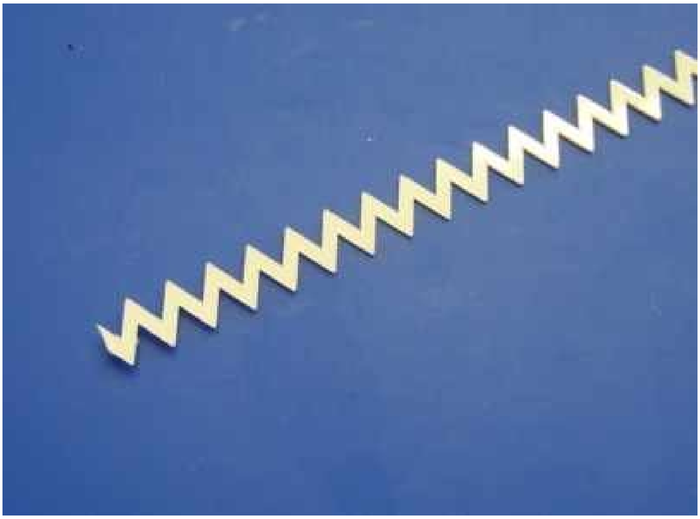

Figure 4: Example of ZigZag turbulator (source:www.iflytalies.com)

4.2 Calculation of Roughness Height

The method chosen was derived by Braslow and Knox in NACA Technical Note 4363 [1]. The method relates the roughness height to a Reynolds number based on the roughness height and the local flow conditions. In general, there exists a critical roughness height which can trigger a given flow to transition from laminar to turbulent. If the element is below this critical height, no transition will occur, however, even a small amount larger than this critical height will cause the flow to transition. If the element is larger than this height, there is a penalty in drag associated with the roughness. Therefore it is desirable to use an element which can trip the flow in all given conditions, but is not overly large limiting the benefits of the boundary layer transition. The effect of roughness drag is also limited as long as the roughness is applied in a thin strip.

The method requires the assumption of "zero pressure gradient on surfaces at equilibrium temperature." The airfoils throughout the test should remain at equilibrium temperature throughout. The assumption of a flat plate is also made for the calculation of boundary layer profile. The testing environments are well within the Mach number limitations of 0 - 4 for the method. Therefore the assumptions listed are considered valid in this case.

The roughness height for given conditions is calculated with Equation 1. The value of η_k is determined based upon a selection of critical Reynolds number at the trip height. This is dependent upon the type of roughness element, which for ZigZag tape can range between 200-400. For this work, the conservative value of 400 has been used.

$$k = 2 * \frac{x}{c} \frac{\eta_k}{\sqrt{R_x}} c \tag{1}$$

Where:
$\frac{x}{c}$ = Relative chord position of trip

η_k = Nondimensional roughness parameter based upon boundary layer
R_x = Reynold's number based on length of x from leading edge and flow conditions outside boundary layer
c = chord

XFoil calculations were used to determine the local Cp at the desired position of 15% chord for a zero angle of attack. From this, the local flow velocity was calculated which in turn was used to calculate R_x. A table has been provided by Braslow et al. to look up η_k for given flow conditions. Table XX highlights the parameters and results of the calculation for roughness height at 15% chord for the PitchVAWT Turbine.

Table 2: Roughness Height Calculation Parameters

Property	Value
Chord	.075 m
Mach	0
x/c	0.15
Cp	-0.75
Re	55000
R_k	400
η_k	1.852
k	0.506 mm

5 Conclusion

The techniques of Braslow and Knox described in the NACA Technical report 4363 have been applied to calculate a height and location of roughness elements for use with the PitchVAWT wind turbine under expected operating conditions. A set of polars have been presented given the trip location at 15% of chord length on both surfaces of the airfoil. A ZigZag type element will be employed with a height of 0.5mm for test cases with PitchVAWT.

References

[1] Albert L. Braslow and Eugene C. Knox. Simplified method for determination of critical height of distributed roughness particles for boundary-layer transition at mach numbers from 0 to 5. Report, National Advisory Committee for Aeronautics, August 21, 1958 1958.

[2] Mark Drela. Xfoil subsonic airfoil development system, 2013.

[3] Bruce P. LeBlanc and C. Simo Ferreira. Experimental determination of thrust loading of a 2-bladed vertical axis wind turbine, June 18, 2018 2018.

[4] Bruce P. LeBlanc and C. Simo Ferreira. Overview and design of pitchvawt: Vertical axis wind turbine with active variable pitch for experimental and numerical comparison, 8-12 January 2018 2018.

B

PitchVAWT Instrumentation

The turbine instrumentation is used for two main purposes, first to control the turbine as directed by the user, and second, two collect useful loading data for scientific measurement campaigns. This requires a suite of instruments which can determine the state of operation of the turbine in coordination with the SCADA (Supervisory Control and Data Acquisition) system, as well as such instruments for measuring thrust, blade loads, or torque for use in verifying performance metrics during testing. Each of the main quantities measured on the turbine are described in this section. An overview illustration of the sensor placements on the turbine is given in figure B.1.

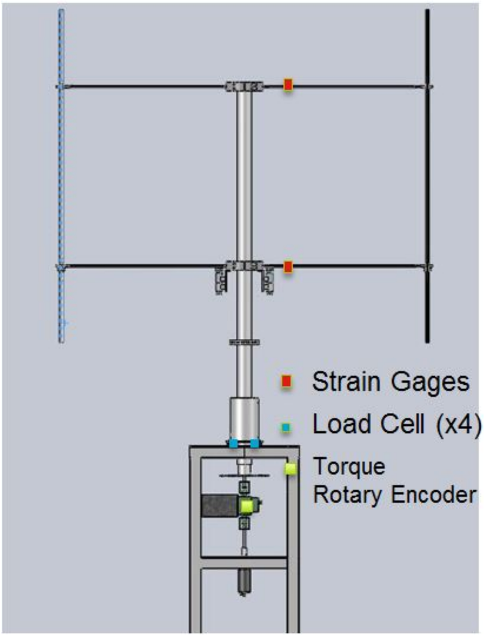

Figure B.1: Installed sensors on PitchVAWT

B.1. Torque

The turbine torque is measured using a torque transducer produced by Burster inc. and is located between the gearbox and the turbine tower. It is shown installed in figure B.2. It is situated between two metal bellow couplings which allow for small misalignments in lateral, axial, and angular dimensions. These couplings have a slip value of 5 N m thereby ensuring the torque sensor is protected against sudden over-torque events. The torque value is digitized directly on the shaft of the sensor, and then converted to an analog voltage with a 1 V to 1 N m output which is read into the DAQ system of the turbine directly.

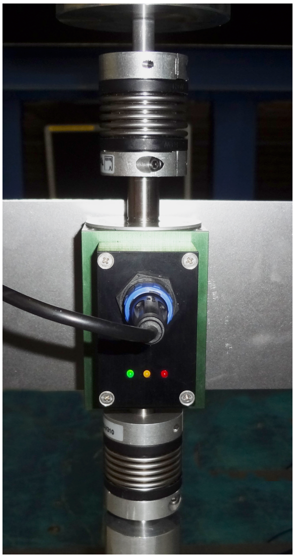

Figure B.2: Torque sensor / rotary encoder installed on turbine

B.2. Azimuth Position

The Burster sensor used for the torque measurement also has an embedded digital incremental optical rotary encoder. This encoder has a 1600 $\mathrm{count\,rev^{-1}}$ or an angular resolution of 0.225°. As the encoder is incremental, as opposed to absolute which always maintains its zero, the zero position needs to be set each time the turbine is powered on. A procedure is given in appendix G to perform this task using a laser alignment system in order to verify that the zero azimuth position lines up correctly with the wind tunnel outlet. The digital output is received directly into a DIO module on the PitchVAWT DAQ system. A Field Programmable Gate Array, FPGA, device is then used to convert this signal set to a rotation count and speed. The controller converts the counts from the sensor into azimuth position and the rotation rate of counts per second into revolutions per minute.

B.3. Platform Motion

Platform motion is measured with a set of accelerometers mounted to the corner of the blue platform. Three single-axis ICP®piezo-electric accelerometers from PCB©are used, one aligned for each principle axis. Each accelerometer has a nominal sensitivity of 100 $\mathrm{mV\,g^{-1}}$. While on their own not sufficient to properly characterize all of the expected platform motion, when tied with the full dynamic characterization and experimental mode shapes of the base and full turbine presented in chapter 4 it is possible to reconstruct the full platform motion from sensors which have active dynamic motion in all mode shapes, as is true for the free corner of the platform. The sensors also provide quality measurements of relative vibration levels for different tip speeds or turbine active loading case studies.

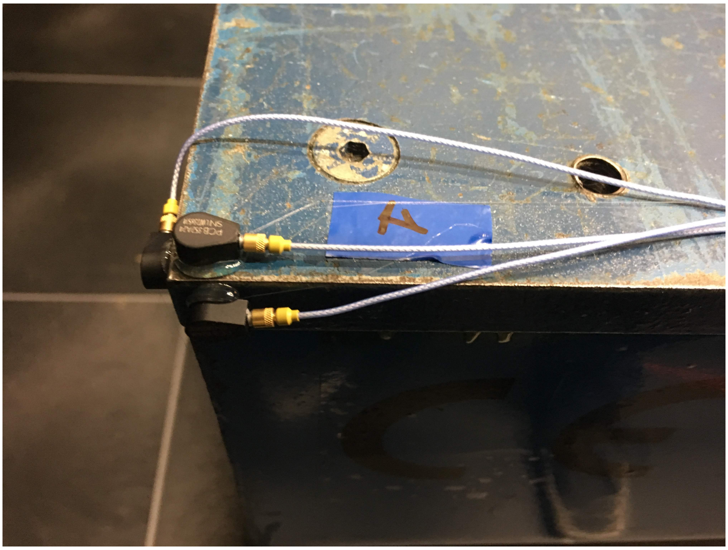

Figure B.3: Teardrop IEPE (ICP®) accelerometers mounted to corner of platform base to measure motion during operation and modal testing.

B.4. Blade Normal Loading

Blade normal loading is measured utilizing the two horizontal struts made of extruded Aluminum are used to mount each blade. The struts are a constant cross-section throughout the length and are in the shape of a NACA 0018 symmetrical airfoil. The airfoil dimensions are given in figure 2.19. Through work performed creating a calibrated finite element model of the turbine, discussed in Section 4.5.1, the material properties of the struts have been measured experimentally, and are given in table B.1.

Table B.1: Strut Material Properties

Property	**Dimension**
ρ_{strut}	2620 kg m^{-3}
E_{strut}	55 GPa
$A_{cross-section}$	143 mm^2

B.4.1. Measurement and Signal Conditioning

The information provided here is based specifically on the setup for PitchVAWT. For derivation of the equations and setup of other strain measurement systems please see[97,98]. The normal load is measured using a set of strain gages on the top strut of the first blade of the turbine. A full-bridge strain gage setup is utilized in an axial configuration in order to compensate for any vertical bending or temperature fluctuations which can occur while testing.

In principle, electrical resistance strain gages measure a small change in resistance of a wire due to its elongation ($\epsilon = \delta l/l_0$.) Generally, the strains which occur in materials due to a generic load are very small, on the order of 1×10^{-6}. In order to measure these very small changes, a wheatstone bridge is used, see figure B.4. Each resistor shown in the figure is a strain gage mounted on the structure. Due to each strain gage having approximately the same resistance, when no load is applied to the structure, the bridge is said to be ”balanced” and no voltage difference is measured across V_{out}. If the resistance changes on any of the legs due to an applied strain, the circuit will go unbalanced and a voltage will be output to V_{out}. When the gages are applied in a specific way, shown in figure B.5, only the axial strain is measured. This is because any bending load will stretch one gage and compress the gage exactly oppositely positioned on the beam the same amount, therefore keeping the two legs of the wheatstone bridge in balance. This is also true for transverse loading due to Poisson effects and for temperature fluctuations. Due to the PitchVAWT struts being a symmetrical cross section, the gages can be safely mounted on the upper and lower surfaces of the airfoil, so long as they are placed in the same radial and chord position on the strut.

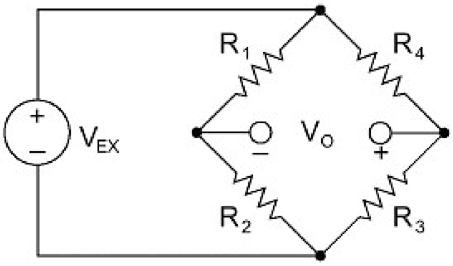

Figure B.4: Wheatstone Bridge

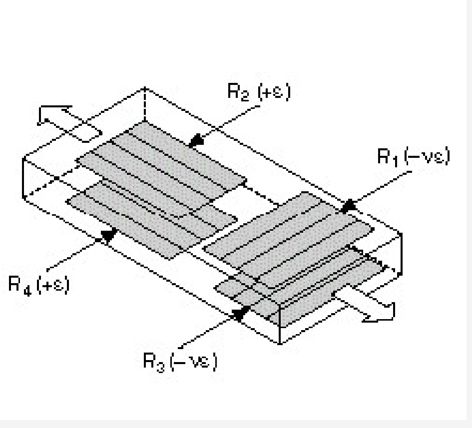

Figure B.5: Strain gage configuration for measuring axial strain[98]

The measured voltage out corresponds to the change in resistance of each strain gage as shown in equationB.1.

$$V_{out} = \frac{V_{ex} R_2 R_3}{(R_2 + R_3)^2} \left(\frac{\Delta R_3}{R_3} + \frac{\Delta R_1}{R_1} - \frac{\Delta R_2}{R_2} - \frac{\Delta R_4}{R_4} \right) \tag{B.1}$$

The voltage due to the strain response is a relative voltage measurement of the measured voltage difference in the wheatstone bridge versus the excitation voltage between strained and un-strained states shown in equation B.2.

$$V_r = \left(\frac{V_{out}}{V_{ex}} \right)_{strained} - \left(\frac{V_{out}}{V_{ex}} \right)_{un-strained} \tag{B.2}$$

The axial strain can then be attained using the known ”strain-gage factor”, provided by the manufacturer, the response voltage, and the Poisson’s Ratio for the material of the strut, assumed to be 0.3, for metals, by using equation B.3.

$$\epsilon_n = \frac{-2V_r}{GF[(\nu+1) - V_r(\nu-1)]} \tag{B.3}$$

The information for the strain gages used on the struts for PitchVAWT is given in table B.2.

Table B.2: Strain Gage Information

Item	Quantity
Manufacturer	Kyowa
Type	KFG-5-120-C1-23
Gage Factor	2.13± 1.0 %
Gage Length	5 mm
Gage Resistance	(120.2 ± 0.2) Ω
Lot No.	Y386S
Batch	281B W02
V_{ex}	3.3 V

Data is collected directly within the PitchVAWT Controller based upon the National Instruments Compact-Rio platform. The strain gage set is wired to a NI 9237 strain gage module. The wires pass through a slip ring up to the top strut for blade 1 of the rotor. A shunt calibration is performed in order to calculate the equivalent voltage drop due to the wiring of the strain gage bridge. However, because a full bridge configuration is used and the gages are placed close together, the local effects of wire resistance is considered negligible. Data is collected within the controller at a rate of 500 Hz. This rate allows capturing the effects of airfoil dynamics directly in the time domain as well as capturing higher frequency content which may be of interest.

B.4.2. Normal Load Calculation

For the included results, two test are performed. One where the turbine is operated at a given set of RPMs which correspond to the target tip speed ratios, however the wind speed is zero. This allows for the calculation of turbine effects that can be removed in post processing. The second is with the turbine operating with fixed zero pitch at a tip speed ratio of 4 in a 4 m s^{-1} wind.

Once the axial strain has been calculated from the measured output of the wheatstone bridge it needs to be converted into the wanted Normal load.

The first major calculation is to transform the measured strain into a stress. This is performed using Hooke’s Law given in equation B.4. The measured strain is multiplied by the known Elastic modulus of the material (given in table B.1. For axial loading the stress on a cross section is the force on that section divided by the area, equation B.5. For this calculation, the force has only been measured on one of the two struts and is therefore doubled, equation B.6. Due to the symmetrical design of the blades and struts, the assumption that the normal loading is equally distributed among the struts is considered valid for this exercise. Data is captured on the bottom strut using a quarter-bridge strain gage, which does not compensate for bending or temperature effects, and is not used in this analysis, although may prove useful as verification in the future.

$$\sigma_n = E\epsilon_n \tag{B.4}$$

$$F_{n_{strut}} = \sigma A_{cross-section} \tag{B.5}$$

$$F_{n_{blade}} = 2F_{n_{strut}} \tag{B.6}$$

Rotational Correction The next correction which needs to be made to the data is removal of the large load due to the rotation of the turbine around the vertical axis. The mass of the blades and struts are located at a radius removed from the rotational axis. This causes a substantial centrifugal load which corresponds to the suspended mass having an acceleration proportional to the square of the rotational frequency. For a point mass this can be simplified to $F_{cent} = mr\omega^2$. However for the real turbine, this is a fairly complex phenomena to perfectly correct for with such an assumption. For the processing here a second order polynomial was fit to the normal load data with respect to the rotational frequency. This accounts for any non-linearities built into the system, as well as the exact sprung mass outboard of the strain gage placement. This correction is given in figure B.6.

Slip Ring Correction The slip ring transfers the strain signals from the rotational frame to the fixed frame. The resistance across the slip ring can vary depending on the azimuth position and rotational speed of the rotor. This gives an effect on the measured load of the turbine as shown in figure B.7. In order to correct for this, the turbine is run at each expected rotational speed that will be run during the experiment. Once the rotational corrections are made to the measured strain, the slip-ring based strain effect can then be removed from the measurement. The result of this correction is given in figure B.8. This slip ring correction adds a level of uncertainty to the measured normal load, so for many measurements, the effected azimuth positions are removed from the data to prevent any false conclusions.

Filtering There are two types of filtering of the loading data discussed here. It is possible to filter the signals directly in the frequency domain using digital filters based upon frequency content in the signal. It is also possible to filter in the azimuthal domain by changing the amount of bins used in the averaging of the load. Each of these will be discussed briefly. It is important to note that this is a mechanical measurement of the reaction forces of the blade which includes more than just the aerodynamic loading component. For instance, the structural dynamics of the operating turbine will also contribute to this load. This is an aeroelastic effect

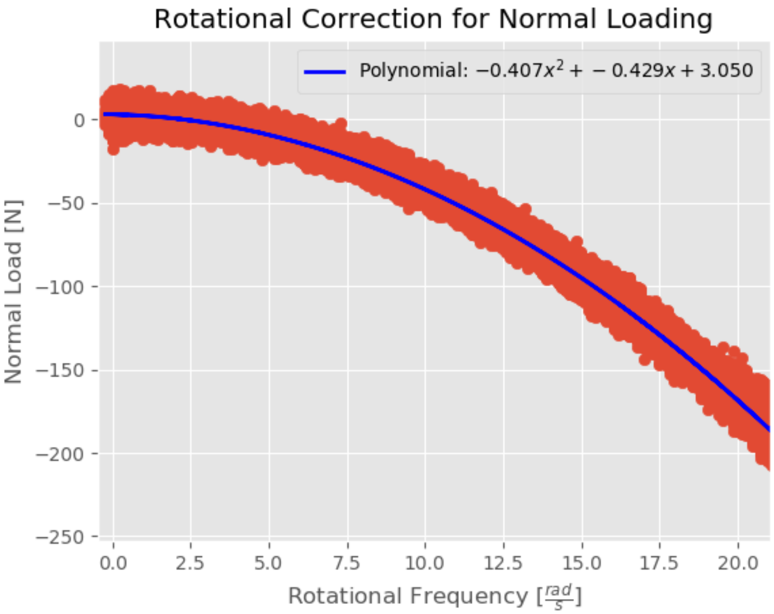

Figure B.6: Rotation correction for Normal loading

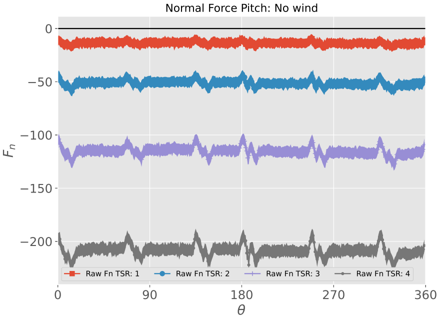

Figure B.7: No wind load response for $\lambda = 1 to 4$

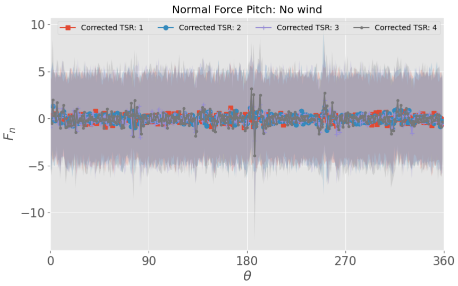

Figure B.8: No wind load when corrected for rotation and slip ring effects, shaded area shows 1 standard deviation for each measurement bin.

which will alter the aerodynamic loading as well. In order to properly account for this a coupled flexible model should be used. It is possible to use filtering to remove these effects, but it also distorts the data, and is difficult to remove without removing the aerodynamic loading of interest. For this work, the data will be presented in both ways in order to highly the effect these frequencies have on the response. A proper coupled model, can be used in the future in order to do comparisons of the structural effects on the experienced aerodynamics.

The time signal of the normal load contains a fair amount of high frequency noise which is a result of the testing environment and wiring. It is possible to see harmonics of the fundamental rotation frequency as well as high frequency noise. The maximum turbine operational frequency is approximately 3.4 Hz and there are few phenomena of interest that occur above ten times this value, therefore low pass filters can be applied to the data. As a demonstration of the filtering effect, a low pass filter at 30 Hz was applied to the data. The high frequency content and the effect of the filter are shown in the Power Spectral Density plot given in B.9. The effects of the filtering are given in figure B.10. A time series of approximately 1 s is shown while operating at $\lambda = 4$ with both the slip ring and rotation corrections applied. The scatter plot dots are the corrected data, while the filtered data maintaining frequency content below the cut-off of the filter is plotted using a black line.

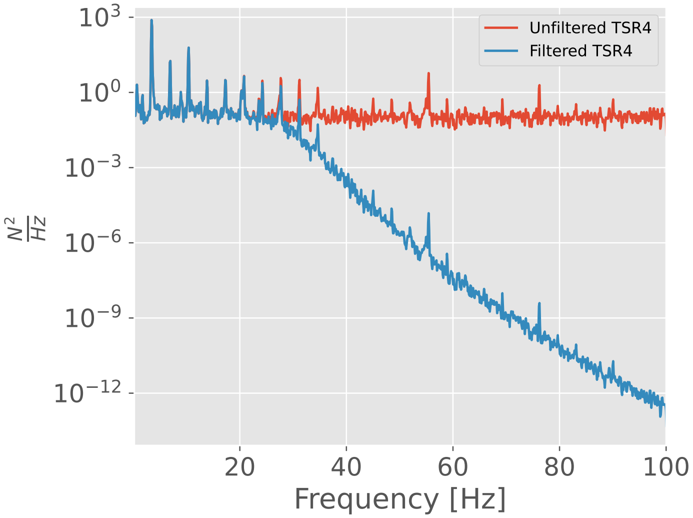

Figure B.9: Power Spectral Density of $F_{n_{blade}}$

Overall, the high frequency effects are relatively small on the scale of the normal load being measured. Therefore the choice of frequency band and whether or not to use the filter is case dependent. If the goal is to understand maximum loading, a lower frequency set of content is probably sufficient, however, if the goal is to understand effects of blade vortex interaction in the downwind region, or dynamic stall around the azimuth, higher frequency information may be critical. Figure B.11 gives an example of the same data, binned into 180 azimuthal bins and averaged, for different frequency cutoffs. The cutoff of 60 Hz allows one to see much more information, than the equivalent at 30 Hz. However, depending on the purpose of the study, the filter can be placed as necessary. That being said, applying these filters does alter the data being presented, so it is crucial to be upfront about what is being filtered out of the original signal and why.

The effects of the turbine structural dynamics on the measured load can be

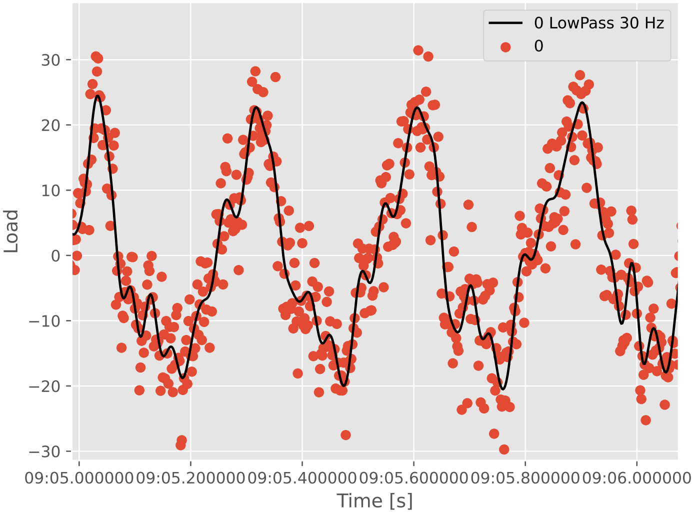

Figure B.10: Time series comparison of measured normal force with and without filtering using a low pass filter at 30 Hz

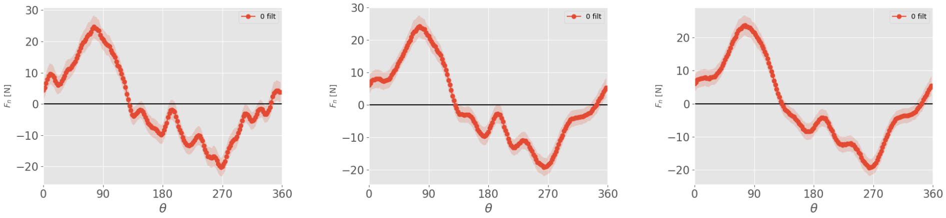

(a) 60 Hz (b) 40 Hz (c) 30 Hz

Figure B.11: Filtering with a low pass filter, 180 azimuthal bins are used for each case. Zero pitch operation at $\lambda = 4$ and $U_\infty = 4\,\mathrm{m\,s^{-1}}$, the shaded region represents $\pm 1\sigma$

great however. A comparison is made between the unfiltered normal load and the same normal load with the low-pass filter at 40 Hz as well as with notch filters that coincide with the frequencies up to 50 Hz that have been measured experimentally and given in table 4.5 along with the turbine Campbell diagram at 200 rev/ min given in figure 4.21, namely the crossing of the 3P loading with the tower backwards whirling mode. The result of the comparison is shown in figure B.12

The turbine records data at 500 Hz, so while rotating at a speed of $\omega = 21$ rad/ sec there is a measurement taken roughly every 2°. However, the rotary encoder has a resolution of 0.25°. Due to the many number of cycles which are measured, a varying resolution can be measured using azimuthal bin averaging, down to 0.5°, depending on how many samples are collected, and how repeatable the signal is.

The effect of azimuth domain filtering is given in figure B.13. No other filters

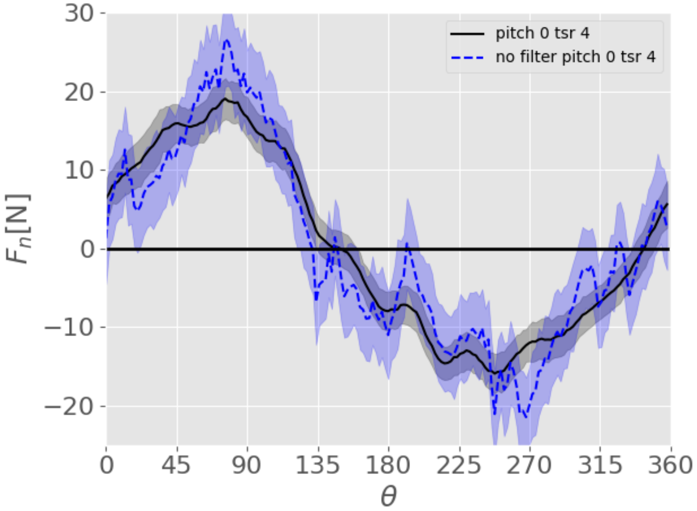

Figure B.12: Comparison of normal loading with and without filters. Filtered data has a low-pass filter at 40 Hz and notch filters at known structural resonance frequencies

are applied to the data outside of the averaging for each azimuthal bin. A similar effect is witnessed to the time domain filtering, as the spatial filter averages data over longer time periods of the rotation, this is expected. It is recommended to use a smaller bin size and a minimal amount of time domain filtering if it is possible. This requires collecting more data at each position in order to properly fill in the azimuthal bins. Although, the turbine collects data fast enough that this should be possible in almost all operating regimes.

B.5. Thrust from Normal Load

The most direct way to measure the aerodynamic thrust for the PitchVAWT is to convert the blade normal loading as measured above into x and y components. If each rotor blade had a set of strain gage measurements, this would entail simply summing up the loads over each blade as a function of azimuth position. However, at least in the initial design of the PitchVAWT, the normal load is only measured for a single rotor blade. As the second rotor blade is designed to mirror the first blade, and the rotor is balanced, the assumption can reasonably be made, that it behaves like that of the first. So by sampling the azimuthal load distribution of the first blade with a 180° offset, it is possible to estimate the experienced aerodynamic thrust load for both blades over the rotation of the turbine. The x and y loads from the measured normal load are given first for the individual blade measurement, and then for the assumption of both blades in figure B.14.

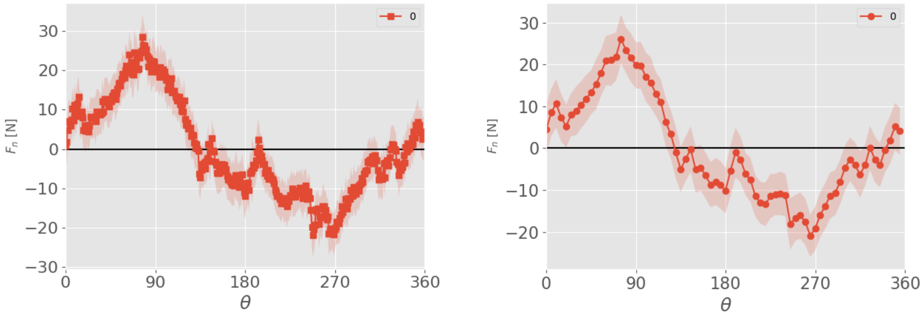

(a) 360 Bins (c) 72 Bins

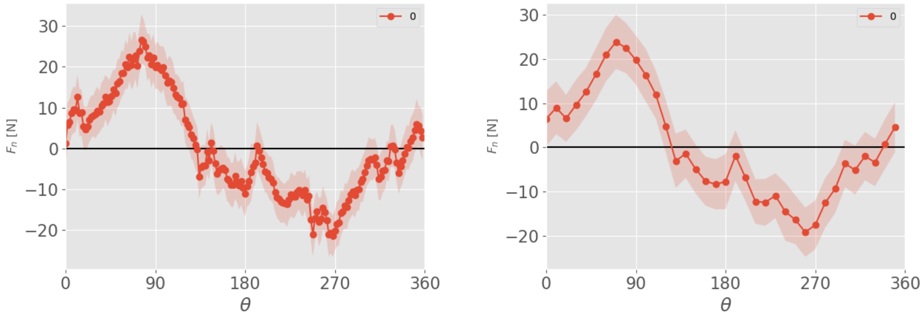

(b) 180 Bins (d) 36 Bins

Figure B.13: Sample of azimuthal binning, zero pitch operation at $\lambda = 4$ and $U_\infty = 4\,\mathrm{m\,s^{-1}}$, no other filters have been applied to the data, the shaded region represents $\pm 1\sigma$

B.5.1. Normal Load Assumption

Due to inherent difficulties with directly measuring the tangential loads on each blade, an assumption is made within the apparatus that measuring the normal loading at each azimuth position provides a good representation of the total turbine loading. In order to verify this assumption, turbine thrust is calculated from the AC Model both with and without inclusion of the tangential force vector. Figure B.15 and table B.3 highlight the effect of ignoring the tangential component of the blade forces on the calculated thrust magnitude and direction. In the direction of the wind, the difference is negligible, however there is a slight underestimation of the cross-flow thrust. This underestimation leads to a offset in calculated thrust direction of approximately ±2.5° for the current model across the pitch schemes. This error is considered acceptable for the current analysis. However, depending on the purpose of the study, as in a rotor or platform dynamic model, this may need to be taken into account.

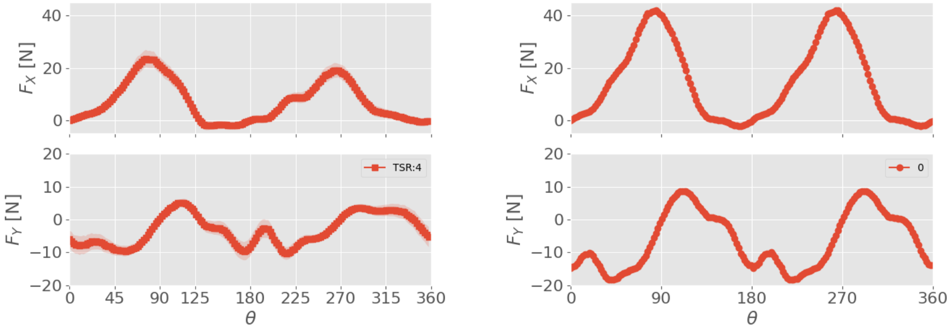

(a) Thrust from Blade 1

(b) Total thrust assuming both blades

Figure B.14: Thrust from blade normal loads

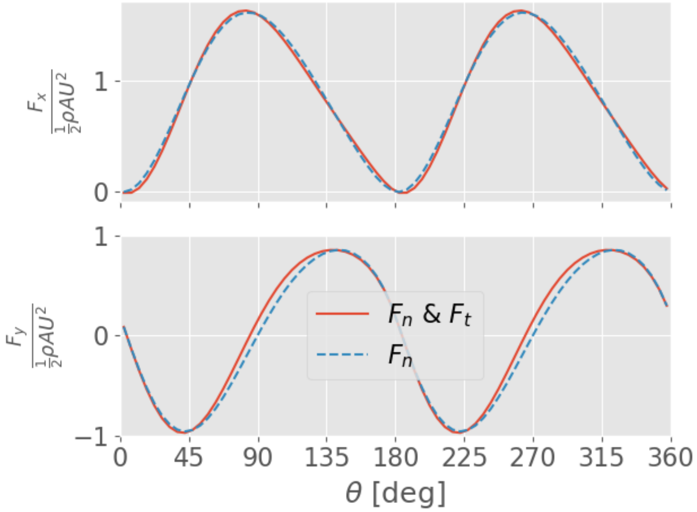

Figure B.15: Thrust with and without tangential load, from Actuator Cylinder Model

Table B.3: Integrated Thrust Values

Pitch	Param	Mag	Dir
0°	F_n, F_t	0.843	89.93°
	F_n	0.848	92.58

B.6. Tower Base Moment

The turbine has four load cell sensors mounted between the tower main bearing assembly and the base support in a square configuration. This is shown in detail in figure B.16. Each load cell has a name corresponding to its location on the turbine as shown in figure B.17. The tower base bending moment is calculated by taking the differential loading between the load cells on either side of the corresponding axis multiplied by the distance between the load cells and the center axis, given in equations B.7 and B.8. Loading in the wind direction is given as the moment about the y-axis, while side-side loading is about the x-axis.

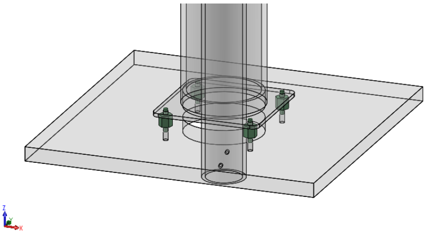

Figure B.16: Dimetric view of load cell arrangement on PitchVAWT

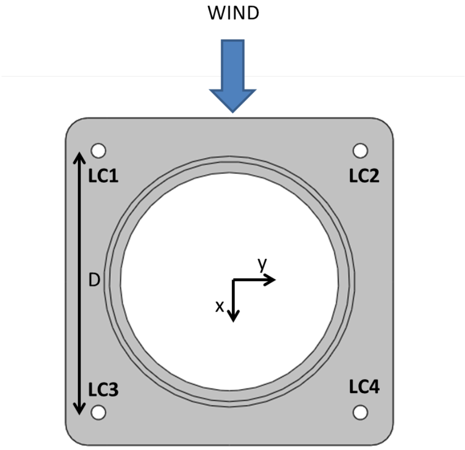

Figure B.17: Load cell naming scheme for tower bending moment

$$M_{yy} = ((LC3 + LC4) - (LC1 + LC2)) * \frac{D}{2} \tag{B.7}$$

$$M_{xx} = ((LC2 + LC4) - (LC1 + LC3)) * \frac{D}{2} \tag{B.8}$$

where:

M_{xx} = Moment about x-axis
M_{yy} = Moment about y-axis
D = Distance between load cells
$LC1 - LC4$ = Individual load cells as depicted in figure B.17

The load cell data is acquired using the NI-9234 sound and vibration measurement module configured to run in IEPE, Integrated Electronic Piezoelectric, signal conditioning mode to interface with the Piezoelectric load cells (PCB 208C04) at a rate of 500 Hz. Due to this signal conditioning the load cell signals are AC-coupled during A/D conversion. This AC - coupling effects the DC offset expected in the X-direction thrust measurement (0 to max load rather than oscillating about zero). Due to the loading phenomena itself occurring at a frequency higher than 0 Hz, minimal loading information is lost during this conversion, although there is no DC offset in the x-direction due to this type of measurement. The raw voltage load cell signals are converted to engineering units of Newtons by applying the individually calibrated sensitivity (about 1 mV N^{-1}) for these load cells. A time series given in figure B.18 shows the vertical force on each load cell while operating at a tip speed ratio of four, with a wind speed of 4 m s^{-1}.

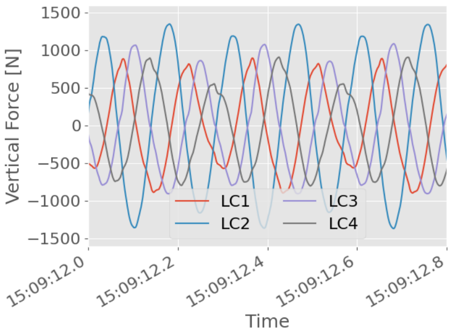

Figure B.18: Time response of load cells, U_∞ = 4 m s^{-1}, $\lambda = 4$

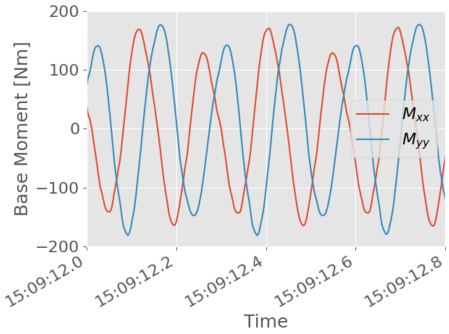

Figure B.19: Example of turbine base moment over time

The base moments about the x and y axes are calculated using equations B.7 and B.8. The time response for the reaction forces are shown in figure B.19. This data is useful with regards to understanding how fatigue loads accumulate over time or for understanding the current state of the turbine for things like controller input, however it is less useful from an aerodynamic comparative analysis standpoint. For that, the data is re-sampled in the azimuthal domain, shown in figure B.20. The data is divided into 180 azimuthal bins and averaged, the standard deviation of the measurement is then plotted as a shaded region over the line plot. As can be seen, the data is very consistent over time.

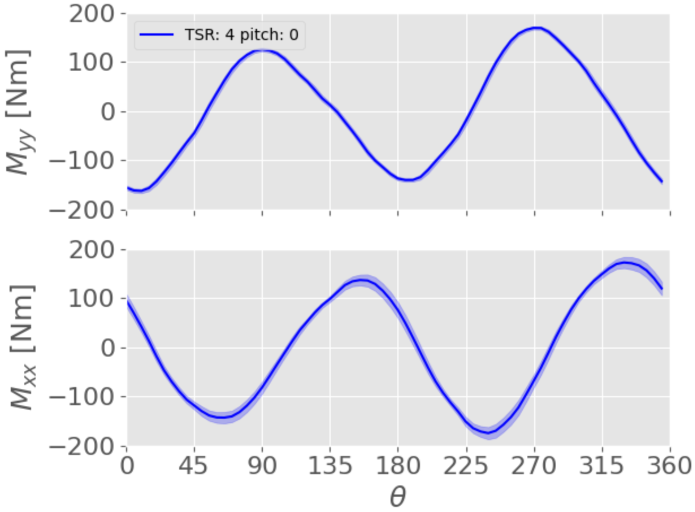

Figure B.20: Example of turbine base moment data re-sampled over rotor azimuth position

C

Calculation of Noca nonporous force term

Calculation of body force for NOCA airfoil load calculations

Bruce LeBlanc

September 2020

1 Introduction

In many sections of work, the PIV data collected on the PitchVAWT rotor is used to calculate aerodynamic forces. The aerodynamic loads are calculated over a boundary surface surrounding the airfoil, however there is a term accounting for the acceleration of the control volume change over time. This doesn't have a lot of documentation available, so this short report serves as a white paper of how I calculate that force.

2 Noca Flux Equation for Loads

A definition of the boundary sources for the calculation of aerodynamic loading on a body is given in figure 1. There are two major surfaces, the inner surface corresponding to the surface of the body, S_b, and the outer surface denoted as S.

The phase averaged Noca Flux equation is given in equation 1, see [2] for derivation. There are three major terms in this equation. The first is the flux over the boundary surface surrounding the airfoil, this is the major target of the analysis. The next two are corrections for the inner boundary of the control volume surface. The second term has to do with flow through the boundary surface of the airfoil, as the airfoil is a solid body, this force goes to zero. The third term, which is due to the change of the internal boundary surface over time, is the focus of this report.

$$\frac{\langle F \rangle}{\rho} = \left\langle \oint_{S(t)} \hat{n} \cdot \gamma_{flux} \, dS \right\rangle_{\theta_1} - \left\langle \oint_{S_{b(t)}} \hat{n} \cdot [(u - u_S)u] \; dS + \frac{d}{dt} \oint_{S_{b(t)}} \hat{n} \cdot (ux) \, dS \right\rangle_{\theta_1} \tag{1}$$

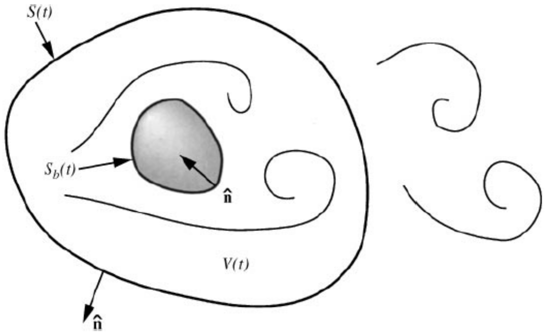

Figure 1. Domain of integration for the evaluation of fluid-dynamic forces on a bluff body.

Figure 1: Definition of control surface boundaries from NOCA [2]

3 Breaking down the body force term

The term we will be focusing on is given in equation 2. It takes the time derivative of the sum of normal velocity moments over the surface of the airfoil.

$$\frac{d}{dt}\oint_{S_{b(t)}} \hat{n}\cdot(ux)\,dS \tag{2}$$

During the experiments, the turbine was operating with a constant rotational speed, so the body force term remains constant throughout the rotation in the frame of the airfoil. Which means the calculation can be performed independent of the azimuth position of the turbine. The force is mainly a function of rotational velocity and to a lesser extent, the airfoil geometry and pitch.

4 Definition of terms for the calculation

Several terms need to be defined in order to perform the calculation. These are the turbine characteristics, the airfoil characteristics, and the operating environment.

4.1 PitchVAWT turbine characteristics

The PitchVAWT turbine is a 2-bladed H-vawt turbine with an aspect ratio, $^{H}\!/\!_{D}$=1. The chord to radius ratio is 0.1. Dimensions are given in figure 2 and the specifications are listed in table 1. More detailed information can be found in [1].

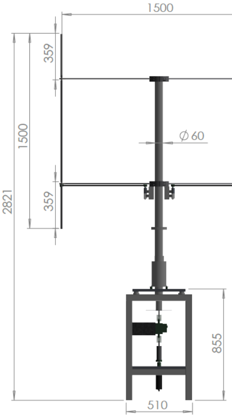

Figure 2: PitchVAWT Turbine

Table 1: PitchVAWT Specifications

Property	**Dimension**
NBlades	2
Height	1.508 m
Diameter	1.48 m
Blade Chord	0.075 m
Strut Chord	0.060 m
Solidity	0.1
Blade Airfoil	NACA0021
Strut Airfoil	NACA0018
TSR	4
U_∞	$4\,\mathrm{m\,s^{-1}}$

4.2 NACA0021 Airfoil

The NACA0021 airfoil on the PitchVAWT turbine will be used in this analysis. It is a 21 % thick symmetric airfoil with a chord length of 0.075 m. The airfoil along with the normal vectors of the airfoil is shown in figure 3.

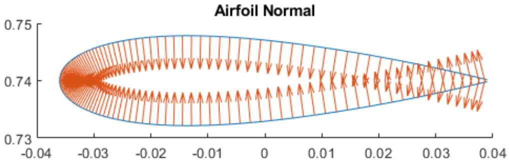

Figure 3: NACA0021 airfoil, normal vectors oriented as shown in figure 1

4.3 Operating conditions

During testing the turbine operates at a TSR of 4 with a wind speed of $4\,\mathrm{m\,s^{-1}}$. Given a radius of 0.74 m, this allows the calculation of the rotational velocity as given in equation 3.

$$\omega = \frac{\lambda u_\infty}{r} = \frac{4 \cdot 4}{0.74} = 21.62\,\mathrm{rad/s} \tag{3}$$

4.4 Time dependence

The body term requires knowing the change in the velocity on the body in the x and y directions over time. To properly handle this, I set a constant time step of $\Delta t = 0.001\,\mathrm{s}$.

5 Performing the calculation

As there can be variation in the loading due to rotational speed and pitch position, I wanted the setup of the calculation to be easily repeatable for any azimuth position, rotational speed or pitch. In order to do this I set up a function which takes in these inputs, performs the calculation and outputs the rotated normal and tangential loading which will need to be subtracted from the flux term given in equation 1.

In order to calculate the local velocities and accelerations on the airfoil due to rotation, a series of five airfoils are positioned surrounding a target azimuth position. Each airfoil is oriented in the proper position in a series of steps:

1. scale the airfoil to the correct size
2. position the center of the airfoil on the pitch axis
3. rotate the airfoil to the proper pitch setting
4. move the airfoil to the correct radius
5. rotate the airfoil to the correct azimuth position as a function of $k\Delta t\omega$ where k is an integer multiple depending on the time step of the airfoil being placed.

The aligned airfoils surrounding an azimuth position of 0° with a pitch of 0° is shown in figure 4. Each airfoil position is given a name corresponding to its position relative to the main azimuth position as shown in the figure.

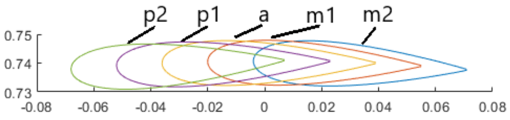

Figure 4: Located airfoils surrounding $\theta = 0$ with 0 pitch

The goal is to use central difference numerical differentiation to calculate the x and y velocities for each surface at positions m1 and p1. The velocity calculated at position m1 is given in figure 5. As a check, the acceleration of the flow was calculated at the middle airfoil position, a, by differentiating across m1 and p1, the normal vectors of the acceleration are plotted in figure 6. As expected they are directed back at the origin of the rotation. This calculation was performed at multiple azimuth locations in order to verify that this holds true.

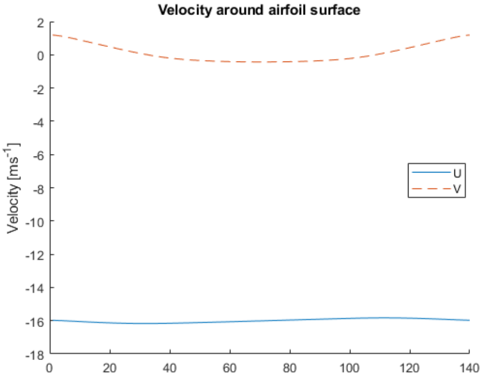

Figure 5: Velocity over the airfoil surface at theta = 0

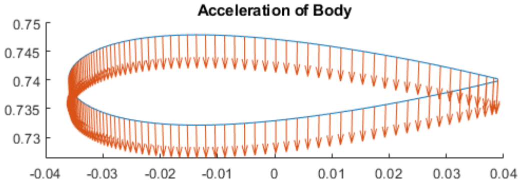

Figure 6: Acceleration vectors point back toward origin as expected

The term given in equation 2 is calculated for positions m1 and p1, and then differentiated over the time elapsed between the positions. The velocity moments which are integrated over the airfoil surface to give the loads are given for each position in figure 7.

The forces in the x and y directions are then rotated to align with the normal and tangential directions of the airfoil, a, and returned. Forces were calculated for several azimuth positions with zero pitch as given in table 2. The results are as expected showing a rotation of the load as far as x and y directions, but

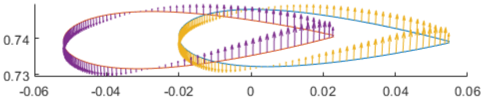

Figure 7: $\hat{n} \cdot (ux)$ for positions m1 and p1.

the normal and tangential force is constant. Table 3 shows results of varying pitch at the azimuth position of zero. As can be expected there is a very small deviation due to the variation of the normal vector orientation, but can generally be neglected in the analysis.

θ	F_x	F_y	F_n	F_t
0	0.083	0.275	0.275	0.083
60	-.197	0.210	0.275	0.083
200	0.016	-.287	0.275	0.083

Table 2: Results for varying azimuth with pitch = 0

β	F_n	F_t
0	0.2754	0.083
5	0.2753	0.083
-5	0.2756	0.0823

Table 3: Results for varying pitch with azimuth = 0

6 Conclusion

A function has been created in order to calculate the body forces due to rotation of the airfoil around the vertical axis for use in the calculation of the aerodynamic loads from velocity data using the Noca flux equation method. A test case was given for the pitchVAWT turbine showing the consistency based upon azimuth position and the very slight deviation based upon the pitch orientation of the airfoil.

References

[1] Bruce P. LeBlanc and C. S. Ferreira. Overview and design of pitchvawt: Vertical axis wind turbine with active variable pitch for experimental and numerical comparison. AIAA SciTech Forum Wind Energy Symposium,

page 11, Kissimmee, Florida, 8-12 January 2018. American Institute of Aeronautics and Astronautics.

[2] F. Noca, D. Shiels, and D. Jeon. Measuring instantaneous fluid dynamic forces on bodies, using only velocity fields and their derivatives. *Journal of Fluids and Structures*, 11(3):345–350, 1997.

A MATLAB Code to test function

```
% script to test body force function
clear all; close all;

tsr = 4;
wind = 4;
radius = 0.74;
chord = 0.075;
omega = tsr * wind / radius;
pitch = 0;
theta = 0;

[fn, ft] = calc_body_force(omega, chord, radius, pitch, theta);
```

B MATLAB code for body force function

```
% This function will compute the force on body due to rotation contained
% within the NOCA function. This represents the second term which is
% subtracted from the calculated flux force. It is a function of the
% rotational acceleration, the airfoil shape, and the turbine geometry as
% far as chord and radius.
% body force = d/dt * integral over surface boundary of normal *
% (u_boundary * x) dS
% Represented in normal and tangential forces fn, ft


function [fn, ft] = calc_body_force(omega, chord, radius, pitch, theta)
% Sinces its a d/dt give a time delta, assume the rotational speed is
% constant, and the pitch is constant over the rotation.
dt = 0.001;
% Load in airfoil
naca0021 = importdata('naca0021.dat',' ');

% Pitch axis as %chord
pitch_axis = 0.48;

% create copy of the airfoil to manipulate, keeping naca0021 as unchanged.
```

```
airfoil = naca0021;

% move to pitch axis
airfoil(:,1) = airfoil(:,1) - pitch_axis;

% scale to real size
airfoil = airfoil * chord;

% Pitch the airfoil
airfoil = rotate_points(airfoil, pitch);

% move to radius assuming its vertical at 0 theta
airfoil(:,2) = airfoil(:,2) + radius;

airfoil = rotate_points(airfoil, theta);

% make 5 airfoils. use central difference to calculate acceleration at t=0
% as a check
t_m2 = -2*dt;
t_m1 = -1*dt;
t = 0;
t_p1 = dt;
t_p2 = 2*dt;

airfoil_m2 = rotate_points(airfoil, rad2deg(t_m2*omega));
airfoil_m1 = rotate_points(airfoil, rad2deg(t_m1*omega));
airfoil_p1 = rotate_points(airfoil, rad2deg(t_p1*omega));
airfoil_p2 = rotate_points(airfoil, rad2deg(t_p2*omega));

u_m1 = (airfoil - airfoil_m2) / (t - t_m2);
u_p1 = (airfoil_p2 - airfoil) / (t_p2 - t);

du_dt = (u_p1 - u_m1) / (t_p1 - t_m1);
% acceleration should be mainly toward the radius at a magnitude of near
% 350 m/s2.
% knowing u_m1 is the velocity vector at position -1dt and u_p1
% is at position +1dt

% calculate length of each panel
panel_length = sqrt(diff(airfoil(:,1)).^2 + diff(airfoil(:,2)).^2);

% Calculate the internal normal vectors
% norm = [-dy,dx] / panel_length
norm = [-1*diff(airfoil(:,2)), diff(airfoil(:,1))] ./ panel_length;
norm_m1 = [-1*diff(airfoil_m1(:,2)), diff(airfoil_m1(:,1))] ./ panel_length;
norm_p1 = [-1*diff(airfoil_p1(:,2)), diff(airfoil_p1(:,1))] ./ panel_length;
```

```
% Calculate the position vector for each panel center
x = [(airfoil(1:end-1,1) + airfoil(2:end,1))/2, ...
    (airfoil(1:end-1,2) + airfoil(2:end,2))/2];
x_m1 = [(airfoil_m1(1:end-1,1) + airfoil_m1(2:end,1))/2, ...
    (airfoil_m1(1:end-1,2) + airfoil_m1(2:end,2))/2];
x_p1 = [(airfoil_p1(1:end-1,1) + airfoil_p1(2:end,1))/2, ...
    (airfoil_p1(1:end-1,2) + airfoil_p1(2:end,2))/2];

% Calculate velocity at each panel center by averaging around it
u_av_m1 = [(u_m1(1:end-1, 1) + u_m1(2:end, 1))/2, ...
    (u_m1(1:end-1, 2) + u_m1(2:end, 2))/2];
u_av_p1 = [(u_p1(1:end-1, 1) + u_p1(2:end, 1))/2, ...
    (u_p1(1:end-1, 2) + u_p1(2:end, 2))/2];

m1_x = (norm_m1(:,1) .* u_av_m1(:,1) + norm_m1(:,2) .* u_av_m1(:,2)).*...
    x_m1(:,1) .* panel_length;
m1_y = (norm_m1(:,1) .* u_av_m1(:,1) + norm_m1(:,2) .* u_av_m1(:,2)).*...
    x_m1(:,2) .* panel_length;

p1_x = (norm_p1(:,1) .* u_av_p1(:,1) + norm_p1(:,2) .* u_av_p1(:,2)).*...
    x_p1(:,1) .* panel_length;
p1_y = (norm_p1(:,1) .* u_av_p1(:,1) + norm_p1(:,2) .* u_av_p1(:,2)).*...
    x_p1(:,2) .* panel_length;

int_m1_x = sum(m1_x);
int_m1_y = sum(m1_y);

int_p1_x  = sum(p1_x);
int_p1_y = sum(p1_y);

force(:,1) = (int_p1_x - int_m1_x)/ (2*dt)
force(:,2) = (int_p1_y - int_m1_y)/ (2*dt)

force_rot = rotate_loads(force,theta);
ft = force_rot(1)
fn = force_rot(2)

% Plot the positioned airfoils.
figure();
hold on;
plot(airfoil_m2(:,1), airfoil_m2(:,2))
plot(airfoil_m1(:,1), airfoil_m1(:,2))
plot(airfoil(:,1), airfoil(:,2))
plot(airfoil_p1(:,1), airfoil_p1(:,2))
plot(airfoil_p2(:,1), airfoil_p2(:,2))
```

```
% origin
daspect([1 1 1])


figure();
hold on;
plot(du_dt(:,1))
plot(du_dt(:,2))
legend('du/dt','dv/dt')

figure();
hold on;
plot(u_m1(:,1))
plot(u_m1(:,2))
legend('U','V')


figure();
hold on;
plot(airfoil(:,1), airfoil(:,2))
quiver(airfoil(:,1), airfoil(:,2), du_dt(:,1), du_dt(:,2))
daspect([1 1 1])
title('Acceleration of Body')

figure();
hold on;
plot(airfoil(:,1), airfoil(:,2))
quiver(x(:,1), x(:,2), norm(:,1), norm(:,2))
daspect([1 1 1])
title('Airfoil Normal')

figure();
hold on;
plot(airfoil_m1(:,1), airfoil_m1(:,2))
plot(airfoil_p1(:,1), airfoil_p1(:,2))
quiver(x_m1(:,1), x_m1(:,2), m1_x, m1_y)
quiver(x_p1(:,1), x_p1(:,2), p1_x, p1_y)
daspect([1 1 1])

end
```

C Rotation functions

```
% This function rotates points.
function data = rotate_points(orig, theta)
```

```
theta_rad = deg2rad(theta);
T = [cos(theta_rad) -sin(theta_rad)
    sin(theta_rad) cos(theta_rad)];
data = orig * T';
end

function data = rotate_loads(orig, theta)
theta_rad = deg2rad(theta);
T = [cos(theta_rad) -sin(theta_rad)
    sin(theta_rad) cos(theta_rad)];
data = orig * T;
end
```

D

Dynamic Stall Code

This section lists the Python code for the Beddoes-Leishman dynamic stall model used within the actuator cylinder flow model.

```
def dynamic_stall(alpha, time, chord, u_rel, polar, constants):
    # Calculates dynamic stall using the Beddoes−Leishman Approach
    # Inputs
    a = 343          # Speed of sound [m/s]
    n_iter = 10      # number of iterations
    n_el = len(alpha)

    # Define cyclic blade pitching oscillations
    dt = time[1] − time[0]        # Time Step
    ds = u_rel ∗ dt / (chord/2)  # relative distance traveled by airfoil
        # in semi−chords

    #extend to size for iterations
    alpha = np.tile(alpha, [1, n_iter])[0]
    time = np.tile(time, [1, n_iter])[0]
    u_rel = np.tile(u_rel, [1, n_iter])[0]
    ds = np.tile(ds, [1, n_iter])[0]

    # constants given directly from Beddoes model
    A1 = 0.3
    A2 = 0.7
    b1 = 0.14
    b2 = 0.53

    eta = 0.95       # recovery factor
    Ka = 0.75

    # Set constants from input variable
    Tp = constants['Tp']
    Tf = constants['Tf']
    Tv = constants['Tv']
    Tvl = constants['Tvl']

    # Polar
    alpha_st = np.deg2rad(polar.alpha)
    cl_st = polar.cl
    cd_st = polar.cd
    cn_st = cl_st ∗ np.cos(alpha_st) + cd_st ∗ np.sin(alpha_st)
    cc_st = cl_st ∗ np.sin(alpha_st) − cd_st ∗ np.cos(alpha_st)
```

```
# find linear range of airfoil between −5 and 5 degrees aoa
a_range = np.where(((alpha_st >= np.deg2rad(−5)) &
                                  (alpha_st <= np.deg2rad(5))))

# calculate zero lift aoa, and lift slope of linear region
alpha_0 = np.interp(0, cl_st[a_range[0]], alpha_st[a_range[0]])
cl_0 = np.interp(0, alpha_st[a_range[0]], cl_st[a_range[0]])
cd_0 = np.interp(0, alpha_st[a_range[0]], cd_st[a_range[0]])
cl_a = np.max(cl_st / (alpha_st − alpha_0))

cn_0 = np.interp(0, alpha_st[a_range[0]], cn_st[a_range[0]])

# Maximal normal force curve slope
cn_a = np.max(cn_st / (alpha_st[a_range[0]] − alpha_0))

# CN limit for vortex shedding
cn_slope = np.gradient(cn_st, alpha_st)

for i, a in enumerate(alpha_st):
    if 'cn_lim_neg' in locals():
        pass
    elif (a >= np.deg2rad(−15)) & (a <= 0):
        if cn_slope[i] <= 0:
            cn_lim_neg = 0.9 ∗ cn_st[i]
    else:
        cn_lim_neg = −1.5
    if 'cn_lim_pos' in locals():
        pass
    elif (a > 0) & (a <= np.deg2rad(15)):
        if cn_slope[i] <= 0:
            cn_lim_pos = 0.9 ∗ cn_st[i]
    else:
        cn_lim_pos = 1.5

# theoretical separation location corrected for NANs
f_st = (2 ∗ np.sqrt(cn_st / (cn_a ∗ (alpha_st − alpha_0))) − 1)∗∗2
f_st[np.isnan(f_st)] = 1

# Initialize all of the variables
length = time.size
d_alpha = np.zeros(length)
x = np.zeros(length)
y = np.zeros(length)
alpha_e = np.zeros(length)
d = np.zeros(length)
cn_c = np.zeros(length)
cn_i = np.zeros(length)
cn_attached = np.zeros(length)
cc_attached = np.zeros(length)
dp = np.zeros(length)
cn_prime = np.zeros(length)
alpha_p = np.zeros(length)
f_p = np.zeros(length)
f_prime = np.zeros(length)
cn_separated = np.zeros(length)
cc_separated = np.zeros(length)
tau_v = np.zeros(length)
df = np.zeros(length)
cn_vortex = np.zeros(length)
kn = np.zeros(length)
cv = np.zeros(length)
cn = np.zeros(length)
cc = np.zeros(length)
cl = np.zeros(length)
cd = np.zeros(length)


# Dynamic Model
```

```
for n in range(1, length):
    d_alpha[n] = alpha[n] - alpha[n-1]

    # Module 1 - Attached flow: circulatory terms, impulsive terms due to
    # angle of attack and pitch rate

    # circulatory
    x[n] = x[n - 1] * np.exp(-b1 * ds[n]) + A1 * d_alpha[n] *
                    np.exp(-b1 * ds[n] / 2)
    y[n] = y[n - 1] * np.exp(-b2 * ds[n]) + A2 * d_alpha[n] *
                    np.exp(-b2 * ds[n] / 2)
    alpha_e[n] = alpha[n] - x[n] - y[n]
    cn_c[n] = cn_a * (alpha_e[n] - alpha_0)

    # Impulsive
    d[n] = d[n - 1] * np.exp(-dt / (Ka * chord/a)) + \
           (d_alpha[n] - d_alpha[n - 1]) / dt *
           np.exp(-dt / (2 * Ka * chord / a))
    cn_i[n] = 3 * chord / u_rel[n] * (d_alpha[n] / dt - d[n])

    # Forces in attached flow
    cn_attached[n] = cn_c[n] + cn_i[n]
    cc_attached[n] = cn_a * (alpha_e[n] - alpha_0)**2

    # Module 2 - Separated flow: leading edge separation

    # Leading edge pressure response
    dp[n] = dp[n - 1] * np.exp(-ds[n] / Tp) +
               (cn_attached[n] - cn_attached[n - 1]) *
               np.exp(-ds[n] / (2 * Tp))
    cn_prime[n] = cn_attached[n] - dp[n]
    alpha_p[n] = (cn_prime[n] - cn_0) / cn_a
    f_p[n] = np.interp(alpha_p[n], alpha_st, f_st)

    # Module 3 - Trailing edge pressure response
    df[n] = df[n - 1] * np.exp(-ds[n] / Tf) + (f_p[n] - f_p[n - 1]) *
                np.exp(-ds[n] / (2 * Tf))
    f_prime[n] = f_p[n] - df[n]

    # Forces in separated flow
    cn_separated[n] = cn_a * ((1 + np.sqrt(f_prime[n]))/2)**2 *
                            alpha_e[n] + cn_i[n]
    cc_separated[n] = eta * cn_a * (alpha_e[n] - alpha_0)**2 *
                            np.sqrt(f_prime[n])

    # Module 4 - Vortex shedding
    # Criteria for dynamic stall vortex shedding

    # Time variable
    if (cn_prime[n] > cn_lim_pos) | (cn_prime[n] < cn_lim_neg):
        tau_v[n] = tau_v[n-1] + dt / (chord/2) * u_rel[n] * 0.45
    else:
        tau_v[n] = 0

    # Vortex normal force coefficient
    kn[n] = (1 + np.sqrt(f_prime[n]))**2 / 4
    cv[n] = cn_c[n] * (1 - kn[n])

    # Accumulated vortex normal force due to leading edge separation
    if ((tau_v[n] < Tvl) & (np.abs(cv[n]) - np.abs(cn[n-1]) > 0)):
        cn_vortex[n] = cn_vortex[n - 1] * np.exp(-ds[n] / Tv) +
            (cv[n] - cv[n - 1]) * np.exp(-ds[n] / (2 * Tv))
    else:
        cn_vortex[n] = cn_vortex[n - 1] * np.exp(-ds[n] / Tv)

    # Final force
    cn[n] = cn_vortex[n] + cn_separated[n]
```

```
        cc[n] = cc_separated[n]
        cl[n] = cn[n] * np.cos(alpha[n]) + cc[n] * np.sin(alpha[n])
        cd[n] = cn[n] * np.sin(alpha[n]) - cc[n] * np.cos(alpha[n]) + cd_0
    # Select last iteration
    cl_final = cl[-n_el:]
    cd_final = cd[-n_el:]
    return cl_final, cd_final    # Return new CL and CD
```

E

Dynamic Stall Verification Code

This section lists the Python code used to verify the dynamic stall model implementation. Polars are created in XFOIL.

```
import pandas as pd
import numpy as np
import matplotlib.pyplot as plt
plt.style.use('ggplot')
import os
import Actuator_Cylinder as ac


def main():

    # Load Polar from NACA 0012 used in Leishman paper
    folder = os.getcwd()
    filename = '\\polars\\NACA_0012_T1_Re2.000_M0.30_N9.0.txt'
    polar = pd.read_csv(folder + filename, delim_whitespace=True, skiprows=8)
    polar.rename(str.lower, axis='columns', inplace=True)

    # Setup flow and model
    a = 343  # m/s
    m = 0.38      # Mach number
    v = m * a    # flow velocity
    chord = .1  # meters. from leishman

    # Dynamic Stall Constants
    Tp = 1.3        # peak pressure - cn lag
    Tf = 5          # Boundary layer = peak pressure lag
    Tv = 6           # vortex decay constant
    Tvl = 5          # trailing edge position, in semichords
    constants = {'Tp': Tp, 'Tf': Tf, 'Tv': Tv, 'Tvl': Tvl}

    alpha_mean = 10.3
    amplitude = 8.1
    k = 0.075
    w = k * v / chord       # reduced frequency to rotational frequency
    f = w / (2 * np.pi)     # rotation / sec
    n = 1                  # rotations
    t = np.linspace(0, n/f, n*100)
```

```
    alpha = np.deg2rad(amplitude * np.sin(w * t) + alpha_mean)
    u_rel = v * np.ones(len(t))

    # run the ds model
    cl, cd = ac.dynamic_stall(alpha, t, chord, u_rel, polar, constants)

    # compare polars by calculating normal coefficients
    #static
    cl_st = polar['cl']
    cd_st = polar['cd']
    alpha_st = polar['alpha']
    cn_st = cl_st * np.cos(np.deg2rad(alpha_st)) +
            cd_st * np.sin(np.deg2rad(alpha_st))

    #dynamic
    cn = cl * np.cos(alpha) + cd * np.sin(alpha)

    # Plot Results

    polar.plot(x='alpha', y=['cl', 'cd'],
               title='Static Polar NACA 0012 Re 2e6 M0.3')

    fig, ax = plt.subplots()
    ax.plot(t, np.rad2deg(alpha))
    ax.set_xlabel('Time [s]')
    ax.set_ylabel('$\\alpha$ [deg]')
    ax.set_title('AOA ${:.2f}^\circ + {}^\circ sin(wt)$ k:{}'.format(
                 alpha_mean, amplitude, k))

    fig, ax = plt.subplots()
    ax.plot(np.rad2deg(alpha), cn, label='Cn dynamic k:{}'.format(k))
    ax.plot(alpha_st, cn_st, '--', label='Cn static')
    ax.set_xlabel('$\\alpha$ [deg]')
    ax.set_ylabel('CN')
    ax.set_title('Polar comparison with dynamic stall model')
    ax.set_ylim([0, 2])
    ax.set_xlim([0, 20])
    ax.legend()

    plt.show()


if __name__ == '__main__':
    main()
```

F

Actuator Cylinder Model Code

This is the implementation of the Actuator Cylinder Model using Python.

```
def mod_lin(a, *data):
    a_lin = data
    y = a - a**2 - a_lin
    return y


def def_eval_points(n_el, f, radius):
    # Define Control Points
    d_theta = 2*np.pi/n_el
    theta = np.arange(d_theta/2, 2*np.pi, d_theta)
    xc = -radius * np.sin(theta)
    yc = radius * np.cos(theta)

    xe = f * xc
    ye = f * yc

    rwx, rwy = calculate_influence_matrix(xe, ye, theta, d_theta)
    return theta, rwx, rwy


def calculate_influence_matrix(xe, ye, theta, theta_d):
    # Calculate the influence matrix
    # returns influence matrices rwx and rwy
    n_el = len(theta)

    rwx = np.zeros([n_el, n_el])
    rwy = np.zeros([n_el, n_el])

    for i in np.arange(n_el):
        theta_int = np.linspace(theta[i]-0.5*theta_d, theta[i] +
                                0.5 * theta_d, 1000)
        for j in np.arange(n_el):
            rx_int = (-1*(xe[j] + np.sin(theta_int)) * np.sin(theta_int) +
                        (ye[j] - np.cos(theta_int)) * np.cos(theta_int)) /
                       ((xe[j] + np.sin(theta_int)) ** 2 +
                       (ye[j] - np.cos(theta_int))**2)
            ry_int = (-1*(xe[j] + np.sin(theta_int)) * np.cos(theta_int) -
                        (ye[j] - np.cos(theta_int)) * np.sin(theta_int)) /
                       ((xe[j] + np.sin(theta_int)) ** 2 +
                       (ye[j] - np.cos(theta_int))**2)
```

```
            rwx[i][j] = -1 * np.trapz(rx_int, theta_int)
            rwy[i][j] = -1 * np.trapz(ry_int, theta_int)
    return rwx, rwy


def actuator_cylinder(blades, TSR, c_r, polar, pitch, n_el, u_inf, DSFlag=0):
    # This function calculates the performance of a VAWT using the
    # actuator cylinder model proposed by Helge Madsen

    # Radius is normalized
    radius = 1
    # Chord is set to maintain C / R ratio
    c = c_r * radius
    twist = 0.                              # Twist Angle

    # u_inf = 1.0                               # Incoming wind speed
    rho = 1.225                               # Air Density
    omega = TSR * u_inf / radius              # Rotational Speed (rad/s)

    f = 1.01                                # Factor for evaluation point
    tol = .0001                                 # Tolerance for while loop
    relax = 0.3                               # Relaxation Parameter
    max_iter = 100                            # Maximum number of iterations

    # Dynamic Stall Constants
    Tp = 1.3        # peak pressure - cn lag
    Tf = 8          # Boundary layer = peak pressure lag
    Tv = 4           # vortex decay constant
    Tvl = 5          # trailing edge position, in semichords
    constants = {'Tp': Tp, 'Tf': Tf, 'Tv': Tv, 'Tvl': Tvl}

    ## Define Evaluation Points
    # Discretize
    theta, rwx, rwy = def_eval_points(n_el, f, radius)

    # Setup variables
    time = theta / omega
    wx = np.zeros(n_el)
    wy = np.zeros(n_el)
    iter = 0
    x_diff = np.ones(n_el)
    y_diff = np.ones(n_el)
    alpha = np.zeros(n_el)
    fn = 0.0
    ft = 0.0
    ct = 0.0
    ka = 0.0

    # Compute Induced Velocities
    while(np.any(x_diff > tol) or np.any(y_diff > tol)) and (iter < max_iter):
    # for z in np.arange(2):
        iter += 1
        wx_old = wx
        wy_old = wy

        # Calculate Velocities
        vx = u_inf + omega * radius * np.cos(theta) + u_inf * wx
        vy = omega * radius * np.sin(theta) + u_inf * wy
        vt = vx * np.cos(theta) + vy * np.sin(theta)# Tangential,
        vn = vx * np.sin(theta) - vy * np.cos(theta)# Radial,
        v_rel = np.sqrt(vx**2 + vy**2)

        # Calculate angle of attack
        phi = np.arctan(vn/vt)
        alpha = phi + pitch - twist
        deg_alpha = np.rad2deg(alpha)

        # interpolate lift and drag
```

```
        if DSFlag:
            cl, cd = dynamic_stall(alpha, time, c, v_rel, polar, constants)
        else:
            cl = np.interp(deg_alpha, polar['alpha'], polar['cl'])
            cd = np.interp(deg_alpha, polar['alpha'], polar['cd'])

        # Blade Loading
        cn = cl * np.cos(alpha) + cd * np.sin(alpha)
        c_tan = cl * np.sin(alpha) - cd * np.cos(alpha)
        fn = 0.5 * rho * v_rel ** 2 * c * cn # Normal, pointing outwards
        ft = 0.5 * rho * v_rel ** 2 * c * c_tan # Tangential, trailing to leading
        qn = blades * (fn * np.cos(pitch) - ft * np.sin(pitch)) /
                (2 * np.pi * radius * rho * u_inf **2)
        qt = -blades * (ft * np.cos(pitch) - fn * np.sin(pitch)) /
                (2 * np.pi * radius * rho * u_inf **2)

        # Influence of control point (i) on other locations (j)
        wx = 1 / (2 * np.pi) * np.matmul(rwx, qn)
        wy = 1 / (2 * np.pi) * np.matmul(qn, rwy)

        # Add effect of cylinder
        if f > 1:
            for j in np.arange(int(n_el/2), n_el):
                wx[j] = wx[j] + qn[j] - qn[n_el - 1 - j]
        elif f < 1:
            for j in np.arange(int(n_el/2)):
                wx[j] = wx[j] - qn[j]
            for j in np.arange(int(n_el/2), n_el):
                wx[j] = wx[j] - qn[n_el - 1 - j]

        # Thrust Coefficient
        ct = np.trapz(qn * np.sin(theta) + qt * np.cos(theta), theta)
        a = 0.0892*ct**3 + 0.0544*ct**2 + 0.2511*ct - 0.0017
        ka = 1/(1-a)
        wx_new = ka * wx
        wy_new = ka * wy

        # Relaxation
        wx = ((1 - relax) * wx_new + relax * wx_old)
        wy = ((1 - relax) * wy_new + relax * wy_old)

        x_diff = abs(wx-wx_old)
        y_diff = abs(wy-wy_old)
        # End While Loop

    # Power Coefficient through Trapezoidal numerical integration
    if iter < max_iter: # means it has converged
        temp = blades * ((ft * np.cos(-pitch) + fn * np.sin(-pitch)) *
                 omega * radius) / (0.5 * rho * 2 * radius * u_inf**3)
        cp = 1 / (2 * np.pi) * np.trapz(temp, theta)
    else:
        cp = np.nan
        ct = np.nan
    cx1 = fn * np.sin(theta) + ft * np.cos(theta)
    cy1 = -fn * np.cos(theta) + ft * np.sin(theta)
    theta2 = np.mod(theta + np.pi, 2*np.pi)
    cx2 = np.interp(theta2, theta, cx1)
    cy2 = np.interp(theta2, theta, cy1)
    cx = cx1 + cx2
    cy = cy1 + cy2

    data = {'ct': ct, 'cp': cp, 'theta': np.rad2deg(theta),
            'alpha': np.rad2deg(alpha), 'cn': cn, 'cx': cx,
            'cy': cy, 'cl': cl, 'cd': cd, 'v_rel': v_rel, 'c_tan': c_tan}
    return data
```

G

PitchVAWT Operation Manual

Pitchvawt Installation and Operation

Bruce LeBlanc

December 2019

1 Introduction

This document explains the design, layout, functionality and operation of the PitchVAWT Controller. The layout of the document is in two fundamental sections. The first section will discuss the installation and operation of the turbine and the second will discuss the design of the software which runs the turbine. The first section is laid out as follows: For context, a simple description of the turbine will be given including operating goals and overall physical design; Next the installation and calibration of the turbine will be discussed; An overview of general operation is presented, followed by a sample data file with descriptions of the variables output.

2 Turbine Description

The PitchVAWT turbine is a two-bladed H-shaped vertical axis wind turbine with two horizontal struts on each blade mounted at approximately 25% and 75% of the blade height. The turbine rotor has both a height and diameter of $1.5m$. Overall turbine design specifications are given in Table 1. The NACA0021 airfoil was chosen for blade geometry due to its fairly common use in VAWT research and its relative thickness for structural stability. The chord-radius ratio of 0.1 was chosen to minimize the effects of flow curvature. A set of thrust bearings transfer the thrust and weight of the rotor to the structural base of the turbine while allowing the rotation and torque to be passed through a torque and speed sensor. The drive-line then extends from the torque sensor to the generator / motor at the very base of the turbine. The full turbine system is then mounted to a blue positioning lift which acts as a foundation for the turbine system. A picture of the installed turbine at the Open Jet Facility in Delft, The Netherlands is shown in Figure 1, with a dimensioned drawing given in Figure 2.

3 Turbine Installation

Physical installation of the turbine is discussed first followed by wiring of the system.

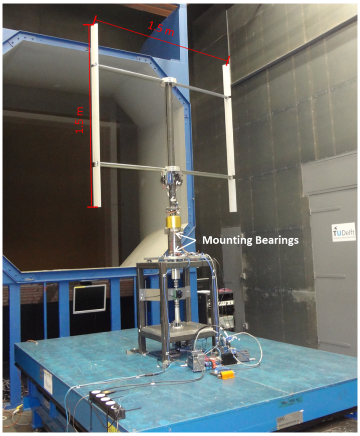

Figure 1: PitchVAWT installed in Open Jet Facility

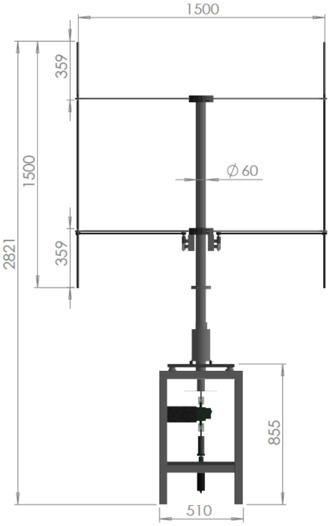

Figure 2: PitchVAWT CAD model, dimensions in *mm*

Table 1: PitchVAWT Design Specifications

Property	Dimension
NBlades	2
NStruts	4
Height	1.5 m
Diameter	1.5 m
Blade Chord	0.075 m
Strut Chord	0.060 m
Solidity	0.1
Blade Airfoil	NACA0021
Strut Airfoil	NACA0018
Operating TSR	1 to 4

3.1 Turbine mounting

The turbine is stored in two pieces. The base, and the rotor, see Figures 3 and 4. The rotor is kept in a separate custom storage box. There is an Up Arrow pointing to which direction should remain up. The box contains the fully assembled rotor including the pitch mechanisms and motors. The base is also fully assembled, including all of the major wiring and sensor connections, however at this point the controller itself is separate for safe keeping in between tests.

The installation is performed in the following procedure:

1. Center the blue platform base a distance of 0.75 m from the opening of the tunnel.
2. Lower the jack screws on each corner of the platform base to support the table.
3. Check the level of the blue platform using a long bubble level and adjust the jack screws accordingly. (This can be done by using the pneumatic lift to take the load off of the jack while it is being adjusted)
4. Set the height of the top of the blue base to 0.725 m.
5. Place the turbine base in the center of the blue table and orient it such that the torque sensor output is facing away from the tunnel outlet.
6. Adjust the four jack screws under the turbine feet until the base is level.
7. Use a set of machine clamps to secure the welded steel tabs at the bottom of each leg of the turbine to the blue table.
8. Mount the rotor to the turbine base using a 17 mm open-end wrench on the 6 bolts from the lower half of the mounting flange

Figure 3: PitchVAWT is stored in two components, the base and the rotor

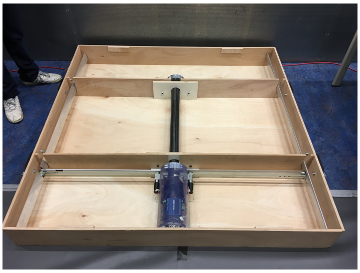

Figure 4: PitchVAWT rotor in storage box

    (a) There is a centering ring flange which helps to align the two shafts
    (b) Be extra careful not to pinch any of the wires coming from the rotor controllers
    (c) Be sure to tighten the mounting bolts well enough so they don't vibrate loose during operation. Arm tight with the good open-end wrench will suffice.

9. The wires on the rotational half of the slip ring are labeled with a number(control signals) or letter(strain gages). Connect each wire to the corresponding letter / number on the rotor.

10. Rotate each turbine blade so the paint markings on the lower bearing mounts coincide with the tape on the airfoil.
    (a) This sets the initial state for the pitch system, and will be more finely tuned during the calibration procedures

Once all of the wire connections are made, the rotor should turn freely.

3.2 Turbine Wiring

3.2.1 Power

The turbine and controller are run off of a 24 VDC power supply. The schematic is shown in Figure 5.

3.2.2 Signals and Controller

The rotor wiring is straight forward from the slip-rings as discussed in the above procedure. The slip-ring transfers 24 VDC power to the motor controllers, control signals for the pitch mechanisms and the analog strain gage data. The bottom turbine controller should be connected as given in the channel layout in Appendix A. Custom cables have been previously made in order to simplify this process as much as possible. The 37-pin d-sub connector cable and breakout only fits with the first module. This module handles most of the generic I/O signals for controlling the turbine. The 8-pin d-sub fits into the second module, this module is connected to a custom cable which runs to the rotary encoder and torque sensor for the turbine. Two wires from this custom cable are labeled + and - 24 VDC. This should be wired to the main power bus on the DIN rail after the main switch. Two wires are labeled as Torque + and Torque -. These are wired into module 3 channels 1 and 2 respectively. If the gust generator is present, the output from the position sensor on the gust generator is wired into channels 3 and 4 of the analog input card (module 3). Module 4 contains the strain gages, each of them are labeled and pre-wired. Plug in the appropriately labeled RJ-50 cable for the bottom and top strain sets as discussed in the appendix. The fifth module is for the load cells. Each of these has been labeled previously. Connect the appropriate BNC Cable to the channels in order

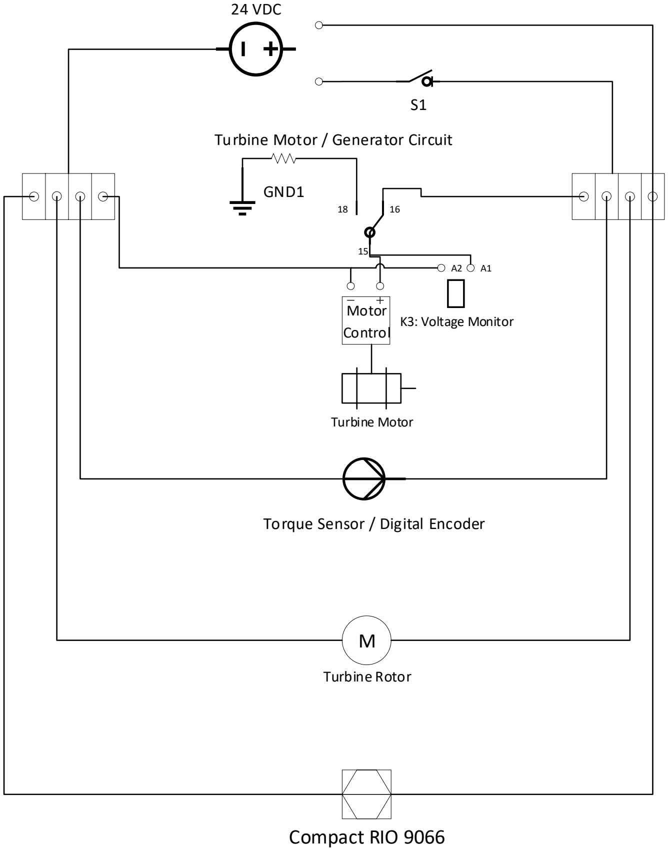

Figure 5: 24V Power layout for PitchVAWT

from 1 to 4. The sixth module is for a tri-axial accelerometer setup which has been mounted on the base in order to measure the platform response.

3.3 Powering On

The National Instruments power supply is wired directly to the National Instruments CRIO-9066 controller. The rest of the signals are wired through a two position switch. Therefore it is possible to control power to the turbine itself, the rotor and the torque / position sensor, independently from the main controller. In order to power up the turbine follow the below procedure:

1. Verify all turbine power and signal connections are wired correctly
2. Put power switch into off or "0" position
3. According to the procedure outlined in section 4, align the rotor to zero.
4. According to the procedure outlined in section 4.3, set the turbine pitch.
5. Plug in the NI 24 VDC power supply into a standard 240 V wall plug.
6. The LED lights on the Compact RIO should flash, and eventually stabilize on with the "Power" and "Status" lights both on green.
7. Throw main power switch to on.
    (a) The Torque and position sensor will flash three LED lights, showing that it is booting up and will stabilize with a green blinking LED.
    (b) Both blade position controllers will show a stable green LED
    (c) The Maxon ESCON 70/10 motor controller will blink a green LED
8. If all lights are functioning as described, the turbine controller is ready.

4 Sensor Calibration

Each sensor on the turbine has to be calibrated in order to develop a sensitivity relating the voltage or current output of the sensor to an engineering value. Two of which are needed for operation of the turbine and change each time the turbine is installed. These two will be discussed in detail here. The detailed calibration for the rest of the sensors is given elsewhere. For the calibration the main tool required is the laser orientation device available in the Open Jet Facility, and a reliable way of measuring distance, for example, a tape measure.

The sensors for azimuth position and for pitch are relative encoders. This means that they measure a change versus the initial condition of the turbine. Therefore prior to powering on the turbine, the azimuth should be placed at zero and the pitch for each blade should be set to their respective starting positions.

4.1 Setup laser alignment system

The Open Jet Facility has a portable laser alignment device, Gadella FL 55 Plus, see Figure 6. This is used to align the pitch and azimuth position to the outlet of the wind tunnel. The general procedure is to align the laser so it is directly underneath the turbine blade 1, at the same distance from the tunnel as the rotational center of the turbine.

1. The table should already be centered and aligned with the outlet of the tunnel.
2. Make a line in the radial direction of the turbine corresponding to the turbine center, this should coincide with the middle of the blue platform base
3. Measure and mark out 0.75 m from the turbine center along the previously marked line. This will serve as a reference to base the further calibrations.
4. Check the alignment of the laser setup by turning on the two vertical alignment lasers, the first should pass directly through the center of the turbine, while the second should be parallel to the ceiling rafters and the wind tunnel outlet

4.2 Azimuth Calibration

The torque measurement sensor also includes an optical rotary encoder which outputs a quadrature signal corresponding to 1600 pulses per revolution, the sensor is shown installed on the turbine in Figure 7. The signal is read into Module 2 digital I/O card discussed in Appendix A. The quadrature count is stored within the digital module. This means that as soon as the controller is powered, the number of counts is being tracked. Because the device is active, it will only output counts if the sensor has power. Therefore it is best to align the rotor to zero theta prior to powering the controller and turbine on. However, if the controller is not actively running the turbine, it is possible to remove and reinstall the digital input card thereby resetting the count.

Step by Step calibration procedure:

1. Start with turbine controller powered off
2. Set up alignment laser with above procedure
3. Rotate turbine until laser aligns with turbine strut and crosses through the pitch-axis of the blade, see Figure 8.
4. Loosen trigger flag at base of turbine: this provides a digital TTL pulse to the controller in order to properly sync external devices such as PIV or Hotwire measurement systems.
5. Align trigger flag so it just passes into the phototransistor as shown in Figure 9.

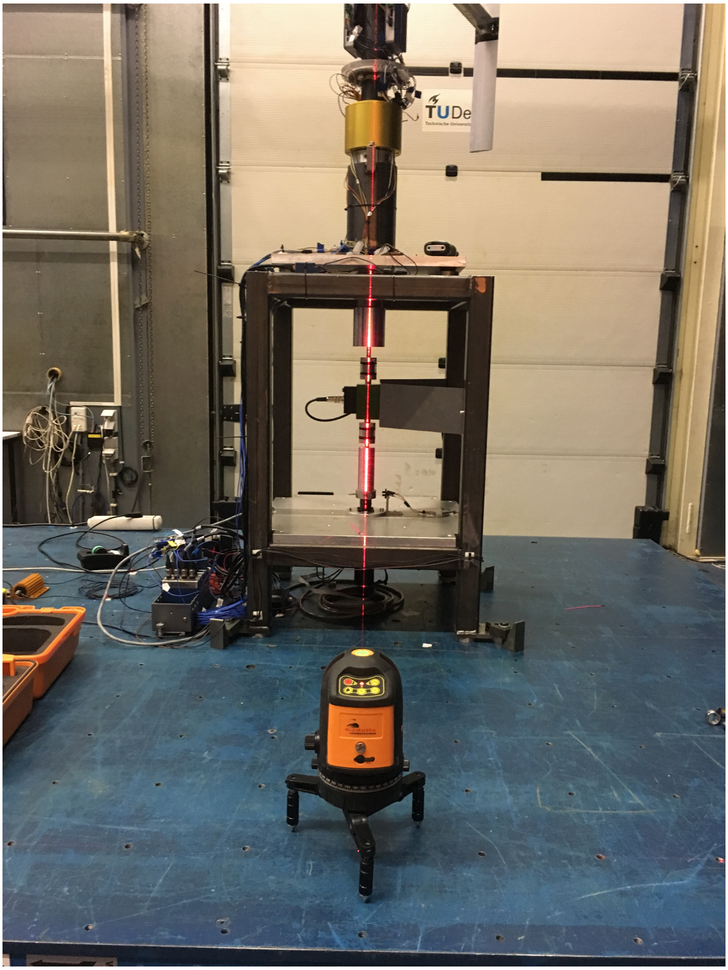

Figure 6: Gadella FL 55 Plus laser alignment system is used to align the azimuth position and pitch position of the PitchVAWT turbine to the Open Jet Facility tunnel outlet.

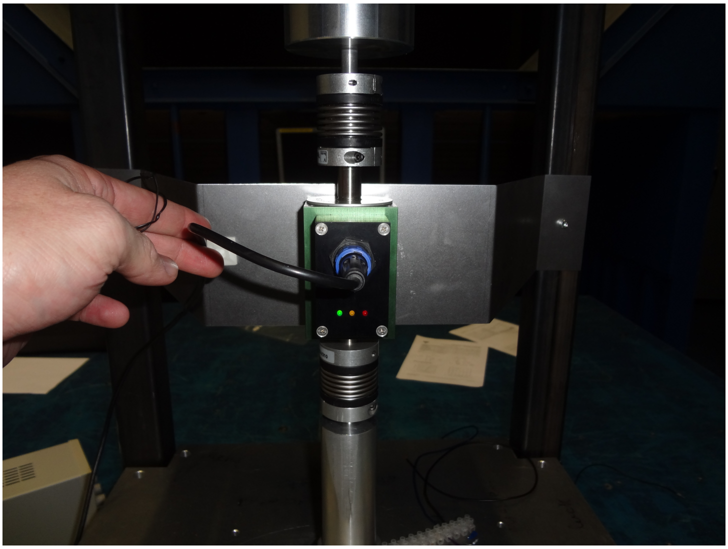

Figure 7: The Burster rotary encoder and torque measurement system installed on the PitchVAWT

6. Tighten the trigger flag to the turbine shaft.
7. Once the turbine is aligned in azimuth, continue with the Powering On procedure given in section 3.3.
8. During operation between tests, periodically check the alignment to ensure that there has been no slippage of the turbine during any high-torque (>5 N m peak) events.

If there has been slippage, it is possible to reset the theta count to zero without completely turning off the controller. This is performed by:

1. Make sure turbine is not rotating and wind is off.
2. Hit STOP button on turbine controller User Interface.
3. Right click on the CRIO in the Labview Project, and click disconnect from target.
4. Remove Module 2 from the CRIO chassis for 10 seconds and replace
5. Reconnect to the controller target and start the turbine. (no rotation).
6. The azimuth should be reset to zero.
7. Make sure to also check the trigger flag to make sure it is still properly aligned.

4.3 Pitch Calibration

The turbine pitch is controlled by independent motor controllers housed on the rotor itself. The pitch system encoder is relative, meaning that the turbine only knows where the pitch is relative to its position when it is powered on. Therefore, the pitch needs to be set to align with the tunnel prior to being powered. This however, is difficult, because the default position without power for the turbine is at the maximum possible, or 24.5° toe-in. This is due to the controller only accepting a positive control voltage. It is achieved through the following procedure:

1. Begin with the turbine off
2. Set up alignment laser with above procedure
3. Set the blade pitch to the positive toe in marker corresponding to the painted line on the pitch bearings
4. Power on the turbine and connect with the controller
5. Blades will automatically pitch to the zero pitch position.

Figure 8: Alignment laser setup for zeroing turbine azimuth position

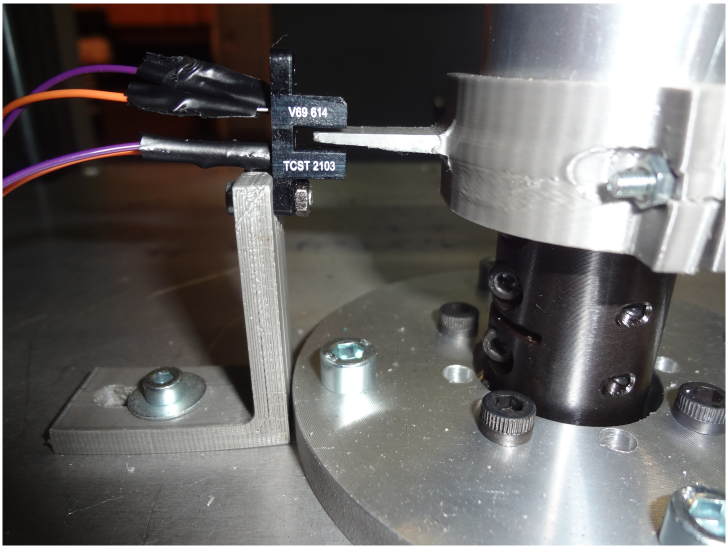

Figure 9: Vishay Transmissive Optical Sensor used as trigger input for PIV

6. Power on the laser alignment device and make sure turbine is aligned with Zero theta position.
7. The lasers should cross the pitch axis of the turbine and hit both the leading and trailing edges of the airfoil as shown in Figure 10.
8. If the pitch needs adjustment:
   (a) Hit STOP button on turbine controller and wait until blades park themselves at the homing position
   (b) Turn off power to the turbine using the power on - off switch. The controller should remained powered during this step
   (c) When power is removed from the pitch motors, they are able to be moved by hand.
   (d) Make the necessary adjustments to the blade pitch
   (e) turn power back on to the turbine
   (f) recheck pitch by reconnecting device and measuring with laser alignment system
   (g) repeat as necessary
9. repeat the process for blade two by rotating the turbine 180° keeping the laser setup in the same spot and making fine adjustments to the radial position of the laser (blades 1 and 2 are slightly different due to manufacturing).

5 Operation

The turbine controller consists of two computers: the embedded real-time controller, and a windows laptop PC. The two are connected with a traditional ethernet cable and communicate over TCP/IP.

5.1 Turbine States

The turbine is always in one of four states:

- OFF
- POWERED
- PAUSE
- RUN

Figure 10: Alignment laser for setting pitch

5.1.1 OFF

"OFF" is as to be expected. In this state the turbine is without power and not connected.

- All motors are free to move by hand
- Turbine has no ability to collect data or control itself
- if moved in this state, the azimuth and pitch will need to be reset prior to advancing states

5.1.2 POWERED

"POWERED" state refers to the time when the turbine has power, however the labview programs are not yet running. In this state the turbine is actively controlling the pitch value of the blades, even if there is no pitch command. The turbine is holding pitch to the home value of positive max pitch. The user computer may or may not be powered on at this point however no data is being logged.

- Blade pitch is actively held at home position
- Data is being collected by controller but not logged
- Rotor is free to rotate by hand
- Rotor position is monitored but not controlled

5.1.3 PAUSE

"PAUSE" state refers to the state where the turbine is powered, the user PC and real-time embedded controller are sharing data through TCP/IP connection, but the turbine is not controlling rotor speed. This state is used whenever a dataset is not actively being taken.

- Data being communicated back to user PC
- Datalog option is available
- Blades controlled based upon user request
- Rotor speed is not controlled, free to rotate by hand as needed
- Do not operate the turbine in this state if wind is present as the controller is not actively controlling the rotational speed of the machine

5.1.4 RUN

In the "RUN" state, all functions of the turbine are active. This is the state used while rotating the turbine for testing.

- Turbine Run function is enabled
- Rotational speed of the turbine is actively controlled
- Blade pitch is actively controlled based upon user selection
- Datalog is available based upon user selection

5.2 Using the controller

There are two main Virtual Instruments (VIs) which need to be run when starting the PitchVAWT turbine. The first is the Real-Time user interface which runs on the embedded controller shown in Figure 11. All that needs to be done with this interface is to click on the white "run" arrow in the top left corner of the VI. This starts running the embedded turbine controller and prepares it for connection to the user PC. The next VI is the main user interface which runs on the user PC. This interface is shown in Figure 12.

This user interface provides all of the turbine controls, including Turbine Run Enable operation, turbine RPM, Datalogging, STOP functionality, and pitch control settings. It also provides close to real-time data output for specific values which can be of use while operating the turbine. This data stream is separate from the datalog, which operates in a separate loop and writes the data directly to disk from the turbine controller.

5.3 Data logging

The file name and location should be set for the datalog prior to starting the User Interface VI. If this is not specified, a default folder and filename are automatically created. Data is only logged when the "DATALOG" switch is flipped to True. Data is saved in a *.txt file of the name given in the dialog box. Data is recorded at a rate of 500 Hz so the size of the file can grow fairly rapidly. The description of each variable that is logged is given in Appendix B

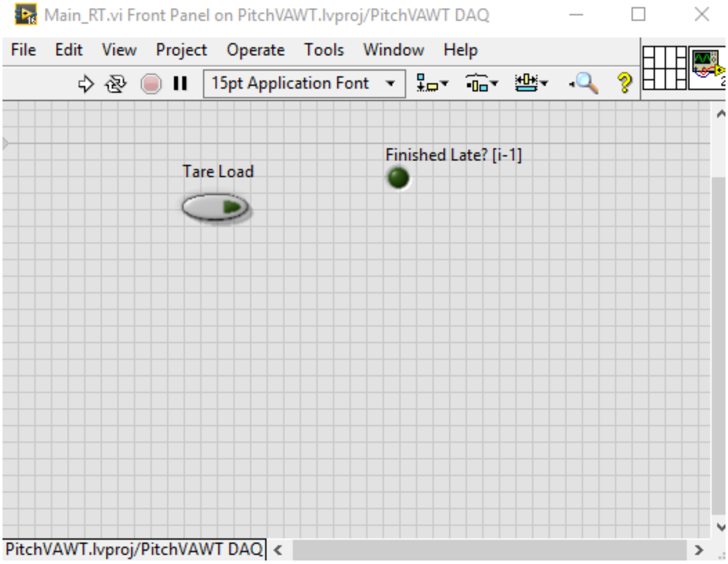

Figure 11: Real-Time interface

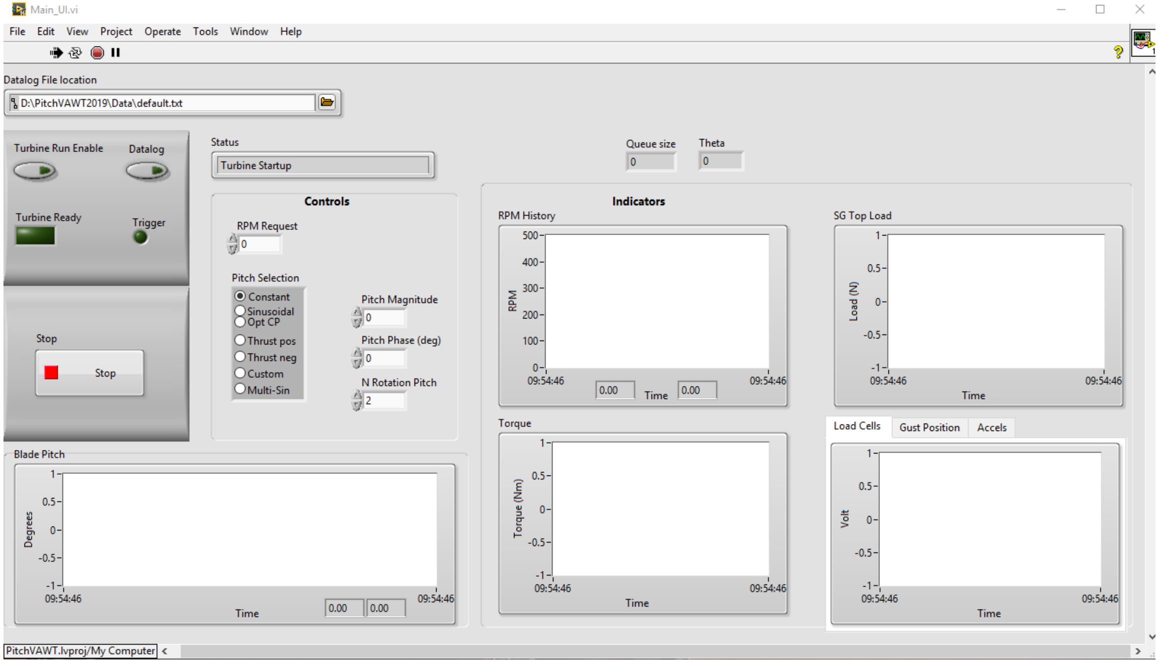

Datalog File location: D:\PitchVAWT2019\Data\default.txt

Status: Turbine Startup

Queue size: 0

Theta: 0

RPM Request: 0

Pitch Selection:
- ● Constant
- ○ Sinusoidal
- ○ Opt CP
- ○ Thrust pos
- ○ Thrust neg
- ○ Custom
- ○ Multi-Sin

Pitch Magnitude: 0

Pitch Phase (deg): 0

N Rotation Pitch: 2

RPM History: 0.00 Time 0.00

Blade Pitch: 0.00 0.00

Figure 12: PitchVAWT user interface

A Channel Layout

Table 2: PitchVAWT Controller Module Layout

Channel	**Label**	**Description**
Module 1: NI 9381 Multifunction I/O		
1	AO0	Motor set point
2	AO1	Blade 1 set point
3	GND	Motor signal ground
4	AO4	PIV Trigger Out
5	AO5	open
6	GND	Rotor signal ground
7	AI0	Motor speed in
8	AI1	Motor current in
9	AI2	open
10	AI3	open
11	AI4	open
12	AI5	open
13	AI6	open
14	AI7	open
15	DIO0	Maxon Motor Controller Enable
16	DIO1	open
17	DIO2	open
18	DIO3	Trigger in
19	GND	open
20	GND	open
21	AO2	Blade 2 set point
22	AO3	open
23	GND	open
24	AO6	open
25	AO7	Voltage source for trigger
26	GND	open
27	GND	open
28	GND	open
29	GND	open
30	GND	open
31	GND	open
32	GND	open
33	GND	open
34	GND	open
35	GND	open
36	GND	open
37	GND	open
Module 2: NI 9401 Digital I/O		
1	DIO	Encoder A

Channel	**Label**	**Description**
2	DIO	Encoder B
3	DIO	Encoder C
4	DIO	open
Module 3: NI 9215 Analog Input		
1	AI0 +	Torque In +
2	AI0 -	Torque In -
3	AI1 +	Gust In +
4	AI1 -	Gust In -
5	AI2 +	open
6	AI2 -	open
7	AI3 +	open
8	AI3 -	open
Module 4: NI 9237 Strain Gage Card		
1	CH0	Bottom Strut Strain
2	CH1	Top Strut Strain
3	CH2	open
4	CH3	open
Module 5: NI 9234 4 Channel IEPE Analog input		
1	AI0	PCB Load Cell 1
2	AI1	PCB Load Cell 2
3	AI2	PCB Load Cell 3
4	AI3	PCB Load Cell 4
Module 6: NI 9234 4 Channel IEPE Analog input		
1	AI0	Accelerometer -X
2	AI1	Accelerometer -Y
3	AI2	Accelerometer +Z
4	AI3	open

Table 3: Strain Gage Pin-out for NI-9237 Channel

Pin	**Label**
1	SC
2	AI +
3	AI -
4	RS +
5	RS -
6	EX +
7	EX -
8	T +
9	T -
10	SC

B Datalog Description

Data is logged at a rate of 500 Hz in a tab separated *.txt file of specified name.
Variables which are logged are defined in Table 4.

Table 4: Description of Datalog Variables

Variable	**Description**
Timestamp	Timestamp of recorded data in format: HH:MM:SS.xxxx
EncoderRPM	Rotational speed of turbine measured from the rotary encoder, RPM
MotorCurrentA	Motor current, Amps
SpeedSetpointRPM	Rotor speed set point from controller, RPM
MotorSpeedRPM	Rotor speed output from maxon controller, RPM
ThetaDEG	Azimuth position of rotor (blade 1), Degrees
TorqueNM	Turbine rotor torque, Newton-meters
Pitch1	Pitch set point for blade 1, degrees
Pitch2	Pitch set point for blade 2, degrees
StrainTop1	output voltage from full bridge strain gages on top strut, Volts
StrainBot1	output voltage from quarter bridge strain gage on bottom strut, Volts
StrainBlade	reserved for blade strain gage, not currently mounted, Volts
LoadCell1	Output from LoadCell 1, Volts
LoadCell2	Output from LoadCell 2, Volts
LoadCell3	Output from LoadCell 3, Volts
LoadCell4	Output from LoadCell 4, Volts
Trigger	Output from phototransistor trigger, Boolean
Status	Run Status, Boolean
PitchSelection	Pitch selection type, String
LoadTopStrutN	pre-calculated normal load based upon top strut strain gages, Newton
AccelMinX	Acceleration from base mounted accelerometer, -X Volts
AccelMinY	Acceleration from base mounted accelerometer, -Y Volts
AccelZ	Acceleration from base mounted accelerometer, +Z Volts
GustPos	Position of the gust generator vanes, Volts

Acknowledgements

This thesis is the culmination of a number of years of work throughout my career which has been influenced and guided along the way by many people. Inevitably I will leave people out, so I will only mention a brief few directly pertaining to the work presented here. First off, many thanks to my promoters, Carlos Ferreira, and Gerard van Bussel. Thank you for seeing something in me those (many at this point) years ago, and giving me a chance to come work in Delft. Gerard thank you for the helpful words and direction throughout the years. Carlos, I truly appreciate the day to day guidance throughout the PhD. I thank you for the sometimes difficult, always productive debates and discussions, and for challenging me to keep growing as a doctoral candidate and researcher. Our relationship went through several growth stages throughout my time here in Delft, I know I learned a lot and am a better researcher and engineer for it. I hope there will be many exciting projects together in the future!

Thanks to the Delft University Wind Group for welcoming me and providing an inspirational place to learn, grow, and mature as researchers. My time here was truly a unique experience I will always cherish. I want to extend my greatest gratitude to the talented team at DEMO who helped with the final design and fabrication of PitchVAWT. Without whom none of this work could have been accomplished. The same goes for the great people working in the wind tunnels and experimental setups of TU Delft: Nando, Ruud, Nico, Stefan, you were always available to give excellent advice and help in planning and technical questions with the tunnels, thank you.

To my PhD colleagues, I really enjoyed our wide ranging conversations from the state of renewable energy development to the taste of great beer. A special shout-out to the Dyna-Night crew! Sebastian, Rene, Daniel, Ashim, Vinit, you are a dynamic group of experts who really know how to bring a smile and some good ole fashion fun to your work and to those around you. It has been a pleasure! Delphine, Ming, I couldn't have asked for better people to work alongside while diving deep into the VAWT. Your enthusiasm, technical understanding, and easy to talk to personalities were really a highlight of my time in Delft. Jaco, Ines, Javier, what can I say, so many great stories and memories. Thanks for keeping me sane and for forging the rare kind of deep friendships throughout these last years which make life worth living. Let's keep the new memories coming far into the future!

And of course I couldn't have even considered taking on such an ambitious project like this without the support of my close friends and family both back home across the states and in the Netherlands, you know who you are, and I love you all.

References

[1] H. Ritchie, *Our world in data,* (2017).

[2] J. Manwell, J. G. McGowan, and A. L. Rogers, *Wind Energy Explained: Theory Design and Application*, second edition ed. (Wiley, West Sussex, United Kingdom, 2009).

[3] E. Möllerström, P. Gipe, J. Beurskens, and F. Ottermo, *A historical review of vertical axis wind turbines rated 100 kw and above,* Renewable and Sustainable Energy Reviews **105**, 13 (2019).

[4] H. J. Sutherland, D. E. Berg, and T. D. Ashwill, *A Retrospective of VAWT Technology*, Report SAND2012-0304 (Sandia National Laboratories, Albuquerque, NM, 2012).

[5] F. Zhao and J. Lee, *Global Wind Report 2019*, Report (Global Wind Energy Council, 2020).

[6] M. Fowler, D. Bull, and A. Goupee, *A Comparison of Platform Options for Deepwater Floating Offshore Vertical Axis Wind Turbines: An Initial Study*, Report SAND2014-16800 (Sandia National Laboratories, Albuquerque, NM, 2014).

[7] D. T. Griffith, J. A. Paquette, M. F. Barone, A. J. Goupee, M. Fowler, D. Bull, and B. Owens, *A study of rotor and platform design trade-offs for large-scale floating vertical axis wind turbines,* The Science of Making Torque from Wind (TORQUE 2016) Journal of Physics: Conference Series **753** (2016), 10.1088/1742-6596/753/10/102003.

[8] F. Huijs, E. Vlasveld, M. Gormand, F. Savenije, M. Caboni, B. P. LeBlanc, C. S. Ferreira, K. Lindenburg, S. Gueydon, W. Otto, and B. Paillard, *Integrated design of a semi-submersible floating vertical axis wind turbine (vawt) with active blade pitch control,* in *EERA DeepWind 2018, 15th Deep Sea Offshore Wind R&D Conference*, Vol. 1104, EERA DeepWind 2018, 15th Deep Sea Offshore Wind R&D Conference (IOP Publishing Ltd, 2018 Published) p. 12.

[9] B. L. Ennis and D. T. Griffith, *System Levelized Cost of Energy Analysis for Floating Offshore Vertical-Axis Wind Turbines*, Report SAND2018-9131 (Sandia National Laboratories, Albuquerque, NM, 2018).

[10] D. T. Griffith and T. D. Ashwill, *The Sandia 100-meter All-glass Baseline Wind Turbine Blade*, Report SAND2011-3779 (Sandia National Laboratories, Albuquerque, NM, 2011).

[11] C. J. Simão Ferreira, *The Near Wake of the VAWT 2D and 3D views of the VAWT Aerodynamics*, Thesis, Delft University of Technology, Delft, The Netherlands (2009).

[12] G. Tescione, D. Ragni, C. He, C. J. Simão Ferreira, and G. J. W. van Bussel, *Near wake flow analysis of a vertical axis wind turbine by stereoscopic particle image velocimetry,* Renewable Energy **70**, 47 (2014).

[13] V. Mendoza and A. Goude, *Improving farm efficiency of interacting vertical-axis wind turbines through wake deflection using pitched struts,* Wind Energy **22**, 538 (2019).

[14] P. Fleming, J. Annoni, J. Shah, L. Wang, S. Ananthan, Z. Zhang, K. Hutchings, P. Wang, W. Chen, and L. Chen, *Field test of wake steering at an offshore wind farm,* Wind Energy Science **2**, 229 (2017).

[15] P. Fleming, J. King, K. Dykes, E. Simley, J. Roadman, A. Scholbrock, P. Murphy, J. K. Lundquist, P. Moriarty, K. Fleming, J. van Dam, C. Bay, R. Mudafort, H. Lopez, J. Skopek, M. Scott, B. Ryan, C. Guernsey, and D. Brake, *Initial results from a field campaign of wake steering applied at a commercial wind farm – part 1,* Wind Energ. Sci. **4**, 273 (2019), wES.

[16] B. de Korte, *Investigating the potential of load and power control on a vawt through active pitch control*, Thesis, Delft University of Technology, Delft, The Netherlands (2019).

[17] B. LeBlanc and C. Ferreira, *Experimental demonstration of thrust vectoring with a vertical axis wind turbine using normal load measurements,* in *The Science of Making Torque from Wind (TORQUE 2020)*, Vol. 1618, The Science of Making Torque from Wind (TORQUE 2020) (IOP Publishing, 2020 Published) p. 11.

[18] B. P. LeBlanc and C. S. Ferreira, *Overview and design of pitchvawt: Vertical axis wind turbine with active variable pitch for experimental and numerical comparison,* in *AIAA SciTech Forum Wind Energy Symposium*, AIAA SciTech Forum Wind Energy Symposium (American Institute of Aeronautics and Astronautics, 2018 Published) p. 11.

[19] D. De Tavernier, A. Vire, and C. Ferreira, *Damping the floater motion of vertical-axis wind turbines using load optimisation,* in *NAWEA WindTech*, Vol. 1452, NAWEA WindTech (Journal of Physics Conference Series, 2020 Published) p. 14.

[20] D. De Tavernier, C. Ferreira, and G. van Bussel, *Airfoil optimisation for vertical axis wind turbines with variable pitch,* Wind Energy **22**, 547 (2018).

[21] K. J. Asztalos and D. Rempfer, *Performance optimization for vertical-axis wind turbines with blade-element method models,* Journal of Propulsion and Power **36**, 10 (2020).

[22] B. K. Kirke, *Evaluation of Self-Starting Vertical Axis Wind Turbines For Stand-Alone Applications*, Thesis, Griffith University, Gold Coast (1998).

[23] B. K. Kirke and B. Paillard, *Predicted and measured performance of a vertical axis wind turbine with passive variable pitch compared to fixed pitch,* Wind Engineering **41**, 74 (2017).

[24] P. Choegule and S. Nielsen, *Overview and design of self-acting pitch control mechanism for vertical axis wind turbine using multi body simulation approach,* in *The Science of Making Torque from Wind*, Vol. 524, edited by J. Mann, The Science of Making Torque from Wind (IOP Science, 2014 Published) p. 11.

[25] J. H. Strickland, *The Darrieus Turbine- A Performance Prediction Model Using Multiple Streamtubes*, Report SAND75-0431 (Sandia National Laboratories, Albuquerque, NM, 1975).

[26] B. F. Blackwell, R. E. Sheldahl, and L. V. Feltz, *Wind Tunnel Performance Data for the Darrieus Wind Turbine with naca0012 Blades*, Report SAND76-0130 (Sandia National Laboratories, Albuquerque, NM, 1976).

[27] M. H. Worstell, *Aerodynamic Performance of the 17-Metre-Diameter Darrieus wind turbine*, Report SAND78-1737 (Sandia National Laboratories, Albuquerque, NM, 1978).

[28] R. E. Sheldahl, P. C. Klimas, and L. V. Feltz, *Aerodynamic Performance of a 5-Metre-Diameter Darrieus Turbine With Extruded Aluminum NACA-0015 Blades*, Report SAND80-0179 (Sandia National Laboratories, Albuquerque, NM, 1980).

[29] R. E. Sheldahl, *Comparison of Field and Wind Tunnel Darrieus Wind Turbine Data*, Report SAND80-2469 (Sandia National Laboratories, Albuquerque, NM, 1981).

[30] D. E. Berg, *An improved double-multiple streamtube model for the darrieus-type vertical axis wind turbine,* in *Sixth Biennial Wind Energy Conference and Workshop*, Sixth Biennial Wind Energy Conference and Workshop (American Solar Energy Society, Inc., 1983 Published) pp. 231–238.

[31] R. Brulle, *Giromill wind tunnel test and analysis,* in *Proceedings of the Third Biennial Conference and Workshop on Wind Energy Conversion Systems* (1978).

[32] H. Drees, *The cycloturbine and its potential for broad application,* in *Proceedings of the Second International Symposium on Wind Energy Systems* (1978).

[33] W. Grylls, B. Dale, and P. Sarre, *A theoretical and experimental investigation into the variable pitch vertical axis wind turbine,* in *Proceedings of the Second International Symposium on Wind Energy Systems* (1978).

[34] A. H. Madsen and K. Lundgren, *The Voith-Schneider Wind Turbine: Some theoretical and experimental results on the aerodynamics of the voith-schneider wind turbine*, Report (Aalborg University, Aalborg, Denmark, 1980).

[35] J. H. Strickland, W. B. T., and T. Nguyen, *A Vortex model of the Darrieus Turbine: An Analytical and Experimental Study*, Report SAND79-7058 (Sandia National Laboratories, Lubbock, Texas, 1979).

[36] T. D. Ashwill, *Measured data for the Sandia 34 meter VAWT*, Report SAND91-2228 (Sandia National Laboratories, Albuquerque, NM, 1992).

[37] L. Battisti, G. Persico, V. Dossena, B. Paradiso, M. Raciti Castelli, A. Brighenti, and E. Benini, *Experimental benchmark data for h-shaped and troposkien vawt architectures,* Renewable Energy **18**, 50 (2018).

[38] I. Mauri, M. Bayati and M. Belloli, *Design and realisation of a high-performance active pitch-controlled h-darrieus vawt for urban installations,* in *Renewable Power Generation Conference*, Vol. 2014, Renewable Power Generation Conference (IET, 2014 Published).

[39] D. Pitance, S. Horb, J. Kluczewska-Bordier, A. Immas, and F. Silvert, *Experimental validation of pharwen code using data from vertical-axis wind turbines,* in *ADWEN offshore France* (ADWEN offshore France, 2016 Published).

[40] G. E. Reis and B. F. Blackwell, *Practical Approximations to a Troposkien by Straight-Line and circular arc Segments*, Report SAND74-0100 (Sandia National Laboratories, Albuquerque, NM, 1974).

[41] D. E. Berg, *Structural Design of the Sandia 34-Meter Vertical Axis Wind Turbine*, Report (Sandia National Laboratories, Albuquerque, NM, 1984).

[42] U. S. Paulsen, A. H. Madsen, K. A. Kragh, P. H. Nielsen, I. Baran, J. H. Hattel, E. Ritchie, K. Leban, H. Svendsen, and P. A. Berthelsen, *Deepwind - from idea to 5 mw concept,* Energy Procedia , 23 (2014).

[43] W. Moran, *Giromill Wind Tunnel Test and Analysis Final Report*, Report COO/2617-4/2 (McDonnell Aircraft Company, St. Louis, MO, 1977).

[44] B. K. Kirke and L. Lazauskas, *Enhancing the performance of a vertical axis wind turbine using a simple variable pitch system,* Wind Engineering **15**, 187 (1991).

[45] E. Vlasveld, F. Huijs, F. Savenije, and B. Paillard, *Coupled dynamics of a vertical axis wind turbine (vawt) with active blade pitch control on a semi-submersible floater,* in *International Conference o n Ocean, Offshore and Arctic Engineering*, International Conference o n Ocean, Offshore and Arctic Engineering (American Society of Mechanical Engineers, OMAE2018-78058, 2018 Published).

[46] D. De Tavernier, C. Ferreira, A. Li, U. S. Paulsen, and H. A. Madsen, *Vawt in double-rotor configuration: the effect on airfoil design,* in *AIAA SciTech Forum*, AIAA SciTech Forum (American Institute of Aeronautics and Astronautics, 2018 Published).

[47] P. R. Ashill, T. Binion, K. R. Cooper, R. Crites, J. L. Everhart, B. F. R. Ewald, J. E. Hackett, H. Holst, A. Krynytzky, N. D. Malmuth, M. Mokry, P. A. Newman, W. L. Sickles, F. W. J. Steinle, C. R. Taylor, N. J. Taylor, R. Voß, and E. H. Wedemeyer, *Wind Tunnel Wall Corrections* (Advisory Group for Aerospace Research and Development, BP 25, 7 RUE ANCELLE, F-92201 NEUILLY-SUR-SEINE CEDEX. FRANCE, 1998) p. 560.

[48] M. Drela, *Xfoil subsonic airfoil development system,* (2013).

[49] A. L. Braslow and E. C. Knox, *Simplified Method for Determination of Critical Height of Distributed Roughness Particles for Boundary-layer Transition at Mach Numbers from 0 to 5*, Report Technical Note 4363 (National Advisory Committee for Aeronautics, Langley Field, Virginia, USA, 1958).

[50] J. G. Leishman, *Principles of Helicopter Aerodynamics*, Cambridge Aerospace (Cambridbe University Press, Cambridge, UK, 2002).

[51] R. C. Reuter and M. H. Worstell, *Torque Ripple in a Vertical Axis Wind Turbine*, Report SAND78-0577 (Sandia National Laboratories, Albuquerque, NM, 1978).

[52] N. Instruments, *Queued message handler template,* (2017).

[53] C. S. Ferreira, H. A. Madsen, M. Barone, B. Roscher, P. Deglaire, and I. Arduin, *Comparison of aerodynamic models for vertical axis wind turbines,* Journal of Physics: Conference Series **524**, 012125 (2014).

[54] H. A. Madsen, *The Actuator Cylinder*, Report 530005953978 (Institute of Industrial Constructions and Energy Technology Aalborg University Centre, Aalborg, 1982).

[55] A. H. Madsen, *On the Ideal and real Energy Conversion in a Straight Bladed Vertical Axis Wind Turbine*, Report (Aalborg University Centre, Aalborg, Denmark, 1983).

[56] A. H. Madsen, T. J. Larsen, U. S. Paulsen, and L. Vita, *Implementation of the actuator cylinder flow model in the hawc2 code for aeroelastic simulations on vertical axis wind turbines,* in *51st AIAA Aerospace Sciences Meeting including the New Horizons Forum and Aerospace Exposition*, Vol. 2013, 51st AIAA Aerospace Sciences Meeting including the New Horizons Forum and Aerospace Exposition (American Institute of Aeronautics and Astronautics, AIAA 2013-0913, 2013 Published) p. 13.

[57] J. Katz and A. Plotkin, *Low-Speed Aerodynamics*, 2nd ed. (Cambridge University Press, New York, NY, 2001).

[58] D. Marten, J. Wendler, G. Pechlivanoglou, C. Nayeri, and C. Paschereit, *Qblade: An open source tool for design and simulation of horizontal and vertical axis wind turbines,* International Journal of Emerging Technology and Advanced Engineering **3**, 264 (2013).

[59] J. C. Murray and M. Barone, *The development of cactus a wind and marine turbine performance simulation code,* in *49th AIAA Aerospace Sciences Meeting including the New Horizons Forum and Aerospace Exposition*, Vol. 49, 49th AIAA Aerospace Sciences Meeting including the New Horizons Forum and Aerospace Exposition (American Institute of Aeronautics and Astronautics, AIAA 2011-147, 2011 Published).

[60] J. C. Murray and M. F. Barone, *CACTUS User's Manual Version 1.1*, Report (Sandia National Laboratories, Albuquerque, NM, 2011).

[61] A. H. Madsen, U. S. Paulsen, and L. Vita, *Analysis of vawt aerodynamics and design using the actuator cylinder flow model,* in *The Science of Making Torque from Wind*, The Science of Making Torque from Wind (IOP Science, 2014 Published) p. 11.

[62] J. G. Holierhoek, J. B. de Vaal, A. H. van Zuijlen, and H. Bijl, *Comparing different dynamic stall models,* Wind Energy **16**, 139 (2012).

[63] J. G. Leishman and T. S. Beddoes, *A semi-empirical model for dynamic stall,* Journal of the American Helicopter Society **34**, 15 (1989).

[64] R. B. d. S. Pereira, *Validating the Beddoes-Leishman Dynamic Stall Model in the Horizontal Axis Wind Turbine Environment*, Thesis, Instituto Superior Tecnico, Portugal (2010).

[65] P. Migliore, *Flow curvature effects on darrieus turbine blade aerodynamics,* Journal of Energy **4**, 49 (1980).

[66] J. L. Cardona, *Flow curvature and dynamic stall simulated with an aerodynamic free-vortex model for vawt,* Wind Engineering **8**, 135 (1984).

[67] S. v. d. Horst, *Airfoil Design For Vertical Axis Wind Turbines Including Correct Simulation of Flow Curvature*, Thesis, Delft University of Technology, Delft, The Netherlands (2015).

[68] A. Bianchini, D. Marten, A. Tonini, F. Balduzzi, C. N. Nayeri, G. Ferrara, and C. O. Paschereit, *Implementation of the virtcual camber transformation into the open source software qblade: Validation and assessment,* in *73rd Conference of the Italian Thermal Machines Engineering Association*, Vol. 148, 73rd Conference of the Italian Thermal Machines Engineering Association (Energy Procedia, 2018 Published) pp. 210–217.

[69] C. Simão Ferreira and F. Scheurich, *Demonstrating that power and instantaneous loads are decoupled in a vertical-axis wind turbine,* Wind Energy **17**, 385 (2014).

[70] B. LeBlanc and C. Ferreira, *Experimental characterization of h-vawt turbine for development of a digital twin,* in *North American Wind Energy Association / Windtech*, Vol. 1452, edited by J. Manwell, North American Wind Energy Association / Windtech (IOP Science, 2019 Published).

[71] P. S. Veers, D. L. Laird, T. G. Carne, and M. J. Sagartz, *Estimation of uncertain material parameters using modal data,* in *1998 ASME Wind Energy Symposium*, Vol. 98, 1998 ASME Wind Energy Symposium (American Institute of Aeronautics and Astronautics, 1998 Published).

[72] D. T. Griffith, J. A. Paquette, and T. G. Carne, *Development of validated blade structural models,* in *46th AIAA Aersopace Sciences Meeting and Exhibit*, Vol. 2008, 46th AIAA Aersopace Sciences Meeting and Exhibit (American Institude of Aeronautics and Astronautics, 2008 Published) p. 11.

[73] D. T. Griffith and T. G. Carne, *Experimental modal analysis of 9-meter research-sized wind turbine blades,* in *International Modal Analysis Conference XXVIII*, International Modal Analysis Conference XXVIII (Society of Experimental Mechanics, Inc., 2010 Published).

[74] T. G. Carne and A. R. Nord, *Modal Testing of a Rotating Wind Turbine*, Report SAND82-0631 (Sandia National Laboratories, Albuquerque, NM, 1982).

[75] G. H. I. James, T. G. Carne, and J. Lauffer, *The natural excitation technique (next) for modal parameter extraction from operating structures,* The International Journal of Analytical and Experimental Modal Analysis **10**, 17 (1995).

[76] S. Manzato, J. R. White, B. P. LeBlanc, and B. Peeters, *Development of techniques for enhanced operational modal analysis of wind turbine,* in *Fifth International Operational Modal Analysis Conference* (Fifth International Operational Modal Analysis Conference, 2013 Published).

[77] B. P. LeBlanc, D. Cloutier, and T. Marinone, *Overview of the dynamic characterization at the doe/snl swift wind facility,* in *International Modal Analysis Conference IMAC XXXII Dynamics of Coupled Structures* (International Modal Analysis Conference IMAC XXXII Dynamics of Coupled Structures, 32i-250, 2014 Published).

[78] R. J. Allemang and D. Brown, *A correlation coefficient for modal vector analysis,* in *International Modal Analysis Conference*, International Modal Analysis Conference (Society of Experimental Mechanics, 1982 Published).

[79] R. Allemang, *The modal assurance criterion - twenty years of use and abuse,* Sound and Vibration , 8 (2003).

[80] B. LeBlanc and C. Ferreira, *Estimation of blade loads for a variable pitch vertical axis wind turbine from particle image velocimetry,* Wind Energy **25**, 313 (2022), https://onlinelibrary.wiley.com/doi/pdf/10.1002/we.2674 .

[81] D. Castelein, D. Ragni, G. Tescione, C. J. Simão Ferreira, and M. Guanaa, *Creating a benchmark of vertical axis wind turbines in dynamic stall for validating numerical models,* in *33rd Wind Energy Symposium AIAA SciTech Forum*, 33rd Wind Energy Symposium AIAA SciTech Forum (American Institute for Aeronautics and Astronautics, 2015 Published).

[82] D. Castelein, *Dynamic Stall on Vertical Axis Wind Turbines, Creating a Benchmark of VAWTS in Dynamic Stall for Validating Numerical Models*, Thesis, Delft University of Technology, Delft, The Netherlands (2015).

[83] D. Greenblatt, A. Ben-Harav, and H. Mueller-Vahl, *Dynamic stall control on a vertical-axis wind turbine using plasma actuators,* AIAA Journal **52** (2014), 10.2514/1.J052776.

[84] J. Edwards, L. A. Danao, and R. Howell, *Piv measurements and cfd simulation of the performance and flow physics of a small scale vertical axis wind turbine,* Wind Energy **18**, 201 (2013).

[85] V. del Campo, D. Ragni, D. Micallef, B. Akay, F. J. Diez, and C. J. Simão Ferreira, *3d load estimation on a horizontal axis wind turbine using spiv,* Wind Energy **17**, 1645 (2013).

[86] V. del Campo, D. Ragni, D. Micallef, F. J. Diez, and C. J. Simão Ferreira, *Estimation of loads on a horizontal axis wind turbine operating in yawed flow conditions,* Wind Energy **18**, 1875 (2014).

[87] F. Noca, D. Shiels, and D. Jeon, *Measuring instantaneous fluid dynamic forces on bodies, using only velocity fields and their derivatives,* Journal of Fluids and Structures **11**, 345 (1997).

[88] F. Noca, D. Shiels, and D. Jeon, *A comparison of methods for evaluating time-dependent fluid dynamic forces on bodies, using only velocity fields and their derivatives,* Journal of Fluids and Structures **13**, 551 (1999).

[89] C. Ferreira, G. J. W. van Bussel, G. A. M. van Kuik, and F. Scarano, *On the use of velocity data for load estimation of a vawt in dynamic stall,* Journal of Solar Energy Engineering **133**, 8 (2011).

[90] B. LeBlanc and C. Ferreira, *Estimation of blade loads for a variable pitch vertical axis wind turbine with strain gage measurements,* Wind Energy **25**, 1030 (2022), https://onlinelibrary.wiley.com/doi/pdf/10.1002/we.2713 .

[91] P. C. Klimas and M. H. Worstell, *Effects of Blade Preset Pitch / Offset on Curved-Blade Darrieus Vertical Axis Wind Turbine Performance*, Report SAND81-1762 (Sandia National Laboratories, 1981).

[92] P. Vittecoq and A. Laneville, *The aerodynamic forces for a darrieus rotor with straight blades,* Journal of Wind Engineering and Industrial Aerodynamics **15**, 381 (1983).

[93] M. Rossander, E. Dyachuk, S. Apelfröjd, K. Trolin, A. Goude, H. Bernhoff, and S. Eriksson, *Evaluation of a blade force measurement system for a vertical axis wind turbine using load cells,* Energies **8**, 5973 (2015).

[94] E. Dyachuk, M. Rossander, A. Goude, and H. Bernhoff, *Measurements of the aerodynamic normal forces on a 12-kw straight-bladed vertical axis wind turbine,* Energies **8**, 8482 (2015).

[95] A. Goude and M. Rossander, *Force measurements on a vawt blade in parked conditions,* Energies **10**, 15 (2017).

[96] D. De Tavernier, C. Ferreira, U. S. Paulsen, and A. H. Madsen, *The 3d effects of a vertical-axis wind turbine: rotor and wake induction,* in *The Science of Making Torque from Wind (TORQUE 2020)*, Vol. 1618, The Science of Making Torque from Wind (TORQUE 2020) (IOP Publishing, 2020 Published) p. 11.

[97] A. J. Wheeler and A. R. Ganji, *Introduction to Engineering Experimentation*, 2nd ed. (Pearson Education, New Jersey, 2004).

[98] N. Instruments, *Measuring strain with strian gages,* (2019).

List of Publications

Journal and Conference Papers

26. **LeBlanc, B.**, Ferreira, C. *Estimation of blade loads for a variable pitch Vertical Axis Wind Turbine with strain gage measurements.* Wind Energy, 10.1002/we.2713, **25**, 6,(1030-1045),(2022).

25. **LeBlanc, B.**, Ferreira, C. *Estimation of blade loads for a variable pitch Vertical Axis Wind Turbine from Particle Image Velocimetry*. Wind Energy. 2022; 25(2): 313-332. doi:10.1002/we.2674

24. Viré, A., **LeBlanc, B.**, Steiner, J., & Timmer, N. *Experimental study of the effect of a slat on the aerodynamic performance of a thick base airfoil*, Wind Energ. Sci. 7,573-584, 2022. doi:10.5194/wes-7-573-2022

23. Brandetti, L., Avallone, F., De Tavernier, D., **LeBlanc, B.**, Ferreira, C., Casalino, D. *Assessment through high-fidelity simulations of a low-fidelity noise prediction tool for a vertical-axis wind turbine.* Renewable Energy. RENE-D-21-01240. *In Review*, 2021.

22. De Tavernier, D., Ferreira, C., Vire, A.,**LeBlanc, B.**, & Bernardy, S. *Controlling dynamic stall using vortex generators on a wind turbine airfoil.* Renewable Energy, 172, 1194-1211. doi:10.1016/j.renene.2021.03.019, 2021.

21. **LeBlanc, B.**, & Ferreira, C. *Experimental Demonstration of Thrust Vectoring with a Vertical Axis Wind Turbine using Normal Load Measurements* The Science of Making Torque from Wind (TORQUE 2020), Delft, The Netherlands. doi:10.1088/1742-6596/1618/5/052030, 2020.

20. Brandetti, L., De Tavernier, D., **LeBlanc, B.**, & Ferreira, C. *Experimental test of variable loads on a vertical-axis wind turbine.* The Science of Making Torque From Wind (TORQUE 2020), Delft, The Netherlands. doi:10.1088/1742-6596/1618/3/032037, 2020.

19. **LeBlanc, B.**, & Ferreira, C. *Experimental characterization of H-VAWT turbine for development of a digital twin* North American Wind Energy Association / Windtech, Amherst, MA, USA. doi:10.1088/1742-6596/1452/1/012057, 2019.

18. **LeBlanc, B. P.**, & Ferreira, C. S. *Experimental Determination of Thrust Loading of a 2-Bladed Vertical Axis Wind Turbine* The Science of Making Torque from Wind, Milan, Italy, doi:10.1088/1742-6596/1037/2/022043, 2018.

17. **LeBlanc, B. P.**, & Ferreira, C. S. *Overview and Design of PitchVAWT: Vertical Axis Wind Turbine With Active Variable Pitch for Experimental and Numerical Comparison* AIAA SciTech Forum Wind Energy Symposium, Kissimmee, Florida, doi:10.2514/6.2018-1243, 2018.

16. Huijs, F., Vlasveld, E., Gormand, M., Savenije, F., Caboni, M., **LeBlanc, B. P.**, Ferreira, C. S., Lindenburg, K., Gueydon, S., Otto, W., & Paillard, B. *Integrated design of a semi-submersible floating vertical axis wind turbine (VAWT) with active blade pitch control* EERA DeepWind 2018, 15th Deep Sea Offshore Wind R&D Conference, Trondheim, Norway. doi:10.1088/1742-6596/1104/1/012022, 2018.

15. Berg, J. C., Bryant, J., **LeBlanc, B. P.**, Maniaci, D., Naughton, B., Paquette, J. A., & Resor, B. R. *Scaled Wind Farm Technolgy Facility Overview* AIAA SciTech Forum / 32nd ASME Wind Energy Symposium, National Harbor, Maryland, 2014.

14. **LeBlanc B.**, Cloutier D., & Marinone T. *Overview of the Dynamic Characterization at the DOE/SNL SWiFT Wind Facility.* In: Allen M., Mayes R., Rixen D. (eds) Dynamics of Coupled Structures, Volume 1. Conference Proceedings of the Society for Experimental Mechanics Series. Springer, Cham. doi:10.1007/978-3-319-04501-6_32, 2014.

13. Marinone T., Cloutier D., **LeBlanc B.**, Carne T., & Andersen P. *Artificial and Natural Excitation Testing of SWiFT Vestas V27 Wind Turbines.* In: Allen M., Mayes R., Rixen D. (eds) Dynamics of Coupled Structures, Volume 1. Conference Proceedings of the Society for Experimental Mechanics Series. Springer, Cham. doi:10.1007/978-3-319-04501-6_33, 2014.

12. Marinone T., Cloutier D., & **LeBlanc B.** *Modal Testing and Model Validation Issues of SWiFT Turbine Tests.* In: Allen M., Mayes R., Rixen D. (eds) Dynamics of Coupled Structures, Volume 1. Conference Proceedings of the Society for Experimental Mechanics Series. Springer, Cham. doi:10.1007/978-3-319-04501-6_36, 2014.

11. Marinone T., Cloutier D., Napolitano K., **LeBlanc B.** *Comparison of Multiple Mass Property Estimation Techniques on SWiFT Vestas V27 Wind Turbine Nacelles and Hubs.* In: Allen M., Mayes R., Rixen D. (eds) Dynamics of Coupled Structures, Volume 1. Conference Proceedings of the Society for Experimental Mechanics Series. Springer, Cham. doi:10.1007/978-3-319-04501-6_31, 2014.

10. Niezrecki, C., Avitabile, P., Chen, J., Sherwood, J., Lundstrom, T., **LeBlanc, B.**, Hughes, S., Desmond, M., Beattie, A., Rumsey, M., Klute, S. M., Pedrazzani, R., Werlink, R., & Newman, J. *Inspection and monitoring of wind turbine blade-embedded wave defects during fatigue testing.* Structural Health Monitoring, 13(6), 629–643. doi:10.1177/1475921714532995, 2014.

9. Manzato S., White J.R., **LeBlanc B.**, Peeters B., Janssens K. *Advanced Identification Techniques for Operational Wind Turbine Data.* In: Allemang R., De Clerck J., Niezrecki C., Wicks A. (eds) Topics in Modal Analysis, Volume 7. Conference Proceedings of the Society for Experimental Mechanics Series. Springer, New York, NY. doi:10.1007/978-1-4614-6585-0_19, 2014.

8. Manzato, S., Santos, F., Peeters, B., **LeBlanc, B. P.**, & White, J. R. *Combined accelerometers-strain gauges Operational Modal Analysis and Application to Wind Turbine Data.*IX International Conference on Structural Dynamics, Porto, Portugal, 2014.

7. **LeBlanc, B.**, Niezrecki, C., Avitabile, P., Chen, J., & Sherwood, J. *Damage detection and full surface characterization of a wind turbine blade using three-dimensional digital image correlation.* Structural Health Monitoring, 12(5–6), 430–439. doi:10.1177/1475921713506766, 2013.

6. Manzato, S., White, J.R., **LeBlanc, B.**, & Peeters, B. *Development of techniques for enhanced operational modal analysis of wind turbine.* 5th International Operational Modal Analysis Conference, IOMAC 2013, 9–9, 2013.

5. Marinone T., **LeBlanc B.**, Harvie J., Niezrecki C., Avitabile P. *Modal Testing of 9 m CX-100 Turbine Blades.* In: Mayes R. et al. (eds) Topics in Experimental Dynamics Substructuring and Wind Turbine Dynamics, Volume 2. Conference Proceedings of the Society for Experimental Mechanics Series. Springer, New York, NY. doi:10.1007/978-1-4614-2422-2_31, 2012.

4. **LeBlanc B.**, Niezrecki C., Avitabile P., Sherwood J., & Chen J. *Surface Stitching of a Wind Turbine Blade Using Digital Image Correlation.* In: Allemang R., De Clerck J., Niezrecki C., Blough J. (eds) Topics in Modal Analysis II, Volume 6. Conference Proceedings of the Society for Experimental Mechanics Series. Springer, New York, NY. doi:10.1007/978-1-4614-2419-2_27, 2012.

3. Thibault L., **LeBlanc B.**, & Avitabile P. *Hybrid Sets of Merged Data for Modal Model Applications.* In: Proulx T. (eds) Linking Models and Experiments, Volume 2. Conference Proceedings of the Society for Experimental Mechanics Series. Springer, New York, NY. doi:10.1007/978-1-4419-9305-2_11, 2011.

2. **LeBlanc, B.**, Niezrecki, C., Avitabile, P., Chen, J., Sherwood, J., & Hughes, S. *Full-Field Inspection of a Wind Turbine Blade Using Three-Dimensional Digital Image Correlation* Industrial and Commercial Applications of Smart Structures Technologies 2011, San Diego, California, 2011.

1. **LeBlanc, B.**, Niezrecki, C., & Avitabile, P. *Structural health monitoring of helicopter hard landing using 3D digital image correlation* (Vol. 7650). SPIE. doi:10.1117/12.847318, 2010.

Technical Reports

4. **LeBlanc, Bruce Philip**, & Paquette, Joshua. *Description and Analysis of the Hardware Safety Systems for the DOE/SNL SWiFT Wind Turbines..* United States. SAND2016-0666. doi:10.2172/1603857, 2016.

3. White, Jonathan, **LeBlanc, Bruce Philip**, Berg, Jonathan Charles, Bryant, Joshua, Johnson, Wesley D., & Paquette, Joshua. *Sandia SWiFT Wind Turbine Manual.* United States. SAND-2016-0746. doi:10.2172/1432434, 2016.

2. Resor, Brian Ray, & **LeBlanc, Bruce Philip**. *An aeroelastic reference model for the SWIFT turbines.* United States. SAND-2014-19136. doi:10.2172/1503792, 2014.

1. Karlson, Benjamin, **LeBlanc, Bruce Philip.**, Minster, David G, Estill, Milford, Miller, Bryan Edward, Busse, Franz, Keck, Chris, Sullivan, Jonathan, Brigada, David, Parker, Lorri, Younger, Richard, & Biddle, Jason. *IFT&E Industry Report Wind Turbine-Radar Interference Test Summary.* SAND2014-19003. United States. doi:10.2172/1163088, 2014.

Presentations & Lectures

6. Ferreira, C. **LeBlanc, B.**, Huang, M. *Introduction to Advanced Topics in Vertical Axis Wind Turbine Aerodynamics*. VKI Lecture series, Sint-Genesius-Rode, Belgium. 2022

5. **LeBlanc, B.**, Ferreira, C. *Variation of rotor loading and wake development due to fixed pitch offsets in Vertical Axis Wind Turbines*. 387. Wind Energy Science Conference, Cork, Ireland. 2019.

4. Savenije, F., **LeBlanc, B.**, Pieterse, E., Lever, H. *Aeroelastic analysis of a VAWT with Δ-wing.* Wind Energy Science Conference, Cork, Ireland. 2019.

3. Leroy Vincent, **Bruce LeBlanc.** *Senior PhD Workshop: Vertical Axis Wind Turbines.*. 14th EAWE PhD Seminar on Wind Energy, Sep 2018, Brussel, Belgium. hal-0287982, 2018.

2. **LeBlanc, B.P.**, de la Garza Cuevas, R., Ferreira, C. *Experimental characterization of individual pitch controlled vertical axis wind turbine*. 1440 Wind Energy Science Conference. Lyngby, Denmark. 2017.

1. **LeBlanc, Bruce Philip**, & White, Jonathan. *DOE / SNL Scaled WInd Farm Technology (SWIFT) Facility at TTU.* United States, SAND2012-2422C, 2012.

Data sets

2. **LeBlanc, B.**, Vire, A., Steiner, J., Timmer, N., Langedijk, E., & Bernardy, S.. *ABIBA Airfoil and Slat Measurement Data* (Version 2). 4TU.ResearchData. doi:10.4121/14170442.v2, 2021.

1. **LeBlanc, B.**, & Ferreira, C.. *PitchVAWT Data* (Version 0). 4TU.ResearchData. doi:10.4121/c.5287879, 2021.

Curriculum Vitæ

Bruce LeBlanc

18-02-1987	Born in East Templeton, Massachusetts.

Education

2001–2005	High School Narragansett Regional High School Baldwinville, Massachusetts
2005–2009	Bachelor of Science Mechanical Engineering University of Massachusetts Lowell Lowell, Massachusetts
2009–2011	Master of Science Mechanical Engineering - Structural Dynamics University of Massachusetts Lowell Lowell, Massachusetts
Thesis	Non-destructive Inspection of Wind Turbine Blades with three-dimensional Digital Image Correlation
Advisor	Prof. Dr. C. Niezrecki
2016–2020	PhD Aerospace Engineering Delft University of Technology Delft, The Netherlands
Thesis	Dynamics of the Pitchable Vertical Axis Wind Turbine
Promotors	Prof. Dr. Carlos Ferreira & Prof. Dr. Gerard van Bussel

Experience

2008–2009	Assistant Design and Manufacturing Engineer Trelleborg Sealing Solutions Northborough, Massachusetts
2009–2011	Graduate Research Assistant Structural Dynamics and Acoustic Systems Laboratory University of Massachusetts Lowell Lowell, Massachusetts
2009–2010	Research Participant Program National Renewable Energy Laboratory Boulder, Colorado
2011–2016	(Senior) Member of Technical Staff Sandia National Laboratories Albuquerque, New Mexico
2016–2021	PhD Researcher Wind Energy Delft University of Technology Delft, The Netherlands
2021–Present	Senior Loads and Controls Engineer Conceptual Blade Development Siemens Gamesa Renewable Energy Boulder, Colorado